INFLUENCE OF FLOW AND GEOMETRIC PARAMETERS ON FILM-COOLING

by

Clement Olaloye Folayan

(N.C.E., B.Sc., M.Sc., D.I.C.)

Thesis submitted for the degree of Doctor of Philosophy in the Faculty of Engineering, University of London.

September 1976

ABSTRACT

Experimental investigations of the influence of flow and geometric parameters on the effectiveness and heat transfer coefficient downstream of two dimensional slots and three-dimensional discrete hole film-cooling slots are presented. For two dimensional slots the influence of longitudinal curvature, slot height, velocity ratio and density ratio are quantified. The three-dimensional slots employed tangential, normal and combined tangential and normal holes. The influence of velocity ratio, density ratio, lip length, lip thickness, open area, open area ratio, pitch-diameter, distance of normal holes to the exit of the tangential holes and ratio of tangential momentum to normal momentum are separately examined.

A two-dimensional procedure to predict the effectiveness downstream of curved surfaces, of multiple slots and on conical walls is described. A finite difference solution of a time-averaged form of the Navier Stokes equations is used to calculate effectiveness and heat transfer downstream of the three-dimensional slots. The relevance of the calculations to practical film cooled combustion chambers is examined.

Experimental and theoretical investigations of impingement cooling are described, and the use of impingement as a way of enhancing film-cooling performance is assessed.

ACKNOWLEDGEMENTS

I wish to express my sincere gratitude to Professor J.H. Whitelaw whose direction, advice, encouragement and excellent supervision were invaluable throughout this research. His interest in my social and academic problems are gratefully acknowledged. I regard working with Professor Whitelaw as a great priviledge.

I shall always be indebted to my wife; Elizabeth Adeniyo whose moral support and encouragement meant more to me than I can express. I am grateful to my brother Moses Adegboye who takes care of my daughter in Nigeria during this research. The encouraging letters from members of my family and friends in Nigeria are gratefully acknowledged.

I wish to thank Mr. Bob King, Mr. O. Vis, Mr. L. Varty and the technical staff in general for their help at all times. My thanks are also due to Miss E.M. Archer and the library staff for cheerfully allowing me unlimited use of departmental library facilities.

I would like to express my thanks to many of my colleagues with whom I have had many useful discussions. I thank Mr. E. Kha Iil for his help in the use of the TEACH programme for calculating impinging flow characteristics.

Finally, I thank the Nigeria Federal Military Government and the British Ministry of Defence for providing the financial support.

My sincere thanks are due to my mother, Elizabeth Oyadoyin, especially for help during my Secondary school years. I dedicate this thesis to my late father, Joseph Oyadiji, who worked hard in order that all his children might receive good education.

C O N T E N T S

CHAPTER ONE

INTRODUCTION

1.1 The Problem Considered

The work reported in this thesis concerns film-cooling which is a method of protecting surfaces exposed to hot gas streams by injecting cool gas along the surface to form a film. The film acts as a thermal sink and reduces the mean boundary layer temperature. The increase in thermal boundary layer thickness, due to the cold film, reduces the convective heat transfer to the wall. The film may also act as radiation sink if its radiation absorbtivity is high.

Although film-cooling has been applied to many engineering situations, the present research is related to combustion chamber design. Figure 1.1 shows typical variations of flow properties through different stages of a jet engine and indicates that the flame temperature in the combustor may rise above $2000^{o}K$. Experience (4) has shown that, when metal temperatures exceed $1200^{o}K$, metallurgical properties such as creep strength, fatigue and oxidation resistance fall rapidly. For long combustor life it is necessary to keep the wall temperatures below that at which desirable metallurgical properties fall rapidly. A method of achieving this is to use a film cooling device.

Other methods of reducing the wall temperature include convection cooling, ablation cooling and transpiration cooling. Comparison of convection, film and transpiration cooling(113) has shown that convective cooling is less effective than film cooling. Transpiration cooling, as discussed by Whitelaw(113) poses many metallurgical problems and because ablation materials cannot

always be recovered, it is used only in rocket engines. The combustor designer is, thus, required to optimise film cooling arrangements perhaps in conjunction with convection and impingement in terms of cooling performance and cost.

In assessing the performance of a film cooling design it is convenient to define the adiabatic-wall effectiveness and the heat-transfer coefficient, as performance criteria. The adiabatic-wall effectiveness is defined as:

$$\eta = \frac{(T_{aw} - T_G)}{(T_c - T_G)} \quad \text{cp constant} \qquad (1.1.1)$$

and represents a measure of preservation of the cooling film in the absence of radiation and chemical reaction. Due to difficulties in obtaining an adiabatic wall, a mass transfer analogy may be used to obtain related information. For such tests, an impervious-wall effectiveness is defined as:

$$\eta = \frac{(m_w - m_G)}{m_c - m_G} \qquad (1.1.2)$$

The effectiveness obtained from equations 1.1.1 and 1.1.2 are equal provided the effective Lewis number equals unity. The second quantity often used for assessing performance is defined as:

$$h_f = \frac{q_w''}{(T_w - Taw)} \qquad (1.1.3)$$

and may be regarded as a measure of resistance of the cold film to heat transfer.

Extensive experimental and numerical investigations of the three quantities defined above have previously been reported (12, 37,44,77) although the assumptions of negligible radiation and

chemical reaction do not apply to real combustors. The major factors affecting film cooling performance are: film cooling slot geometry, cooling film fluid properties, hot stream fluid properties and combustor geometry. The present research quantifies the influences of these factors, in order to provide optimization criteria.

1.2 Specific Objectives of present research

The specific objectives of the research were as follows:

1. To measure the effectiveness of two-dimensional, film-cooling slots over curved walls.
2. To develop a numerical procedure to calculate film cooling effectiveness over curved walls, film cooling effectiveness of multiple slots and film cooling effectiveness over conical walls.
3. To perform a systematic experimental investigation of the influences of important flow and geometric parameters on the effectiveness and heat transfer characteristics of three-dimensional film cooling slots employing normal and tangential injection.
4. To develop a numerical procedure to represent the influences determined in 3.
5. To perform an experimental and theoretical investigation of impingement cooling and to assess the advantages of impingement as a means of enhancing the performance of film cooling arrangements.

1.3 Outline of the thesis

The following chapter contains a brief literature review with particular emphasis on the influences of major parameters. The review indicates a lack of systematic investigation of performance

of normal and combined normal and tangential film cooling arrangements.

Chapter 3 presents results of the present research on the influence of longitudinal curvature and film build up. Limited calculations were presented on the stretching of films. Chapter 4 relates to an experimental and numerical investigation of three-dimensional discrete-hole cooling and, Chapter 5 describes the experimental and numerical investigation of the heat transfer characteristics of two-dimensional plane impinging jets.

Chapter 6 presents calculated wall temperatures resulting from two-dimensional slots, combined normal and tangential slots, and an arrangement of impingement followed by combined normal and tangential injection. Chapter 7 presents brief conclusions and makes suggestions for further work.

CHAPTER TWO

2.0 LITERATURE SURVEY

Introduction

Detailed reviews of previous film-cooling investigations up to 1971 may be found in references 37,77 and 89. The purpose of the present review is to identify film cooling conditions which have previously been investigated and to determine the direction for further research. The review provided below is sub-divided into: experimental two-dimensional film-cooling, experimental three-dimensional film-cooling and theoretical two and three-dimensional film-cooling investigations.

Sections 2.1 and 2.3 show that detailed measurements and calculations of two dimensional film cooling slots are available. It is however demonstrated that the influences of longitudinal curvature, multiple slots and shape of combustor exit have not been investigated systematically.

Reference 89 describes experimental investigations of three-dimensional film-cooling slots up to 1972. Table 2.2.2 shows that, except for investigations on full coverage cooling, there has been little addition to the list provided in reference 89. A critical review of available numerical procedures is provided in 89.

Some of the references mentioned in this review have been reviewed before (37,77,89) but are mentioned here for completeness.

2.1 PREVIOUS EXPERIMENTAL INVESTIGATIONS OF TWO-DIMENSIONAL FILM-COOLING

Figure 2.1.1 shows some two-dimensional film cooling geometries that have been used for previous investigations. The important flow and geometric variables are indicated. Table 2.1.1 gives details of some of the previous works. The references in table 2.1.1 are specially selected to indicate parameters of major influence for two dimensional film-cooling effectiveness and heat transfer.

For slots with tangential injection, the investigations of Kacker and Whitelaw (45), Pai and Whitelaw (79) and Sivasegaram et al (98) show that, for thin lip slots ($t/y_c < 0.2$), a near unity velocity ratio resulted in maximum effectiveness for unity density ratio. Further investigations by Pai and Whitelaw (79) showed that for density ratios greater than unity, increase in mass flux ($\rho_c U_c/\rho_G U_G$) beyond two led to increasingly smaller increase in effectiveness. For $\rho_c/\rho_G < 1$, the effectiveness increases monotonically with increase in velocity ratio.

The experiments of Pai and Whitelaw (79), Burns and Stollery (12) cover the range $0.069 < \rho_c/\rho_G < 4.17$. Both investigations using tangential injection show that it is advantageous to blow heavier gas at a particular velocity ratio. Pai and Whitelaw (79) indicated further that advantage of high density ratio is maintained only when the mass flux ratio is greater than or equal to 2.

A systematic investigation of theinfluence of slot lip thickness reported by Kacker and Whitelaw (46) showed that an increase in lip thickness reduces effectiveness. This trend was confirmed by Sivasegaram et al

Table 2.1.1.

Previous Experimental Investigations of two-dimensional slots

AUTHOR	YEAR	GEOMETRY	INITIAL CONDITIONS U_C/U_G	ρ_C/ρ_G	t/y_C	δ_G/y_C	θ	$\sqrt{u^2}/U_G$	K_P	M	K	REMARKS
Kacker & Whitelaw (45,46)	1968 1969	Fig2.1.1a	3-2.7	1	0.04-	1-3	-	0.04-0.085	-	-	-	Maximum η at $\frac{U_C}{U_G} \simeq 1$ when $t/y_C < 0.2$ Influence of $\sqrt{u^2}/U_G$ is small.
Sivasegaram & Whitelaw (98)	1969	Fig2.1.1a & c	0.4-5	1	0.05-1.6	-	30^o 60^o 90^o	-	-	-	-	For $t/y_C > 0.4$, maximum in η for $U_C/U_G \simeq 1$ disappeared. η decreased as t/y_C increased. η decreased as θ increased (See Fig. 2.2.2)
Pai & Whitelaw (78)	1970	Fig2.1.1a	.3-3.1	0.069-4.17	-	-	-	-	-1. 1.-3≃3 *10^{-6}	-	-	For $\rho_C/\rho_G < 1.0$, η increased with increased U_C/U_G. For $\rho_C/\rho_G = 1.0$, maximum η at $\frac{U_C}{U_G} \simeq 1$. For $\rho_C/\rho_G > 1$. Maximum η at $\rho_C U_C/\rho_G U_G \simeq 2$ Increased $-\frac{dP}{dx}$ decreased η.
Artt, Brown & Miller (2)	1970	Fig2.1.1c	.32-1.0	1	-	-	15^o 30^o	-	-	-	-	There may be an optimum slot injection angle. Injection through angled slots can be correlated into single curves by suitable choice of empirical relation
Burns & Stollery (12)	1969	Fig2.1.1a	0.5-4.0	0.14-4.17	0-2.	0.9 2.54	-	-	-	-	-	η increased with ρ_C/ρ_G. Increased δ_G/y_C and t/y_C decreased η.

Table 2.1.1 Contd.

AUTHOR YEAR	GEOMETRY	U_C/U_G	ρ_C/ρ_G	t/y_C	δ_G/y_C	β or θ	$\sqrt{u^2}/U_G$	K_p	M	K	REMARKS
Carlson & Talmor (13) 1968	Fig2.1.1c and d	0.19 -0.9	2.76	-	-	$\theta=20^o$ $\beta=30^o$, 45^o, 60^o	3% - 22%	-	-	-	η decreased as β increased η decreased as $\sqrt{u^2}/U_G$ increased
Matthews (58) 1973	Fig2.1.1 c,d,e	.7- 2.0	1,2	.125	-	$\beta=30^o$ 45^o $\theta=30^o$ 45^o	-	-	-	-	same as above. Also η increased as ρ_C/ρ_G. η decreased with increase y_L. η decreased as θ increased
Smith (100) 1974	Fig2.1.1 c	-	1.7 -3.3	-	-	30^o	-	-	0.2 .5 .7	-	Momentum flux ratio correlates results better than mass flux
FosterR.C. &Sheikh H. (28) 1975	Fig2.1.1 c	0-1.14	1	-	-	90^o	-	-	-	-	Normal injection may cause separation and reduced effectiveness

(98) and by Burns and Stollery (12). Nina (73) demonstrated that reducing the effective lip thickness by tapering the lip led to improved effectiveness. Although above investigations show that lip thickness is detrimental to high effectiveness and increases wall heat transfer, combustors use reasonable sizes ($0.3 < t/y_c < 0.8$) to ensure structural stiffness and to prevent the lip from burning off. A finite lip may prevent the possibility of near wall combustion but may also provide a flame stabilizer at an undesirable location.

Pai and Whitelaw (79), and Harnett (41) have demonstrated that the influence of longitudinal pressure gradient on slot effectiveness is small except close to laminarisation ($K_p > 3.3 * 10^{-6}$). A favourable pressure gradient tends to reduce effectiveness while an adverse pressure gradient tends to result in increased effectiveness. Harnett (41), Nicoll and Whitelaw (118) and Stollery and El-Ehwany (106) have provided correlations to include influence of longitudinal pressure on slot effectiveness. For the configuration 2.1.1d, Matthews (58) demonstrated that favourable pressure gradient decreased effectiveness.

Kacker (44), and Burns and Stollery (12) have demonstrated that thick upper lip boundary layers reduced effectiveness when t/y_c is small. When the slot lip is thick, its influence overshadows any influence due to upper lip boundary layer thickness.

The measurements of Kacker and Whitelaw (45) show that the influence of slot turbulence intensity is small. Carlson and Talmor (13) found that increasing the free stream turbulence intensity reduced the adiabatic wall effectiveness. The difference in measured trends may be caused by differences in flow arrangements and free stream scale of turbulence.

The review by Goldstein (37) tends to indicate that supersonic conditions resulted in a longer length immediately downstream of slot exit where the effectiveness is close to unity although further downstream the effectiveness diminishes more rapidly with distance than with subsonic film cooling. Barry's (5) comparison indicated that compressibility exerts its influence on effectiveness through the shock pattern at slot exit.

Pai (77) and Kacker (44) have separately investigated the influence of slot flow velocity profiles. They found that a fully developed velocity profile led to faster decrease in effectiveness.

For slots (Figure 2.2.1c,d) in which the two streams meet at an angle, Sivasegaram (98), Matthews (58) and Metzger (63) have shown that increasing angle decreases the effectiveness and increases the heat transfer coefficient. The investigations by Artt et al (2) indicated that there may be an optimum injection angle because injection at 30^{o} was found to be more effective than injection at 15^{o}. The measurements of Matthews (58) and Artt et al (2) are in close agreement for 30^{o} injection. For a 90^{o} injection, Foster et al (28) demonstrated that there is a separated region immediately downstream of slot. In this region the effectiveness is low and the heat transfer coefficient is high.

The review so far has not discussed the influence of surface curvature although surface curvature in the flow direction is relevant to the upstream region of combustors where concave surfaces require to be cooled and to the downstream flare where the cooling of concave and convex surfaces may be necessary. It is also relevant to gas turbine blade cooling. Bradshaw's review (11) shows that stream line curvature has a significant influence on the

aerodynamic properties of wall jets. Thoman (110), Dannenberg (37) have shown that convex surfaces can result in heat transfer coefficients which are 20% less than those for corresponding flat plate, while a concave surface resulted in 20% increase in heat transfer coefficients. Thoman and Dannenberg performed their experiments at Mach numbers of 2.8 and 10 respectively. To the author's knowledge the influence of longitudinal wall curvature on effectiveness at moderate coolant velocities have not been investigated.

The experiments of Chin et al (14) concerns adiabatic wall effectiveness downstream of multiple slots. Measured effectiveness downstream of last slot were presented. Warner and Guinn (111) also demonstrated that a dual jet arrangement is more effective than a single jet. Although Chin et al experiments are informative of the influence of film build up, it is difficult to determine the best slot spacing required for the requirement of a minimum effectiveness.

The slot geometry shown on figure 2.1.1d (tangential injection along converging walls) approximately represents the exit section of a gas turbine combustor. The flows in the section are characterised by non coincidence of direction of the secondary and the main flow, longitudinal and normal pressure gradients and the free stream acceleration. These influences are inter related and it is difficult to separate them. In fact, the typical combustor flare is conical at this end. The influence of divergence due to conical flare on effectiveness have not been examined.

2.2 PREVIOUS EXPERIMENTAL INVESTIGATION OF THREE-DIMENSIONAL FILM-COOLING

Figure 2.2.1 illustrates typical three-dimensional film-cooling arrangements. When a set of discrete holes (with no impingement lip) are provided over all the surface to be cooled - it is called full coverage film cooling. Table 2.2.1 contains some of the available experimental investigations. The eight references on table 2.2.1 relate to discrete hole/full coverage cooling. The other references describe investigations of the performance of figure 2.2.1,b,c,d. In general, table 2.2.1 shows that the qualitative influences of U_C/U_G, ρ_C/ρ_G, t/y_C and θ are the same as for two-dimensional slots. However, three-dimensional slots introduce additional geometric parameters like pitch-diameter ratio, open area ratio, lip length and the inclination of the holes to z direction (α).

Discrete Holes/Full Coverage (Fig.2.2.1a)

The investigations of Goldstein et al (38) and Kruse (51) show that the effectiveness of a row of discrete holes tends to a maximum at a mass flux ratio $(\frac{\rho_C U_C}{\rho_G U_G})$ of 0.5. At higher blowing rates, jet penetration reduces effectiveness. At blowing rates less than 0.4 the effectiveness drops rapidly. The maximum effectiveness at blowing rate of 0.5 for a row of discrete holes without impingement lip is consistent with the findings of Eriksen et al (20) and Rastogi (89) who film cooled a cylinder in a cross flow with holes located at an angle to the mainstream.

The investigations of Launder et al (53), Crawford et al (16), Mayle and Camarata (59), Shvets et al (97) and Yefimchuk et al (117)

Table 2.2.1.

Previous Experimental Investigation of Discrete Holes/Full Coverage Film Cooling

AUTHOR	YEAR	GEOMETRY	INITIAL CONDITIONS U_C/U_G	ρ_C/ρ_G	y_G/D	α	θ	K_p	P/D	REMARKS
Goldstein et al (38)	1974	Fig2.2.2a cylindrical and beveled holes	0.5 -2.2	1,4.17	0.04	-	35^o	-	3,6	For the same flow rate, beveled holes are more effective. Cylindrical holes give maximum η at $\rho_C U_C/\rho_G U_G \simeq 0.5$. .Higher ρ_C/ρ_G give higher η but increase y_G/D give lower η.
Metzger (67)	1973	Full coverage	0.1, 0.2	1	-	-	90^o	-	4.8	Measured η agreed with calculations of super position of single holes
Launder & York (53)	1974	Full coverage	0-.53	1-4.17	-	-	45^o	0,2	8	Increase K_p delays transition to turbulence, improved η and reduces lateral spreading. Increase turbulence intensity may reduce η.
Crawford et al (16)	1975	Full coverage	0-1.3	1	-	-	30^o 90^o	-	5,10	St number decreased with θ. For $\theta=90^o$ low $\rho_C U_C/\rho_G U_G$ gave minimum St no in the initial region but downstream higher $\rho_C U_C/\rho_G U_G$ gave large reduction. For $\theta=30^o$, $U_C/U_G \simeq 0.4$ gave minimum St no in injection region.
Mayle & Camarata	1975	Full coverage	0 -2	1	-	30^o	45^o	-	8-14	Maximum η for $0.5 < \frac{U_C}{U_G} < 1.0$ for near injection region but maximum η at $\frac{U_C}{U_G} \simeq 1.5$ for downstream regions. For near injection, η decreased with increased P/D. The St no increased with U_C/U_G

19

Table 2.2.1 Contd.

INITIAL CONDITIONS

AUTHOR	YEAR	GEOMETRY	U_C/U_G	ρ_C/ρ_G	δ_G/D	α	θ	K_p	P/D	REMARKS
Shvets et al (97)	1973	Fig2.2.2a circular & rectangular holes	0.35 -1.7	1	-	-	30^o	-	-	Equivalent rectangular holes are more effective than circular holes. Equivalent two dimensional slots are the most effective.
Yefimchuk et al (117)	1973	Circular holes, beveled holes	.35	≃2.2	-	-	12^o	-	-	Cooling effectiveness at blade trail ing edge was insensitive to slot geometry but increased with increas-ed blowing rate
Kruse (51)	1974	Fig2.2.2a	0-3	≃1	1	-	30^o 90^o	-	2.5,5	Increased θ reduced η. 2 row inject-ion more effective than single row. 90^o injection may cause near slot separation

relate to full coverage cooling. Table 2.2.1 shows that effectiveness decreases with increasing angle and increasing pitch-diameter ratio. Mayle et al (59) also indicates that increasing pitch-diameter ratio increases the heat transfer coefficients.

A comparison of the performance of two dimensional slots, two rows of discrete holes and two rows of rectangular holes by Shvets et al(97) showed that the rectangular holes was more effective than the circular holes. The two dimensional slot was the most effective. Goldstein et al (38) also demonstrated that beveled cylindrical holes are more effective than cylindrical holes. This is because of the increased open area and reduced exit velocity.

The experimental results of Launder and York (53) show that for initially laminar situations, a favourable pressure gradient may delay transition to turbulence with the consequent increase in effectiveness.

The contributions presented on table 2.2.2 relates to configurations on figures 2.2. b,c,d. In addition to the parameters presented on table 2.2.1, these geometries introduce the influences of lip length, open area ratio, height of backward facing step and lip thickness. Except for the contributions of Metzger (66) and Rastogi and Whitelaw (91), the contributions by Nina and Whitelaw (74), Palmer (80), Nobbs and Rice (75) have been reviewed in great detail in 89.

Total Head Cooling (Fig.2.2.1b)

For total head cooling, the investigations of Nina and Whitelaw (75), Rastogi and Whitelaw (91) show that increasing lip length, velocity ratio, density ratio and number of rows of holes leads to improved effectiveness while increasing lip thickness, pitch-

Table 2.2.2

Previous Experimental Investigation of normal, tangential or combined normal and tangential Three-Dimensional Film Cooling Arrangements

			INITIAL CONDITIONS						
AUTHOR	YEAR	GEOMETRY	U_C/U_G	ρ_C/ρ_G	L/y_C	t/y_C	P/D	K_p	REMARKS
Nobb & Rice (75)	1968	Fig2.2.2d	8 -4	1	4.8	0.2-0.5	2	-	η decrease as t/y_C increased
Nina & Whitelaw (74)	1971	Fig2.2.2b and d	.3- 2.5	1	0 -4.	0.125 0.5	1.22 -3.45	-	η increased as L/y_C increased η decreased as P, and t/y_C increased
Metzger (67)	1972	Fig2.2.2c	.49 -1.55	1	4 .5.5	.4 -.8	2-6	-	η increased as A_0/A, L/y_C increased η decreased as P/D increased
Rastogi& Whitelaw (91)	1973	Fig2.2.2b and 3 rows of tangential holes	.3 -2.	1,2, 4.17	0	0.2 -0.85	1.4, 2	-	η increased with decreased P/D, t/y_C η increased with increased ρ_C/ρ_G, U_C/U_G $\frac{A_0}{A}$ and number of row of holes

diameter ratio and height of backward facing step decreases the effectiveness. A comparison of total head cooling devices in high temperature flows by Juhasz et al (43) suggest that the lip thickness is the most important geometric parameter. It may be noted here that the investigation of Rastogi and Whitelaw (91) on total head cooling is detailed enough to allow optimisation of total head cooling rings.

Normal Injection Cooling (Fig. 2.2.2c)

The investigations of Palmer (80) and Metzger (66) concerned the performance of normal injection cooling with and without a convoluted wiggle strip. Comparison of normal injection cooling with total head cooling by Palmer indicated the former was more effective. This conclusion must be taken with caution as the geometries compared can not be described as equivalent in many respects. Metzger (66) noted that the effectiveness increases with lip length and open area ratio. Metzger's(66) results were not detailed enough to allow further deductions.

Combined Normal and Tangential Cooling (Fig. 2.2.2d)

The investigations of Nobbs and Rice (75) and Nina and Whitelaw (74) on combined normal and tangential cooling showed that effectiveness decreases with increase in lip thickness, but increases with velocity ratio. The comparisons of combined normal and tangential cooling with total head cooling by Nina and Whitelaw (74) indicated that total head holes are more effective. They also noted that in line and staggered holes are equally effective.

From the above review it is obvious that there is no systematic information as regards the effectiveness and heat transfer

characteristics of normal and combined normal and tangential cooling. Both normal and combined normal and tangential cooling slots are in use in combustors. It is necessary to provide sufficient information on these film cooling slots in order to allow optimisation.

2.3 THEORETICAL INVESTIGATIONS

The previous sections have demonstrated the complexity of the influences affecting performance of film cooling arrangements. This has led to different approaches for calculating influences of various parameters in order to reduce the number of experiments. Kacker (44) classified available numerical methods as correlation, integral or differential methods.

2.3.1 CORRELATION & INTEGRAL METHODS

Detailed review of previous work using the heat sink or energy balance in a boundary layer are reviewed by Goldstein (37). The correlative approach like those of Weighardt and Spalding (37) are based on dimensional analysis, while the integral methods integrates the conservation equations by assuming the shape of velocity and temperature profiles. The uncertainties associated with correlation approaches means that they are not reliable outside the range of experimental data used to determine the correlation constants.

The integral methods results in improvement on correlations based on dimensional analysis. Because of the complexity of the flows no simple polynomial or

algebraic expression can represent the details of the film cooling flows. However these methods have been used successfully by Stollery and El-Ehwany (106), Nicoll and Whitelaw (118) and Artt et al (2) to calculate influences of various parameters including free stream acceleration and injection angle. The approach may qualitatively represent the influences but the absolute values must be regarded with caution.

2.3.2 THE DIFFERENTIAL METHODS

Differential methods solve numerically the partial differential equations for conservation of mass, momentum and enthalpy. Table 2.3.1 shows some of the finite difference procedures that have been applied to specific film cooling arrangements.

One method of solving the boundary layer forms of the Navier Stokes equations is to transform them to finite-difference forms which allow a marching solution. The marching solution requires no iteration as calculation proceeds downstream by forward steps. Starting with known initial conditions, the unknown are calculated for a short distance downstream. The calculated values then become upstream values and the front of computation moves downstream in the main direction of flow. This method is suitable for flow with no forward recirculation. The finite difference methods that employ the marching solution technique are described as parabolic in table 2.3.1. The terms 2D, 3D implies two dimensional and three dimensional respectively.

For flows with forward recirculation e.g. film-cooling slots with high backward facing step, marching solution can not be used,

Table 2.3.1

Previous Finite Difference Calculations for Film Cooling

AUTHOR	GEOMETRY	NUMERICAL PROCEDURE	PHYSICAL ASSUMPTION	CALCULATED PROPERTIES	CALCULATED INFLUENCES	COMMENT
Pai & Whitelaw (1971)	2D, $0.13<t/y_C<1.14$	2D, Parabolic	Prandtl mixing length	η, h, T	ρ_C/ρ_h, $\frac{U_C}{U_G}$, $\frac{dP}{dx}$, $\frac{\delta G}{y_C}$	Reasonable
Kacker & Whitelaw (1971)	2D, $0.13<t/y_C<1.14$	2D, Elliptic	Prandtl-Kolmogorov	η, U, k, Cf	t/y_C, $\frac{\delta G}{y_C}$, $\frac{U_C}{U_G}$	Greater details of flow
Matthews, Rastogi & Whitelaw (1971)	2D, with backward facing step	2D, parabolic 2D, Elliptic for $\frac{x}{y_C} < 20$	Prandtl-Kolmogorov	η	t/y_C, ρ_C/ρ_G, $\frac{U_C}{U_G}$	Good agreement for $\rho_C/\rho_G \simeq 1$
Metzger (1972)	2D, angled injection	2D, Parabolic	Prandtl mixing length	U, St, T		Reasonable
Matthews (1973)	2D, angled injection	2D, Elliptic	k-ε model	η, U, k	t/y_C, ρ_C/ρ_G, $\frac{U_C}{U_G}$	Good
Patankar &Spalding (1971)	3D, square tangential hole	3D, Parabolic	Laminar	η		Plausible
Patankar Rastogi & Whitelaw (1973)	3D, row of round holes, tangential to mainstream	3D, Parabolic	Prandtl mixing length	η	ρ_C/ρ_G, t/y_C, L/y_C Pi/D, $\frac{U_C}{U_G}$, $\frac{\delta_G}{D}$	Good

Table 2.3.1 Contd.

AUTHOR	GEOMETRY	NUMERICAL PROCEDURE	PHYSICAL ASSUMPTION	CALCULATED PROPERTIES	CALCULATED INFLUENCES	COMMENT
Bergeless et al (1975)	3D, Angled holes	3D, Semi-elliptic	Laminar	η,T,U		Plausible
Patankar &Spalding (1973)	3D,square and tangential hole	3D, Elliptic	k-ε, radiation and combustion	T,h		Plausible

because upstream flow is influenced by downstream flow. In such situations the differential equations are solved by iterative procedures (e.g. Gosman et al (40)) which accounts for both lateral and longitudinal diffusive fluxes. Such procedures are described as elliptic in table 2.3.1.

Differential methods need physical hypotheses for turbulent transport of momentum, heat and mass. Table 2.3.1 shows the hypotheses used by different authors. The Prandtl mixing length approach determines the effective viscosity through an algebraically prescribed turbulence length scale and the velocity gradient. The Prandtl-Kolmogorov assumption defines effective viscosity via a turbulence kinetic and a prescribed turbulence scale. The 'k-ε model' determines the effective viscosity from the turbulence kinetic energy and turbulence dissipation. Higher order turbulence model (e.g. a Reynolds stress model) are available in literature but since they have not been applied to film cooling problems they will not be described in this review.

Table 2.3.1 provides a summary of previous calculations using different numerical schemes. Pai and Whitelaw (78) used a parabolic procedure and obtained reasonable agreement between measurements and calculations. Kacker and Whitelaw (47) used an elliptic procedure for slots with thick lip. In order to reduce computing time, Matthews, Rastogi and Whitelaw (57) used elliptic procedures for distances less than 20 slot gaps and parabolic procedures for distances further downstream. This combination reduced computing time as opposed to elliptic procedures for geometry and distance under consideration. They obtained accurate results. Metzger's(68) used a

parabolic procedure to calculate effectiveness of a 20^{o} slot injection. The agreement between calculation and experiment was poor due to flow separation. The use of a k-ε turbulence model and an elliptic procedure by Matthews (58) for similar geometry led to better agreement between calculations and measurements.

Patankar and Spalding (83) applied a three-dimensional parabolic procedure to calculate effectiveness downstream of tangential square hole. The flow was assumed laminar. The calculated results were not compared with any measurements.

Patankar, Rastogi and Whitelaw (84) calculated effectiveness downstream of a row of tangential holes. Their comparison with experiment showed good agreement. Bergeles et al (8) applied a semi elliptic procedure to calculate effectiveness of full coverage. The semi elliptic procedure is essentially a parabolic procedure in which the longitudinal pressure gradients are calculated from upstream pressures.

Patankar and Spalding (85) applied a three-dimensional elliptic procedure to calculate the temperature field in a typical combustor.

This review has shown, among other things, that finite difference procedures have not been applied either to normal injection 3D cooling or combined normal and tangential cooling. The complexity of these film-cooling slots are such that it is uneconomical to perform parametric investigations to determine the influences of all the variables. It is necessary to develop a numerical procedure to calculate these complex influences.

2.4 CONCLUSIONS

The literature review of sections 2.1 to 2.3 allow the following conclusions.

1. Although extensive experimental and numerical investigations on two-dimensional film cooling slots have been reported; investigations relating to the influence of longitudinal curvature, multiple slots and conical walls on effectiveness of film cooling slots are few. More systematic investigations on the influence of above geometric parameters are necessary.

2. Detailed experimental and theoretical investigations on the effectiveness and heat transfer characteristics of tangential three-dimensional slots have been reported. Similar investigations are necessary for normal and combined normal and tangential three-dimensional film cooling slots as basis for optimization.

3. Comparison of the performance of practical film cooling slots with the requirements for higher turbine entry temperatures tend to indicate that, the requirement for still higher entry temperatures outpaces advances in film cooling designs. It may therefore be necessary to enhance the performance of film-cooling devices by composite arrangements.

CHAPTER THREE

TWO-DIMENSIONAL FILM-COOLING

3.0 INTRODUCTION

The literature survey of the previous chapter identified parameters which can influence film-cooling and for which information is lacking. In particular, the following influences have not been satisfactorily quantified:

(i) the influence of wall curvature on effectiveness and heat transfer.

(ii) the influence of successive slots and their longitudinal spacing.

(iii) the influence of film stretching on a conical surface.

Surface curvature, in the flow direction, is relevant to the upstream region of a combustor where concave surfaces require to be cooled; and to the downstream flare where the cooling of concave and convex surfaces may be necessary. The film cooling of curved surfaces is also relevant to gas turbine blades. Sections 3.1 and 3.2 describe experimental and theoretical investigations of the influence of longitudinal curvature on effectiveness respectively.

In gas turbine combustion chambers, film cooling arrangements frequently make use of up to 5 slots in series. The increasing thermal boundary layer thickness and static pressures are likely to influence the effectiveness and section 3.3 describes a numerical investigation of film build up. Section 3.4 describes the calculation of the influence of film stretching on a conical surface and is relevant to the downstream end of combustors.

3.1.0 EXPERIMENTAL INVESTIGATION OF THE INFLUENCE OF LONGITUDINAL CURVATURE ON EFFECTIVENESS

Section 3.1.1 describes the equipment and instrumentation used for the experiments. Essential details of the concentration measuring device are described. The concentration measuring technique is described and the precision and reliability of the present measurements are assessed. Section 3.1.3 discusses the preliminary tests performed to demonstrate the two-dimensionality of the flow and presents measurements of static pressures and impervious-wall effectiveness for a range of parameters shown on table 3.1.

3.1.1 DETAILS OF EXPERIMENTAL ARRANGEMENT

This section describes the equipment and instrumentation used in the experimental investigation. Because many of the components of the equipment have been used and described before by Rastogi (89), the descriptions provided here are brief and attention is focused on essential differences between the previous and present arrangement.

Main Flow Circuit

The essential features of the main air supply and contraction unit are shown on figure 3.1.1a and plate 3.1. The belt and pulley drives allow a change in the fan speed by changing the pulley ratios. The contraction section and the test section were mounted on channel steel frames which were supported on the floor by anti-vibration rubber pads. The exit flange of the contraction section was joined with cloth tape to the inlet flange of the test section.

The test section was 300 mm by 200 mm by 900 mm in z, y and x directions respectively. The roof of test section was made of perspex strips of various sizes and allowed the placement of traversing mechanism at convenient positions. Side wall static-pressure holes allowed the longitudinal pressure gradient to be checked, and a 1 mm wire trip. located 60 mm from the leading edge, promote early transition to turbulent flow.

The Secondary Flow Circuit

Figure 3.1.1b shows the secondary flow circuit used for all the measurements reported in this chapter. The skirt of the plenum box allowed the test plates to be changed easily and the slot height adjusted. A one-horse power, three-phase blower was used to supply the secondary air. The air and arcton 12 flow rates were controlled with the throttle valves shown in figure 3.1.1b. The quantities of air and arcton 12 were measured with 38.5 mm diameter orifice meters with D and D/2 pressure tappings. The meters were designed, in accordance with BS 1042.

The plenum chamber was the same that had been used and described before by Rastogi and Whitelaw (91).

Test Plates

The flat plate measurements were obtained with the base plate of reference 89 and contained 0.5 mm diameter holes through which gas samples were conveniently drawn. The curved test plates of figure 3.1.4 were initially made of perspex which warped and resulted in three dimensional flow. The curved plates used for the present measurements were machined from wood and were provided with 0.5 mm diameter sampling holes at 7.5^{o} intervals.

Instrumentation

Pressure Measuring Devices

T.E.M. optical manometers were used to measure the pressure drops across the orifice meters. These were capable of measuring pressures from 0 - 600 mm of water and were graduated in 0.1 mm of water. Because the arcton 12 flow was manually adjusted it was subject to small fluctuations due to feed back from the main pipe. As a consequence, the pressure drop across the orifice plate for arcton 12 was measured with a Furness Control variable capacitance pressure transducer with variable ranges 0-25 mm, 0-50 mm and 0-125 mm of water. The total and static pressures were measured with a Furness Universal Manometer with a range 0-2000 mm of water and a resolution better than 0.0001 mm.

Concentration Measuring Device

The thermal conductivity cell used was a Servomex micro-Katharometer (MK 158). A flow diagram of the cell is shown in figure 3.1.2. It consisted of two chambers 2.6$\mu\ell$ containing platinum filaments. The resulting bridge had a resistance of approximately 25 ohms in each arm at room temperature. The cell was placed in a Shandon oven shown on plate 3.1 and maintained at a constant temperature of approximately 50^{o}C. The flow was drawn through the arms of the bridge by a vacuum pump and regulated with rotameters capable of measuring 0-5 ml/s. Air was used as the reference gas. Because of the differences in the thermal conductivity of the sample and reference gases a potential difference develops across the bridge. As shown in reference 47a this potential difference is given by

$$E = \frac{\frac{1}{4}.I.R.(t_w - t_c)\alpha\varepsilon}{(1 + \alpha\, t_w)} \qquad 3.1.1$$

where ε = relative change in thermal conductivity of the sample

α = resistance coefficient of the filaments

R = resistance of the filaments.

The relative change ε may be regarded as a direct measurement of the mass concentration of tracer or arcton 12.

To calibrate the cell, a two-dimensional, 2.54 mm slot was set up. A known quantity of helium was mixed with a known quantity of air flow through the slot. The helium flow rate was measured with a previously calibrated rotameter and the air flow rate was measured with the orifice plate of figure 3.1.1b. The air and the helium are well mixed in the plenum chamber. Samples of the mixture were passed through the katharometer and the potential difference noted. As regards helium, mass fractions varying from 0.25% to 2.5% of helium were tested. For arcton-air mixtures the mass fraction was varied from zero to 100% arcton. Figure 3.1.2 shows the calibration curve for arcton and helium traces. The calibration curve for helium traces was linear while that for arcton was non linear. One implication of the non linear arcton-air mixture curve is that the conductivity of the mixture lags on the mass fraction. Comparison of calibration with those of Pai (77) and Rastogi (89) showed reasonable agreement.

To determine an optimum sampling rate, samples were taken at 1, 2, 3, 4, 5 ml/s respectively and the potential difference across the bridge noted. The response time was also noted. It was observed that the measured potential difference at 5 slot gaps

from slot exit was insensitive to sampling rates from 1 - 3 ml/s. At higher sampling rates, the measured effectiveness dropped gradually so that its value was 4% less at 5 ml/s. The response time decreased from 25 seconds at 1 ml/s to less than 5 seconds at 5 ml/s. The suction rate of 3 ml/s was therefore regarded as optimum because it gave maximum potential difference with minimum response time. It was assumed that, at sampling rates greater than 3 ml/s, the suction was strong enough to suck the boundary layer.

3.1.2 METHOD OF MEASURING IMPERVIOUS WALL EFFECTIVENESS

Appropriate test plate and slot height were carefully set to ensure two-dimensionality of slot height and flow. The tunnel was operated at the desired mainflow velocity by adjusting the pulley ratio. The secondary fan was then switched on and the desired flow rate through the pipe adjusted with the throttle valves. The two dimensionality of the flow was tested by measuring the velocity profiles at the slot exit. The static pressure holes on the test plate were connected to Norgen selector valves by 1 mm stainless steel tubing. The common port of the valves was connected to the katharometer sample inlet port, and the flow rates in the bridge arms adjusted to be equal. When more than one selector valve was used, the valves were connected to the katharometer one after the other. A current of 100 mA was then passed through the katharometer and the bridge was balanced for air passing both arms of the bridge.

For unity density ratio measurements, a small quantity of helium (< 1% of the secondary air flow) was passed into the

secondary flow. When non-unity density ratios were required, the arcton-12 bottles were opened to provide a predetermined pressure drop across the orifice meter. The predetermined pressure drop was maintained constant manually throughout the run as an indication that a constant flow rate of arcton-12 was in use. Samples were taken from the plenum box and different locations on the test plate. The readings at downstream positions were normalized with the plenum box value to obtain effectiveness at that position.

Figure 3.1.3 shows a comparison of present measurements with those of Whitelaw (112). The two geometries compared are similar and the agreement between the two measurements confirm the reliability of present procedure. Previous calibration of katharometer by Pai (77) and Rastogi (89) were made with samples of air-gas mixtures over a column of water. Present calibration using a continuous flow system removes the possible influence of water vapour on the conductivity of the air-gas mixtures. The accuracy of the measurements is limited by rotameter metering accuracy which is not better than ±5%.

Precision of effectiveness measurements

The reproducibility of the helium tracer measurements was better than ±2% while that of arcton-12 air mixture were better than ±4%. The large figure for arcton-12 was due to the manual adjustments of the arcton-12 flow rate.

As noted earlier, sampling at flow rates beyond 3 ml/s led to consistently lower values as the suction rate began to influence the boundary layer. The maximum effect observed at a sampling rate of 5 ml/s was 4% and the present results were obtained with much lower sampling rates.

The implication of equation 3.1.1 is that the bridge sensitivity $\frac{\Delta E}{E}$ may be expressed as:

$$\frac{\Delta E}{E} \approx \sqrt{\frac{1}{I^2} + \left(\frac{1 - \alpha t_c}{1 + \alpha t_w}\right)^2 + \frac{1}{\varepsilon^2} + \frac{1}{R^2}} \qquad 3.1.2$$

Evaluation of this equation with typical experimental values shows, that the bridge sensitivity was very high. The uncertainties due to bridge readings may be assumed negligible.

3.1.3 RESULTS

The measurements presented here were obtained in the wind tunnel described in section 3.1.1 and shown on figures 3.1.1 and plate 3.1. The secondary flow circuit are also shown on figure 3.1.1. The slot configurations used are shown on figure 3.1.4 and, in each case, the upper lip of the slot was tapered at an angle of 2.5 degrees to give an effective lip thickness of 0.5 mm. Measurements were obtained with the slot height of 2.54 mm and 5.1mm is indicated in table 3.1.

The two-dimensionality of the flows were tested by measuring velocity profiles and wall concentration of tracer gas over the centre 100 mm of each plate. The slot height at exit was found to vary in the cross-stream direction by less than 1%. Cross-stream measurements of wall concentration agreed to better than 1% of the slot concentration at all downstream stations. The velocity measurements were performed with a flattened Pitot tube of external dimensions 1.5 mm x 0.5 mm.

In the case of the flat-plate flows, the free-stream velocity was 18.5 m/s and was constant in the flow direction: the boundary-layer thickness on the lip was approximately 13 mm (i.e. where $U = 0.99\ U_G$). With the convex flow, the initial values were similar to those for the flat-plate but, as can be seen from figure 3.1.5 a non-uniform pressure distribution existed in the tunnel and its magnitude varied with position, velocity ratio and geometry: far from the surface, the adverse velocity variation was less than 10% over the range of effectiveness measurement. The concave surface led to a favourable pressure gradient, at a distance of 74 mm from the surface, which was also small; in this case, the initial free stream velocity was also 18.5 m/s. The wall values of static pressure were measured with the same 0.5 mm diameter holes used for gas-sampling purposes. Profiles of static pressure were measured with a probe of 2.0 mm outside diameter and four 0.3 mm holes located 10.0 mm from its leading edge. The values of static pressure measured away from the wall may be in error by up to approximately 10% due to the non-coincidence of the probe axis and the streamlines.

In arranging the flow over the concave surface, preliminary tests with a free stream velocity of 10 m/s showed that the initial boundary layer was unexpectedly thick ($\simeq$ 120 mm) and had a non-turbulent form. Changes to the leading edge of the upstream splitter plate and the use of various tripping devices did not change this boundary layer significantly and it was presumed to stem, at least in part, from the downstream geometry. Smoke tests confirmed that the flow did not separate at any point in the measurement region.

The initial velocity profile for the measurements of effectiveness was turbulent in form and had a thickness of approximately 100 mm.

Although side wall visibility was poor, the smoke tests, shown on plate 3.2, indicated that there was a gradual thinning of the film along the concave wall. The smoke tests also tend to show that the influence of the centripetal and the Coriolis forces are significant. As a result of these forces and the downstream geometry, there appears to be a region of reverse flow which was responsible for the thickness of the boundary layer.

The second picture of plate 3.2 corresponds to a velocity ratio greater than unity. This shows a more gradual thinning of the film. The third picture corresponds to introduction of the smoke into the main stream at a high velocity ratio.

The wall pressure measurements of figure 3.1.5 show that the flow separates from the convex wall at longitudinal distances which depend on the radius of curvature, the slot gap and the velocity ratio. Thus, with the 76 mm radius, the film was destroyed at downstream distances of less than 120 mm, i.e. $x/y_c = 47$, and this distance shortened almost exponentially as the velocity ratio decreases. The larger slot gap resulted in a slight increase in the length of the film and the larger radius in a larger increase. These results are in general agreement with those of Kind (49) and it may be exptected that they will be reflected in the effectiveness results.

Impervious Wall Effectiveness

Figure 3.1.6 presents measurements of impervious-wall effectiveness obtained on the flat, convex and concave surfaces: the

symbols are in accord with those of table 3.1. These results agree with the calculations of reference 90, in that they indicate that a convex surface results in improved effectiveness and a concave surface a reduced effectiveness. As suggested above, however, the convex surface results in separation of the flow and, downstream of the location where this occurs, in a very rapid reduction in effectiveness. The effect of the flow separation is very much more important than the differences in effectiveness observed in the regions of attached flow: the deviations of the curved-surface results from the flat-surface results do not exceed 10% except where separation exists. The figure shows that separation occurs at lower values of x/y_c for the lower velocity ratios and for smaller radii. In the particular case of a velocity ratio of ~~unity~~ 0.5 and the 76 mm radius, the effects of separation are noticeable almost from the slot exit.

The influence of density ratio may be deduced by comparing figures 3.1.6a and 3.1.6b. In general, the larger density ratio results in improved effectiveness and delays the onset of separation for the convex-surface results.

The influence of slot height is shown on figures 3.1.7a and 3.1.7b for convex and concave surfaces respectively. Figure 3.1.7a indicates that the larger slot height leads to earlier separation but is to be preferred in the region of attached flow. An increase in jet momentum tends to delay separation provided the increased momentum is close to the wall as was achieved by increasing the velocity or density ratio with the same slot gap: if the jet momentum is increased by increasing the slot gap, there will be

improved effectiveness for velocity ratios in the vicinity of unity due to the reduced ratio of effective lip thickness to slot height but earlier separation due to the increased momentum away from the wall. On the concave surface, figure 3.1.7b the larger slot height results in improved effectiveness, though the influence decreases with increasing velocity ratio.

The most important result of the above measurements is the rapid reduction in effectiveness associated with flow separation on convex surfaces. Surfaces of this type and with dimensions similar to those investigated are to be found at the downstream end of combustors where the flow is contracted to the exit of the combustor. It is clear that care must be taken in such regions to ensure that separation does not occur and, as a consequence, result in high wall temperatures and distorted exit temperature profiles.

3.2 NUMERICAL INVESTIGATION OF THE INFLUENCE OF LONGITUDINAL CURVATURE ON EFFECTIVENESS

In reference 90 Rastogi and Whitelaw presented calculations of aerodynamic flow properties corresponding to the curved wall jets of several authors and demonstrated reasonable agreement with the experimental results. Sample calculations of effectiveness were also reported but there were no experimental data for comparison. The present section is concerned with demonstrating that the procedure of reference 90 with small alterations, is capable of calculating the measurements reported in the previous section and, with this validation, of reliable calculations outside the range of measurements. The following subsection described the conservation equations solved; section 3.2.2 describes and discusses the physical

assumptions embodied in these equations. Comparisons of calculations and measurements are contained in section 3.2.3 which also includes calculations outside the range of measurements.

3.2.1 CONSERVATION EQUATIONS

The conservation equations solved here are identical to those of reference 90. They may be written in the form:

$$\frac{\partial U}{\partial x} + \frac{\partial}{\partial y} \quad (1 + Ky)\, V \quad = 0 \qquad 3.2.1$$

$$U \frac{\partial U}{\partial x} = (1 + Ky)\, V \frac{\partial U}{\partial y} + KUV = -\frac{1}{\rho}\frac{\partial P}{\partial x} + \frac{1}{\rho} \quad (1 + Ky) \frac{\partial \tau}{\partial y}\, \text{eff} + 2K\tau_{\text{eff}} \qquad 3.2.2$$

$$KU^2 = \frac{1 + Ky}{\rho}\frac{\partial P}{\partial y} \qquad 3.2.3$$

$$U \frac{\partial \emptyset}{\partial x} + (1 + Ky)\, V \frac{\partial \emptyset}{\partial y} + K\emptyset V = -\frac{1}{\rho} \quad (1 + Ky) \frac{\partial\, J_{\text{eff}}}{\partial y} + 2K\, J_{\text{eff}} \qquad 3.2.4$$

and represent, respectively, equations of conservation of mass, longitudinal momentum, momentum normal to the surface and species or temperature.

The corresponding boundary conditions are:

$$x = 0 : U = U(y),\ \emptyset = \emptyset\ (y)$$

where $U(y)$ and $\emptyset\ (y)$ are functions corresponding to experimental information: and

$$x > 0 : U = V = 0 \quad y = 0$$

$$U \to U_G;\ \emptyset \to 0;\ y \to y_G$$

where $U_G\ (x, y_G)$ was also determined experimentally.

These equations were solved, together with the forms of τ_{eff} and J_{eff} discussed in the following section, using the numerical procedure of reference 90, this procedure was derived from that of reference 82.

Normal Pressure

A consequence of solving equations 3.2.1 - 3.2.4 is the need to specify the free stream pressure field and to provide a relationship between equations 3.2.2 and 3.2.3.

The momentum balance equation for a fluid of mass m, rotating about a circle of radius r, at a velocity $\hat{V}$ is:

$$m \frac{d\hat{V}}{dt} = - \frac{\rho U^2}{r} - \frac{dP}{dy} \qquad 3.2.5$$

For steady rotation equation 3.2.5 can be integrated to give:

$$P_y = P_G + \int_{y_G}^{y} \frac{\rho U^2}{r} \, dy \qquad 3.2.6$$

which can be differentiated to give the longitudinal pressure gradient:

$$\frac{\partial P_y}{\partial x} = \frac{\partial P_G}{\partial x} + \frac{\partial}{\partial x}\left[\int_{y_G}^{y} \frac{\rho U^2}{r} \, dy\right] \qquad 3.2.7$$

Because the longitudinal pressure gradient is a function of y location, the solution of equation 3.2.2 requires that both the free steam pressure and the local integral in equation 3.2.7 must be known.

The free stream pressure gradient can either be specified, as in the present investigation, or reduced to a negligible value by

varying the radii of curvature with longitudinal distance. The second integral may be evaluated by assuming a linear relation between radius of curvature and the y location, as adopted by So and Mellor (102) or by assuming a linear relationship between U/r and the fractional mass flux according to Rastogi and Whitelaw (90). In the present numerical solution the integral

$$\int_{y_G}^{y} \frac{\rho U^2}{r} \, dy = \int_{y_G}^{y} \frac{U}{r} \, d\psi$$

was integrated by parts to give:

$$\int_{y_G}^{y} \frac{\rho U^2}{r} \, dy = \frac{U}{r} (\psi - \psi_G) - \int_{y_G}^{y} (\psi - \psi_G) \frac{\partial}{\partial y} (U/r) \qquad 3.2.8$$

The first part of this integral represents the centrifugal contribution to the pressure gradient, while the second part accounts for Coriolis component since V was assumed negligible. It may be expected that as V becomes significant equation 3.2.8 will break down.

Some previous experimental evidences, including that of So and Mellor (102), suggest the existence of Taylor-Goertler vortices in the boundary-layer flow over concave surfaces in the presence of zero free stream pressure gradient. The existence of Taylor-Goertler longitudinal vortices makes the flow on concave surfaces three dimensional. In the present investigation, velocity profiles were measured at the slot exit and downstream of curved section over the central 100 mm. None of these results showed measureable three dimensionality. Similarly the smoke test did not indicate the presence of any system of longitudinal vortices.

3.2.2 PHYSICAL ASSUMPTIONS

Although the experiments of references 22 and 36 indicate that there are structural differences in the turbulence observed near flat and curved surfaces, the experience of Bradshaw (11) suggests that there is insufficient evidence to justify turbulence closures which are significantly more complex than those at the eddy viscosity level. Consequently, and in accord with reference 90 the shear steess was defined as:

$$\tau_{eff} = \ell^2 \mid \partial U/\partial y \mid \left(\frac{\partial U}{\partial y} - A \frac{U}{r} \right) \qquad 3.2.9$$

$$= \mu_{eff} \left(\frac{\partial U}{\partial y} - A \frac{U}{r} \right)$$

Thus equation 3.2.2 becomes:

$$U \frac{\partial U}{\partial x} + (1 + Ky) V \frac{\partial U}{\partial y} + KUV = - \frac{1}{\rho} \frac{\partial P}{\partial x} - \frac{1}{\rho} (1 + Ky) \frac{\partial}{\partial y} \left(\mu_{eff} \left(\frac{\partial U}{\partial y} - \frac{AU}{r} \right) \right)$$

$$+ 2K \mu_{eff} \left(\frac{\partial U}{\partial y} - \frac{AU}{r} \right) \qquad 3.2.10$$

and with the scalar flux defined by:

$$J_{eff} = \left(- \mu_{eff} / \sigma_{eff} \right) \frac{\partial \phi}{\partial y}$$

equation 3.2.4 becomes:

$$U \frac{\partial \phi}{\partial x} + (1 + Ky) \frac{V \partial \phi}{\partial y} + K \phi V = \frac{1}{\rho} (1 + Ky) \frac{\partial}{\partial y} \left(\frac{\mu_{eff}}{\sigma_{eff}} \frac{\partial \phi}{\partial y} \right)$$

$$- \frac{2K \mu_{eff}}{\mu_{eff}} \frac{\partial \phi}{\partial y} \qquad 3.2.11$$

Equations 3.2.1, 3.2.3, 3.2.10 and 3.2.11 were solved with the appropriate boundary conditions and the following empirical specifications:

$$\ell = \ell_o (1 - \beta R_i)$$

$$\ell_o = 0.41y \quad , \quad 0 < 0.41\, y < 0.09y_G$$

$$\ell_o = 0.09y_G \quad , \quad 0.41\, y > 0.09y_G$$

$$\beta = 1$$

$$R_i = \frac{U}{r} \frac{1}{\partial U/\partial y}$$

$$\sigma_{eff} = 1$$

$$A = 5$$

For reference purposes, table 3.2 presents physical assumptions used by previous authors.

It is useful to note that coupling of the longitudinal and normal momentum takes place through the Coriolis term, KUV, and equation 3.2.3. Rotta suggested that this coupling is responsible for amplification of the longitudinal-velocity fluctuations on convex surfaces and their suppression on concave surfaces. The former tends to aid the onset of separation and the latter to suppress it but with the additional possibility of inducing an augmented near-wall laminar region.

The diffusion term, i.e. the second term on the right hand side of equation 3.2.7, has two components, the first due to the mean velocity gradient and the second to a combination of streamline curvature and the mean velocity gradient. An implication of this second term is that the diffusion of momentum increases with y on a convex surface and decreases with y on a concave surface. This implies a greater entrainment for a convex flow than for a concave flow and is consistent with the present experimental observation that an increase in slot height improves the effectiveness for a concave surface. It also improves the effectiveness for a convex surface although flow separation is brought about closer to the

Table 3.2

Previous turbulence assumptions

Reference	Assumptions	Wall Law	Geometries Considered	Properties Calculated
Giles, Hays, & Sawyer (1966)	$\tau_{eff}=XbU\left(\frac{\partial U}{\partial y}-3\frac{U}{r_o}\right)$ b = jet thickness U = maximum velocity X = 1/4xb		logarithmic spiral surfaces	U, τ_w
Rotta (1967)	$\tau_{eff}=\rho l^2\left\|\frac{\partial U}{\partial y}-\frac{U}{R}\left(1+\frac{\overline{\rho v u}}{\rho u' v'}\right)\right\|\cdot\left[\frac{\partial U}{\partial y}-\frac{U}{R}\left(1+\frac{\overline{\rho v u}}{\rho u' v'}\right)\right]$ $\varepsilon=\frac{\rho\left\|\overline{u v}\right\|^{3/2}}{l}$ $l=0.4y\left[1-\exp\frac{(-y(\tau_w\rho)^{\frac{1}{2}})}{A}\right]$	$\frac{\tau_w(R_w)^2}{R}=\rho\overline{u v}+\mu R\frac{\partial}{\partial y}\frac{U}{R}$	concave convex	τ_w,U,H τ_w,P
Rastogi and Whitelaw (1971)	$\tau_{eff}=-\rho l^2\left\|\frac{\partial U}{\partial y}\right\|\left(\frac{\partial U}{\partial y}-\frac{9U}{r}\right)$ $l=0.435y \quad 0<y<0.02.4\ y_G$ $l=0.09\ y_G \quad y>0.0214\ y_G$	$\frac{\tau w}{\frac{1}{2}\rho U^2}=\frac{\mu}{(\rho U y)}-y_{2.5}\frac{dP}{dx}2.5-\frac{\psi_1}{R_R}$ 2.5 2.5	concave convex logarithmic spiral surfaces	τ_w,U P,η
So and Mellor (1972)	$=\rho\nu_e\left(\frac{\partial U}{\partial y}+KU\right)$ $\nu_e=\nu_{eF}\left\{\frac{1-\beta\ KU\left(\frac{\partial U}{\partial y}+KU\right)}{\left(\frac{\partial U}{\partial y}-KU\right)^2}\right\}^{3/2}\left\|1-\frac{KU}{\frac{\partial U}{\partial y}}\right\|$ $\beta=\frac{72\left(\frac{l_1}{\lambda}\right)}{1-6\left(l_1/\lambda\right)}$ $\nu_{eF}=(l_1\lambda^{1/3})^{3/2}(1-6\frac{l_1}{\lambda})^{3/2}\left\|\frac{\partial U}{\partial y}\right\|$ l_1/λ defined emperically	$\left(\frac{2}{Cf}\right)^{\frac{1}{2}}=5.6\log R\overline{\delta}+B+A$ $\overline{\delta}=\int_0^{U_p}1-\frac{U}{U_p}dy$ $A=A(\delta/R'\beta)$ U_μ	concave convex	τ_w,H,U θ
Bradshaw (1973)	Transport equation for $-\rho\overline{uv}$, $L/L_o=1+\frac{\beta e}{(\partial U\ \partial y)}$ L_o = empirical $e=-\frac{U}{r}$ $\epsilon=\frac{(-\overline{uv})^{3/2}}{L}$	$\frac{U}{U_\tau}=\frac{1}{x}\log\frac{U_\tau y}{\nu}+\frac{5}{6}\frac{\beta U\ y}{Ur}$	concave convex	τ_w,U,St.

Contd./.....

Table 3.2 Contd.

Reference	Assumptions	Wall Law	Geometries Considered	Properties Calculated
Koosinlin Launder Sharma (1973)	$\mu_t = \rho\, l^2 \left[\left(\frac{\partial U}{\partial y}\right)^2 + \left(r\,\frac{\partial (V\theta\, r)^2}{\partial y}\right)\right]^{\frac{1}{2}}$ $\mu_{eff} = \mu_t + \mu_{laminar}$ $l = l_o\,(1 - Ri)$ $l_o = 0.42y\,[1-\exp(-y_+\tau_+^{3/2})]$; $l_o > 0.085y_G$ $l_o = 0.085\, y_G$ $\quad l_o > 0.085y_G$	$\frac{\tau_w}{\frac{1}{2}\rho U^2}_{2.5} = \frac{\mu}{(\rho U y)_{2.5}} - \frac{y_{2.5}\frac{dP}{dx}}{\rho U^2_{2.5}}$	spinning disc spinning cone spinning cylinder	$\frac{V\theta}{rw}, U_{rw}$ SH, NU

slot: the increased entrainment reduces the increase in effectiveness caused by the larger coolant mass flow.

In contrast to the calculations of reference 90, most of the present results were obtained with a wall function of the form:

$$\frac{\tau_w}{\frac{1}{2}\rho U^2_{2.5}} = K^2/\ell n \left[ER\ (S+F)^{\frac{1}{2}}\right]^2 \qquad 3.2.12$$

where F accounts for the influence of the near-wall pressure gradient and is defined by:

$$F = \frac{y_{2.5}}{\rho U^2_{2.5}} \frac{\partial}{\partial x}\left[P_G + \int_{y_G}^{y} \frac{(\rho U^2)}{R+y}\, dy\right] \qquad 3.2.13$$

The experiments of reference 102 suggested that a logarithmic wall law is appropriate to convex surfaces but not to concave surfaces. Bradshaw (11) proposed that the flow near both surfaces could be represented by a wall function of the form:

$$\frac{U}{U_\tau} = \frac{1}{K}\ \ell n\ \frac{(U_\tau y)}{\nu} + \frac{5}{6}\frac{\beta U y}{U_\tau (R+y)} \qquad 3.2.14$$

where U/(R+y) represents the extra strain due to curvature. The F - function in equat.3.2.12 may also be regarded as representing the added strain due to curvature.

3.2.3 RESULTS AND DISCUSSION

Figures 3.2.1 and 3.2.2 present comparisons between the calculations and measurements of static pressures and impervious-wall effectiveness of section 3.1.

Calculated and measured distributions of wall pressure are presented on figure 3.2.1 and, particularly for the convex surfaces, indicate quantitative differences but similar trends: the velocity ratio of 2.0 was chosen because it shows the largest variation in pressure. The corresponding calculated values of drag coefficient are also shown and confirm that the beginning of the separation region can be identified from the discontinuities in the calculations.

If Reynolds analogy is assumed, the calculated values of the skin friction coefficient are proportional to values of Stanton number and indicate trends which are similar to those observed by Thomann (110). The convex surface with the larger radius resulted in values which, far downstream of the slot, are 16% lower than the corresponding flat-plate values: in the near-slot region, the skin-friction coefficient rises above the flat-plate curve. The surface with the smaller radius of convex curvature resulted in an even greater decrease in skin-friction coefficient. The concave surface caused an increase of more than 20%. For both convex and concave surfaces, an increase in slot gap resulted in a reduction in skin-friction coefficient.

Figure 3.2.2a demonstrates the extent to which the flat-plate measurements are represented by the calculation method: the agreement is satisfactory except at the lowest velocity ratio. Similar trends can be observed on figure 3.2.2b,c and d where the convex surface results are presented, except in regions where flow separation occurred. The dashed lines show discontinuity in the calculations. A comparison between the measurements and calculations for the concave surface and the two slot gaps, figures 3.2.2e and f, indicates reasonable agreement with some

differences at the lower velocity ratios. In general, the comparisons allowed by figure 3.2.2 suggest that the calculated values follow the same trends as the measurements, except in the vicinity of flow separation. The agreement is quantitatively correct particularly at higher velocity ratios and away from separation. It may be anticipated that calculations outside the range of measurements will also correctly represent trends but confidence in absolute values must diminish as the stream line curvature increases.

The more general validity of the present calculation procedure can be assessed by comparing its results with the measurements of Kind (49) and So and Mellor (102). Comparisons are presented on figures 3.2.2 and 3.2.4.

Figure 3.2.3 shows Kind's measurements of pressure coefficient, wall-shear stress and velocity profiles. The calculated values of shear stress indicate separation at an $\frac{x}{y_c}$ location of approximately 48 (i.e. 82 degrees) whereas the experimental results suggest that the flow remains attached at least until an x/y_c location of 56 (i.e. 120 degrees). The configuration of Kind may have given rise to a flow which was not fully turbulent but it is certain that, in the region close to separation, the calculation procedure will give incorrect results due to the parabolic nature of the equations. The discrepancies between measured and calculated values of pressure coefficient may also stem from, in part, the use of parabolic equations but they are undoubtedly influenced, as indicated for example in reference 11, by the present simple turbulence model, which gives rise to the indicated velocity profile.

In contrast to the results of figure 3.2.3 the calculation of wake-type flows are in excellent agreement with measurements, even though the ratio of boundary layer thickness to radius of curvature is small. This is demonstrated in relation to the measurements of So and Mellor on figure 3.2.4. Thus, the calculation of wall-wake flows may be expected to be more precise than those of wall-jet flows and, in both cases, the results will become less precise as separation is approached.

The influence of surface curvature is shown clearly on figure 3.2.5 for a number of velocity ratios, downstream distances and for two density ratios. As indicated by the measurements and calculations of figure 3.2.2 a positive curvature results in improved effectiveness and a negative curvature in reduced effectiveness. The effects are not large in the range of downstream distances appropriate to gas turbine combustor cooling, $0 < x/y_c < 25$ say, except for negative radii less than around 100 mm. As shown by figure 3.2.6 this situation is complicated by the choice of a value for slot gap. An increase in slot gap tends to improve the effectiveness except, for the convex case, where it results in early separation with consequent rapid reduction in effectiveness: the range of parameters for which separation can occur is well within that of significance to gas turbines.

3.3 TWO-DIMENSIONAL MULTI-SLOT FILM COOLING

In gas turbine combustion chambers, film cooling arrangements which result in two and three-dimensional slot flows are to be found and frequently make use of more than two slots. The specification of the spacing of the injection slots are often determined from the performance of single slots, and the slots are often evenly spaced. Evenly spaced slots may result in low effectiveness at upstream positions and high effectiveness at downstream positions due to the influence of upstream slots.

This section presents comparison between present calculations and measurements obtained downstream of three successive film-cooling slots. With this agreement as confirmation of the appropriateness of the calculation procedure, calculated values of effectiveness are presented for nine evenly spaced slots; as an example, it is shown that the requirement of minimum effectiveness of 0.8 can be met with seven slots separated by particular distances.

3.3.1 CALCULATION PROCEDURE

The calculation procedure is similar to that described in reference 82. A finite-difference method was used to solve the following equations;

$$\frac{\partial U}{\partial x} + \frac{\partial V}{\partial y} = 0 \qquad 3.3.1$$

$$U \frac{\partial U}{\partial x} + V \frac{\partial U}{\partial y} = \frac{\partial}{\partial y} \left(\mu_{eff} \frac{\partial U}{y}\right) \qquad 3.3.2$$

$$U \frac{\partial T}{\partial x} + V \frac{\partial T}{\partial y} = \frac{\partial}{\partial y} \left(\frac{\mu_{eff}}{\sigma_{eff}} \frac{\partial T}{\partial y}\right) \qquad 3.3.3$$

$$\mu_{eff} = \rho \ell^2 \left| \frac{\partial U}{\partial y} \right| \qquad 3.3.4$$

$$\ell = 0.41y, \; 0 < y < \frac{0.09}{0.41} y_G$$

$$\ell = 0.09, \; \frac{0.09}{0.41} y_G < y < y_G \qquad 3.3.5$$

$$_{eff} = 1.0$$

and boundary conditions,

$$y = 0, \; U = 0, \; \frac{\partial T}{\partial y} = 0$$

$$y \to y_G, \; U \to U_G, \; T \to T_G$$

The corresponding initial conditions were

$$U = U_c, \; T = T_c, \; 0 < y < y_c$$

and estimated upper lip velocity and temperature profiles for the first slot; similar slot conditions, but calculated upper-lip boundary-layer profiles were used for each subsequent slot. Twenty three grid nodes were used to cover the solution domain in the plane of the first slot. Twelve of these grid nodes lay within the slot, and subsequent slots added twelve nodes to the number of nodes in the solution domain.

3.3.2 RESULTS

Figure 3.3.1 shows typical velocity and temperature profiles downstream of 5 consecutive slots. Both the thermal and velocity boundary layers grow with downstream distance . This is in qualitative agreement with the measurements of Chin et al (14).

Figure 3.2.2 compares calculated values of adiabatic-wall effectiveness with measurements obtained in a non-adiabatic experimental configuration of reference 17 which, it is estimated, resulted in values of effectiveness approximately seven per cent of unity lower than the corresponding adiabatic-wall values. The agreement between the calculations and the measurement, corrected for the finite wall-heat transfer, is satisfactory for the three slot configurations and for the three velocity ratios shown. The density ratio for these results was approximately 2.38 at the first slot and the ratio of slot height to slot-lip thickness was 2.0.

The change in the shape of the calculated effectiveness curves from the first to the third slot is due partly to the increasing velocity-boundary-layer thickness, but mainly to the increase in the thermal-boundary-layer thickness. The tendency for the experimental values to increase as a subsequent injection slot is approached is due to the finite conduction heat transfer through the base plate.

Figure 3.3.3a presents, for an initial velocity ratio of 0.4 and a density ratio of 2.38, effectiveness results downstream of nine consecutive slots; the results obtained with the seventh, eighth and ninth slots are essentially the same. As can be seen, this arrangement results in low effectiveness values immediately upstream of the first four slots and very good cooling far downstream. A more efficient arrangement, for many practical purposes, is shown in figure 3.3.3b which, for the same initial conditions, indicates an arrangement of slots designed to ensure that, except for the first two slots, the

effectiveness does not fall below 0.8. As can be seen only seven slots are required.

The calculations presented above presume that the surface cooled by the first slot represents the upper lip of the subsequent slot. Thus, the total momentum in the flow increases with downstream distance. The influence of any possible increase in static pressure, however, is neglected.

The dashed line shown in figure 3.3.3a represents the effectiveness obtained with a single slot and the same mass flow as the first five slots of the multi-slot arrangement, i.e. the dashed line represents the effectiveness obtained with a single slot of geometry similar to that of the multi-slots but with a velocity ratio of 2.0. It can be seen that the five slot arrangement is more effective. Also, as shown on figure 3.3.3b, if it is required that the effectiveness should not fall below 0.8, for $x/y_c > 60$ the single slot is satisfactory to a distance of 72 slot heights, whereas the five slots are satisfactory to 132 slot heights. The multi-slot arrangement is clearly more effective than the single slot.

The conclusion of the previous paragraph is to be expected since increasing the number of slots in a given distance leads asymptotically to transpiration cooling. It should also be noted that greater effectiveness could have been obtained with the arrangements considered on figure 3.3.3 if the slot height had been chosen to allow an initial velocity ratio close to unity; for a higher density ratio, a velocity ratio close to two would be required.

3.4 CALCULATED INFLUENCE OF CONICAL WALL ON EFFECTIVENESS

Introduction

Combustors may be designed with a conical flame tube or a conical flare at the exit. The conical wall implies that a film injected tangentially would be subject to divergence or convergence. The extent of the divergence is dependent on the cone angle. The calculations presented here qualifies the influence of conical divergence on impervious wall effectiveness.

3.4.1 CALCULATION PROCEDURE

The calculation procedure of section 3.3.1 was used here. The equations solved were similar to 3.3.1 - 3.3.3 but were recast in polar coordinates. The local radius of curvature was calculated from

$$r = r_w + y \cos \alpha \qquad 3.4.1$$

where r_w is the radius of the cone and α half the cone angle. The numerical procedure is described in great detail in reference 82 and is capable of solving equations 3.3.1 - 3.3.3 in either Cartesian or polar coordinates. The effective viscosity definition was similar to that of section 3.3.1.

3.4.2 RESULTS

The configuration for the present calculations is shown on figure 3.4.1 and it was scaled from an existing combustor. The cone angle was 82^0 and the truncated section had an initial radius of 125 mm.

Figure 3.4.1 shows the calculations for four slots in series and corresponds to the flow conditions for figure 3.3.3. The comparison on figure 3.4.1 shows that the conical wall led to a reduction in effectiveness.

Figure 3.4.2 shows that for 0.8 minimum effectiveness requirement, the influence of conical wall increases with density ratio and downstream distance.

Figure 3.4.3 demonstrates that the influence of conical wall increases with velocity ratio; for example, the maximum influence of wall curvature at the end of the first three slots on the conical wall was 9% for velocity ratio of 0.5 and 4% for velocity ratio of 0.3 for the chosen radius and cone angle.

Figure 3.4.4 shows the performance of six slots in series. Three of these slots are on a surface of constant radius and three on a conical wall. The cone angle was 82^{o} and the velocity ratio was 0.4. The figure 3.4.4 shows that the influence of multiple slot is significant as the minimum effectiveness rose from 48% at the end of the first slot to 75% at the end of the third slot. The fourth slot was introduced at a conical end and, due to the conical divergence, the effectiveness dropped more rapidly. The influence of the conical section was therefore to reduce the influence of film build up by up to 12% for the present configuration.

Calculations of this nature can be performed for varying flow and geometric parameters. It is anticipated that the calculated trends can be extended to a wide range of cone angle and velocity ratios but the absolute values must be extrapolated with caution for the following reasons:

(i) the flow at the combustor flare is often subject to favourable pressure gradient which may cause laminarisation.

(ii) the present calculations assumed that the main flow is in a direction parallel to the conical wall.

(iii) the normal pressure gradient was assumed to be negligible.

(iv) the calculation assumed that the flow is stretched over a solid angle of 360^{o}. Stretching may take place over less than 120^{o} of the cone and lead to three-dimensional flows.

In spite of these limitations, it is expected that the calculated trends would be right.

3.5 CONCLUSIONS

The following conclusions may be extracted from the investigations reported in sections 3.1 to 3.4.

1. The influence of surface curvature on the effectiveness of film cooling is small except where, for convex surfaces, the flow separates. The range of parameters for which separation can occur is of significance to gas turbine combustor cooling.
2. Outside the range of parameters which result in separation, an increase in convex curvature tends to improve effectiveness and an increase in concave curvature to decrease effectiveness.
3. An increase in slot gap tends to result in earlier separation for convex surfaces.

4. The numerical solution procedure, which is based on the solution of the continuity, momentum, species and energy correctly predicts the trends of the measurements: the magnitude of effectiveness is correctly predicted over an extensive range but becomes increasingly incorrect as separation is approached.
5. A modified version of the calculation procedure of reference 78 confirms the experimental findings of reference 17 that the influence of film build up on effectiveness of subsequent slots is significant. It is also demonstrated that the spacing of the slots can be determined conveniently, for a given requirement with the same procedure.
6. The influence of divergence due to a conical wall is small (<10%) for moderate cone angles ($\alpha < 45^{o}$) and velocity ratio of practical interest ($^{U}c/U_{G} < 2$). For a minimum film cooling effectiveness requirement the influence of conical wall increases with distance from slot exit.

CHAPTER FOUR

THREE-DIMENSIONAL FILM COOLING

4.0 INTRODUCTION

The purpose of the present chapter is to report the investigation of the influence of various flow and geometric parameters on the performance of three-dimensional film-cooling slots. Structural reasons preclude the use of ideal two-dimensional slots in practice and combustors, therefore, use discrete hole three dimensional-film cooling arrangements. These may consist of rows of tangential holes, normal holes with or without impingement lip, full coverage holes without impingement lip or combined normal and tangential holes, as shown in figure 2.2.1.

The work described in this chapter is concerned with tangential holes, normal holes with an impingement lip and combined normal and tangential holes. The experiments on tangential holes are few and are supplementary to the earlier detailed investigation of Rastogi and Whitelaw (91). The experimental investigation of normal and combined normal and tangential holes is however extensive and new. The experimental investigation is supported by a numerical investigation which developed a numerical procedure for the calculation of the influence of important parameters on the performance of each arrangement.

Section 4.1 describes the experimental equipment and instrumentation. The experimental results are presented and discussed in Section 4.2. The basic equations and physical assumptions of the calculation method are presented in section 4.3 and section 4.4 discusses the results of the theoretical investigations.

The calculated results are presented under two sub-headings which correspond to calculations within and outside the range of measurements: the former allow an assessment of the reliability and precision of the calculation and the latter provide new information which should be viewed subject to the previous assessment.

4.1.1 DETAILS OF EXPERIMENTAL ARRANGEMENT

The Main Flow Circuit

The essential features of the main flow circuit have been described in section 3.1.1. The schematic diagram is shown on figure 4.1.1a. The arrangement resulted in a two dimensional, low turbulence, boundary layer flow in the test section.

Secondary Flow Circuit

The secondary flow system as shown by figures 4.1.1b and d allowed air or airgas mixtures to be introduced into the flow through the slots. A three phase, eight-horse power motor drove the blower and was found to be adequate for all the measurements. The amount of air was controlled with a 'butterfly' throttle valve at blower exit. Three globe valves controlled the quantities of arcton and air through the normal holes and through the tangential holes.

The quantities of arcton and air thorugh the respective pipe lines were measured with 38.5 mm diameter orifice meters; with D and D/2 pressure tappings. The meters were calibrated in accordance with BS 1042.

Each secondary pipe was connected to a plenum chamber through two 90^{o} elbow joints (as shown in figure 4.1.1b and d) and a diverging transition section. The plenum chamber contained two 20 mesh 28 swg screens and a honeycomb of 9.6 mm cell size, each 76 mm long.

The plenum chamber opened into the test section thorugh slot arrangement under test. The test slots were easily replaced and arranged for tangential, normal or combined normal and tangential injection.

For heat transfer measurements the arcton-12 pipe line was removed and a 9KW sekomak heater, as shown in figure 4.1.1f, was placed in the air line. The heater was connected to three variac transformers to allow the air to be raised in temperature by about $25^{o}C$ above atmospheric temperature.

Test Plates

For concentration measurements the duralumin plate previously described by Rastogi and Whitelaw (91) was used. It had five rows of 0.5 mm diameter static pressure holes through which samples were taken. For heat transfer measurements a new 'hot plate' was designed and built. It consisted of 500 mm tufnol plate on top of which was glued three 0.125 mm thick stainless steel sheets. Each sheet was 153 mm by 300 mm. Double sided sellotape was used to secure stainless steel sheet to the tufnol and was satisfactory for plate temperatures below $75^{o}C$. The three sections of the stainless sheet were separated by 2 mm gaps which were filled with selac glue. These gaps were necessary to prevent the sheets from buckling due to thermal expansion. At the lower side of the tufnol plate, brass pieces were screwed into the plate to hold the sheets firmly against the plate and to act as lower buss bar. Twenty four evenly spaced power leads were provided to ensure that the sheets were evenly heated. The power leads were made of equal lengths of heavy duty electrical cables, carefully soldered to the buss bars. The main power supply leads were connected to two bolts on the angled upper

buss bar. Two tufnol side walls allowed the plate to be used both in a wind tunnel and a swivel arrangement. A cross section of the plate is provided in figure 5.2.1.

Figure 4.1.1g shows the arrangement of the thermocouples on the stainless steel sheets. 60 swg Saxona copper-constantum thermocouples were spot welded to the bottom surface of each stainless steel sheet through holes in the tufnol plate. The holes were subsequently blocked with pieces of wood. The resulting 180 thermocouple junctions provided the required detailed information of the temperature for a constant heat flux boundary condition.

Traversing Mechanism

A sketch of the traversing mechanism, also previously used by Rastogi, is provided in figure 4.1.1e. It made use of a DISA vertical traverse mechanism (type 55Hol) and had resolution of 0.01 mm. The resolution in the longitudinal and lateral direction was better than 0.025 mm.

Instrumentation

The total and static pressures were measured with the pressure measuring devices described earlier in chapter 3. The concentration measuring device used was the same as described earlier in chapter 3.

Heat Transfer Measuring Devices

A high current (0-1000 amperes) variac transformer was used to heat the thin stainless steel sheet. An ammeter was used to measure the current, after it has been stepped down in the ratio of 200:1; a Fenlow digital voltmeter measured the thermo e.m.f of the thermocouple and a Solartron precision a.c. millivoltmeter measured the potential difference across the stainless steel sheet. Plate 5.2 shows the equipment and instruments used to determine the uniform heat transfer rate and the temperature distribution of the plate.

4.1.2 METHOD OF MEASURING IMPERVIOUS WALL EFFECTIVENESS

The present arrangement allowed measurements to be made for tangential holes, normal holes or combined tangential and normal holes. The geometry of interest was first set. For tangential injection only, the splitter plate on top of plenum B of figure 4.1.1b was replaced with a plate with no holes and the throttle valve B was closed. Similarly, for normal injection only the tangential slot was replaced with a piece with no holes and throttle valve A closed. The tangential slots were glued to the splitter plate and impingement plate with double sided sellotapes. The splitter plate was levelled with the test plate and the joint between the splitter plate and the test plate made smooth with plasticine where necessary.

The procedure for measuring impervious wall effectiveness is similar to that described in section 3.1.2. However, in the case of combined normal and tangential injection, samples from the secondary boxes were measured to ensure that they gave the same values: this indicated that the tracer gas was well mixed with the flow before exiting from the slots. Particular care was also taken to ensure that the flow through each pipe line was kept constant for the duration of the run.

The reproducibility and precision of present measurements are similar to those of section 3.1.2.

4.1.3 METHOD OF MEASURING THE HEAT TRANSFER COEFFICIENT

To determine the heat loss from the stainless steel sheets to the surroundings and insulation, a constant current was passed through the sheets with no flow in the test section and after some two hours, which allowed steady state to be achieved, the potential

difference between the buss bars was measured. Measurements at different points across the stainless steel sheets showed differences of less than 0.02 volts along the entire heated length. Under steady conditions, the electrical power input into the stainless steel was equal to the heat loss by free convection and conduction through the insulation. The free convection heat loss coefficient was calculated from McAdams equation:

$$h_L = 0.27\ (\theta/\ell)^{0.25} \qquad 4.1.1$$

The stainless steel sheet temperatures were measured and the heat loss by conduction through insulation was obtained by subtracting the free convection from power input. The heat loss coefficient was based on the temperature difference between the surface and the surroundings. Table 4.1.1 shows the temperature distribution in micro volts as recorded by the thermo-e.m.f.

Table 4.1.1.

mm	mm	mm	mm	mm	mm	mm	mm	mm	mm	mm	mm	mm	mm
x/z	100	50	25	18.0	12.5	6.15	0	6.25	12.5	18.0	25	50	100
82	152	151	150	150	150	148	150	150	150	150	150	150	147
112	172	173	173	173	172	173	173	173	172	172	172	172	164
162	189	189	190	190	190	190	190	190	190	190	190	188	174
212	183	184	185	185	184	185	184	184	184	184	184	182	176
262	181	182	184	182	182	182	183	182	183	183	183	182	171
292	185	186	186	187	189	188	188	187	187	187	187	185	173
312	186	187	188	189	190	189	190	189	189	189	189	186	
332	187	187	189	190	187	189	189	189	189	189	189	187	175
362	186	186		187	184	190	187	186	186	186	187	185	173
412	183	183	184	184	184	184	183	183	183	183	183	182	171
462	173	174	176	176	176	176	175	175	175	176	175	174	166
512			157	156	157	157	157	157	157	158	159		157

The implication of above table is that, although the stainless steel sheet was uniformly heated, temperature differences of up to $8\,^{o}C$ arise due to edge losses.

To obtain both the adiabatic wall temperatures and the heat-transfer coefficients, the geometry of interest and the required velocity ratio were set and the secondary air was raised in temperature by $20^{o}C$ - $25^{o}C$ above the room temperature. At steady conditions the temperature distributions in the stainless sheet sheet and at slot exit were noted. A current of 150 amperes was then passed through the sheets. When steady conditions were once again attained, after a further hour, the temperatures of the stainless steel and the potential difference across the stainless steel sheets were measured. The product of the voltage drop and the current gave the rate of heat generation. An energy balance for an element of the stainless steel sheets led to the following equation:

$$\dot{q}'' = h_f\,(T_w - T_{aw}) + h_L\,(T_w - T_{room}) \qquad 4.1.2$$

Simultaneous solution of above equation for two values of heat flux and wall temperatures led to values of h_f and T_{aw} for a particular run and location.

Precision of heat transfer measurements

The resolution of digital voltmeter was $10\,\mu V$. This implies that the accuracy of measurements of the e.m.f. was not better than ± 10 uV; equivalent to $\pm 0.25^{o}C$. In situations where the difference between the wall temperature and the wall adiabatic temperature is less than $2.5^{o}C$, this resolution implies errors greater than 10% in heat transfer coefficient. The corresponding error for adiabatic wall effectiveness is less than 1%.

One source of error is the temperature differences due to edge losses. As table 4.1.1 shows, the temperature differences within the central 200 mm of any downstream location was less than 2% of the mean value. To reduce the effect of edge losses on h_f the mean temperatures in the central region was used to evaluate both the effectiveness and the heat transfer coefficient.

4.2 EXPERIMENTAL RESULTS AND DISCUSSION

4.2.1 FILM-COOLING AND HEAT TRANSFER DOWNSTREAM OF TANGENTIAL HOLES

Detailed investigations of film-cooling performance of three-dimensional tangential holes have been reported by Rastogi and Whitelaw (91). The same authors later reported the heat transfer, characteristics of some of these slots in an experimental and theoretical investigation (89). For most practical purposes the investigations may be regarded as having identified and quantified the major influences in such arrangements.

Essential information for situations outside the range of available experimental data were provided by calculations. Two sets of data are provided here to - (1) complement available information on multi row cooling (2) to validate some of Rastogi's(89) calculations for which data were not available.

In reference (91) Rastogi and Whitelaw showed that a three row tangential slot resulted in better cooling performance than a single row with the same open area, open area ratio and mass flow. It was also noted that the multi row slot compared very well with two dimensional slots for velocity ratios above approximately 1.4. It is of practical significance to note that the driving pressure requirement for a multi row slot is considerably higher than for a

single row due to higher friction losses. One other factor against increasing the number of rows for a specified open area is that, as the number of rows increases the machining cost also increases. A compromise between desired effectiveness, available pumping power, machining cost, and number of rows is therefore necessary.

Figure 4.2.1 was prepared to show that as the number of rows increases, the effectiveness increases if the open area, open area ratio, lip thickness and lip length are kept constant. When the lip length is increased however the two row slot with a finite lip performs better than the three row slot with no lip. In fact, a comparison of the single row with finite lip and a two row with no lip shows that the two are almost identical. Figure 4.2.1 demonstrates therefore that the number of rows can be reduced by having a finite lip length. The two row arrangement with finite lip is comparable to two dimensional slots with thin lip.

Figure 4.2.2 demonstrates that a finite lip with tangential holes promote such rapid mixing before the exit plane that the impervious wall effectiveness was nearly two-dimensional beyond five slot gaps. Comparison of the cross stream profiles of effectiveness for single row and two row slots showed that the single row was more three dimensional at corresponding positions. The three dimensionality of the single row did not conform to perfect symmetry. Measurements along centre line of the holes did not necessarily correspond to maximum effectiveness at a given down stream station. The 4-5% asymmetry of effectiveness distribution probably stemmed from turbulence generated randomness. Far downstream the flow was more two dimensional and more symmetric.

Figure 4.2.3 shows once again that a finite lip improves both effectiveness and heat transfer characteristics of tangential holes. The improvement in effectiveness and heat transfer are in accord with previous calculations of Rastogi (89).

4.2.2 EFFECTIVENESS DOWNSTREAM OF NORMAL HOLES

Introduction

Table 4.2.2 shows the range of parameters for which effectiveness were measured for the flow configurations shown in figure 4.4.1. The experimental numbers below each figure described in section 4.2.2 relate to the experiment numbers on table 4.2.2.

Each of the flow arrangements was carefully set and to test the symmetry of the flow, velocity profiles were measured downstream of two hole centres and two mid pitches. These showed symmetry to within 1% at centres and mid pitches. Longitudinal velocity measurements were made to detect any longitudinal pressure gradient. Within the working distance there was no noticeable difference. Initial cross stream effectiveness profiles also indicated symmetry within 2.5% and this permitted subsequent measurements of effectiveness to be made only at the hole centre and mid pitches.

To reveal the nature of the flow, mean longitudinal velocity profiles at the slot exit were made for two slots, and for three velocity ratios. Figure 4.2.4a shows that, for the slot with P/D of 1.4, the variation in z direction is small. Measurements of velocity profiles indicated that the flow was two-dimensional within six diameters downstream of slot exit. Integrating the area under the at the slot exit curve and multiplying by half pitch distance it was found that the

longitudinal velocity at the lip accounts for 99% of the mass from the jets

$$\left(\int_0^{6.25}\int_0^{12} \rho U \, dz \, dy = 0.00064,\ \rho \bar{U} \frac{\pi . D^2}{8} = 0.00065\right)$$

This mass conservation explains why the impervious wall effectiveness values measured at distances further than ten slot heights were two-dimensional. The mean velocity profiles for P/D of 2 are less two-dimensional as shown on figure 4.2.4b. The integral $\int_0^{12.5}\int_0^{12} \rho U \, dz \, dy$ accounts for only 75% of the mass exiting from jets: this flow had considerable lateral and vertical velocities and regions of forward recirculation. In such situations, the total head probe may not correctly record the mean longitudinal velocities. The effectiveness was three-dimensional for considerable distance downstream of slot exit.

Impervious wall Effectiveness

It is clear that, for film-cooling purposes, it is necessary to prevent the jets of cool gas from mixing rapidly with the hot free stream gas. The slot lip has the effect of turning the cold gas and causing it to issue from the slot at an angle which is less than 90° and depends on the length of the lip. In the gas turbine the impingement prevents it from attaining too high a temperature. The longer the lip the greater the possibility of part of the lip attaining a high temperature and burning off. On the other hand, the longer the lip the more two-dimensional will be the flow and the more tangential to the surface to be cooled. A compromise between these two requirements is necessary.

Figure 4.2.5a presents measurements of impervious-wall effectiveness, measured along the line downstream of a hole centre line for two lip lengths and for a value of P/D of 1.4. It shows that

the effectiveness in line with a hole centre line loses its dependence on lip length at a downstream distance of 40 slot heights. In the upstream region the longer lip leads to effectiveness values which are 5% less than those of Kacker and Whitelaw's two-dimensional slot for the same t/y_c and average mass flow in the plane of the end of the lip. The effectiveness with the shorter lip length is some 7% less than for Rastogi and Whitelaw's (91) tangential injection with the same pitch/diameter, open area and lip thickness but no lip. The effectiveness with the longer lip is almost identical to that obtained in reference 91 with tangential injection and no lip.

The results shown in Figure 4.2.5b are for a value of P/D of 2 and indicate larger differences between values of effectiveness with the two lip lengths. The open area in the plane of the slot exit was the same for the measurements of Figure 4.2.5a and b. The velocity profiles for the case of P/D of 2, Figure 4.2.4. show that this flow was less two-dimensional; for a given downstream station, differences as high as 10% of unity were measured for effectiveness at the centre line and mid-pitch. A comparison between the results presented on Figure 4.2.5a and b shows that the influence of lip length prevails much further downstream for the case of the larger pitch/diameter, corresponding to the more three-dimensional flow. Figure 4.2.5c presents effectiveness values obtained with the same value of P/D as Figure 4.2.5a buth with smaller values of open area and open area ratio. Since the results of Figure 4.2.5c correspond to a mass flow half that of Figure 4.2.5b the effectiveness values are significantly reduced; they also show, however, that the influence of lip length is significantly reduced suggesting that the greater number of holes associated with Figure 4.2.5c resulted in more rapid mixing and a more two-dimensional flow.

A comparison between Figure 4.2.5a and d indicates that the influence of lip length is not significantly affected by density ratio. It is also clear that the higher density ratio leads to lower values of effectiveness for low values of $\rho_C U_C / \rho_G U_G$, corresponding to lower velocity ratios.

The influence of the pitch to diameter ratio may be deduced from Figure 4.2.6. It can be seen from Figure 4.2.6a and b that the influence of the pitch to diameter ratio extends from the near-slot region to a downstream distance corresponding to more than 40 slot heights. As might be expected the difference is greater with the shorter value of lip length, corresponding to the more three-dimensional downstream flow. These results are in general agreement with those of reference 66 where similar trends were observed with a pitch to diameter ratio of 1.6 to 5.

Measurements obtained with a density ratio of 2.25 are compared with those of unity density ratio in Figure 4.2.7a,b,c and d. In practice the compressor air for cooling combustors has a higher density than the products of combustion in the chamber and the influence of the higher density ratio must be known. The present measurements show that a lip length of four diameters is not sufficient to allow any benefit from the larger density ratio except at distances less than ten slot heights and mass-velocity ratios greater than 1.7. For low P/D, the velocity-ratio advantage is lost beyond 25 slot heights. The small open area resulted in poor performance at all distances and velocity ratios. The slot with L/D of 2.5 resulted in low values of effectiveness because of the relatively high momentum of the jets exiting from the slot at a large angle to the tangential direction.

Figures 4.2.8a and b show that an increase in the open area ratio is advantageous up to a value of velocity ratio which varies with downstream distances. The two geometries considered are similar with respect to P/D, L/D and t/y_c. The measurements of reference 66 include an examination of the influence of open area ratio. They confirm the trend that the effectiveness increases with open area but provide no information on the influence of mass velocity ratio.

The results of tests with two row slots in Figure 4.2.9a and b show a considerable improvement over the single row slot of the same open area, P/D, and t/y_c. In spite of the longer over-hanging lip on the single row slot, the two-row slot resulted in effectiveness values approximately 20% of unity better than those for the single row. The better performance of the two-row slot was largely due to the staggered pitch of the holes which resulted in a more two-dimensional flow than the single row.

The influence of lip thickness is shown in Figure 4.2.10 and is similar to the two-dimensional result of reference 46. The effectiveness is reduced by an increase in lip thickness. The magnitude of the effect may be expected to increase with any geometric changewhich results in a more two-dimensional flow at the slot exit.

The influence of location of the holes relative to the vertical surface is shown in Figure 4.2.11. It appears that, when the holes are located nearer to the vertical surface in such a way that the vertical surface interferes with the spreading of the jets, there is a deterioration of about 5% in the downstream effectiveness. This conclusion is similar to that of Nobbs and Rice (75) based on different dimensions.

Measurements to determine the influence of slot height showed a deterioration in performance with decrease in slot height. This trend, shown in Figure 4.2.12, is in agreement with the conclusions of Kacker and Whitelaw (45) for two-dimensional slots. It may be, and this is partly confirmed by comparison with the data of reference 66 that the trend is not monotonic. The trend displayed on Figure 3.4.12 can readily be attributed to the influence of the ratio of t/y_c as discussed, for example, in reference 46. A reduction in y_c also has the effect, for a given lip length, of causing the flow to be more two-dimensional at the slot exit. Consequently, the effectiveness may increase again for lower values of y_c than those of Figure 4.2.12.

Figure 4.2.13 compares the present measurements with those of Kacker and Whitelaw and of Nina and Whitelaw. The comparisons are inexact due to small variations in the open area and other geometric parameters but allow the relative merits of a two-dimensional slot, a three-dimensional slot with tangential injection and two three-dimensional slots with normal injection to be demonstrated. The average mass-velocity ratios at the slot exit were essentially the same for each comparison. The two-dimensional slot results of Kacker and Whitelaw and the results obtained with normal injection through two rows of normal injection holes reveal that the two-dimensional slot has a much better performance for all velocity ratios and downstream locations. A similar comparison between a two-dimensional slot and a slot consisting of three rows of tangential holes was contained in reference 89 and indicated that the two resulted in identical values of effectiveness.

Tangential and normal-hole injection through a single row of holes reveals that the former results in a consistently higher

value of effectiveness. The results suggest that, for the particular arrangements compared on Figure 4.2.13, the difference may become negligible for values of $\rho_C U_C / \rho_G U_G$ greater than 1.5.

The conclusions indicated in the previous two paragraphs are likely to remain valid for density ratios up to 2.25 provided the effective slot lip length for the normal injection case is greater than 2.5.

4.2.3 EFFECTIVENESS & HEAT TRANSFER DOWNSTREAM OF COMBINED NORMAL& TANGENTIAL HOLES

Introduction

Chapter 2 reviewed available information of the performance of tangential holes, reference (66) and section 4.2.2 outlined the important parameters for optimising normal injection arrangements, with a finite lip. The information available on combined normal and tangential holes is surprisingly small in view of the many years of use of this geometry. References 74 and 75 are concerned with some parameters that influence the performance of combined normal and tangential holes but the number of parameters investigated is significantly fewer than necessary to allow optimisation of the slot geometry. The present section extends the investigated number and ranges of parameters considerably and, in contrast to references 74 and 75, provides information of the cross stream distribution of velocity and effectiveness.

The continuing use of splash cooling arrangements in the primary zones of combustors is due to the fact that tangential holes cannot always be designed to provide sufficient cooling air. As will be shown, the splash cooling arrangement provides a means to

increase a slot open area ratio and consequently the two dimensionality of the downstream flow. Since it is likely to remain in use for many years and since a basis for the optimisation of geometrical arrangements does not exist, the present work was undertaken with the following objectives (i) to quantify the influence of geometry and flow parameters on the downstream effectiveness and thereby to provide information to assist optimisation of splash cooling arrangements (ii) to provide measurements of impervious-wall effectiveness and necessary boundary conditions which will allow the testing of procedures designed for the calculation of film-cooling performance.

Aerodynamic Properties

The total pressure was measured with a flattened probe of external dimensions 2.5 mm by 0.5 mm. It had an arm of 70 mm which considerably reduced the interference of the probe with the flow. The static pressures were obtained with a 2.0 mm outside diameter probe with 4,0.3 mm diameter holes located 10 mm from its leading edge.

To test the symmetry of the slot-exit profiles, velocity measurements were made at five locations in line with the centres of different tangential jets. The asymmetry, in the case of the longer lip, was less than 3% on a mass flux basis but the local velocity asymmetry was as high as 10%. The corresponding figures for the shorter slot lip were 5% and 10%. It was noted from the pressure readings that the profiles varied with time and that the asymmetry did not, therefore stem from the geometry but rather from jet interactions. The flow in the plane of the slot exit had regions of substantial normal pressure gradient and recirculation and consequently probes cannot be expected to result in accurate

values. A sample number of measurements were obtained with a probe of arm length 25 mm and resulted in total head values, in the proximity of recirculating flow, which were up to 40% less than those obtained with the probe described earlier. The above comments relating to asymmetry were supported by sample measurements of Figure 4.2.22a and b.

Velocity profiles were obtained for three velocity ratios at three longitudinal positions and are shown in Figure 4.2.14. The total head and the static pressures were obtained separately and the static pressures were, at all locations, less than 20% of the total head except for velocity ratios less than unity when the static pressures were as high as 50% of the total heads at slot exit. The static pressures fell rapidly with increase in y and x. At all locations further than 5 slot gaps downstream, the static pressure was less than 10% of the total head. The regions of negative velocity can be identified on Figure 4.2.14 and further downstream it is clear that the flow is boundary layer like. The profiles appear nearly two-dimensional at locations well below twenty slot-gaps from the slot exit and suggest rapid mixing of the normal, tangential and mainstream flows. This is in agreement with Nina and Whitelaw's (74) earlier observation that the adiabatic-wall effectiveness became two dimensional within 4 to 5 slot gaps from slot exit.

Previous investigations of film cooling with total head holes have indicated that a long-lip results in near two-dimensional flow and, because of decreasing mixing, improves the effectiveness of the film. However, the longer the lip, the greater the possibility that part of it will attain a high temperature and burn off. The

normal jet has the effect of cooling the lip and, for it to perform this function efficiently, it should be located such that it impinges sufficiently close to the end of the lip to prevent the temperature rising above a prescribed maximum: at the same time, the normal jet must be located far enough from the slot exit to ensure that the coolant flow does not have a substantial normal velocity component downstream of the slot exit. As the velocity profiles in Figure 4.2.14 show, a lip length of 4.4 is too long since the normal jet has reattached to the lower wall. With this lip length, although better impervious-wall effectiveness is likely to be attained, part of this lip is likely to be burnt off in practice. The results for the lip length of 2.2 indicate that part of the normal jet may be lost into the mainstream and that there is a region of separated flow near slot exit.

Impervious Wall Effectiveness

The impervious-wall effectiveness was measured for the range of parameters listed in Table 4.2.3. The experimental programme was designed to allow the influence of the different flow and geometrical parameters to be separated. The experiment numbers below the figures correspond to the numbers on table 4.2.3. For each experiment, impervious-wall effectiveness was measured at 9 lateral positions. The aim was to estimate the three dimensionality and possible asymmetry. The results shown on Figures 4.2.15 to 4.2.23 are, however, based on an average spanwise effectiveness because, in a combustion chamber, conduction heat transfer tends to even out the variations in effectiveness. The average spanwise effectiveness was taken as the arithmetic average of the nine values taken over a cross stream distance of eight pitch diameters.

Figure 4.2.15a compares measured values of impervious-wall effectiveness for two lip lengths and two density ratios. The longer lip leads to effectiveness values which are 12% higher near the slot exit: this advantage of long lip decreases with downstream distance to 5% at 40 slot gaps. The larger density ratio reduces the advantage to a constant value of around 8% at all stations. The results obtained with uniform density ratio are in agreement with the previously observed trends of Nina and Whitelaw (74). The higher density ratio results in higher effectiveness but the trends obtained with the two density ratios were otherwise similar. The influence of lip length is considerably reduced by increasing the tangential momentum as indicated in Figure 4.2.15a and b.

The six sets of results shown on Figure 4.2.16a were obtained with the same A_o,A_o/A,L/y_c,l/D,t/y_c and y_L/y_c: the values of P/D and y_T/y_c were however varied. The need for the same open area ratio necessitated a different value of y_T/y_c. For the uniform density case, the difference in performance with pitch to diameter ratios of 2 and 2.8 is small for distances greater than 30 slot gaps. For a pitch to diameter ratio of 4, however, a significant difference can be observed at 40 slot gaps. Increases in both density ratio and tangential momentum did not change these trends. A higher pitch to diameter ratio results in a more three-dimensional slot flow with consequent decrease in effectiveness.

Experiments 5, 6, 9 and 10 of table 4.2.3 were performed with an open area of 1530 mm^2: the slots for experiments 25 and 26 had a gap of 14 mm and 5 and 6 a gap of 7.25 mm. The open area ratio was changed by increasing y_T/y_c. Figure 4.2.17 shows that, for a given coolant flow rate, the slot with the smaller open area ratio

had better performance near the slot exit. This is because a decrease in open area ratio reduces the average slot exit velocity and increases the concentration boundary layer thickness. This advantage is not maintained at downstream locations: the figures show that, at downstream positions greater than 10, the larger open area ratio results in better performance. This trend is maintained at higher density and higher tangential momentum ratios.

The influence of open area is shown on Figure 4.2.18 where plots of effectiveness against mass flow rate are presented. Both figures show that, for uniform density and fixed coolant flow rate, the open area should be arranged to give a near unity average exit velocity ratio. Thus, for the coolant flow rate at which the slot with the smallest open area had attained its maximum effectiveness, the effectiveness achieved with larger slots was still increasing with increasing coolant flow rate. With the larger density ratio, the smaller open area, corresponding to a higher average exit velocity, had better performance for all velocity ratios.

It was noted earlier that an important practical function of the normal jets is to prevent the lip from burning off. It is advantageous to minimise the normal momentum however, because this can result in a smaller component of normal velocity downstream of the slot exit and can reduce the turbulence intensity of the exiting coolant. Figure 4.2.19 shows that a reduction in the normal momentum had a marginal advantage, not greater than 6%, at a given coolant flow rate. Experiments 10 and 12 show that an increase in density ratio increases this advantage to around 10%. There is, however, a tendency for weak normal jets to allow the main stream to come between the tangential jets and thereby to reduce the effectiveness.

Figure 4.2.20 shows that an increase in density ratio increases the effectiveness: the comparatively small increase is probably due to the fact that, at the higher density ratio and shorter lip length coolant is lost to the mainstream at slot exit. An increase in tangential momentum ratio results in a greater influence of density ratio.

Figure 4.2.21 compares the performance of five geometries at equal coolant mass flow rates and shows that, in general, normal injection results in poorest performance. If, however, the open area ratio is increased by decreasing the slot gap, as in reference 66, it is expected that this would lead to better performance. Alternatively, the number of rows may be increased as in section 4.2.2. A two row arrangement of tangential holes results in excellent cooling performance. The next best to a two row tangential arrangement is the single ~~two~~ rows tangential cooling with a pitch-diameter of 1.4: Rastogi and Whitelaw (91) showed that, even when this arrangement was used without a slot lip, its performance is better than that of a splash cooling slot with the same open area ratio but a pitch to diameter ratio of 2 and a lip length of 2.2 slot gaps. Comparisons of single row of tangential holes with a pitch to diameter ratio of 2 (experiments 22 and 23) and a splash cooling arrangement of the same pitch to diameter open area and open area ratio shows that the latter arrangement was more effective. This is probably due to the fact that the splash cooling arrangement had 48 holes through which coolant was injected while the tangential slot had 12 holes. Experiments 17 and 19 show that if the splash cooling slot had a total of 12 holes through which injection took place, the single row of tangential holes is to be preferred.

Figure 4.2.22c,d and e show that asymmetry in the impervious-wall effectiveness is always less than ±4% of a mean spanwise value. This is less than the asymmetry in local velocity values mentioned earlier and indicated in Figure 4.2.22a,b. The lack of symmetry associated with these velocity profiles and the effectiveness values of Figure 4.2.22a,b,e is not constant in time but is typical of the magnitude of the effects. The slot configurations were symmetrical to better than 0.2% of the hole diameter and the mass flow through each of the individual holes was the same to better than 1%. There was a tendency for the individual jets to interact and to result in quasi-steady but asymmetric flows. The extent of the asymmetry and interaction varied with flow and geometrical arrangement. Neglecting the side wall effects, this asymmetry was minimised with the single row tangential slot shown in Figure 4.2.22e. Measurements with only normal injection also showed less asymmetry than a combined tangential and normal hole arrangement. Considerable asymmetry had previously been observed by Goldstein et al (38) for an arrangement of normal holes. Effects of this type are not likely to seriously influence the spanwise average values of effectiveness reported in the previous figures.

The influence of certain geometrical parameters have not been considered in this investigation. The influence of lip thickness is omitted because the earlier investigations of Kacker and Whitelaw and Nobbs and Rice (75) were considered to provide sufficient information. Also, the experiments of reference (89) had indicated that high values of y_L/y_c lead to poor performance. In the experiments reported here, y_L had a minimum value compatible with easy manufacture of cooling rings. Reference (75) and section 4.2.2 indicated

that a finite value of l/D is advantageous and Figure 4.2.23 here demonstrates that, for splash cooling arrangements, a finite l/D is necessary.

Adiabatic Wall Effectiveness & Heat Transfer Coefficient

As indicated in the introduction to this thesis, a complete assessment of the performance of a film-cooling arrangement requires a knowledge of the heat transfer coefficients. The adiabatic-wall effectiveness and the heat transfer coefficient were obtained for some of the configurations described earlier. In general, the measured adiabatic wall effectiveness are lower than the impervious wall effectiveness. This is because of the difficulty in making the experimental arrangement truly adiabatic. The scatter in the measured values of heat transfer coefficient are greater than 10%. This level of scatter was also observed in the measurements of Pai and Whitelaw (78).

Figure 4.2.24 was prepared to show the influence of U_t/un on both effectiveness and heat transfer coefficients. The value of U_t/u_n is 2, corresponding to smaller U_c/u_G shows lower effectiveness and higher heat transfer coefficient. At the higher velocity ratios corresponding to U_c/u_G greater than unity, the influence of U_t/u_n is small.

Figure 4.2.25 demonstrates that larger pitch-diameter ratios lead to lower effectiveness and higher heat transfer coefficients. This trend is in agreement with the findings of Rastogi and Whitelaw for tangential holes.

The comparison of 3 geometries in figure 4.2.26 shows that the influence of injection geometry is complex. The complexity stems from the fact that it is difficult to design three arrangements that

are identical in all respects. At the highest velocity ratio, the normal injection gave the highest heat transfer coefficient and the lowest effectiveness. At lowest velocity ratio, the trend is more complex; resulting in the lowest heat transfer coefficient and the highest effectiveness for combined normal and tangential holes.

4.2.4 CONCLUSIONS

The measurements presented in sections 4.2.1 - 4.2.3 allow the following conclusions to be drawn:

1. For a fixed open area and open area ratio, increasing the number of rows of holes improves the effectiveness of tangential and normal holes. Moderate lip length may be used to obtain a greater increase in effectiveness for smaller number of rows of holes
2. The impervious-wall effectiveness, for all the three arrangements, increases with increase in velocity, ratio, lip length and open area ratio.
3. The influence of pitch to diameter ratio extends to a downstream distance greater than 40 slot gaps: it increases with increase in velocity ratio. In general, the effectiveness decreases with increasing pitch to diameter ratio while the heat transfer coefficient increases with pitch to diameter ratio.
4. In common with two-dimensional slots, the arrangements of combined normal and tangential holes shows that, the optimum effectiveness for uniform density is obtained with an open area arranged to give a near unity velocity ratio; for non-uniform density, the highest velocity ratio compatible with mechanical strength results in best effectiveness.
5. For a given coolant flow rate, the influence of increasing the ratio of tangential momentum to normal is small and tends to improve

the effectiveness.

6. In general, increasing the density of the slot flow improves the effectiveness; except at high pitch to diameter ratio and for combined normal and tangential holes only where an increase in density may lead to poorer performance.

7. By increasing the number of rows or decreasing the pitch to diameter ratio for a fixed open area and open area ratio, the tangential holes arrangement may be superior to normal/combined holes. The investigations however, demonstrates the influence of geometry is complex. A combined tangential and normal hole arrangement can always be optimised to provide effectiveness comparable to two dimensional slots.

8. The flows through all the three arrangements are three dimensional. In addition, both the normal and the combined normal and tangential arrangements are subject to recirculation in the injection region. The influences of flow and geometric parameters are complex. It is necessary to develop a prediction procedure to calculate influences of parameters outside the present range of investigation. The available experimental data may be used to aid the development and assessment of such a prediction procedure.

THEORETICAL INVESTIGATION

4.3.0 INTRODUCTION

This part of the thesis is concerned with the calculation of adiabatic or impervious-wall effectiveness and heat transfer downstream of three-dimensional film-cooling slots. The purpose is to present values of effectiveness and heat transfer calculated with a modified version of Patankar and Spalding (83) procedure previously

used successfully for tangential three-dimensional film-cooling by Patankar, Rastogi and Whitelaw (91). The basic algorithm solves a steady three-dimensional form of the Navier-Stokes equations in which forward recirculation is assumed negligible. Although the calculation procedure does not take account of forward recirculation (and this is known to be present as indicated in section 4.2), it was used to calculate the mean properties downstream of tangential, normal and combined normal and tangential film-cooling slots. The presentation provides an assessment of the magnitude of the error caused by imposing the condition that negative velocities should be regarded as zero. Comparison of experiments with calculations quantifies the discrepancies and the reliability of calculations outside the range of existing measurements.

A simple mixing length was used to determine the effective viscosity. Higher order turbulence models, such as the two-equation turbulence model (e.g. the k-ε model used by Tatchell (109) for rectangular-duct calculations) or a Reynolds stress closure as used by Pope and Whitelaw (88) can be used with this procedure. However, the neglect of forward recirculation in the equations represent an approximation which suggests that the possible advantages of a higher order turbulence closure may not be justified. Besides, a closure of higher order than the present requires an increase in computing storage and time of at least 40% and this was difficult to justify. The measurements of section 4.2 suggest such rapid mixing that, except for the immediate vicinity of injection, a simple turbulence model and a parabolic procedure may be adequate.

Details of the calculation procedure have been described by Rastogi (89), Patankar and Spalding (83), Tatchell (109) and Sharma (96).

Section 4.3 therefore describes only the important features and the modifications required by the present investigation. A more detailed description is provided for completeness in appendix A. Section 4.4 discusses the results of the comparison between measurements and calculations and suggests reasons for the discrepancies. Calculations outside the range of measurements are presented and it may be assumed that their reliability is of the same order as indicated by comparison.

4.3.1 RELEVANT CONSERVATION EQUATIONS

The time averaged conservation equations for momentum, scalar property and mass continuity for a steady, incompressible three-dimensional flow in Cartesian coordinates can be written as:

x- momentum

$$\frac{\partial}{\partial x}(\rho U^2) + \frac{\partial}{\partial y}(\rho VU) + \frac{\partial}{\partial z}(\rho WU)$$
$$= -\frac{\partial P}{\partial x} - \left(\frac{\partial \tau_{xx}}{\partial x} + \frac{\partial \tau_{xy}}{\partial y} + \frac{\partial \tau_{zx}}{\partial z}\right) - \left(\frac{\partial}{\partial x}(\overline{\rho u}^2) + \frac{\partial}{\partial y}(\overline{\rho u\, v}) + \frac{\partial}{\partial z}(\overline{\rho u\, w})\right) \qquad 4.3.1$$

y- momentum

$$\frac{\partial}{\partial x}(\rho UV) + \frac{\partial}{\partial y}(\rho V^2) + \frac{\partial}{\partial z}(\rho WV)$$
$$= -\frac{\partial P}{\partial y} - \left(\frac{\partial}{\partial x}\tau_{xy} + \frac{\partial}{\partial y}\tau_{yy} + \frac{\partial \tau_{zy}}{\partial z}\right) - \left(\frac{\partial}{\partial x}(\overline{\rho u\, v}) + \frac{\partial}{\partial y}(\overline{\rho v}^2) + \frac{\partial}{\partial z}(\overline{\rho v\, w})\right) \qquad 4.3.2$$

z- momentum

$$\frac{\partial}{\partial x}(\rho UW) + \frac{\partial}{\partial y}(\rho VW) + \frac{\partial}{\partial z}(\rho W^2)$$

$$= -\frac{\partial P}{\partial z} - \left(\frac{\partial}{\partial x}\tau_{xz} + \frac{\partial}{\partial y}\tau_{yz} + \frac{\partial \tau}{\partial z}zz\right) - \left(\frac{\partial}{\partial x}(\rho\overline{u\,w}) + \frac{\partial}{\partial y}(\rho\overline{v\,w}) + \frac{\partial}{\partial z}(\rho\overline{w^2})\right) \qquad 4.3.3$$

Species concentration/stagnation enthalpy (ϕ)

$$\frac{\partial}{\partial x}(\rho U\phi) + \frac{\partial}{\partial y}(\rho V\phi) + \frac{\partial}{\partial z}(\rho W\phi)$$

$$= \frac{\partial}{\partial x}\left(\Gamma\phi\frac{\partial\phi}{\partial x}\right) + \frac{\partial}{\partial y}\left(\Gamma\phi\frac{\partial\phi}{\partial y}\right) + \frac{\partial}{\partial z}\left(\Gamma\phi\frac{\partial\phi}{\partial z}\right)$$

$$-\left(\frac{\partial}{\partial x}(\overline{\rho u\,\phi}) + \frac{\partial}{\partial y}(\overline{\rho v\,\phi}) + \frac{\partial}{\partial z}(\overline{\rho w\,\phi})\right) + S\phi. \qquad 4.3.4$$

Mass Continuity

$$\frac{\partial}{\partial x}(\rho U) + \frac{\partial}{\partial y}(\rho V) + \frac{\partial}{\partial z}(\rho W) = 0 \qquad 4.3.5$$

The laminar stresses can be defined as:

$$\tau_{xx} = -\mu\left(2\frac{\partial U}{\partial x} - \frac{2}{3}\,\mathrm{div}\,V\right)$$

$$\tau_{yy} = -\mu\left(2\frac{\partial V}{\partial y} - \frac{2}{3}\,\mathrm{div}\,V\right)$$

$$\tau_{zz} = -\mu\left(2\frac{\partial W}{\partial z} - \frac{2}{3}\,\mathrm{div}\,V\right)$$

$$\tau_{xy} = \tau yx = -\mu\left(\frac{\partial U}{\partial y} + \frac{\partial V}{\partial x}\right) \qquad 4.3.6$$

$$\tau_{yz} = \tau zy = -\mu\left(\frac{\partial V}{\partial z} + \frac{\partial W}{\partial y}\right)$$

$$\tau_{zx} = \tau xz = -\mu\left(\frac{\partial W}{\partial x} + \frac{\partial U}{\partial z}\right)$$

$$\Gamma_\phi = \mu/\sigma\phi$$

where:

$$\text{div } V = \frac{\partial U}{\partial x} + \frac{\partial V}{\partial y} + \frac{\partial W}{\partial z} = 0$$ for incompressible flow and in analogy with laminar stresses, the Reynolds stresses can be defined as:

$$\overline{\rho u\, v} = -\mu_t \left(\frac{\partial U}{\partial y} + \frac{\partial V}{\partial x}\right)$$

$$\overline{\rho u\, w} = -\mu_t \left(\frac{\partial U}{\partial z} + \frac{\partial W}{\partial x}\right)$$

$$\overline{\rho v^2} = -\mu_t \left(2\frac{\partial V}{\partial y} - \frac{2}{3}\,\text{div } V\right)$$

$$\overline{\rho w\, v} = -\mu_t \left(\frac{\partial V}{\partial z} + \frac{\partial W}{\partial y}\right)$$

$$\overline{\rho w^2} = -\mu_t \left(2\frac{\partial W}{\partial z} - \frac{2}{3}\,\text{div } V\right)$$

$$\overline{\rho u^2} = -\mu_t \left(2\frac{\partial U}{\partial x} - \frac{2}{3}\,\text{div } V\right)$$

$$\overline{\rho \phi\, v} = \Gamma_{t,\phi} \frac{\partial \phi}{\partial y}$$

$$\overline{\rho \phi\, w} = \Gamma_{t,\phi} \frac{\partial \phi}{\partial z}$$

$$\overline{\rho \phi\, u} = \Gamma_{t,\phi} \frac{\partial \phi}{\partial x}. \qquad 4.3.7$$

Because of the similarity in the definitions of laminar and Reynold stresses, an effective viscosity can be defined as:

$$\mu_{eff} = \mu + \mu_t \qquad 4.3.8$$

In deriving boundary layer form of the conservation equations, with an effective viscosity hypothesis, the definitions 4.3.6 - 4.3.8 are used and the following assumptions are made about the flow:

(i) the flow is steady, incompressible and fully turbulent.

(ii) there is no forward recirculation and hence the diffusion of momentum, heat and mass are negligible in the x- direction. The axial diffusive fluxes and stresses are, therefore, omitted in the equations.

(iii) the downstream pressure field has no influence on the upstream flow conditions. Thus, a pressure $\bar{p}$, spatially averaged over y-z plane can be used in the representation of the pressure gradient in the x- momentum equation.

For the present calculations, the conservation equations for momentum and species/enthalpy therefore become:

$$\frac{\partial}{\partial x}(\rho U^2) + \frac{\partial}{\partial y}(\rho UV) + \frac{\partial}{\partial z}(\rho UW)$$

$$= -\frac{\partial \bar{P}}{\partial x} + \frac{\partial}{\partial y}\left(\mu_{eff,y}\frac{\partial U}{\partial y}\right) + \frac{\partial}{\partial z}\left(\mu_{eff,z}\frac{\partial U}{\partial z}\right) \qquad 4.3.9$$

$$\frac{\partial}{\partial x}(\rho UV) + \frac{\partial}{\partial y}(\rho V^2) + \frac{\partial}{\partial z}(\rho VW)$$

$$= -\frac{\partial P}{\partial y} + \frac{\partial}{\partial y}\left(\mu_{eff,y}\left(2\frac{\partial V}{\partial y}\right)\right) + \frac{\partial}{\partial z}\left(\mu_{eff,z}\left(\frac{\partial V}{\partial z} + \frac{\partial W}{\partial y}\right)\right) \qquad 4.3.10$$

$$\frac{\partial}{\partial x}(\rho UW) + \frac{\partial}{\partial y}(\rho VW) + \frac{\partial}{\partial z}(\rho W^2)$$

$$= -\frac{\partial P}{\partial z} + \frac{\partial}{\partial y}\left(\mu_{eff,y}\left(\frac{\partial V}{\partial z} + \frac{\partial W}{\partial y}\right)\right) + \frac{\partial}{\partial z}\left(\mu_{eff,z}\left(2\frac{\partial W}{\partial z}\right)\right) \qquad 4.3.11$$

$$\frac{\partial}{\partial x}(\rho U\phi) + \frac{\partial}{\partial y}(\rho V\phi) + \frac{\partial}{\partial z}(\rho W\phi)$$

$$= \frac{\partial}{\partial y}\left(\frac{\mu_{eff,y}}{\sigma_{eff}}\frac{\partial \phi}{\partial y}\right) + \frac{\partial}{\partial z}\left(\frac{\mu_{eff,z}}{\sigma_{eff}}\frac{\partial \phi}{\partial z}\right) \qquad 4.3.12$$

where $\mu_{eff,y}$ and $\mu_{eff,z}$ are the effective viscoties in the y and z directions respectively and are defined by equations 4.3.13 and 4.3.14. σ_{eff} is the effective Prandtl numbers which was taken as unity for all calculations described below.

4.3.2 SOLUTION PROCEDURE

Details of the computational method are described in references (89,96,109) and appendix A. Features of importance for the present

application include:

(i) The solution employs a staggered grid arrangement, shown in figure A2.1, which allows the lateral velocities to be stored at locations where they are needed for the calculation of convection fluxes.

(ii) The convective and source terms of ϕ vary in a stepwise manner in yz planes but the diffussion terms in xy and xz planes vary linearly. For lateral convection in xy and xz planes, the arithmetic mean value of ϕ on each side of the face is assumed. The variation of diffussion terms is allowed to deviate from linearity to prevent physically unrealistic results when the lateral convective terms become too large. Equations 4.3.9 - 4.3.12 were thus put in finite difference form

$$\phi_P = A_N\phi_N + A_E\phi_E + A_S\phi_S + A_W\phi_W + B_P$$

where the A's incorporate appropriate flow areas (shown on figure A2.3 - A2.5) and density and B_P any source term, the subscripts denote north, south, east and west.

(iii) The equations are solved by successive use of a tri-diagonal matrix in the y and z directions as described in appendix A.

(iv) The lateral velocities and pressures are obtained by use of a "guess and correct" method. The lateral pressures are obtained from local continuity while the longitudinal pressure is obtained from over all continuity.

4.3.3 SPECIFIC MODIFICATION FOR PRESENT APPLICATION

(i) Effective Viscosity Assumptions

The assumption of an effective viscosity implies that auxiliary information about the viscosity law must be supplied to allow the solution of equations 4.3.9-4.3.12. The effective viscosity laws

used were:

$$\mu_{eff,y} = \rho \ell^2 \sqrt{\left(\frac{\partial u}{\partial y}\right)^2 + \left(\frac{\partial u}{\partial z}\right)^2} + 0.05 \left(t/y_c\right)^2 \rho_w \delta_w U_w \qquad 4.3.13$$

$$\mu_{eff,z} = 1 + 2.5(1 - y/y_G)\ \mu_{eff,y} \qquad 4.3.14$$

where

$$\ell = \frac{2\, C_u\, y_1\, y_2\, z_1\, z_2}{y_1 z_1 \sqrt{y_2^2+z_2^2} + y_1 z_2 \sqrt{y_2^2} + z_1^2 + y_2 z_1 \sqrt{y_1^2+z_2^2} + y_2 z_2 \sqrt{y_1^2+z_1^2}} \qquad 4.3.15$$

for positions within covering lip

y_1, y_2 ≡ distances of a point P(y,z) from one pair of walls parallel to the z direction

z_1, z_2 ≡ distance of point P from the pair of walls parallel to the y- direction.

For distances beyond the lip

$$\ell = 0.42y \qquad 0 < y < 0.0214y_G$$

$$\ell = 0.09y_G \qquad y > 0.0214y_G \qquad 4.3.16$$

δ_w is the distance between minimum and maximum velocity locations and U_w is the average of maximum and minimum velocities beyond the lip.

Equation 4.3.13 is identical to that of Patankar, Rastogi and Whitelaw (84). Calculations using equation 4.3.13 and the assumption $\mu_{eff,y} = \mu_{eff,z}$ lead to predictions in which, contrary to experiments, the effectiveness values were higher at the centre of normal holes than at the centre of tangential holes as shown in figure 3.3.1. It was assumed that an isotropic effective viscosity caused this as it under estimates the lateral mixing. The algebraic expressions of equation 4.3.14 was used to represent a non-isotropic effective viscosity. The use of equation 4.3.14 promoted lateral

mixing and accords with experiments which show that, two-dimensionality in effectiveness was attained within 20 slot gaps of the plane of slot exit.

Equation 4.3.15 represents a form of mixing length for flows in rectangular ducts. It was first suggested by Buleev (96) and was successfully used by Sharma (96) for flow in ducts of varying aspect ratio.

It is not claimed that equations 4.3.13 - 4.3.16 model the complex turbulence structure created by normal or combined normal and tangential jets. Modelling of this flow would probably require a Reynolds stress closure in conjuction with an elliptic three-dimensional procedure. In addition, the accuracy depends on initial profiles which are difficult to obtain for practical geometries. The need for economy is however an important justification for the present approach.

(ii) Control Volume and Boundary Conditions

To calculate flows downstream of tangential, normal or combined normal and tangential holes, the solution domain (figure 4.9) was Pi/2 wide in z direction. Symmetry was assumed between neighbouring pairs of holes. The left and the right faces of the control volume conform to planes of symmetry. The lower boundary conforms to the base plate and the free stream (determined by position where $U = 0.99\ U_G$) was the upper boundary. The boundary conditions may therefore be written as:

$U, V, W, \frac{\partial \phi}{\partial y} = 0$ at $y = 0$ (wall boundary)

$W, \phi = 0$ at $y \to \infty$

$U = U_G$ $y \to \infty$ (free boundary)

$$\frac{\partial U}{\partial z}, \frac{\partial V}{\partial z}, W, \frac{\partial \phi}{\partial z} = 0 \text{ at } z = 0 \text{ or } {}^{Pi}/2 \qquad \text{(symmetry planes)}$$

(iii) Initial Profiles

Since initial profiles could not be measured without disturbing the flow, the velocity was assumed uniform from the hole centre to 85% of the radius. In the last 15% of the radius a boundary layer with a seventh law velocity profile was assumed. The initial free stream boundary layer conforms to experimental values when available.

(iv) Grids

For all calculations ten grid nodes were used in the lateral (z) direction. The number of grid lines in the normal (y) direction vary from 12 to 18. For all calculations with ${}^{t}/y_{c} < 0.2$, and measured free stream conditions 12 x 10 grids were used.

When the boundary layer thickness is greater than measured values, the use of 12 x 10 grid nodes resulted in effectiveness values which were 2% lower than those obtained with 15 x 10 grid nodes.

For geometrices with ${}^{t}/y_{c} > 0.2$, the use of 12 x 10 grid nodes resulted in up to 8% loss in species near the slot exit. Fluctuations up to 2% in total specie flux were also observed. Grid nodes were made to conform with the top and bottom edges of the lip. An increase in number of grid points from 12 x 10 to 18 x 10 reduced the maximum specie loss to 6%. The loss in species was probably due to the negative velocities at the lip exit which were set to zero.

To reduce the specie fluctuation and losses further, false positive velocities varying from 1% to 5% of the mainstream values were prescribed at the slot exit (as shown in figure 4.3.1). This reduced the fluctuations to negligible values and the maximum

species loss to 4% for all situations investigated.

For the thin lip species was conserved within 1%. The introduced false velocities at the lip prevented $\frac{\partial U}{\partial y}$ from becoming zero at any point - hence an unrealistic situation which could result from the use of Prandtl mixing length was avoided. For calculations within normal injection forward steps of 5% of the slot gap were used. This accounted for more than 99% of the exiting fluid.

The increase in number of grid nodes and smaller forward steps for thick lip calculations, imply more computer time and storage. For thin lip calculations the CDC 6600 required 120 seconds to solve for 5 dependent variables from the slot exit to a location 45 slot gaps downstream. With the increase in grid nodes required for the thick lip the same distance required 400 seconds.

(v) Longitudinal Pressure

Due to the injection through the normal holes there was an increase in mass flux with downstream distance. This increase in mass flux affected both the static pressures and the longitudinal pressure gradients. The mass flux rate in for the cases of injection through both normal and tangential holes was evaluated from

$$m = m_t + \varepsilon\rho V_w \Delta X \Delta Z$$

where

m_t = total mass flux from tangential hole

V_w = normal injection velocity

The pressure correction equation (A33) therefore written as

$$\left(\frac{\partial \bar{P}}{\partial x}\right) = \frac{m_t + \varepsilon\rho V_w \Delta X \Delta Z - \varepsilon\rho U \Delta y \Delta z}{\varepsilon\rho D^U \Delta y \Delta z} \qquad 4.3.17$$

This pressure correction presumes that even in the normal injection region an average over the yz plane represents the complex pressure field.

A more complete expression for cross stream pressure correction equation A·28 is:

$$P_p' = A_N P_N' + A_S P_S' + A_W P_W' + A_E P_E' + B_P + B_P^V + B_P^W \qquad 4.3.18$$

where B_P^V, B_P^W ≡ secondary mass sources due to normal and lateral velocities respectively. The procedure of neglecting B_P^V, B_P^W was adopted, however, since their inclusion would bring values of velocities other than the four surrounding points into relationship for P_P' and consequently the downstream properties may affect the upstream flow properties. A linear relationship between velocity corrections for neighbouring points, as used by Tatchel (109) for laminar flow, was tested and found to have no significant influence on present calculations.

(vi) Influence of Impingement lip

A consequence of an average pressure gradient in the yz plane is the over estimation of pressure gradients at certain locations and under estimation at other locations. In particular, comparison between measured and calculated velocities in the tangential injection region were over estimated while those in the normal injection region were under estimated. As a consequence for the calculations of figure 4.4.10 - 4.4.22 it was assumed that the impingement lip acted as a redistributive source for longitudinal momentum equation. Its influence was accounted for by a term:

$$S_u \equiv \frac{\rho V_w^2 \; y/y_c}{\delta x} \qquad 4.3.19$$

where V_w is the normal injection velocity and the term S_u is finite only with normal injection region.

The addition of this term improved agreement between measured and calculated velocity profiles. The improvement was probably due to a considerable decrease in the calculated longitudinal pressure gradient. For example, the calculated pressure gradients at the same downstream location near the slot exit were 3250 KN/m^3 and 2640 KN/m^3 without and with the redistributive source term respectively. This represents a decrease of 20% in longitudinal pressure gradient. The influence of this change on velocity values can be as much as 20% and its influence on effectiveness is less than 2%.

4.4 RESULTS

This section presents the results of the application of the numerical procedure described in section 4.3 to normal and combined normal and tangential film cooling arrangements. The calculations for each arrangement are presented under two sub-headings: comparison and trends. The experiments of section 4.2 and other available data are used to assess the reliability and precision of the calculation procedure. The calculated trends provide new information outside the range of existing experimental information.

For normal holes only, equation 4.3.10 was used to evaluate the effective viscosity in y and z directions in common with the practices of Patankar, Rastogi and Whitelaw (84). The calculated results for normal and combined normal and tangential holes are presented in sections 4.4.1, 4.4.2, 4.4.3 respectively.

4.4.1 CALCULATED EFFECTIVENESS DOWNSTREAM OF NORMAL HOLES

Comparisons

The flow configurations for the calculations presented in

this section is shown in figure 4.4.1. Calculations are not presented for two row normal holes.

Figure 4.4.2 has been prepared to demonstrate the extent to which predictions of effectiveness agree with the measurements of section 4.2. The comparison covers a range of velocity ratios from 0.8 to 2.0, three hole diameters and two pitch to diameter ratios. The results on figure 4.4.2a correspond to hole diameters of 12.5mm: the predicted values indicate the same trends as the measurements but tend to be high by amounts which vary up to 15% of unity. The comparison indicated by figure 4.4.2b is similar to that of figure 4.4.2a except that the region of maximum discrepancy tends to correspond to low values of U_c/U_G and x/D rather than high values. Figure 4.3 corresponds to a lower value of P/D and reveals discrepancies at low values of U_c/U_G and x/D.

The quality of the comparison indicated by figures 4.4.2 and 4.4.3 certainly less than perfect and this is due partly to the incomplete form of the equations which form the basis for the numerical procedure and partly due to the comparatively simple form of turbulence model. Nevertheless, the trends are correctly predicted and the magnitudes are of the correct order. Consequently the following paragraphs describe calculations which have been performed, with the present procedure, to demonstrate the influence of various parameters which have practical significance but which have not been investigated experimentally. Where available, experimental values have been added to the figures.

Predicted Trends

Figure 4.4.4 is concerned with the influence of pitch to diameter ratio and presents diagrams which reveal the separate

influence of pitch and diameter for one velocity ratio. Increasing the pitch results in effectiveness values which decrease and tend to values which would be obtained with a single-hole configuration. Decreasing the diameter also results in effectiveness values which decrease but, in this case, the limiting value is zero. The apparent reduction in effectiveness with increasing diameters for values of P/D less than 2 indicates that the cross-stream mixing has resulted in a corresponding increase in effectiveness at locations away from the line of hole centre and a more two-dimenional flow.

The influence of density ratio is shown on figure 4.4.5 for one geometrical arrangement, corresponding to that of figure 4.4.3 and for two velocity ratios. The calculations show that the effectiveness increases with density ratio but that the increase is small for values of ρ_C/ρ_G greater than 2. It can be anticipated that, for lower values of L/D, the increase in effectiveness with density ratio will diminish and at very low values it will become a decrease.

Figure 4.4.6 demonstrates the influence of t/y_C for the same geometrical arrangement as that of figure 4.4.3 for a velocity ratio of unity and for two density ratios. The value U_e/U_G of unity corresponds to an average velocity ratio at the slot exit of approximately 0.5 and it can be anticipated that the influence of t/y_C would increase as the average velocity ratio at the slot exit tends to unity. The influence of t/y_C decreases with increasing density ratio. A comparison with results obtained in two-dimensional slot configurations reveals that t/y_C has a greater effect in these cases: in the present three-dimensional case, the mixing caused by the slot lip is a smaller proportion of the total mixing.

Corresponding to a value of t/y_C of 0.15 and again to the geometrical arrangement of figure 4.4.3, figure 4.4.7 presents the influence of y_G/y_C for a value of U_C/U_G of unity and for values of density ratio. Again as expected, the effectiveness decreases with increasing y_G/y_C and the decrease becomes negligible at a value of y_G/y_C of approximately 3. All previous calculations were performed with a value of y_G/y_C of unity and consequently the predicted effectiveness values would be significantly lowered if repeated with higher values of y_G/y_C. The influence revealed by the calculations is slightly exaggerated by a small loss of species (approximately 5%) associated with the comparatively coarse grid and the thicker boundary layers.

The predicted values presented so far have corresponded to impervious-wall effectiveness downstream of the centre line of a hole. Figure 4.4.8 has been prepared to indicate calculated values of effectiveness within the slot lip, downstream of the slot lip and in the cross-stream direction and to demonstrate the extent to which the calculation procedure is able to represent the velocity profiles in the plane of the slot exit. The calculations within the slot lip show that the effectiveness reaches a minimum, corresponding to the reattachment downstream of the separation region: the location of this minimum changes with cross-stream location. This calculated minimum value is unlikely to be important for gas-turbine combustor designs except as a warning that regions of separated flow which can exist downstream of the slot exit (and which probably existed locally for some of the present measurements) will have corresponding minima in the adiabatic-wall effectiveness. The measured velocity profiles shown on figure 4.4.8 indicate near

separation and also demonstrate the inability of the present parabolic, three-dimensional numerical procedure to represent the flow in this near-separation condition. The third diagram of figure 4.4.8 shows that the three-dimensionality of the flow has become insignificant at x/D of 30.

4.4.2 CALCULATED EFFECTIVENESS AND HEAT TRANSFER DOWNSTREAM OF COMBINED NORMAL AND TANGENTIAL HOLES

The experiments of section 4.2 were performed partly to allow an assessment of the extent to which a calculation procedure based on the solution of three-dimensional parabolic equations and the simple turbulence model of section4.3, could represent the film-cooling effectiveness downstream of combined normal and tangential holes. The flow configurations for combined normal and tangential holes are shown on figure 4.4.9.

Comparisons

Figure 4.4.10 allows a comparison between the present calculations and the velocity measurements of section4.2. It can be seen that discrepancies are greatest near the slot exit, where negative velocities were observed experimentally immediately downstream of the normal jets and in the central region of the slot. The measurements of section 4.2 showed that the flow develops rapidly and that the regions of reverse flow did not extend beyond 5 slot gaps. An obvious discrepancy between calculated and measured profiles at the slot exit is that the calculated mass flux was greater than the measured mass flux by values up to 40% in the central plane of the tangential jet. This is largely due to errors introduced in the

measurements by virtue of the use of probes in regions of recirculation and near recirculation, the integration of measured velocity profiles indicated that mass was not conserved. The integrated velocity profiles showed up to 20% loss in mass flux. One other reason for discrepancies is the fact that the procedure sets negative velocities to zero. This can distort the velocity profiles in situation with appreciable reverse flow. The assumption of a mean pressure gradient in a three-dimensional pressure field led to overestimation near tangential jets and under estimation near normal jets. The over simplified turbulence assumption, no doubt adds to the level of discrepancy.

In general, the discrepancies decrease with velocity ratio and downstream distance. The discrepancies are less than 10% at all locations greater than 5 slot gaps. Local quantitative discrepancies at lip exit are up to 50% of mean exit velocities.

The application of the present procedure to the geometry and flow conditions of Nina and Whitelaw (74) is shown in figure 4.4.11a. The calculations of effectiveness correspond to two lip lengths and two open area ratios. For the longer lip the maximum discrepancy for velocity ratios greater than unity is less than 12%. For the smaller velocity ratios, where the ellipticity of the flows is greater, the discrepancy rises to 20%. With the shorter lip length the discrepancy is less than 8%. It would appear that, for the shorter lip length, the influence of the assumed pressure gradient is reduced (due to shorter confined section of the flow) and consequently better agreement was achieved. The magnitude of the discrepancies can be attributed, in part, to the assumed initial

flow conditions (such as the mainstream velocity profile of upper lip boundary layer) which were not reported by Nina and Whitelaw. It may also be noted that Nina and Whitelaw did not take particular care to reduce y_L/y_c. This may be significant in reducing the ellipticity of the flow and in increasing the appropriateness of a parabolic procedure. The contributions of the over simplified turbulence assumption to the discrepancy can not be over stated.

Figures 4.4.11b, c, d show comparisons of effectiveness calculations with the measurements of section 4.2. The agreement is satisfactory at the higher velocity ratios and at a density ratio of unity: the discrepancies increase with decreasing velocity ratios and are greater with higher density ratio. Reasons for discrepancies are similar to those stated above for Nina and Whitelaw measurements - but it should be remembered that the uncertainty in higher density ratio measurements are up to ±4% due to the manual adjustments of the flow rate.

Figures 4.4.11e and f allow comparison of calculations with recent measurements from Rolls-Royce (1971) Ltd. The agreement between calculations and measurements is very satisfactory for non-wake flows. The capability of the procedure to accomodate many flow and geometric variables is demonstrated in figure 4.4.11e and f. A comparison of the two figures shows that, if the coolant flow is reduced by 37.5% due to a reduction in the diameter of the normal jets, a reduction of up to 7% in effectiveness may result. Calculations show a reduction of 6%.

Figure 4.4.12 show the capability of the prediction procedure to calculate the adiabatic wall effectiveness and heat transfer

coefficient. The discrepancies for the wake flows are higher than for the jet flows. The calculations tend to over estimate the adiabatic wall effectiveness while the heat transfer coefficients are under estimated. The non adiabatic experimental conditions may account for part of the discrepancies.

Predicted Trends

Figure 4.4.13 demonstrates that increasing lip thickness decreases impervious wall effectiveness. This is consistent with the findings of Kacker and Whitelaw (46) for two dimensional slots and Rastogi and Whitelaw (91) for three dimensional slots. Figure 4.4.14 shows the calculated influence of the upper lip boundary layer thickness is in qualitative agreement with previous work (89) and in reasonable agreement with the measurements of section 4.2.

Figure 4.4.15 shows the influence of pitch to diameter ratio on the effectiveness for a fixed pitch and for a fixed diameter. For a fixed pitch the mass flow rate increases with decrease in pitch to diameter ratio at a given velocity ratio. As expected. therefore, the effectiveness increases with decreasing pitch to diameter ratio. For a fixed diameter but increasing pitch, the three dimensionality of the flow is increased and this leads to a reduction in effectiveness values.

Figure 4.4.16 demonstrates that the influence of density ratio is well predicted and that quantitative comparisons show reasonable agreement. An increase in density ratio improves the impervious-wall effectiveness.

The calculated influence of lip length is shown to be small in figure 4.4.17. The calculations appear to under estimate the influence of this parameter by approximately 8%. For the unity

density ratio and lip lengths greater than 5, there is a tendency to show negative influence. This may result largely from the way in which the longitudinal pressure gradient was calculated. The procedure tends to over estimate the pressure gradient at certain positions while it under estimates it at other locations. The influence of the way in which the pressure gradient is calculated become more significant as the lip length increases. Of course, previous measurements show that favourable pressure gradient led to lower impervious-wall effectiveness.

For a fixed mass flow rate the influence of the ratio of tangential to normal momentum is shown to be small in figure 4.4.18. The influence of diameter ratios is shown in figure 4.4.19: as the size of the normal jet is reduced, the performance rapidly falls to that of a single tangential jet.

Figures 4.4.20 - 4.4.22 show the calculated influences of lip thickness, lip length, pitch-diameter ratio and density ratio on heat transfer coefficient. The figures show that the influence of lip thickness and lip length on heat transfer coefficient are small while the influences of pitch-diameter ratio and density ratio are more significant. In agreement with Rastogi's (89) calculations for tangential jets, the heat transfer coefficient decreases with decreasing holes due to the smaller coolant flow rate. The heat transfer coefficient increases with increasing density ratio.

4.4.3 DISCUSSION

The comparisons presented in section 4.4.1 - 4.4.3 allow an assessment of the reliability of the prediction procedure. The discrepancies for the jet flows are less than 15% while for wake flows discrepancies up to 25% may be obtained. This level of discrepancy is significantly lower than that obtained by Tatchel (109) who used the same numerical procedure for calculating effectivness downstream of a square jet in a cross flow and found discrepancies up to 50%. The improved agreement for the present calculations indicates that the procedure is more appropriate for the present flow configurations than those of Tatchel(109).

In general the results indicate that the discrepancies between measurement and calculation may stem from the following:

(i) The parabolic nature of the equations: this resulted in the need to set negative velocities to zero and to assume a spatially averaged pressure gradient. An improved procedure would solve the fully elliptic equations to represent the recirculation zone.

Undoubted a fully elliptic procedure would also be considerably more expensive of computer time and storage.

(ii) The Turbulence Assumption: the use of a more elaborate numerical procedure suggests that a higher order turbulence model than the simple mixing length might be advantageous. The Reynolds stress model is perhaps a reasonable alternative but would require the solution of additional equations. Pope and Whitelaw (88) indicated that even a Reynolds stress model may not calculate the mean properties of a wake accurately - although it improves the accuracy of calculated turbulence properties. The present flow is

likely to be even more difficult to represent. The use of a turbulence model more complicated than an effective viscosity model can not be justified unless it can be shown that discrepancies stem mainly from the turbulence assumption.

4.4.4 CONCLUSIONS

From the results and discussion the following conclusions may be drawn:

1. Although the near slot exit properties are poorly predicted, owing to the elliptic nature of the flow in this region, the calculated trends are correct and further demonstrate that the calculations are in reasonable quantitative agreement with measurements of effectiveness and heat transfer coefficient.
2. In general, the procedure predicts an increase in effectiveness with increase in velocity ratio, density ratio, and lip length. The effectiveness decreases with increasing pitch to diameter ratio, lip thickness, and upper lip boundary layer thickness. The influence of tangential to normal momentum ratio may be small provided the total flow rate is constant.

CHAPTER FIVE

5.0 IMPINGEMENT COOLING

Introduction

In reference 113 Whitelaw compared the performance of convection-cooled airfoils and film-cooled air foils. From the comparison it was evident that although film-cooling allowed operation with higher turbine entry temperatures, the tendency towards still higher turbine entry temperatures is likely to outpace advances in design of film cooling arrangements. The laboratory evidence for transpiration cooling, as alternative to film-cooling, appeared attractive. Material limitations and the attendant aerodynamic problems are however against the use of transpiration cooling inspite of its excellent cooling capability. It is therefore necessary to find ways of enhancing the performance of film cooling arrangements. It is useful to note that the coolant thermal capacity is usually not fully used before the coolant mixes with the main stream. It can be more fully utilised by composite arrangements that enhance cooling performance.

The performance of film cooling arrangements may be enhanced by making use of the cooling air on the cold side of the combustor wall before using it to form a film. It may be used in the following ways: (i) counter flow convection (ii) straight finned counter flow convection (iii) helical finned counter flow convection (iv) impingement and counter flow convection. Rastogi (89) has demonstrated that (i) improves the cooling performance as opposed to a combination of parallel flow convection cooling and film cooling by up to 3%. Colladay (15) demonstrated that (ii) leads to better performance than (i). The third arrangement (iii)

is akin to those found in nuclear reactor rods: it has not been applied to film cooling and it may be anticipated that such an arrangement would require a higher pressure drop. Heat transfer coefficients for impinging flow are often several times higher than those in boundary layer flows. A slot arrangement which combines the advantages of impingement heat transfer, internal convection and film cooling could, therefore, be advantageous. Experiments by Gauntner et al (33-35) demonstrate that the practical modifications necessary to combine impingement and film cooling may be cheap and easy. To improve available knowledge of impingement this chapter reports experimental and numerical investigations of impingement heat transfer. The information obtained is subsequently applied to combustor cooling in chapter 6, which demonstrates that the combination of impingement and film cooling can lead to lower combustor wall temperatures.

Section 5.1.1 discusses experimental methods for evaluating impingement heat transfer. Section 5.1.2, assembles, however, the previous findings and emphasizes apparent discrepancies in conclusions. Table 5.1.3 presents some of the available correlations and indicates their limitations and section 5.1.4 describes the previous theoretical attempts to represent impingement and suggests that a more comprehensive representation of the turbulence structure is essential to further progress. Section 5.2 describes the present experimental investigation and section 5.3 the theoretical investigation which makes use of a turbulence model that is more comprehensive than those used by previous workers (94,116). This resulted in reasonably good qualitative and quantitative agreement between measurements and theory.

5.1 PREVIOUS INVESTIGATIONS

The following subsections describe possible experimental methods, previous experimental determination of the influences of possible parameters, correlations due to previous workers and previous theoretical investigations respectively.

5.1.1 EXPERIMENTAL METHODS

One of the common methods used to determine the heat transfer coefficients is to make use of a mass transfer analogy and to determine the mass transfer coefficient by measuring the rate of naphthalene sublimation. In this method (52) the mass transfer by an impinging jet is calculated from the contour of the naphthalene surface measured before and after impingement over a known period. The heat transfer coefficient is then deduced from the relation:

$$Nu = \left(Pr/S_c\right)^n . Sh \qquad 5.1.1$$

where n is usually between 0.33 and 0.4.

Gardon et al (30,31,32) and Beer et al (6) have used a heat flux meter which produces an e.m.f. proportional to the heat flux. The small size of this meter (0.9 mm diameter) enabled Gardon et al to obtain detailed variations of impingement heat transfer coefficients on a heated isothermal aluminium plate. Friedman and Mueller (29) used an isothermal plate heated with steam and, from the steam condensation rate and the plate temperature, determined the impingement heat transfer. Friedman and Mueller

technique can not be used to determine the local heat transfer coefficients. Perry (87) used a 16 mm diameter water calorimeter fixed to an impingement plate. The plate could be located at different positions and orientations but the local resolution was poor due to large size of the meter.

The experiments by Metzger et al (62,63,64,65) and of Huang (42) made use of the transient response of a heated metal block. This method is based on the assumption that the temperature distribution in the block remains spatially uniform and that the convective heat transfer is related to the decrease in internal energy of the block. A single thermocouple measures the temperatures at the beginning and end of a known time interval. The heat transfer coefficient is obtained from the equation:

$$h = \frac{-C}{(\tau_1-\tau_0)} \ln \frac{(t_1-t_\infty)}{(t_0-t_\infty)} - \text{leakage.} \qquad 5.1.2$$

Local values of heat transfer coefficient can not be obtained with this technique.

Another technique used in impingement heat transfer experiments is to instrument a thin foil with thermocouples. A heated jet impinges on the supported foil which has been well insulated at the other surface to reduce heat losses. The temperatures of the plate under steady conditions are noted for zero heat flux and finite heat flux. Goldstein (10), Sparrow (104), Dyban and Mazur (18) used this technique. The local heat transfer coefficients can be obtained as described in chapter 4. Because this technique provides both the local adiabatic wall effectiveness and local heat transfer coefficients, it was used for the

present investigation. In contrast to Goldstein et al, the heat transfer coefficient was evaluated from local wall temperatures and local adiabatic wall temperatures. Goldstein et al calculated the heat transfer coefficients from measured recovery temperatures and local wall temperatures.

5.1.2 PREVIOUS EXPERIMENTAL STUDIES OF IMPINGEMENT COOLING

The review of previous studies by Wilcock (115) indicates that available literature on impingement cooling is extensive. It is, however, difficult to draw conclusion because previous investigations were insufficiently detailed and possible parameters were not systematically investigated. Table 5.1.2 has been prepared to show the main findings of previous studies and the following conclusions relate to the information on table 5.1.2.

1. A nozzle to plate distance of around 8 leads to highest impingement heat transfer for slot jets while a nozzle plate distance of 6 leads to highest heat transfer for circular jets. When the impingement plate is concave, a nozzle plate spacing of 3.5 gives highest heat transfer coefficient for slot jets while a nozzle plate distance of 1 is best for circular jets. Gauntner et al (34) measured temperatures of impingement cooled air foils and noted that lower airfoil temperatures were obtained for nozzle plate spacing of 1 than for nozzle plate spacing of 6.
2. For a given flow rate and for the flow configurations of Metzger et al (62) and Tabakoff et al (107) rows of circular holes produce a higher overall heat transfer coefficient than a single row of holes or a slot. The slot produces the lowest overall heat transfer coefficient.

When a row of slot jets is used and the nozzle plate distance is greater than 6, the identity of each jet may be lost due to jet interaction. The resulting heat transfer coefficient is lower than for a single slot at the stagnation line.

3. A concave impingement plate may increase the stagnation line heat transfer coefficient by up to 30%. For highly curved plates like those of Dyban and Mazur (18) the profile of the heat transfer coefficient may be U shaped with a minimum at the stagnation line and higher values downstream of stagnation line.

4. McMurray et al (61) investigation with water jet indicated that there may be an optimum impingement angle for stagnation line heat transfer coefficient. Due probably to poor spatial resolution, Perry's investigation indicated a monotonic decrease of heat transfer coefficient with decrease in impingement angle.

5. The influence of cross flow (flow in a direction at right angles to the main direction of flow of the impinging jet) on impingement heat transfer coefficient is small provided the impingement velocity is much higher than the cross flow mean velocity.

6. The influence of Reynolds number and jet turbulence intensity on heat transfer coefficient are significant. The heat transfer coefficient increases with increase in Reynolds number and turbulence intensity.

The experimental evidence on table 5.1.2 do not justify more specific statements than the above. In many cases, the average heat transfer coefficient is measured whereas spatial values are necessary for design optimization.

Table 5.1.2

INFLUENCE	REFERENCE	GEOMETRY	IMPORTANT PARAMETERS	SPECIAL FEATURES	CONCLUSIONS
Nozzle-plate distance (y_n)	Sparrow(105)	Single slot jet	$2 < Y < 20$	Laminar jet $276 < Re < 1750$	Sh decreases with increasing Y
	Gardon et al (31)	Single slot jet	$\frac{1}{3} < Y < 80$	$450 < Re < 22000$	For $Re < 950$, h_o decreases with increasing Y. For $Re > 1000$, h_o is maximum at Y=8
	Schuh and Petterson (95)	3 slot jets in a row	$Y = 2,8,16$	$316 < Re < 31600$	h max occurs at Y = 8
	Metzger (62)	Single slot jet, row of circular jets	$4.65<Y<55.6$	$1000 < Re < 6300$ flat plate, concave plate	Slot: h max occurs at Y=8 for flat plate; h max " " Y=3.5 for concave plate. row: h max occurs at Y=1 for concave
	Tabakoff (107)	Single slot jet, row of circular jets, many rows of circular jets	$Y = 1,6$	$5000 < Re < 15000$ concave plate of R = 63.5 mm	Slot: h max occurs at Y=6. row/rows: h max occurs at Y=1
	Gardon et al (30)	Single circular jet	$\frac{1}{4} < Y < 24$	Re = 28,000	h_o is max at Y = 6 for $Y > 0.5$
	Sparrow et al (104)	Single circular jet	$3 < Y < 12$	Cross flow present	h_o is maximum at Y = 6 when mass velocity ratio is greater than 8

Notes:

$Y \equiv \frac{y_n}{y_c}$ $h_o \equiv$ stagnation point heat transfer coefficient $h \equiv$ overall heat transfer coefficient Sh ≡ Local Sherwood numbers

INFLUENCE	REFERENCES	GEOMETRY	IMPORTANT PARAMETERS	SPECIAL FEATURES	CONCLUSIONS
	Friedman & Mueller (29)	Single slot jet single row of circular holes many rows of circular holes	$5 < Y < 30$ $90^{o}, 22.5^{o}, 45^{o}$	steam condensation technique h measured	For same flow, rows of circular holes produced highest heat transfer rate. Slot jet was poorest
NOZZLE GEOMETRY	Tabakoff et al (107)	same as above	$Y = 1, 6$	$5000 < Re < 15000$ concave plate h measured	For same flow rate, rows of circular jets produced highest heat transfer rate, slot jet was poorest. For slot jets, smaller open area give higher heat transfer rate
	Metzger et al (62)	single slot jet row of circular holes	$4.65 < Y < 55.6$	$1000 < Re < 6300$ concave plate h measured	Row of circular holes is superior to a slot jet for same mass flow rate
	Gardon et al (31)	Single slot jet row of slot jets	$Y = 4, 16, 40$	$Re = 5,500$	For $Y > 6$, identity of each jet is lost due to jet interaction. h_o is lower than for a single jet. For $Y < 6$ h_o is nearly same as for single jet but secondary peaks develop in-between jets if $Pn < 16$
	Schuh and Petterson (95)	6 slot jets 6 rows of circular holes		$5 < Pn < 100$	For $Pn \to 100$, slot jets are superior to equivalent circular holes. $Pn \simeq 14$ gave max. average heat transfer coefficient. Single slot jet is superior to row of slot jets.

INFLUENCE	REFERENCES	GEOMETRY	IMPORTANT PARAMETERS	SPECIAL FEATURES	CONCLUSIONS
Nozzle geometry	Dyban & Mazur (18)	Slot jet, row of holes	2.6 < Y < 13	Flat plate, parabolically shaped concave plate with 5mm apex radius	At same Re and absolute distance from apex, row of holes gave 40% increase on average heat transfer coefficient of slot jet
PLATE GEOMETRY	Dyban & Mazur (18)	same as above	same as above	same as above	Profile of heat transfer coefficient on concave plate is U shaped with a minimum at stagnation point while on a flat plate it is bell-shaped with max. at the stagnation point. Mean heat transfer over concave surface was 35-40% higher than on flat surface
	Metzger, Baltzer et al (65)	Slot jet, row of circular holes	10 < Y < 84	2000 < Re < 6000 Concave plates Flat plate	Sharp leading edge increases the mean heat transfer coefficient by up to 30%
	Metzger (62)	Slot jet, row of circular jets	4.65 < Y < 55.6	1000 < Re < 6300	Maximum heat transfer rate occurs at Y=8 on flat plate while it occurs at Y=3.5 on concave surface

INFLUENCE	REFERENCES	GEOMETRY	IMPORTANT PARAMETERS	SPECIAL FEATURES	CONCLUSIONS
Impingement angle θ	Perry (87)	Single circular jet	θ = 90,75,60,45, 30,15	7000 < Re < 30000 16mm water calorimeter	h_o decreases as θ decreases
	McMurray (61)	Slot jet	θ = 90,60°,30°	63000 < Re < 120,000, water jet	Correlated experimental data shows that laminar jets has maximum h_o at θ=76.5° while turbulent jets has maximum h_o at 63°
	Friedman & Mueller (29)	Row of circular holes	θ = 45°,22.5°		Impingement at 45° produces higher heat transfer coefficient than impingement at 22.5%
Cross-Flow	Bouchez et al (10)	Single circular hole	Y = 6,12	Cross-flow	At cross-flow velocity ratio of 3, impingement heat transfer is reduced by up to 60%
	Metzger & Korstad (64)	Row of circular holes	2 < Y < 6.7 Cross-flow velocity ratio vary from 1 to 3	2.5 < $\frac{P}{d}$ < 5	Cross-flow augments downstream heat transfer and reduces up stream heat transfer. The magnitude increases with increasing P/d
	Schuh et al (95)	6 slot jets 6 rows of circular holes			Cross-flow due to upstream impinging jets has no influence on average heat transfer coefficient
	Gaunter et al (35)	row of circular holes		impingement on internal surface of typical airfoil	

INFLUENCE	REFERENCES	GEOMETRY	IMPORTANT PARAMETERS	SPECIAL FEATURES	CONCLUSIONS
Reynolds number	Gardon et al (30)	Single slot jet	$\frac{1}{3} < Y < 80$	$450 < Re < 22000$	h_o increases with Reynolds number
	Sparrow (105)	Single slot jet	$2 < Y < 20$	laminar jet $276 < Re < 22000$	Sh increases with Reynolds number
	Perry (87)	Single circular jet		$7000 < Re < 30000$	For all θ, h_o increases with Reynolds number
Turbulence Intensity	Gardon et al (31)	Single slot jet	$Y = 2, Re = 11000$	Exit turbulence intensity increased from 2.5% to 18%	The increase from 2.5% to 18% produced 70% increase in h_o. The secondary peaks disappear
Nozzle Mean Exit Velocity Profile	Sparrow et al (105)	Single slot jet		Uniform exit profile of Gardon et al used fully developed laminar profile (Umax/Umean=1.5)	Comparison of h for uniform velocity profile and fully developed indicate a 30% increase in h for fully developed
	Foss & Klein (27)	Single circular jet			Uniform velocity profile decays at a rate 30% faster than fully developed

Table 5.1.3

REF	CORRELATION	REF	CORRELATION
52	$Sh_o=1.42\ Re^{0.58}Y^{-0.62}$ $Sh_x=0.076\ Re^{0.8}Y^{-0.6}X^{-0.37}$ $Sh=0.0069Sc^{0.4}Rea$, $Rea<20000$ $Sh=0.05S_c^{0.4}Rea^{0.8}$, $20000<Rea\leq 10^5$ $Sh=0.36Sc^{0.4}Rea^{0.63}10^5\ Rea$ where $10^4< Re< 1.5\times 10^4$ $10< Y< 40, 0< X< 30$	95	$St=0.461\ Pn^{-0.327}Re^{-0.402}$ for $1200 < Re < 10^5, 5 < Pn < 100$ $Y \simeq 4$ for array of slot jets
		1	$Nu_x=0.097\ Re^{0.8}X^{-0.6}$ for $30< x< 80$ (For slot wall jets, i.e. $Y< 0.5$)
31	$Nuo=1.2\ Re^{0.58}Y^{-0.62}$ $Re > 2000$, $Y > 14$ $Nu=0.36\ Rea^{0.62}$ (for array of slot jets)	87	$Nux=0.181\ Rea^{0.7}Pr^{1/3}$ for $\theta = 90^o$ (Single circular jet); experimental multiplying factors for $\theta < 90^o$.
99	For single slot jets $Nu_x=0.88\ Re^{0.75}$, for $10^3< Re< 10^6, 10< Y <60$ $2< x< 70$ For array of slot jets $Nu=0.34\ Re^{0.7}\exp(-0.37Y)$ $(\frac{1}{P})^{-0.2}$ for $10^4< Re<10^5$, $5< P_n< 40<5< Y< (P_n+5)$	7	$Nu_o=0.8\ Pr^{0.4}Re^{0.5}Y^{-0.08}$ $(1+0.8\ \varepsilon^{1.1}\ Re^{0.28})$ where $\varepsilon = \sqrt{u^2}/U$ at nozzle exit
		30	$Nu_o=13\ Rea^{1}/Y$, for $Rea\ 14000$ $Nu=0.286\ Rea^{0.625}$ for array of circular jets
		64	$St=0.0822\ M^{-0.049}Re^{-0.338}$ for $X = \pm 10$, $Y = 2$ $1 < M < 3, 2.5 < P < 5$
18	$Nu_o=0.31\ Re_{hD}Y^{-0.22}$ for $3000< Re_{hD}< 120000$ $Nu_x=0.167Re_x^{0.63}Y^{0.7}$ for Y $x>4.7$ $Nu_x=0.493Re_x^{0.63}$ for $Y<4.7$ concave plate	62	$St_o=0.23\ Re^{-0.27}$ $St_{max}=0.355\ Re^{-0.27}\ X^{-0.52}$ for $1150< Re< 6300$, $4.65< X< 55.6$ concave plates
61	$Nu_o=0.75Pr^{1/3}(\eta\ Re)^{0.5}$ $Nu_x=0.47\ (1+.63in(\theta/0.85))Pr^{1/3}(\eta\ Re)^{0.5}$ for laminar $Nu_x=0.31(1+.22\ \sin(\theta/0.7))Pr^{1/3}(\eta\ Re)^{0.8}$ η = local velocity/exit velocity for plane water jet		

5.1.3 CORRELATIONS

Table 5.1.3 lists correlation equations, provided by various authors, which relative the heat transfer coefficient to Reynolds number and to other parameters of impinging flows. As with most correlations, their use outside the range of parameters used to derive them must be regarded with caution.

Notes on tables 5.1.3

Re ≡ Reynolds number based on mean nozzle exit velocity

Rea ≡ Reynolds number based on arrival velocity

Y ≡ Nozzle plate distance ($^{y}n/y_c$)

X ≡ stream wise location (x/y_c)

Pn = distance between adjacent slot nozzles or distance between adjacent rows of holes (P/y_c or P/d)

5.1.4 PREVIOUS THEORETICAL INVESTIGATIONS

Previous attempts to calculate impinging jet flows are reviewed in great detail by Wilcock (115) who classified previous theoretical investigations into two groups: inviscid flow solutions and boundary layer and energy solutions. However, the solutions described as inviscid by Wilcock (115) is an hybrid of potential-flow solutions and similarity solutions of boundary layer equations. Another group of solutions use iterative finite difference procedures to solve the relevant elliptic equations. The brief review provided here is grouped into potential-flow boundary layer solutions and the solutions based on elliptic partial differential equations.

The Potential-flow boundary layer solutions

In this group of solutions, the flow is assumed to consist of two parts. The outer part is assumed inviscid and an appropriate potential flow solution is used to provide the free stream velocity for the wall boundary layer on the impingement surface. The boundary layer equations are then transformed into convenient forms by using suitable similarity variables. The resulting differential equations are then solved by finite difference method.

Investigations using the above approach and previously reviewed by Wilcock included those of Shen (115), Brady and Ludwig (115), Strand (115) and Siegal (115). A recent contribution not included in the review of Wilcock (115) is that of Sparrow and Lee, whose calculations were made for a fully developed, laminar plane jet impinging normally on a flat wall. In contrast to many of the previous attempts using potential-flow boundary layer solutions, Sparrow and Lee used a non uniform initial velocity profile and arrived at the useful conclusion that fully developed velocity profile can increase impingement heat transfer.

Miyazaki and Silberman (70) also used a potential flow solution to obtain the free stream velocity and this was subsequently used in solving the transformed wall boundary layer equations.

Table 5.1.4 shows that the calculations of Sparrow and Lee (103) were within 10% of experimental results for a nozzle plate distance of two. The solution was insensitive to nozzle-plate distances greater than three. The results obtained by Miyazaki and Silberman (70) can be described as qualitatively plausible although no comparison was made with measurements.

Numerical methods similar to those outlined above have been used to calculate characteristics of both round and plane jets impinging on flat and curved plates. The calculation of the heat transfer characteristic in the wall jet region of the impinging jet by Tabakoff et al (107) used Glauerts similarity solutions. In Glauerts similarity solutions the outer layer is assumed to have a constant eddy viscosity given by Prandtls hypothesis and the wall boundary layer is assumed to be governed by Blasius formula for turbulent pipe flow. Comparison of calculations using Glauerts similarity solution with experiments by Tabakoff et al (107) and Porch (115) indicated considerable discrepancies. Porch (115) suggested that the discrepancies might stem from the viscosity model.

A major limitation of the potential-flow boundary layer solution is that it can not be applied to stagnation point since infinite velocities would be predicted.

Solutions of Elliptic Partial differential Equations

In this class of solutions, the elliptic partial differential equations are solved by iterative numerical procedures. Both the longitudinal and lateral diffusion fluxes are accounted for in this class of solution..

In the particular solution procedures used by Wolfshtein (116), Russel and Hatton (94), vorticity, stream function and turbulence kinetic energy were the primary variables while velocities and pressures were derived variables.

The use of this group of solutions also require that the turbulence viscosity must be characterised. The calculations of Wolfshtein,

Russel and Hatton described on table 5.1.4 defined the turbulence viscosity by an algebraically prescribed turbulence length scale and turbulence kinetic energy.

Wolfshtein's calculations of skin friction and pressures showed reasonable agreement with measurement. Comparison of calculation with measurements by Russel and Hatton showed that the turbulence properties were less precisely calculated. Comparison of Stanton numbers with Gardon et al (30) measurements indicated considerable discrepancies. Russel and Hatton indicated that the turbulence model need improvement as up to 400% discrepancies were obtained between assumed turbulence length scale and measured length scale.

The above review of theoretical investigations of impinging jets demonstrate that although progress has been made, the agreement between measurements and calculations is not very satisfactory. It is probable that much of the discrepancy stems, as suggested by Porch (115), and Russel and Hatton from turbulence assumptions and present investigation was conducted to determine the extent to which this is true. At the same time, an improved numerical method (48) allows the calculations to be obtained with greater convenience and consequently reduce possible numerical errors. The numerical procedure described in (48) allows pressures, velocities and turbulence properties to be determined with greater convenience and makes use of a more advanced turbulence model than previously used for impinging flows. This procedure described fully in section 5.3 is used for the present investigations.

Table 5.1.4

REFERENCES	EQUATIONS SOLVED	PHYSICAL ASSUMPTIONS	NUMERICAL DETAILS	CONCLUSIONS & COMMENTS
Sparrow & Lee (103)	$\frac{\partial^2\psi}{\partial x^2} + \frac{\partial^2\psi}{\partial Y^2} = f(\psi)$ where $\psi=\sin(\pi X/2)$ $V_y=-\frac{\pi}{2}\cos(\pi X/2)$ $f(\psi)=-(\frac{\pi}{2})^2\psi$ With the b.c, $\psi=0$ at symmetry line & at the wall $\psi=1, R=R(\theta), \theta_D < \theta < \theta_C$ for the free boundary	Impinging jet is inviscid Wall boundary layer is laminar	Separation of variables employed and the resulting Bessel function truncated. .Bernoullis equation used to determine boundary values. .Algebraic equations are generated for each point and the unknown coefficients determined by least square method.	Comparison of calculation with experiment show agreement within 10%. .Solution is insensitive to nozzle plate distance.
Miyazaki & Silberman (70)	$\frac{\partial U}{\partial x} + \frac{\partial V}{\partial y} = 0$ $U\frac{\partial U}{\partial x} + V\frac{\partial V}{\partial y} =$ $Us\frac{\partial U}{\partial x} + \nu\frac{\partial^2 U}{\partial y^2}$ $u\frac{\partial t}{\partial x} + V\frac{\partial t}{\partial y} =$ $k\frac{\partial^2 t}{\partial y^2}$	Impinging jet is inviscid	Us obtained from potential flow solution An implicit finite difference method used to solve the boundary layer equations	.Calculations show that Cf increases from zero at stagnation point to a maximum and drops to flat plate value far downstream .Maximum Cf increases with decreasing Y_n. .Nu remains constant near impingement but attains a maximum shortly beyond the impingement point. .Nu depends on Re, Y_n and Prandtl number

Table 5.1.4 Contd.

REFERENCES	EQUATIONS SOLVED	PHYSICAL ASSUMPTIONS	NUMERICAL DETAILS	CONCLUSIONS & COMMENTS
Wolfshtein (116)	$U\frac{\partial\phi}{\partial x} + V\frac{\partial\phi}{\partial y} = \frac{\partial}{\partial x}\Gamma_{eff}\frac{\partial\phi}{\partial x} + \frac{\partial}{\partial y}\Gamma_{eff}\frac{\partial\phi}{\partial y} + G - D$ where G ≡ generation of conserved property ϕ D ≡ Dissipation of conserved property	$\Gamma_{eff} = \frac{\mu_{eff}}{\sigma_{eff}}$ $\mu_{eff} = \mu_\ell + \mu t$ $\mu_t = C_\mu \rho \ell k$ ℓ is prescribed	ψ,w,k solved for by an iterative finite difference procedure	Calculated Cf and pressure agree with measurements. .Reasonable agreement between calculated St and measurements for low Reynolds number, but qualitative as well as quantitative discrepancies (>50%) are observed at high Reynolds number
Russel & Hatton (94)	Same as Wolfshtein	Same as above, and experimentally derived ℓ	Same as above	A uniform k profile as initial condition is unrealistic as experiment indicated up to 400% variation. Theory and experiment in qualitative agreement

5.2 EXPERIMENTAL INVESTIGATION

Introduction

The review in section 5.1 demonstrates that many flow parameters for impinging jets have not been investigated systematically. In cases where geometric parameters have been systematically investigated (e.g. Metzger et al) only the average heat transfer coefficients were reported. To optimise spacing distances between jets for impingement-convection film cooling arrangements (fig.6.3.4) the local heat transfer coefficient is required to calculate combustor wall temperatures. As a consequence, the present investigation was undertaken and makes use of a slot jet with fully developed exit mean velocity profiles. It has the following objectives:

(i) to measure $\underset{\sim}{U}$,h,n, and P as a function of flow Reynolds number and impingement angles,

(ii) to determine the influence of a shrouding plate on h and n.

(iii) the experimental data were required to test the viability of a prediction procedure for impinging flows, and the detail of measurements reflect this requirement.

Although heat transfer coefficients have been presented for single slot jets, the corresponding velocities and pressures have not been presented and these are necessary because the aerodynamic field must be known in order to calculate the convective heat transfer. The influence of impingement angle has been demonstrated by McMurray (61) for a slot water jet. It has also been shown, for a single circular air jet, by Perry (87). It has not been quantified for a single slot air jet, although in practical situations, impingement cooling with air jets may have to be applied at angles other than 90^{o}. The influence of shrouding have not been investigated,

although this also is relevant to combustor and airfoil designs.

The subsequent subsections describe an investigation intended to remove some of these deficiencies. The equipment and instrument, the experimental procedures and the results are presented in sections 5.2.1, 5.2.2 and 5.2.3 respectively. The more important conclusions are presented in section 5.2.4.

5.2.1 EQUIPMENT AND INSTRUMENTATION

The Flow

Figure 5.2.1 and plate 5.2.1 show the essential details of the flow arrangement. An electro static filter connected to the inlet of the blower ensured that the air was clean and free from particles. The air was heated by a 9 killowatt Secomak heater which was connected to variac transformers to regulate the power output.

The flow rate was controlled by a throttle valve and an orifice meter, calibrated in accordance with the BS1042, measured the flow rate. The transition section, which provides a contraction ratio of 1.4 in a length of 305 mm allowed a smooth transition from a pipe flow to a channel flow. The section marked SS on figure 5.2.1 consisted of a 30x30 wire mesh at the upstream and downstream ends. In between the wire meshes, a 25 mm long, 2 mm by 2 mm honey comb was inserted. The arrangement provided a uniform inlet velocity profile for the channel section, which had a length of 500 mm and a cross section of 305 by 5 mm. The channel wall thickness was 8 mm and the length of 500 mm, or 100, channel gaps was sufficient to ensure fully developed flow at the exit.

The Impingement Plates

The heat transfer plate described earlier in chapter 3 was used to determine the variation of local heat transfer coefficient. A cross section of the plate is shown on figure 5.2.1 and the arrangement of the thermocouples is shown on plate 5.2.2.

Figure 5.2.1 illustrates the swivel arrangement: a flange with a hole through it was fixed to the plate and the plate-flange rotated about the centre of a lockable tapered bolt. A protractor fixed on the support and a pointer on the plate measured the relative angles between the two within $\pm 0.5^{o}$. The impingement plate was supported on a compound table that allowed accurate positioning of the plate relative to the channel exit.

The cold plate was machined from dura lumin with 180 static pressure holes of 0.5 mm diameter. Figure 5.2.1 shows the probe traversing arrangement which was an integral part of the plate so that the total head probe measured the component of velocity parallel to the wall at all inclinations. The arrangement allowed traversing in three orthogonal planes: traversing normal to the plate was carried out with the aid of a micrometer which allowed location of the probe to within 0.025 mm. The cold plate was also supported on the swivel arrangements.

Instrumentation

The instruments used for heat transfer measurements were the same as those described in chapter 4. They are shown on plate 5.2.2. The total pressures were measured with a flattened pitot probe of internal dimensions 0.5 mm by 1.5 mm. A Furness precision universal manometer was used for recording the pressures.

5.2.2 EXPERIMENTAL PROCEDURES

To obtain the heat transfer coefficients and the adiabatic wall effectiveness, the desired nozzle plate orientation and flow rate were preset and the variacs of the heater adjusted to obtain an air temperature rise of about 25°C. Further procedures for obtaining the heat transfer and adiabatic wall effectiveness were the same as those used and described in chapter 4. Because the plate is not horizontal, the natural convective heat loss was calculated from the equation:

$$h_L = 0.29\ (\theta/\ell)^{0.25} \qquad 5.2.1$$

For all situations tested, the Grashof number was less than 10^8 and the natural convective flow over the plate was assumed laminar.

Symmetry tests and precision of measurements

To test the two-dimensionality of the slot jet, velocity profiles were obtained at five lateral locations. Initial profiles showed that the maximum velocity at the central plane was 5% lower than at locations 100 mm from each side of the central plane. The channel gap was measured at different lateral positions for the situations when there was no flow and when there was flow. Without the flow the gap was uniform within 0.025 mm on the central 200 mm. With the flow, the pressure in the channel increased the channel gap from 5 mm at centre to 5.05 mm. Although this influence of the channel pressure decreased as the channel end walls were approached, it was sufficient to produce a 5% difference in the maximum mean velocities at the centre and at 100 mm from the centre. To reduce

this difference and thereby improve the two dimensionality of the flow, clamps were applied on both sides of the channel and at 5 equally spaced locations. This reduced the maximum difference between the mean velocities at the same y positions to 2.5% in the central 200 mm. To ensure that the asymmetry was not caused by differences in skin friction at the channel exit velocity profiles were obtained at ten locations 2 mm from channel exit. Figure 5.2.2 shows the mean velocity profiles at five lateral locations. The two dimensionality in mean velocity values is within 2.5%. Figure 5.2.2 also shows a clauser plot for ten profiles at a location 2 mm from exit. The profiles are indistinguishable and this demonstrates that asymmetry was not caused by differences in skin friction.

Figure 5.2.2 also shows the turbulence intensity measured with a hot wire system. The maximum velocity decay also shown on figure 5.2.2 demonstrates that the inverse square law slightly over estimates the decay of the present jet. The normalised mean velocity and Bradbury's correlation are also shown on figure 5.2.2. The precision of micrometer movements was of the order of than 0.1 mm. The location of the edge of the jet was thus within ±0.1 mm. Steps of 0.25 mm were taken in measurements within the jet.

The precision of temperature measurements was of the order of ±0.25 ^{o}C. In situations where the difference between wall temperature and wall adiabatic temperature was about 2^{o}C this may create uncertainties of up to 10 % in heat transfer coefficients at the stagnation point. However, because higher temperature differences were involved in the calculation of adiabatic wall effectiveness the uncertainty of 0.25^{o}C had little influence on the effectiveness values.

5.2.3 RESULTS AND DISCUSSION

Figure 5.2.3 shows that the static pressure distributions are symmetric for 90^{o} impingement but, at other angles, they are negatively skewed. The static pressures at the plane of symmetry decrease with the angle of impingement such that, the static pressure is zero at 30^{o} for all nozzle-plate distances.

Figure 5.2.4 shows the mean velocity profiles, along the impingement wall for two nozzle plate distances and three angular positions. It is apparent that mixing of the impinging jet is so rapid that a wall jet was established well before two channel gap distances downstream of the plane of symmetry. The y location for maximum velocity (edge of the boundary layer) decreases as the angle of impingement increases. The total jet width tends to be insensitive to impingement angle except near the stagnation region. The maximum velocity decay shows that decreasing the impingement angle increases the forward momentum and consequently decreases the velocity decay. The growth in the jet width shows that entrainment is significant. This observation is consistent with that of Russel and Hatton (94) who noticed increases of up to 20% in mass flux at distances less than 40 slot gaps.

Figure 5.2.5 was drawn to show the influence of Reynolds number on the impingement heat transfer. In accordance with the previously observed trends by Gardon and Akfirat (31) there is a systematic reduction in heat transfer coefficient with Reynolds number. One significant difference between the present measurements and those of Gardon and Akfirat (31) is that neither the 'inner' nor 'outer' secondary peaks were observed in the present profiles.

It is not certain whether this disappearence is due to thermo-couple resolution or if it is a property of the present flow. However, figure 5.2.2 shows that the present jet had a minimum turbulence intensity of 3.9% rising to 22% at the edge of the jet. Gardon and Akfirat had a jet with a 2.5% turbulence intensity. The 2.5% turbulence intensity suggested a non fully developed velocity profile. The disappearence of the secondary peaks in the present flow may be attributed to the higher turbulence intensity. The figure also demonstrates the anomalous behaviour of the plane impinging jet at a nozzle-plate spacing of 8. At this spacing a maximum heat transfer coefficient is observed for all Reynolds numbers.

Figure 5.2.6 shows the influence of nozzle plate distances for four nozzle-plate distances and three angular positions. For all angular orientations, the 8 nozzle-plate distance gives a maximum coefficient except for an angular position 60^{o} and a nozzle plate distance of 6 where the heat transfer coefficients are higher than for 8. The skewness of impingement coefficients becomes appreciable as the impingement angle decreases.

The influence of impingement angle is shown to be significant in figure 5.2.7. The influence of impingement angle on wall static pressure and maximum velocity decay are shown on figures 5.2.3 and 5.2.4. As expected, the aerodynamic field influences the heat transfer characteristics such that the position of maximum heat transfer coefficients is different from the plane of symmetry for all angles less than 90^{o}. In general, the influence of impingement angle is complex but four regions are apparent in figure 5.2.7.

The first covers the location - 40 yc to-5 yc - where the heat transfer coefficient decreases monotonically with decreasing angle. Within the region -5 yc and 0 from the plane of symmetry, the flow is particularly complex and results in highest heat transfer coefficient for 60^{0} impingement and lowest for 30^{0}. The highest at 60^{0} is consistent with the previous findings of McMurray for impingement of a plane water jet. In the section from 0 to 10 yc, decreasing the impingement angle tends to reduce the heat transfer coefficient. However, because of increased forward momentum for smaller impingement angles, the heat transfer coefficient at downstream distances greater than 10 slot gaps increases with decreasing angle. Figure 5.2.7 demonstrates that the process is much more complicated than can be described by the above simple classifications. The singular behaviour of impingement at a nozzle plate spacing of 6 and impingement angle of 60^{0} shows that this orientation tends to give best performance for all downstream distances.

In practical situations such as impingement-cooled airfoils, the impinging jet may be confined by a parallel wall. Figure 5.2.8 shows that a shrouding wall may reduce the performance of an impinging jet. The reduction in performance was probably due to a retarded growth of the turbulence intensity. Measurements of wall static pressures showed a drop in the static pressures and an increase in the streamwise pressure gradient. Launder and York (53) had indicated that a favourable pressure may delay transition to fully turbulent situations. The present influence of a shrouding wall is consistent with the findings of Sparrow et al (104) who noticed that a splitter plate reduces heat transfer coefficient of an impinging jet in a cross flow.

Figure 5.2.8 also demonstrates that a shrouding wall improves the adiabatic wall effectiveness. This is because of reduced mixing of the hot jet with the cold free stream.

The experiment arrangement was such that the impingement plate rotated about the symmetry line of impingement. The nozzle plate distances are therefore not affected by angular rotation. Figure 5.2.9 demonstrates the variation of heat transfer coefficients with angular positions. The stagnation points can not be located precisely due to thermo couple resolution. Figure 5.2.10 shows that the differences in boundary conditions for the present experiment from those of Gardon and Akfirat (31) do not significantly affect the heat transfer coefficients.

The degree of mixing between the impinging jet and the surrounding fluid may be quantified by the adiabatic wall effectiveness as shown in figure 5.2.11 which indicates that increasing the nozzle plate distance decreases the adiabatic wall effectiveness. The adiabatic wall effectiveness is a measure of enthalpy recovery factor and as discussed in chapter 6 it is important for determining the temperatures on a film cooled wall. One feature of the effectiveness is that values greater than unity were obtained for impingement at 30^{o} and at locations opposite to the main direction of flow. This may be indicative of flow separation.

5.2.4 CONCLUSIONS

From the above presentation of experimental results, the following conclusions may be drawn.

1. Impingement heat transfer increases with flow Reynolds number.
2. For an impinging plane jet, the optimum nozzle plate spacing is 8 slot gaps, except for impingement at 60^{o} when a nozzle plate spacing of 6 slot gaps leads to better performance.
3. Impingement at 60^{o} gives maximum stagnation point heat transfer for all nozzle plate distances.
4. The favourable pressure gradient due to a confining wall may reduce the heat transfer coefficient by up to 20%

5.3 THEORETICAL INVESTIGATION

Introduction

The review of section 5.1 indicated that the discrepancies between measurements and calculations of flow properties of impinging jets may stem from over simplified turbulence assumptions.

The present investigation uses the numerical procedure and turbulence assumptions previously used successfully for many flow configurations by Khalil and Whitelaw (48). In contrast to the numerical algorithm of Wolfshtein (116), which solves for vorticity and stream function, the present procedure solves for velocities and pressures as primary variables. The turbulence assumption is that of an effective viscosity which is related to turbulence kinetic energy and turbulence dissipation. This turbulence model is more advanced than that of Wolfshtein (116) or any other one that has ever been applied to calculate impinging jets. It is hoped that this model will be successfully in this situation as it has been for other flow configurations.

Section 5.3.1 describes the conservation equations and the boundary conditions. The turbulence assumptions are described in

section 5.3.2. The important features of the solution procedure are provided in section 5.3.3 while the comparison of calculations with experiments are presented in section 5.3.4. Calculations outside the range of the measurements are also presented.

5.3.1 CONSERVATION EQUATIONS AND BOUNDARY CONDITIONS

The conservation equation for the time averaged properties appropriate to an impinging two-dimensional jet have the common form;

$$\frac{\partial}{\partial x}(\rho U\phi) + \frac{\partial}{\partial y}(\rho V\phi) = \frac{\partial}{\partial x}\Gamma_\phi \frac{\partial \phi}{\partial x} + \frac{\partial}{\partial y}\Gamma_\phi \frac{\partial \phi}{\partial y} + S_\phi \qquad 5.3.1$$

where

ϕ stands for U,V,k,ε, or h and Γ_ϕ ,S_ϕ are defined as follows:

Table 5.3.1

VARIABLE ϕ	Γ_ϕ	S_ϕ
U	μ_{eff}	$\frac{\partial}{\partial x}(\mu_{eff}\frac{\partial U}{\partial x}) + \frac{\partial}{\partial y}(\mu_{eff}\frac{\partial V}{\partial x}) - \frac{\partial P}{\partial x}$
V	μ_{eff}	$\frac{\partial}{\partial x}(\mu_{eff}\frac{\partial V}{\partial y}) + \frac{\partial}{\partial y}(\mu_{eff}\frac{\partial V}{\partial y}) - \frac{\partial P}{\partial y}$
k	$\frac{\mu_{eff}}{\sigma k}$	$Gk_1 - P\,\varepsilon$
ε	$\mu_{eff}/\sigma\varepsilon$	$\frac{\varepsilon}{k}(C_1 Gk_1 - C_2\,\rho\varepsilon)$
h	$\frac{\mu_{eff}}{\sigma\, h}$	Q_W

with

Q_W = energy flux at the wall

$$\mu_{eff} = C_\mu \frac{\rho k^2}{\varepsilon} + \mu$$

$$Gk_1 = \mu_{eff}\left(2\left(\left(\frac{\partial U}{\partial x}\right)^2 + \left(\frac{\partial V}{\partial y}\right)^2\right) + \left(\frac{\partial U}{\partial y} + \frac{\partial V}{\partial x}\right)^2\right) \qquad 5.3.2.$$

$C_\mu = 0.09$, $C_1 = 1.44$, and $C_2 = 1.92$.

The above definitions stem from an effective viscosity assumption. The constants are those used successfully for free shear flows (23) and two-dimensional confined flows (48).

Figure 5.3.1 shows the control volume for the present calculations, and the relevant boundary conditions are:

$$U,V,\ \frac{\partial h}{\partial y} = 0 \quad \text{at} \quad y = 0 \qquad \text{(wall boundary)}$$

$$\frac{\partial \phi}{\partial x} = 0 \quad \text{at} \quad x = 0 \qquad \text{(symmetry line)} \qquad 5.3.3$$

$$\phi = \phi_G,\ \frac{\partial \phi}{\partial y} = 0 \text{ at } y = y_n \text{ and } x > y_{c/2} \qquad \text{(free boundary)}$$

$$\phi = \phi_G = \frac{\partial \phi}{\partial x} = 0 \text{ at } x > 120\ y_c \qquad \text{(free boundary)}$$

The initial profiles correspond to experimental values wherever available. For quantities not measured reasonable assumptions were made.The initial profile of dissipation rate, for example was determined from the equation:

$$\varepsilon = \frac{k^{3/2}}{(y_c - y)} \frac{C_\mu^{3/4}}{0.42} \qquad 5.3.4$$

which corresponds to fully developed channel flow.

5.3.2 TURBULENCE ASSUMPTIONS

The elliptic nature of the equations appropriate to an impinging two-dimensional flow implies the need for a two equation turbulence model.

Wolfshtein (116) used a one equation turbulence model in which turbulent viscosity was defined as

$$\mu_t = \rho k^{\frac{1}{2}} \ell \qquad 5.3.5$$

and ℓ is prescribed algebraically: as noted earlier, his results showed differences from experimental values of heat transfer coefficient of up to 50%. The two equation turbulence model used for the present calculations involves the solution of equations of conservation of turbulence kinetic energy and dissipation together with the definitions:

$$\begin{aligned} -\rho\overline{uv} &= \mu_t\left(\frac{\partial U}{\partial y} + \frac{\partial V}{\partial x}\right) \\ -\rho\overline{u^2} &= 2\mu_t\left(\frac{\partial U}{\partial x}\right) - \frac{2}{3}\rho k \\ -\rho\overline{v^2} &= 2\mu_t\left(\frac{\partial V}{\partial y}\right) - \frac{2}{3}\rho k \end{aligned} \qquad 5.3.6$$

$$\mu_t = C_\mu \rho k^2/\varepsilon$$

$$\mu_{eff} = \mu_t + \mu$$

These definitions, and the assumed forms of dissipation and diffusion terms for dissipation rate and turbulent kinetic energy, imply isotropic turbulent viscosity. The isotropic turbulence assumption represents a limitation of the k - ε model as measurements of turbulence properties (94) do not confirm isotropy. The

use of a Reynold stress model may ultimately prove to be better but its use can not be justified until the merits and difficulties of the two equation model have been demonstrated.

5.3.3 SOLUTION PROCEDURE

The differential equations represented by equation 5.3.1 and table 5.3.1 were expressed in the finite difference form of reference 48 and solved by the algorithm of that paper. The 20 x 20 grid nodes used for the present calculations allowed the solution of 6 equations in 300 seconds of CDC 6600 computing time.

The number of iterations varied, with nozzle-plate distance, from 350 to 400. Convergence was assumed when the maximum normalized residue in any of the conservation equations

$$(\text{convection} + \text{diffusion} + \text{source})_{j+1/\phi_j} < 10^{-4}$$

at any grid node.

The numerical algorithm of this procedure is similar to that of chapter 4 except that the present flow is two-dimensional. The pressures are also obtained by the guess and correct method described for the procedure in chapter 4.

5.3.4 RESULT

Figure 5.3.2 shows a comparison between measured and calculated pressure coefficients. The qualitative agreement is resonable At pressure coefficients less than 10%. the quantitative disagreement was up to 50% in situations where experimental uncertainties are up to 20% of a mean value. For pressure coefficients greater

than 30% the discrepancies are less than 20%. In agreement with experiment, the maximum pressure coefficient decreases with increasing nozzle plate distances.

Figure 5.3.3 demonstrates reasonable agreement between measured and calculated mean velocities parallel to the impingement plate. The maximum discrepancies occur at the outer edges of the jets which are experimentally difficult to determine due to the small pressures involved.

The variation of calculated turbulence kinetic energy at various locations is shown on figure 5.3.4. These results show qualitative agreements with measurements of Russel and Hatton (94). In contrast to the calculations with a one equation model, which showed maximum kinetic energy at stagnation point, the $k-\varepsilon$ model shows that the maximum turbulence kinetic energy increases from stagnation point to its greatest value at about seven slot distances from stagnation point and then decreases monotonically with increasing distance. This trend is in perfect agreement with the experimental observation of 94. The maximum turbulence kinetic energy was 40% for a nozzle plate distance of six and 30% for nozzle plate distance of twelve.

Figure 5.4.4 shows the comparison between measured and calculated adiabatic wall effectiveness and heat transfer coefficients. The agreement can be seen to be reasonably good. The comparison for local heat transfer coefficients shows greater discrepancies which may be attributed, in part, to experimental uncertainties of $\pm 0.25^{o}C$ and consequent errors of up to 10% in stagnation point heat transfer coefficient. The numerical uncertainties in calculating temperature differences less than $2^{o}C$ may also be significant.

The discrepancies indicated by the present comparisons are less than 30% at any position. This represents an improvement on previous calculations of Wolfshtein (116). Although the comparison presented above shows that the agreement between measurement and calculations are far from perfect, the present procedure represents a step forward in the theoretical modelling of impinging jets. In particular the procedure can be used to calculate the influences of nozzle plate distances and nozzle Reynolds number on impingement heat transfer characteristics.

5.3.5 CONCLUSIONS

1. The numerical procedure described above can be used to calculate the characteristics of impinging jets with an acceptable precision for design purposes.
2. The procedure above and that described in chapter four can be used to obtain wall temperature profiles for a combined impingement-film cooling arrangements.

CHAPTER SIX

CALCULATION OF FILM-COOLED WALL TEMPERATURES

INTRODUCTION

The end goal of film-cooling investigations is to determine the temperature of the surface of a combustor or blade. The results presented in chapters 3 - 5 relate to ideal experimental situations. Practical situations do not conform to these idealization in the following respects:

(i) the flame-tube is not adiabatic. Large radiative heat fluxes are incident on the wall and there is also heat transfer to the outer casing through radiation.

(ii) the flow is asymmetric, three-dimensional and strongly elliptic in the dilution zone. The flow may also be periodic in the recirculation region.

(iii) there are large gradients in flow properties due to chemical reactions.

In spite of the above difficulties, this chapter presents calculated wall temperatures for practical situations using the procedures described in chapters 3 and 4. Comparison with experimental data are made where possible and reasons for discrepancies are discussed. The specific tasks carried out and the results of which are presented in section 6.3 are as follows:

(i) The procedure of chapter 3 was applied to the adiabatic situations of Odgers and Winter (76) to assess the capability of the procedure to calculate the aerodynamics of film-cooled combustors.

(ii) The procedure of chapter 3 was then applied to non-adiabatic situations of Milford and Spiers (69) to estimate further errors incurred through the assumed radiation laws.

(iii) The wall temperatures of a combustor cooled with an arrangement of three-dimensional slots was then calculated to demonstrate the influence of pitch-diameter ratio and lip length. With the above estimate of errors incurred through radiation laws and the errors obtained in using the procedure of chapter 4 to calculate adiabatic wall effectiveness and heat transfer coefficient, an estimate of the errors involved in using the procedure of chapter 4 to calculate real combustor temperatures can be made. The slot dimensions and flow conditions used for the present calculations are identical to those of an existing Rolls Royce (1971) Ltd. combustor.

(iv) Chapter 5 indicated a need to enhance the performance of film cooling slots. Thus the procedure of chapter 4 was combined with the impingement heat transfer coefficient measurements of chapter 5 to calculate the resulting wall temperature distribution for the composite arrangement: i.e. an impingement-film cooling slot. Although absolute values of wall temperatures thus obtained may be wrong by up to 15% the trends are expected to be right and such results can aid the design of impingement-film cooling.

Section 6.1 reviews previous attempts to make calculations of this type and indicates limitations which justify the present approach. The modifications made to the present procedure are described in section 6.2, and the results presented and discussed in section 6.3. The more important conclusions are presented in section 6.4.

6.1 PREVIOUS PREDICTIONS

This section reviews attempts to calculate combustor wall temperatures. The difficulties encountered in dealing with flame radiation, flow asymmetry, chemical reaction and specification of boundary conditions are treated briefly below to provide a justification for the present approach. The advantages and limitations of each approach is pointed out.

Flame Radiation

Calculations of wall temperature in the presence of film-cooling have been reported by Pai and Whitelaw (78), Milford and Spiers (69), Whittaker (114), Ballal and Lefebvre (3) and Rastogi (89). In accounting for flame radiation these investigators assumed the semi-empirical radiation law originally proposed by Lefebvre and Herbert (55). For each geometry under consideration a near wall energy balance was assumed (equation 6.2.7) and, by an iterative procedure, the wall temperatures were obtained. With the exception of Pai and Whitelaw (78) and Rastogi (89), the above authors obtained values of effectiveness and heat transfer coefficient from correlations. The validity of the correlations is very limited in view of the sensitivity of the effectiveness and heat transfer to both geometry and flow conditions. Rastogi (89) solved equations similar to those of section 4.3 to obtain values of effectiveness and heat transfer and calculated temperature values within 150^{o}C of measured values. The discrepancy was attributed partly to inaccuracies in measurement, partly to the semi-empirical radiation laws, and partly to the inadequately known free-stream boundary condition.

An alternative method for calculating flame radiation is to make use of a 'flux model'. In this method, finite difference equations are used for radiation fluxes in each direction and the resultant gradients are used as source terms for the enthalpy equation. This method has been used by Khalil and Whitelaw (48), and Gosman and Lockwood (39) for calculation of the temperature field in furnaces and by Patankar and Spalding (85) for combustion chambers.

The flux model appears attractive because of the successes achieved by Khalil and Whitelaw (48) who observed discrepancies between experiments and calculated value of less than 15% of experimental values. However, the use of a flux model for the present calculations can not be justified since the aerodynamic fields of the present flow configurations have not been calculated with a precision better than 15%. The use of a flux model would imply more equations to solve and more computer time and storage. The treatment of radiation for the present calculations was therefore similar to that of Rastogi (89) in spite of its limitations.

Flow Asymmetry

As regards asymmetry and the elliptic three-dimensional flow in a combustor, the numerical algorithm of Patankar and Spalding (85) may be expected to represent the combustor flow better if calculations are made for the whole of combustor geometry. The calculations of Patankar and Spalding at present assumes symmetry over sectors. Even when calculations are made for the whole of combustor geometry, the periodicity in the recirculating region

poses the problem of selecting the right physical mixing laws. Due to the non isotropic nature of recirculating flows, even a Reynolds stress model has been shown by Pope and Whitelaw (88) as inadequate. The use of a three-dimensional elliptic procedure for the present flow may have to be delayed until turbulence models capable of accurately calculating details of recirculating flows are developed. For the wall temperature calculations, the parabolic procedure of chapter 4 was therefore used.

Chemical Reaction

Large flow property gradients are caused by combustion. The calculation of combustor wall temperature can not be done accurately until the combustion phenomena are well modelled. Khalil and Whitelaw (48) tested the validity of three combustion models and found that the best gave discrepancies up to 15% in the centre line temperature distribution. This implies an uncertainty of up to 300^{o}K in a combustor where temperatures rise up to 2000^{o}K. Of course, the use of combustion model in conjuction with a three-dimensional elliptic procedure would remove the uncertainty as to the free stream boundary conditions which is uncertain in present calculations and in the calculation of flow over curved surfaces,

Such a step would require the solution of more equations (e.g. Patankar and Spalding (85) solved 11 finite difference equations) and, since there are no reliable combustor flow measurements against which to test such a procedure, it was considered unjustifiable to include combustion in the present attempt to calculate combustor wall temperatures.

For the above reasons, the present calculation is similar to that of Rastogi (89) except that different flow configurations are investigated and wall temperature calculation for combined impingement-film arrangements are presented. It may be expected that the present calculations will have similar limitations.

6.2 MODIFICATIONS FOR CALCULATING FILM COOLED WALL TEMPERATURES

In common with Pai and Whitelaw (78) and Ballal and Lefebvre (3), it was assumed that there was a balance between the energy received by the flame tube through convection and radiation and the energy lost by flame tube through convection and radiation. Conduction was assumed to be small. The components of the energy balance were calculated by the method described in the following paragraph.

The heat transfer to the inside of the combustor wall by convection was calculated from the equation;

$$C_I = h_f (T_{aw} - T_w) \qquad 6.2.1$$

The two-dimensional parabolic procedure of chapter 3 and the three-dimensional procedure of chapter 4 were used to calculate local adiabatic wall temperatures and heat transfer coefficients for appropriate slot geometries. Thus wall temperatures corresponding to figures 6.3.1 and 6.3.2 were obtained with the procedures of chapter 3, while for situations corresponding to figures 6.3.3 and 6.3.4 the procedures described in chapter 4 was used.

The heat transfer from the combustor wall due to flow in the annulus between the combustor and casing was calculated with the equation:

$$C_o = h_o (T_w - T_c) \qquad 6.2.2$$

where $h_o = 0.037\ Re_x^{0.8}\ Pr^{0.3}\ \frac{k}{x}$ 6.2.3

and the initial origin of the boundary layer was assumed to be 20 mm upstream of slot exit. This distance has been shown by Rastogi (89) to have no significant influence on wall temperature. In principle, h_o can be calculated using the numerical procedure of chapter 4, but the annulus flow is complex in that the total mass flow reduces with increasing number of slots and dilution holes. The initial conditions for such a calculation is uncertain.

The flame radiation to the flame tube was obtained from the equation:

$$R_I = \sigma \frac{(1 + \varepsilon_w)}{2} \varepsilon_G T_G^{1.5} (T_G^{2.5} - T_w^{2.5}) \qquad 6.2.4$$

and flame emissivity from Lefebvre's (55) empirical expression. The luminosity factor was taken as 4 and the beam length was assumed equal to 60% of the hydraulic diameter of the combustor, after Milford and Spiers (69).

The radiation from the flame tube to the outer casing was calculated from:

$$R_o = \sigma \varepsilon'w (T_w^4 - T_c^4) \qquad 6.2.5$$

Assuming that the energy received by the flame tube through convection and radiation equals the energy lost through convection and radiation, the energy balanced for the flame tube was written as with equations 6.2.1, 6.2.2, 6.2.4 and 6.2.5 providing

the four components:

$$R_I + C_I = R_o + C_o \qquad 6.2.6$$

An iterative procedure allowed the determination of wall temperature values.

6.3 RESULTS

The measurements of Odgers and Winter (76) were made for an arrangement consisting of an insulated cylinder through which hot air flowed. Film-cooling air was introduced through an annular gap. The cylinder was well instrumented with thermocouples which indicated negligible circumferencial difference in temperature.

Figure 6.3.1 was prepared to demonstrate the capability of the procedure, described in section 3.3, to calculate values of adiabatic wall temperatures for the flow configuration of Odgers and Winter (76). Although the wall was insulated, the use of hot and cold air makes the flow arrangement a little closer to real situations than cold flow measurements. The agreement between experiment and calculation is excellent except for the wake flows where considerable discrepancies are observed. Because of the above agreement, it may be expected that any increase in discrepancies between measurement and calculation for non adiabatic situation can be attributed to over simplified assumptions in radiation calculations.

The configuration for Tacina and Marek's (108) measurements is similar to that of Odgers and Winter (76) except that the wall

was not insulated. Comparison between measurements and calculations shows discrepancies up to 200^{o}C. The small velocity ratios used may cause recirculation and reduce the validity of the assumptions for the solution procedure.

The experiments of Milford and Spiers (69) were performed to simulate the after burner situations. The walls were not adiabatic. Figure 6.3.2 shows that for velocity ratios greater than unity, the discrepancies between measurements and calculations are surprisingly low. However, for small velocity ratios, discrepancies greater than 200^{o}C are observed. It would appear that, for velocity ratios greater than unity, the calculation procedure of chapter 3 may be expected to result in wall temperatures close to practical values. This expectation needs further confirmation. The implication of such a confirmation may be that for situations where the numerical procedure closely represents the flow, the radiation models of equations 6.2.4 and 6.2.5 would result in practically useful wall temperature calculations.

The procedure described in chapter 4 was used to calculate the influence of pitch to diameter ratio and lip length for the configurations shown in figure 6.3.3. The dimensions of the slot geometry were scaled from a Rolls Royce (1971) Ltd. design. As expected, the average wall temperature increases with increasing pitch-diameter ratio. An increase in lip length results in lower average wall temperatures due to higher adiabatic wall effectiveness. The three dimensionality in temperature field for all downstream positions greater than ten slot gaps was less than

1 %. This may represent a real situation or it may be caused by an over simplified turbulence assumption. However, the measurements of effectiveness by Rolls Royce (1971) Ltd. for geometries similar to those of figure 6.3.3 showed less than 1% three-dimensionality for similar downstream positions.

Figure 6.3.4 represents a composite arrangement of impingement-convection-film-cooling. The calculations were performed in order to assess the advantages of such an arrangement. The calculations on figure 6.3.4 were obtained by combining the procedure described in chapter 4 with the measurements of chapter 5, and provides a justification for the work reported in chapter 5. Although extensive calculations are not presented, the two sets of calculations in figure 6.3.4 are probably sufficient to allow important conclusions. For the calculations, it was assumed that all other variables remained constant except for the external heat transfer coefficient as it is affected by impingement Reynolds number.

This figure demonstrates that increasing the impingement Reynolds number reduces the resulting wall temperatures. For the configurations used, impingement at a Reynolds number of 7,100 led to perfect cooling at the stagnation line while impingement at a Reynolds number of 1,750 led to a temperature rise of up to 150^{0}C at the stagnation line. The implication of the above trends is that it is advantageous to use high impingement Reynolds number whenever there is enough pressure drive and the resulting static pressures would not create undesirable stresses in the flame tube.

An important feature of the wall temperature profiles shown on figure 6.3.4 is that the combined impingement-film cooling profiles have maximum points while the film+convection showed a monotonic increase of temperature with downstream distance. This is because the heat transfer coefficient for an impinging jet drops rapidly.

The tendency for the composite arrangement of impingement-film to produce a maximum is practically undesirable as this may increase the flame tube thermal stresses.

One way to reduce this high temperature gradient is to introduce the impinging jets at short spacing distances. As the experiments of Gardon et al (31) have shown, this will reduce the variation of the impingement heat transfer coefficient along the outer side of the flame tube. Figure 6.3.4 shows that if impinging jets are located at downstream positions not greater than 20 slot gaps for the present arrangement the average wall temperature would be lower than that of a film-convection cooling arrangement.

6.4 CONCLUSIONS

The results presented in the previous section allow the following conclusions to be drawn:

1. The calculation procedures described in chapters 3 and 4, in conjuction with semi-empirical radiation laws, can be used to calculate combustor wall temperatures. Comparison with the

limited available experimental data suggests that the absolute temperatures may be calculated within limits useful for design purposes.

2. The influence of geometric and flow variables on wall temperature can be well calculated.

3. A combination of impingement-convection film arrangement leads to lower combustor wall temperature than a convection-film arrangement provided the impinging jet is placed at distances not greater than 20 slot gaps downstream of slot exit.

CHAPTER SEVEN

CONCLUSIONS AND RECOMMENDATIONS FOR FURTHER WORK

At the end of each section or chapter, relevant specific conclusions have been provided. This chapter presents general conclusions and assesses the extent to which the objectives of the present research have been achieved. Recommendations for further research are provided in section 7.2.

7.1 CONCLUSIONS

1. The experimental and theoretical investigations of two-dimensional film cooling in chapter 3 showed that:

   (a) the influence of longitudinal wall curvature on the effectiveness of two-dimensional film cooling slot is small except where, for convex surfaces the flow separates. The range of parameters for which separation can occur is of significance to gas turbine combustor cooling.

   (b) in a multi-slot arrangement film build up may improve the effectiveness of subsequent slots by up to 15%. As the number of slots increases, the corresponding increase in effectiveness decreases.

   (c) the influence of film stretching on effectiveness is small for parameters of importance to combustor cooling.

2. The measurements reported in chapter 4 show that the effects of flow and geometric parameters on the effectiveness and heat transfer coefficients of three-dimensional film cooling arrangements are complex and can be represented by a modified version

of the numerical procedure used by Patankar, Rastogi and Whitelaw (84). The influences of velocity ratio, density ratio, pitch-diameter, lip length, open area ratio and slot geometry are calculated within 10% of measurements.

3. The measurements of chapter 5 show that the influences of impingement angle, nozzle plate distance, Reynolds number and shrouding plate are also complex. It was shown that a modified version of the procedure used by Khalil and Whitelaw (48) satisfactorily calculates the impinging jet characteristics and can be used for calculating influences outside the range of validating experiments.

4. Combustor wall temperatures were evaluated from a balance of convective and radiative heat fluxes on the two sides of a combustor flame tube. The numerical procedures of chapter 3 and 4 allowed the determination of the convective terms. Comparison of calculated and measured wall temperatures indicated discrepancies for wake flows and acceptable agreement for jet type flows. The calculations of wall temperature with impingement cooling on the annulus side of the flame tube and heat transfer coefficients determined from the experiments of chapter 5 showed that impingement - film cooling arrangements can result in lower flame tube temperatures. Design criteria are suggested.

7.2 SUGGESTIONS FOR FURTHER WORK

1. Although the present calculations of effectiveness over curved surfaces showed reasonable agreement with measurement,

insufficient is known of the mixing processes on curved walls. As a result, discrepancies greater than 30% between measurement and calculated static pressures and effectiveness have been observed close to separation. The separation point is not known with precision and this is necessary for design purposes.

A detailed experimental investigation of the aerodynamic properties downstream of similarly curved wall jets is necessary for an understanding of the mixing processes. This should be accompanied by a numerical investigation based on elliptic equations and a higher order turbulence model. This should help to overcome the discrepancies in chapter 3 due largely to the inability of the parabolic procedure to represent the substantial normal pressure gradients. Indeed, the modified mixing length of section 3.2; in part compensates for a numerical inadequacy by physical assumptions. An elliptic procedure could also overcome the need to specify the free stream pressure distribution.

2. Practical limitations may necessitate the use of velocity ratios less than unity and it was observed in chapter 4 that these were less well represented by the calculation method. Substantial improvements will probably require the solution of three-dimensional fully elliptic equations at least in the upstream region and this would justify a two equation turbulence model. The cost of calculations of this type will be considerable and a Reynolds stress model is unlikely to be justified.

3. Measured cross stream effectiveness and velocities indicated 10% asymmetry in velocities and 4% in effectiveness. In the

ordered (nearly periodic) flows observed in combustors, these asymmetries may be greater and are probably responsible for local hot spots even in apparently over cooled combustors. The present investigation showed that an increase in open area ratio or the use of tangential jets reduced such asymmetry in effectiveness. A fundamental understanding of the causes of such asymmetry is likely to be of considerable value to the combustor designer.

4. The literature review on impingement heat transfer indicated detailed investigation of the heat transfer characteristics of a row of jets impinging on flat and curved surfaces have not been investigated. A systematic experimental investigation of such geometries, to identify the parameters of importance, would be of great help in optimising design of impingement-film cooling arrangements.

REFERENCES

1. Akfirat, J.C. (1966) Transfer of heat from an isothermal flat plate to a two-dimensional wall jet. 3rd Int. Heat Transfer Conference Chicago, Proceedings 2, 274.

2. Artt, D.W., Brown, A. and Miller, P.P. (1970) An Experimental Investigation into Film-cooling with particular application to cooled turbine blades. 4th International Heat Transfer Conference, 1970, 2, F.C.1.7

3. Ballal, D.R. (1973) Estimation and optimization of film-cooling requirements in a gas turbine combustion chamber. Cranfield Institute of Technology, Report SME No.5, 1973.

4. Ballal, D.R. & Lefebvre, A.H. (1972) A proposed Method for calculating film cooled wall temperatures in a gas turbine combustion chambers. ASME 72-WA/HT-24.

5. Barry, B. (1976) The aerodynamic penalties associated with turbine blade cooling. Turbine Research Report TRR 90146. Rolls Royce (1971) Ltd. Derby Engine Division.

6. Beer, J.M. & Chigier, N.A. (1968) Impinging jet flames. Combustion and Flame 12, 575.

7. Belov, I.A. et al (1972) Experimental Study of Heat Transfer in a Subsonic Jet Impinging Normally to a Plane Baffle. Heat Transfer-Soviet Research 4, No.4, 17.

8. Bergeles, G., Gosman, A.D. & Launder, B.E. (1975) The Prediction of Three-Dimensional Discrete Hole Cooling Processes. 1 - Laminar Flow, ASME 75 - WA/HT-109.

9. Blair, M.F. & Launder, R.D. (1975) New Techniques for Measuring Film Cooling and Heat Transfer. J. of Heat Transfer 97, 539.

10. Bouchez, J.P. & Goldstein, R.J. (1975) Impingement Cooling from a Circular Jet in a Cross Flow. Int. J. of Heat-Mass Transfer 18, 719.

11. Bradshaw, P. (1973) Effect of Streamline Curvature on Turbulent Flow. Agardograph No. 169.

12. Burns, W.K. & Stollery (1969) The Influence of Foreign Gas Injection and Slot Geometry on Film-Cooling Effectiveness. Int. J. of Heat-Mass Transfer 12, 935.

13. Carlson, L.W. & Talmor, E. (1968) Gaseous Film Cooling at Various Degrees of Hot Gas Acceleration and Turbulence Levels. Int. J. of Heat-Mass Transfer 11, 1695.

14. Chin, et al (1961) Film Cooling with Multiple Slots and Louvers. J. of Heat Transfer 83, 281.

15. Colladay, R.S. (1972) Analysis and Comparison of Wall Cooling Schemes for advanced Gas Turbine Applications. NASA TMD -6633.

16. Crawford, et al (1975) Full Coverage Film Cooling Heat Transfer Studies - a summary of the data for normal injection and 30° slant hole injection. Dept. of Mech. Eng. Thermo Sciences Division, Stanford University. Report HMT - 19, NAS3 - 14336.

17. Darchem Eng. Ltd. (1974) Private Communication.

18. Dyban, Y.E. & Mazur, A.I. (1970) Heat Transfer from a Flat Air Jet Flowing into a Concave Surface. Heat Transfer-Soviet Research 2, No.3, 15.

19. Eriksen, V.L. (1971) Film Cooling Effectiveness and Heat Transfer with Injection Through Holes. NASA CR 72991.

20. Eriksen, V.L., Eckert, E.R.G. & Goldstein, R.J. (1971) A Model for Analysis of the Temperature Field Downstream of a Heated Jet Injected into an Isothermal Cross Flow at an angle of 90°. NASA CR - 72990.

21. Escudier, M.P. & Whitelaw, J.H. (1968) The Influence of Strong Adverse Pressure Gradients on the Effectiveness of Film-Cooling. Int. J. of Heat-Mass Transfer 11, 1289.

22. Eskinazi, S. & Yeh, H. (1956) An Investigation on Fully Developed Turbulent Flows in a Curved Channel. J. of Aeronautical Sciences 23, 23.

23. Folayan, C.O. (1972) Application of Optical Techniques for the Measurement of Velocity and Concentration. M.Sc. Thesis, University of London.

24. Folayan, C.O. & Whitelaw, J.H. (1974) Multi-slot Film-Cooling. Letters in Heat and Mass Transfer 1, 31.

25. Folayan, C.O. & Whitelaw, J.H. (1976) The effectiveness of Two-Dimensional Film-Cooling over Curved Surfaces. ASME Paper No 76-HT-31.

26. Folayan, C.O. & Whitelaw, J.H. (1976) The Effectiveness of Combined Tangential and Normal Film-Cooling Slots with Finite Lip. ASME Paper No 76-HT-30.

27. Foss, J. & Kleiss, S.J. (1972) The Oblique Impingement of an Axisymmetric Jet. Division of Engineering Research, Michigan State University, East Lansing.

28. Foster, R.C. & Haji-Sheikh, A. (1975) An Experimental Investigation of Boundary Layer and Heat Transfer in the Region of Separated Flow Downstream of Normal Injection Slots. J. of Heat Transfer 97, 260.

29. Friedman, S.J. & Mueller, A.C. (1951) Heat Transfer to Flat Plate Surfaces. Proceedings of the General Discussion on Heat Transfer. I.M.E. ASME.

30. Gardon, R. & Cobonpue, J. (1962) Heat Transfer Between a Flat Plate and Jets of Air Impinging on it. Proceedings of 2nd International Heat Transfer Conference New York, 454-460.

31. Gardon, R. & Akfirat, J.C. (1965) The role of Turbulence in Determining the Heat Transfer Characteristics of Impinging Jets. Int. J. of Heat-Mass Transfer 8, 1261.

32. Gardon, R. & Akfirat, J.C. (1966) Heat Transfer Characteristics of Impinging Two-Dimensional Air Jets. J. Of Heat Transfer Transactions ASME, 101-108.

33. Gauntner D.J. (1973) Comparison of Temperature Data from an Engine Investigation for Film-Cooled and non Film-Cooled Spanwise Finned Vanes, incorporating Impingement Cooling. NASA TMX 2819.

34. Gauntner J.W. & Livingood, J.N.B. (1973) Engine Investigation of an Impingement Cooled Turbine Rotor Blade. NASA TMX 2791.

35. Gauntner, J.W. et al (1974) Cross Flow Effects on Impingement Cooling of Turbine Vane. NASA TMX 3029.

36. Giles, J.A., Hays, A.P. & Sawyer, R.A. (1966) Turbulent Wall Jets on Logarithmic Spiral Surfaces. 17, 201.

37. Goldstein, R.J. (1971) Film-Cooling. Advances in Heat Transfer 7, 321.

38. Goldstein, R.J.et al (1974) Effect of Holes Geometry and Density on Three-Dimensional Film Cooling. Int. J. of Heat-Mass Transfer 17, 595.

39. Gosman, A.D. & Lockwood, F.C. (1973) Incorporation of a Flux Model for Radiation into a Finite-Difference Procedure for Furnace Calculation. 14th Symposium (International) on Combustion, 661.

40. Gosman, A.D. et al (1969) Heat and Mass Transfer in Recirculating Flows. Academic Press.

41. Harnett, J.P. et al (1961) Velocity Distributions, Temperature Distributions, Effectiveness and Heat Transfer of a Surface with a Pressure gradient. ASME Int. Developments in Heat Transfer partiv, 682.

42. Huang, G.C. (1963) Investigation of Heat Transfer Coefficients for Air Flow through Round Jets Impinging Normal to a Heat Transfer Surface. J. of Heat Transfer 85, 237.

43. Juhasz, A.J. & Marek, C.J. (1974) Combustor Liner Film-Cooling in the Presence of High Free Stream Turbulence. NASA TND 7513.

44. Kacker, S.C. (1969) The Influence of Slot Geometry on the Two Dimensional Turbulent Wall Jet. Ph.D. Thesis, University of London.

45. Kacker, S.C. & Whitelaw, J.H. (1968) The Effect of Slot Height and Slot Turbulence Intensity on the Effectiveness of Uniform Density Two-Dimensional Wall Jet. J. of Heat Transfer 90, 469.

46. Kacker, S.C. & Whitelaw, J.H. (1969) An Experimental Investigation of the Influence of slot lip Thickness on the Impervious Wall Effectiveness of the Uniform-density, two-Dimensional Wall Jet. Int. J. of Heat-Mass Transfer 12, 1196.

47. Kacker, S.C. & Whitelaw, J.H. (1970) The Prediction of Wall-Jet and Wall-Wake Flows. J. of Mechanical Engineering Science 12, No.6, 404.

47a Keulemans, A.I.M. (1957) Gas Chromatography. Reinhold Publishing Corporation, New York.

48. Khalil, E.E., Spalding, D.B. & Whitelaw, J.H. (1975) Calculation of Local Flow Properties in Two-Dimensional Furnaces. Int. J. of Heat-Mass Transfer 18, 775.

49. Kind, R.J. (1968) A Calculation Method for Circulation Control by Tangential Blowing around a Bluff Trailing Edge. Aero. Quarterly 19, 205.

50. Koosinlin , et al (1973) Prediction of Momentum, Heat and Mass Transfer in Swirling Turbulent Boundary Layers. Imperial College, Mech. Eng. Report. HTS/73/50.

51. Kruse, H. (1975) Film-Cooling Measurements. Internal Report 352-7419 of DFVLR, Jet Engine Institute Porz-Wahn.

52. Kumada, M. & Mabuchi, I. (1970) Studies of Impinging Jet. Japanese Society of Mechanical Engineers 13, 77.

53. Launder, B.E. & York, J. (1974) Discrete Hole Cooling in the Presence of Free Stream Turbulence and Strong Favourable Pressure Gradient. Int. J. of Heat-Mass Transfer 17, 1403.

54. Le Febvre, A.H. (1968) Radiation from Flames in Gas Turbines and Rocket Engines. 12th Symposium (International) on Combustion, 1247.

55. Lefebvre, A.H. & Herbert, M.V. (1960) Heat Transfer Processes in Gas Turbine. Proceedings, Ints. Mech. Engineers 174, 12.

56. Marsland, J., Odgers, J. & Winter, J. (1960) The Effects of Flame Radiation on Flame Tube Temperatures. 12th Symposium (International) on Combustion, 1265.

57. Matthews, L., Rastogi, A.K. & Whitelaw, J.H. (1971) The Application of Numerical Methods to Film-Cooling and Associated Practical Problems. 1st National Heat and Mass Transfer Conference, Indian Institute of Technology, Madras.

58. Matthews, L. (1973) Performance of some Two-Dimensional Film-Cooling Geometries. Ph.D. Thesis, University of London.

59. Mayle, R.E. & Camarata, F.J. (1975) Multi-hole Cooling Film Effectiveness and Heat Transfer. J. of Heat Transfer 18, 535.

60. McDonald, H. (1973) Effect of Free Stream Turbulence on Turbulent Boundary Layer. United Aircraft Research Laboratories Report M 110887 - 1.

61. McMurray, D.C., Myers, P.S. & Uyehara, A.O. (1966) Influence of Impinging Jet Variables on Local Heat Transfer Coefficients along a Flat Surface with Constant Heat Flux. 3rd International Heat Transfer Conference, Chicago, Proceedings 2, 274.

62. Metzger, D.E. et al (1969) Impingement Cooling of Concave Surfaces with Lines of Circular Air Jets. J. of Engineering for Power 91, 149.

63. Metzger, D.E. & Fletcher, D. (1971) Evaluation of Heat Transfer for Film-Cooled Turbine Components. J. of Aircraft 8, 1, 34.

64. Metzger, D.E. & Korstad, R.J. (1972) Effects of Cross-Flow on Impingement Heat Transfer. J. of Engineering for Power 94, 35.

65. Metzger, D.E., Baltzer, R.T. & Jenkins, C.W. (1972) Impingement Cooling Performance in Gas Turbine Airfoils including Effects of Leading Edge Sharpness. J. of Engineering for Power 94, 219.

66. Metzger, D.E. et al (1972) Heat Transfer to Film Cooled Combustion Chamber Liners. ASME Paper 72-WA/HT-32.

67. Metzger, D.E. et al (1973) Effectiveness and Heat Transfer with Full Coverage Film-Cooling. ASME Paper 73-GT-18.

68. Metzger, D.E. et al (1972) Predicted Film-Cooling Near Flush Slots. Comparison with Experiments. AIAA paper 72-291.

69. Milford, C.M. & Spiers, D.M. (1961) An Investigation into Film Cooling by Slots. International Developments in Heat Transfer Part IV, 669.

70. Miyazaki, H. & Silberman (1972) Flow and Heat Transfer on a Flat Plate Normal to a Two-Dimensional Laminar Jet Issuing from a Nozzle of Finite Height. Int. J. of Heat-Mass Transfer 15, 2097.

71. Miyazaki, H. & Sparrow, E.M. (1975) Flow and Heat Transfer in Curved Wall Jets on Circular Surfaces. Int. J. of Heat-Mass Transfer 18, 779.

72. Newman, B.G. (1969) The Prediction of Turbulent Jets and Wall Jets. Canadian Aerospace Journal 15, 288.

73. Nina, M.N.R. (1969) The Influence of Three-Dimensional Slot Geometries on Film-Cooling. M.Sc. Thesis, University of London.

74. Nina, M.N.R. & Whitelaw, J.H. (1971) The Effectiveness of Three-Dimensional Slot Geometries. J. of Engineering Power 93, 425.

75. Nobbs, K.W. & Rice, P. (1968) The Performance of Splash Impingement Cooling Devices. Dept. of Aircraft Propulsion, College of Aeronautics, Cranfield.

76. Odgers, J. & Winter, J. (1963) Wall Cooling Processes in Gas Turbine Combustion Chambers. Lucas Gas Turbine Equipment Ltd. Report No.B 48314.

77. Pai, B.R. (1969) The Effectiveness of Film-Cooling. Ph.D. Thesis, University of London.

78. Pai, B.R. & Whitelaw, J.H. (1971) The Prediction of Wall Temperatures in the Presence of Film-Cooling. Int. J. of Heat-Mass Transfer 14, 409.

79. Pai, B.R. & Whitelaw, J.H. (1970) Influence of Strong Pressure Gradients on Film-Cooling. 4th International Heat Transfer Conference, FG.1. 11.

80. Palmer, J.F. (1964) Interim Report on Performance Investigations of Two-dimensional Models of Splash Type Film-Cooling. Bristol Siddeley Report No.1248.

81. Palmer, J.F. (1965) Second Interim Report on Performance of Two-Dimensional Models of Film-Cooling. Bristol Siddeley Report No. P.D. 1396.

82. Patankar, S.V. & Spalding, D.B. (1970) Heat and Mass Transfer In Boundary Layers. Intertext books.

83. Patankar, S.V. & Spalding, D.B. (1972) A Calculation Procedure for Heat, Mass and Momentum Transfer in Three-dimensional Parabolic Flows. Int. J. of Heat-Mass Transfer 15, 1787.

84. Patankar, S.V., Rastogi, A.K. & Whitelaw, J.H. (1973) The Effectiveness of Three-dimensional Film-cooling slots - Predictions. Int. J. of Heat-Mass Transfer 16, 1673.

85. Patankar, S.V. & Spalding, D.B. (1973) Simultaneous Prediction of Flow Pattern and Radiation for Three-dimensional Flames. Imperial College Mechanical Engineering Dept. Report HTS/73/39.

86. Patel, V.C. (1968) Effects of Curvature on Turbulent Boundary Layers. Aeronautical Research Council Reports and Memoranda 3.599.

87. Perry, K. (1954) Heat Transfer by Convection from a Hot Gas Jet to a Plane Surface. Proceedings of the Institution of Mechanical Engineers 168, 775.

88. Pope, S.B. & Whitelaw, J.H. (1976) The Calculation of Near Wake Flows. J. of Fluid Mechanics 73, 9.

89. Rastogi, A.K. (1972) Effectiveness and Heat Transfer Downs-ream of Three-dimensional Film-cooling slots. Ph.D. thesis, University of London.

90. Rastogi, A.K. & Whitelaw, J.H. (1971) Procedure for Predicting the Influence of Longitudinal Curvature on Boundary Layers. ASME paper 71-WA/FE - 37.

91. Rastogi, A.K. & Whitelaw, J.H. (1973) The Effectiveness of Three-dimensional Film-cooling Slots - measurements. Int. J. of Heat-Mass Transfer 16, 1665.

92. Repukhov, V.M. et al (1970) A Study of Film-cooling of Rotating Cylindrical Surface by Air Injection through a Tangential Slot. Heat Transfer - Soviet research 2, No.1 156.

93. Rotta, J.C. (1967) Effect of Stream Line Curvature on Compressible Turbulent Boundary Layers. Physics of Fluids Supplement 5 174.

94. Russel, P.J. & Hatton, A.P. (1972) Turbulent Flow Characteristics of an Impinging Jet. Proceedings of the Inst. of Mechanical Engineers, 186, 635.

95. Schuh, H. & Petterson (1966) Heat Transfer by Arrays of Two-dimensional Jets Directed Normal to Surfaces - including the effects of a superposed wall-parallel flow. 3rd International Heat Transfer Conference, Chicago. Proc. 2, 280.

96. Sharma, D. (1974) Turbulent Convective Phenomena in Straight Rectangular Sectioned Diffusers. Ph.D. Thesis, University of London.

97. Shvets, I.T. et al (1973) Effectiveness of Film-cooling of an Adiabatic Wall Downstream of the Perforated Section. Heat Transfer - Soviet research 5, 3, 57.

98. Sivasegaram, S. & Whitelaw, J.H. (1969) Film-cooling Slots; the importance of lip thickness and injection angle. J. of Mechanical Engineering Science 11, 1, 22.

99. Smirnov, A.A. (1973) Convective Heat Transfer during the Flow of a System of Plane-parallel Jets on a Flat Surface. Heat Transfer - Soviet research 5, 2, 115.

100. Smith, M.R. (1974) A Study of Film-cooling Effectiveness with Discrete Holes and Slots. Ph.D. Thesis, University of Oxford.

101. So, R.M.C. (1975) A Turbulent Velocity Scale for Curved Shear Flows. J. of Fluid Mechanics 70, 37.

102. So, R.M.C. & Mellor, G. (1972) An Experimental Investigation of Turbulent Boundary Layers along Curved Surfaces. NASA CR- -940.

103. Sparrow, E.M. & Lee, L. (1975) Analysis of Flow Field and Impingement Heat-Mass Transfer due to a Non Uniform Slot Jet. J. of Heat Transfer 97, 191.

104. Sparrow, E.M. et al (1975) Effect of Nozzle-surface Separation on Impingement Heat Transfer for a Jet in a Cross Flow. J. of Heat Transfer 97, 528.

105. Sparrow, E.M. & Wong, T.C. (1975) Impingement Transfer Coefficients due to Initially Laminar Slot Jets. Int. J. of Heat-Mass Transfer 18, 597.

106a Sridhar, K. & Tu, P.K.C. (1969) Experimental Investigation of Curvature Effects on Turbulent Wall Jets. J. of Royal Aero. Society 73, 977.

106. Stollery, J.L. & El-Ehwany, A.A. On the use of a Boundary-layer Model for Correlating Film-cooling Data. Int. J. of Heat-Mass Transfer 10, 101.

107. Tabakoff, W. & Clevenger, W. (1972) Gas Turbine Blade Heat Transfer Augmentation by Impingement of Air Jets having Various Configurations. J. of Engineering Power 94 51.

108. Tacina, R.R. & Marek, C.J. (1974) Film-cooling in Combustor Operating at Fuel Rich exit Conditions. NASA TND 7513.

109. Tatchel, D.G. (1975) Convection Processes in Confined Three-dimensional Boundary Layers. Ph.D. Thesis, University of London.

110. Thomann, H. (1968) Effect of Wall Curvature on Heat Transfer in a Turbulent Boundary Layer. J. of Fluid Mech. 33, 283.

111. Warner, C.F. & Guinn, G.R. (1966) An Experimental Study of Liquid Film-cooling accomplished by Dual-slot Injection. J. Space Craft Rockets 3, 1545.

112. Whitelaw, J.H. (1967) The Effect of Slot Height on the Effectiveness of the Uniform Density, Two-dimensional Wall Jet. Imperial College. Mech. Eng. Dept. Report EHT/TN/4.

113. Whitelaw, J.H. (1972) M.Sc. Lectures on Transpiration Cooling. Mech. Eng. Dept. Imperial College.

114. Whittaker, M. (1969) Theoretical Assessment of Flame Tube Temperatures in Combustor Operating at Typical S.S.T. Conditions. Combustion and Heat Transfer in Gas Turbine Systems. Cranfield International Symposium Series 11.

115. Wilcock, D. (1975) Impingement Heat Transfer - a literature review. Lancaster Polytechnic, Dept. of Mech. Eng. Memo ME 434.

116. Wolfshtein, M. (1968) Convective Processes in Impinging Jets. Ph.D. dissertation. London University.

117. Yefimckuk, L.A. et al (1973) Experimental Investigation of Film-cooling of Exit Edges of Stationary Blading. Heat Transfer - Soviet research 5, 3, 126.

118. Ziebland, H. & Parkison, R.C. (1971) Heat Transfer in Rocket Engines. Agardograph No.148.

NOMENCLATURE

Symbol	Meaning
A	area of slot exit (table 4.2.1,4.2.2), constant in equation (2.2), or coefficients in difference equations of Appendix A.
A_o	total area of holes
B	coefficients in difference equations of Appendix A
C_f	shear stress coefficient
C_I	internal convection to the flame tube equation 6.2
C_o	external convection from the flame tube equation 6.2
C_p	pressure coefficient
D	diameter of the holes
E	constant in the law of the wall
F	pressure gradient parameter equation 3.2.13
h_f	heat transfer coefficient in the presence of film cooling
h_L	heat loss transfer coefficient
h_o	heat transfer coefficient at the outer side of the flame tube
H	shape factor
J	diffusional flux
k	kinetic energy of turbulence/thermal conductivity (equation 6.2.3)
K	reciprocal of radius of curvature or von Karman constant in the law of the wall
K_p	pressure gradient parameter $\nu/U_G^2 . \frac{dU_G}{dx}$
ℓ	distance of normal holes from the tangential holes exit or adjoining vertical wall; Figs. 4.1.1 or Prandtl's mixing length
L	lip length
m	total mass flow rate through the holes (Kg/s)

Symbol	Meaning
mp	mass source in equation A.22
N	No of row of holes
NU_C	Nusselt number based on the slot gap
NU_D	Nusselt number based on the hole diameter
$\overline{P}$	average pressure in the x direction momentum equation
P	pressure on the cross stream momentum equation; pitch of the holes
Pr	Prandtl number
$\dot{q}"$	generated heat-flux
Qw	heat flux at the wall
r	radial coordinate (R+y)
R	radius of curvature
Rea	Reynolds number based on arrival velocity
Re	Reynolds number
Rex	Reynolds number based on longitudinal distance
R_I	internal radiation (equation 6.2)
R_0	external radiation
S	wall shear stress coefficient ($\tau w/\frac{1}{2}\rho U^2_{2.5}$)
t	lip thickness
T	temperature
u	fluctuating component of velocity in x-direction
$\overline{uv}$	turbulent shear stress
U	mean velocity in x-direction
U_c	average velocity based on flow through holes and total area
U_G	free-stream velocity
U_n	average velocity through the normal holes
U_t	average velocity through the tangential holes

Symbol	Meaning
U_w	velocity deficit in the wake $\left(\frac{U_{c\,max}+U_G}{2} - U\ min\right)$
v	fluctuating component of velocity in y-direction
V	mean velocity in y direction
w	fluctuating component of velocity in z-direction
W	mean velocity in z-direction
x	longitudinal distance
X	correlation parameter (table 5.1.3)
y	distance normal to the wall
Y	correlation parameter (table 5.1.3)
y_C	slot height (fig. 2.2.1)
y_G	boundary layer thickness corresponding to the location where $u = 0.99\ U_G$
y_L	height of tangential hole from lower wall (fig. 2.2.1)
y_T	height of tangential hole from the upper lip (fig. 2.2.1)
Z	lateral distance
α_w	flame absorptivity at the wall
Γ	diffusivity
β	constant
Δx	length of forward step
$\Delta y, \Delta z$	cross-stream dimensions of the control volume (fig.A.2-A.3)
$\delta y, \delta z$	distances between neighbouring grid points (fig.A.2-A.3)
$\delta 1$	displacement thickness
δ_w	width of the wake
ε	dissipation of turbulence kinetic energy
ε_G	emissivity of the flame
ε_w	emissivity of flame-tube wall

Symbol	Meaning
ε_w'	emissivity of combustion chamber outer casing
η	film-cooling effectiveness
λ	mixing length constant
μ	viscosity
ν	kinematic viscosity
ρ	density
ρ_w	average density in the wake
τ	shear stress
ϕ	a conserved scalar property
ψ	stream function
σ	Prandtl or Schmidt number
σ_B	Stefan-Boltzman constant
w	vorticity

Subscripts	Meaning
aw	adiabatic wall
c	secondary flow
cm	secondary maximum
e	mid east point (fig. A.2)
E	east point
eff	effective
G	main flow
n	mid north point (fig. A.2) or nozzle
N	north point
P	grid point
s	mid south point

Subscripts	Meaning
S	south point
t	turbulent component
w	wall, or mid west point
W	west point
y	location y
ε	dissipation of turbulence kinetic energy

Superscripts	Meaning
P	pressure
U	mean longitudinal velocity
V	mean velocity in y-direction
W	mean velocity in z-direction
*	corresponding to guessed values
'	correction to guessed values

APPENDIX A

SOLUTION PROCEDURE

This appendix provides further numerical details for the solution procedure described in section 4.3.2. Figure A.1 shows the staggered grid arrangement and Figure A.2 a typical control volume for the finite-difference procedure. Because of the staggered grid arrangement, the cross stream areas for solutions of U,V,W are different. These are defined by Figures A.3 - A.5.

The subsequent sections of this appendix describes the integration of equations 3.3.9 - 3.3.12, the calculation of lateral velocities and pressure, longitudinal pressure, and the solution of final finite difference form by a tridiagonal matrix algorithm.

A.1 INTEGRATION OF MASS CONTINUITY EQUATION AND ϕ CONSERVATION

The integration of equations 4.3.5 and 4.3.9 - 4.3.12 required the following assumptions to be made:

(i) The general variable ϕ varies in a stepwise manner so that the downstream value prevails for the interval X_U to X_D except at X_U where the upstream value prevails.

(ii) For calculation of x-direction convection and source terms, ϕ varies in a stepwise manner in the yz plane. Thus the value of ϕ remains uniform and equal to ϕ_P over the dotted rectangle in Figure A.2 and changes sharply to ϕ_N, ϕ_S, ϕ_E, ϕ_W outside the rectangle.

(iii) For cross-stream convection from the xy and xz faces of the control volume, the value of ϕ convected, is taken to be

the arithmetic mean of the ϕ values on either side of that face.

(iv) For diffusion across the xy and xz faces of the control volume, ϕ varies linearly between grid points except when 'high lateral flux' dictates otherwise.

With above assumptions, the following form of the conservation equations are obtained.

Mass Continuity

$$\int_{Zw}^{Ze}\int_{y_s}^{yn}\int_{xU}^{xD} \left\{\frac{\partial}{\partial x}(\rho U) + \frac{\partial}{\partial y}(\rho V) + \frac{\partial}{\partial z}(\rho W)\right\} dx\, dy\, dz = 0 \qquad \text{A.1}$$

$$A_x\left[(\rho U)_P - (\rho U)_U\right] + A_y\left[\rho_n U_N - \rho_s V_P\right] + A_z\left[\rho_e W_E - \rho_w W_P\right] = 0 \qquad \text{A.2}$$

where Ax, Ay, Az denote the areas of the faces of cell (Fig.A.2 - A.3) and are defined as follows:

$$\begin{aligned} A_x &= \Delta y\, \Delta z \\ A_y &= \Delta x\, \Delta z \\ A_z &= \Delta x\, \Delta y \end{aligned} \qquad \text{A.3}$$

The ϕ Conservation

$$\int_{Z_w}^{z_e}\int_{y_s}^{y_n}\int_{x_U}^{x_D} \left[\frac{\partial}{\partial x}(\rho U\phi) + \frac{\partial}{\partial y}(\rho V\phi) + \frac{\partial}{\partial z}(\rho W\phi)\right] dx\, dy\, dz$$

$$= \int_{z_w}^{Ze}\int_{y_s}^{y_n}\int_{x_U}^{x_D} \left[\Gamma_{eff,y}\frac{\partial^2\phi}{\partial y^2} + \Gamma_{eff,z}\frac{\partial^2\phi}{\partial Z^2} + S\phi\right] dx\, dy\, dz \qquad \text{A.4}$$

The x-direction convection integrates to

$$A_x \left[g_D \phi_P - g_U \phi_U\right] \qquad \text{A.5}$$

where

$$g_D = \rho_P \, U_P \qquad \text{A.6}$$

$$g_U = \rho_{P,U} \, U_{P,U}$$

and P,U stands for upstream values. The source term integrates to

$$S\phi_P \, \Delta x \, \Delta y \, \Delta z = S_U^{\phi} + S_P^{\phi} \, \phi_P \qquad \text{A.7}$$

and the lateral convection and diffusion terms integrate to

$$\begin{aligned} &A_y \, g_n \left[(1 - F_n) \, \phi_N + F_n \, \phi_P\right] \\ &-A_y \, g_s \left[F_s \, \phi_S + (1 - F_s) \, \phi_P\right] \\ &+A_z \, g_e \left[(1 - F_e) \, \phi_E + F_e \, \phi_P\right] \\ &-A_z \, g_w \left[F_w \, \phi_W + (1 - F_w) \, \phi_P\right] \end{aligned} \qquad \text{A.8}$$

where $F_n = \dfrac{(1 + Pe_n^{-1})}{2}$ for $|Pe_n| > 2$

$$F_n = 1 \quad \text{for } Pe \geq 2 \qquad \text{A.9}$$

$$F_n = 0 \quad \text{for } Pe \leq 2$$

$g_n = \rho_n V_n$

and

$$Pe_n = \frac{\rho_n V_n \, \delta_y}{\Gamma_{eff,n}} \qquad \text{A.10}$$

Combination of equations A.5, A.7 and A.8 lead to

$$A_x (g_D \phi_P - g_U \phi_{P,U}) = A_y g_n [(F_n - 1) \phi_N - F_n \phi_P]$$
$$+A_y g_s [F_s \phi_S + (1 - F_s) \phi_P]$$
$$+A_z g_e [(F_e - 1) \phi_E - F_e \phi_P]$$
$$+A_z g_w [F_w \phi_W + (1 - F_w) \phi_P] + S^{\phi}_U - S^{\phi} \phi_P \qquad \text{A.11}$$

The coefficients of ϕ_P from equation A.11 can be written as

$$(A_x g_D - A_y g_n + A_y g_s - A_z g_e + A_z g_w) - S^{\phi}_P$$
$$+A_y g_n (F_n - 1) + A_y g_s F_s + A_z g_e (F_e - 1)$$
$$+A_z g_w F_w \qquad \text{A.12}$$

By continuity, the first term in bracket in equation A.12 equals $A_x g_U$. Equation A.11 can therefore be written as

$$[A_x g_U - S^{\phi}_P + A_y g_n (F_n - 1) + A_y g_s F_s +$$
$$A_z g_e (F_e - 1) + A_z g_w F_w] \phi_P$$
$$= A_y g_n (F_n - 1) \phi_N + A_y g_s F_s \phi_S$$
$$+A_z g_e (F_e - 1) \phi_E + A_z g_w F_w \phi_W$$
$$+S_u{}^{\phi} + A_x g_U \phi_{P,U} \qquad \text{A.13}$$

Equation A.13 can be written as

$$A'_P{}^{\phi} \phi = A'_N{}^{\phi} \phi_N + A'{}^{\phi} \phi_S + A'_E{}^{\phi} \phi_E$$
$$+ A'_W{}^{\phi} \phi_W + B'_P{}^{\phi} \qquad \text{A.14}$$

where the A'^{ϕ}s denote the coefficients in equation A.13 and B'^{ϕ}_P is the source terms $S_U^{\phi} + A_x\, g_U\, \phi_{P,U}$. The final form of finite difference equation is written as

$$\phi_P = A_N^{\phi}\phi_N + A_s^{\phi}\phi_s + A_E^{\phi}\phi_E + A_w^{\phi}\phi_W + B^{\phi} \qquad \text{A.15}$$

From the similarity of the form of equations 4.3.9 - 4.3.12, the above numerical procedures can be repeated for the momentum equations, using the appropriate flow areas shown on Figure A.3-5 for each equation. The results may be expressed as:

$$U_P = A_N^U U_N + A_s^U U_s + A_E^U U_E + A_W^U U_w + B^U \qquad \text{A.16}$$
$$+ D^U\left(\frac{\partial \overline{P}}{\partial x}\right)$$

$$V_P = A^V{}_N\, V_N + A_s^V\, V_s + A^V{}_E\, V_E + A^V{}_W\, V_W + B^V$$
$$+ D^V\,(P_P - P_s) \qquad \text{A.17}$$

$$W_P = A^W{}_N\, W_N + A^W{}_s\, W_s + A^W{}_E\, W_E + A^W{}_W\, W_W + B^W$$
$$+ D^W\,(P_P - P_w) \qquad \text{A.18}$$

where $D^U = \dfrac{\Delta y \Delta z}{A'^U{}_P}$

$$D^V = \frac{\Delta x \Delta z^V}{A'^V{}_P} \qquad \text{A.19}$$

$$D^W = \frac{\Delta x \Delta y^W}{A'^W{}_P}$$

and

$$A_x{}^V = \Delta y^V\, \Delta\, z^V \;;\; A_x{}^W = \Delta y^W\, \Delta z^W$$

$$A_y^V = \Delta x\, \Delta z^V \; ; \; A_y^W = \Delta x \Delta z^W$$

$$A_z^V = \Delta x \Delta y^V \; ; \; A_z^W = \Delta x \Delta y^W$$

are the cell face areas for V and W cells shown on Figure A.3-5.

A.2 CALCULATION OF LATERAL VELOCITIES AND PRESSURE

These quantities are calculated by a guess and correct procedure in which the momentum equation are first solved for an estimated pressure field and then the pressures and velocities are corrected so as to satisfy local continuity everywhere. The preliminary velocities are calculated from:

$$V_P^* = A^V_N V_N^* + A^V_E V_E^* + A^V_S V_S^* + A^V_W V_W^* + B^V + D^V (P_S^* - P_P^*) \qquad \text{A.20}$$

$$W_P^* = A^W_N W_N^* + A^W_E W_E^* + A^W_S W_S^* + A^W_W W_W^* + B^W + D^W (P_W^* - P_P^*) \qquad \text{A.21}$$

where * denote estimated values.

The velocities so obtained will not, in general, satisfy the continuity equation. There will exist at each cell a finite mass source mp defined as:

$$mp = A_x \left[(\rho U)_P - (\rho U)_{P,U}\right] + A_y \left[\rho_n V_n^* - \rho_s V_P^*\right] + A_z \left[\rho_e W_E^* - \rho_W W_P^*\right] \qquad \text{A.22}$$

It is necessary to correct the pressure and velocities to make the mass source zero. Thus a linear relationship is assumed

between correct, guessed and the necessary pressure correction.

$$P_P = P_P^* + P_P' \qquad A.23$$

Substituting for P_P in equation A.17 and subtracting equation A.20 V_P can be written as:

$$V_P = V^*_P + D^V \left(P_P' - P_s'\right) + A^V_N \left(V_N - V_N^*\right) + A^V_s \left(V_s - V^*_s\right) + A^V_E \left(V_i - V_E^*\right) + A^V_W \left(V_W - V_W^*\right) \qquad A.24$$

By dropping the last four terms, the expression for V_P becomes:

$$V_P = V_P^* + D^V \left(P_P' - P_s'\right) \qquad A.25$$

Similarly $W_P = W_P^* + D^W \left(P_P' - P_W'\right)$ A.26

To obtain expression for the pressure correction V_P, V_N, W_P, W_E are substituted for in equation A.2

$$A_x\left[(\rho U)_p - (\rho U)_{p,}\right] + A_y\left[\rho_n V_N^* + D^V \rho_n \left(P_P' - P_N'\right) - \rho_s V_P^* - \rho_s D^V \left(P_P' - P_S'\right)\right] + A_z \left[\rho_e W_E^* + \rho_w D^W \left(P_P' - P_E'\right) - \rho_w W_P^* - D^W \rho_w \left(P_P' - P_W'\right)\right] = 0 \qquad A.27$$

In a similar way to momentum equations, Equation A.27 can be manipulated to give the general form

$$P_P' = A_N^P P_N' + A_S^P P_S' + A_E^P P_E' + A_W^P P_W' + B^P \qquad A.28$$

A.3 CALCULATION OF LONGITUDINAL PRESSURE GRADIENT

As for the calculation of lateral pressure, a guess and correct method is used. An estimated value of pressure field is first used to calculate the U^* field.

$$U^*_P = A_N^U U_N^* + A_S^U U_S^* + A_E^U U_E^* + A_W^U U_W^* + B^U + D^U\left(\frac{\partial \bar{P}}{\partial x}\right)^* \qquad A.29$$

This velocity field implies a total mass flow rate $\epsilon\rho U^* \Delta y \Delta z$ (taken over the solution domain) which will generally be different from the known flow rate. The difference is used to correct the pressure gradient.

$$\left(\frac{\partial \bar{P}}{\partial x}\right) = \left(\frac{\partial \bar{P}}{\partial x}\right)^* + \left(\frac{\partial \bar{P}}{\partial x}\right)' \qquad A.30$$

$$U_P = U^*_P + D^U\left(\frac{\partial \bar{P}}{\partial x}\right) \qquad A.31$$

Since $\epsilon\rho U \Delta y \Delta z = m$ A.32

the unknown pressure correction is obtained by substituting U_P for U in equation A.32.

$$\left(\frac{\partial \bar{P}}{\partial x}\right)' = \frac{m - \epsilon\rho U^* \Delta y \Delta z}{\epsilon\rho D^U \Delta y \Delta z} \qquad A.33$$

A.4 SOLUTION OF THE FINITE DIFFERENCE EQUATIONS

The tridiagonal matrix algorithm provides a means of solving a set of linear simultaneous equations of the form

$$\phi_i = A_i \phi_{i+1} + B_i \phi_{i-1} + C_i$$

Equations A.15, A.16 - A.18 and A.28 were solved by successive application of the tridiagonal matrix in the y and z directions.

For the y- direction sweep, the equations are solved as

$$\phi^I{}_P = A_N{}^\phi \phi_N{}^I + A_s{}^\phi \phi_s{}^I + (A_E{}^\phi \phi_{E,U} + A_W{}^\phi \phi_{W,U} + B^\phi)$$

and for the z direction sweep, the solution is:

$$\phi_P{}^{II} = A_E{}^\phi \phi_E{}^{II} + A^\phi \phi_W{}^{II} + (A_N{}^\phi \phi_N{}^I + A_s \phi_s{}^I + B^\phi)$$

The expressions in parenthesis are treated as known. The superscripts denote the values obtained from the respective sweeps.

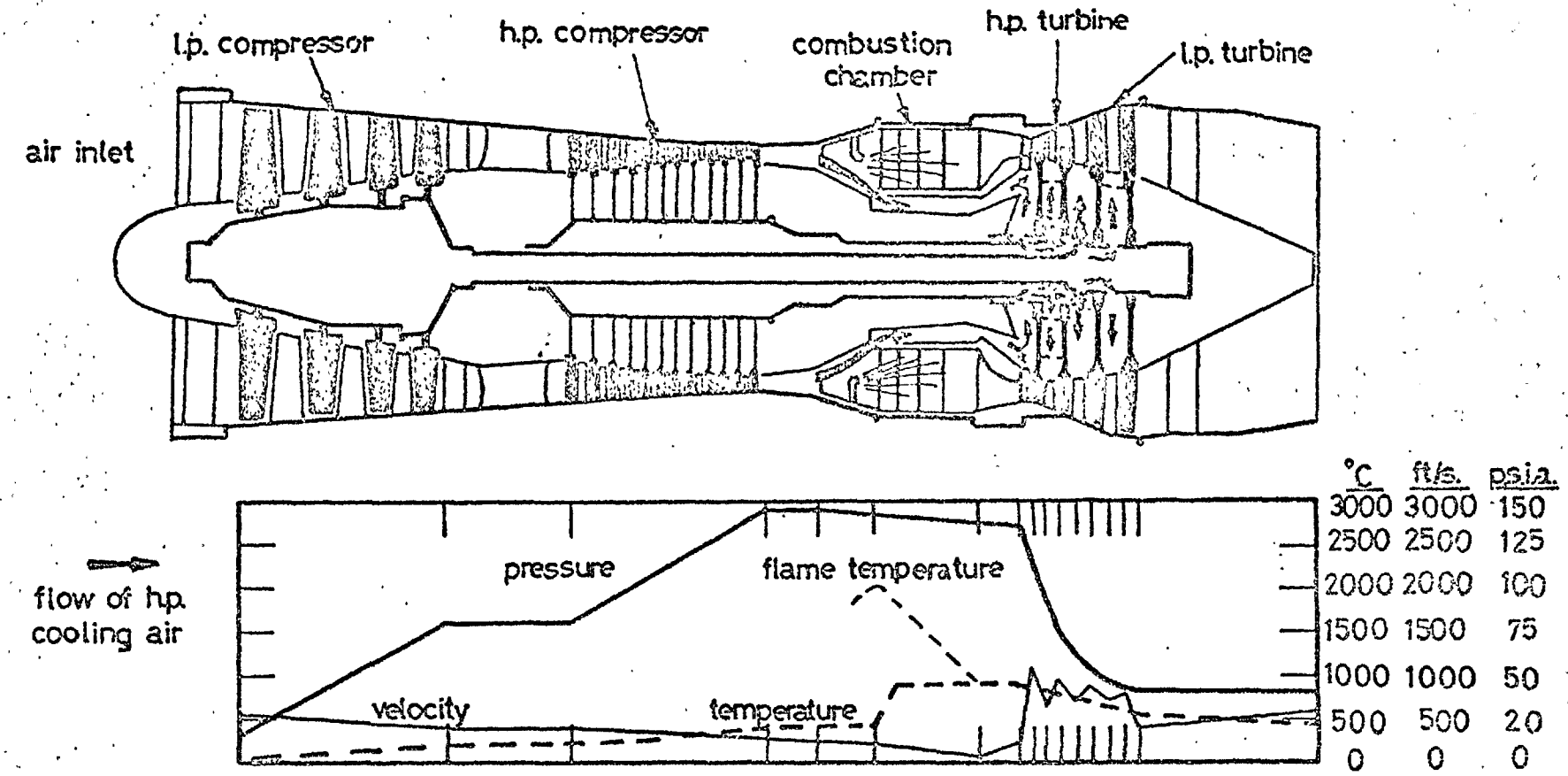

Figure 1.1 Schematic diagram of a typical jet engine, showing the path taken by the air used for film cooling, and the variation of pressure, velocity and temperature through the engine.

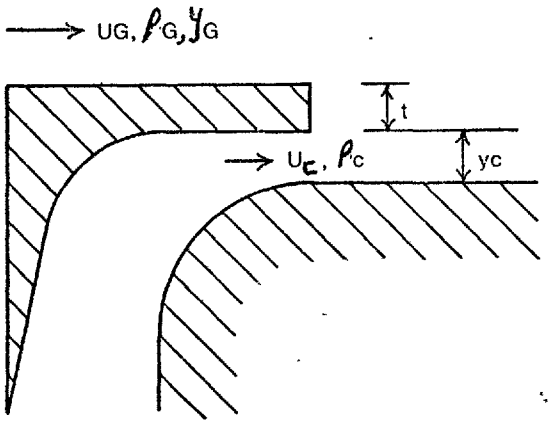

STEP DOWN SLOT
(a)

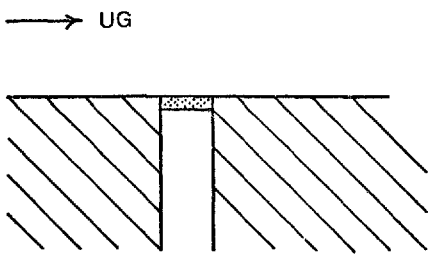

POROUS SLOT
(b)

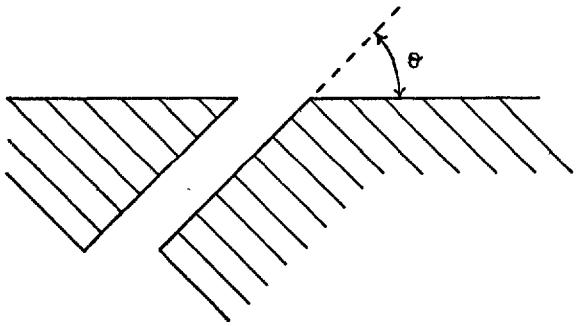

FLUSH ANGLED SLOT
(c)

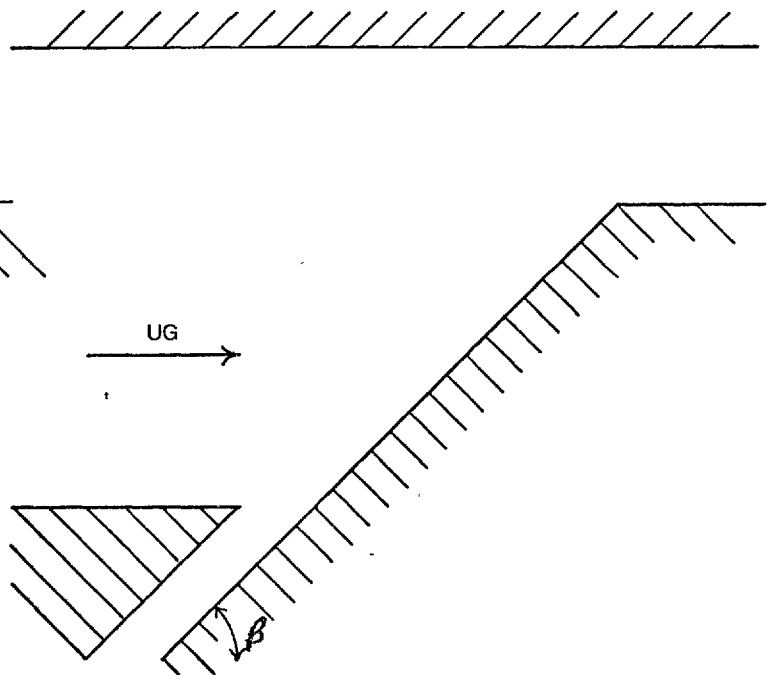

INJECTION PARALLEL TO CONVERGING WALLS
(d)

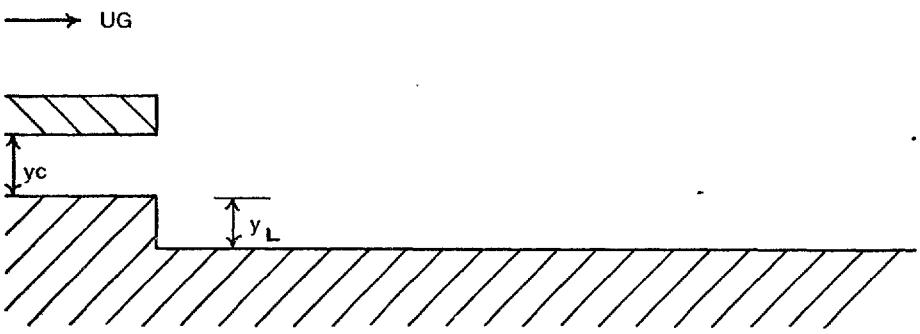

TANGENTIAL SLOT WITH A BACKWARD FACING STEP
(e)

FIG. 2.1.1 Two dimensional slots

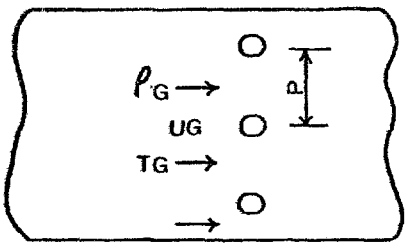

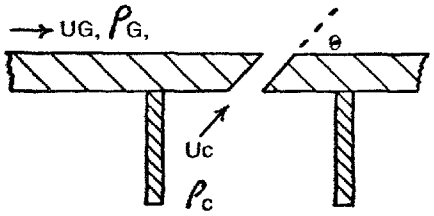

a DISCRETE HOLES (NO IMPINGEMENT LIP)

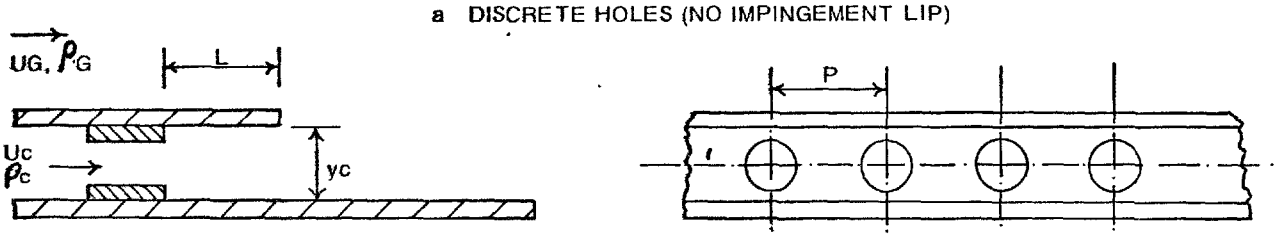

b TOTAL HEAD COOLING

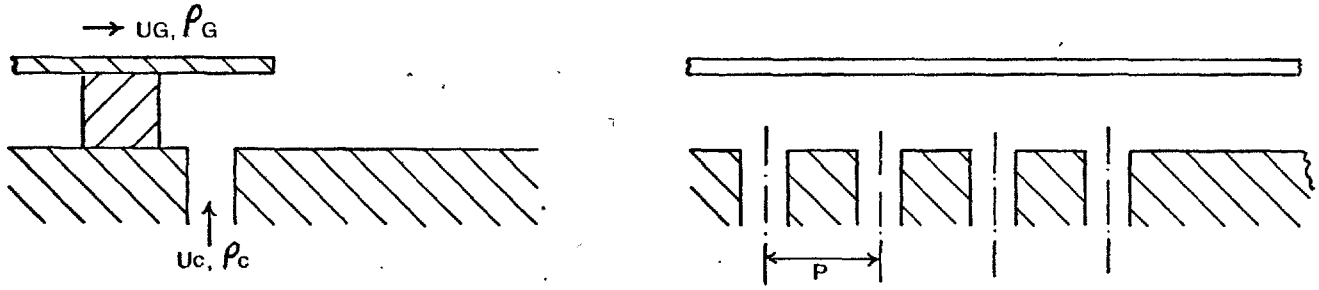

c NORMAL INJECTION COOLING

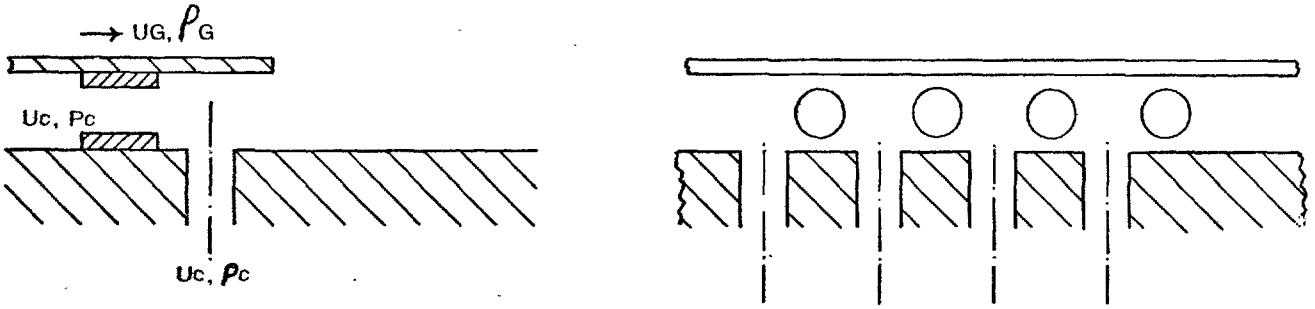

d COMBINED NORMAL AND TANGENTIAL COOLING

FIG. 2.2.1 Three Dimensional Slots

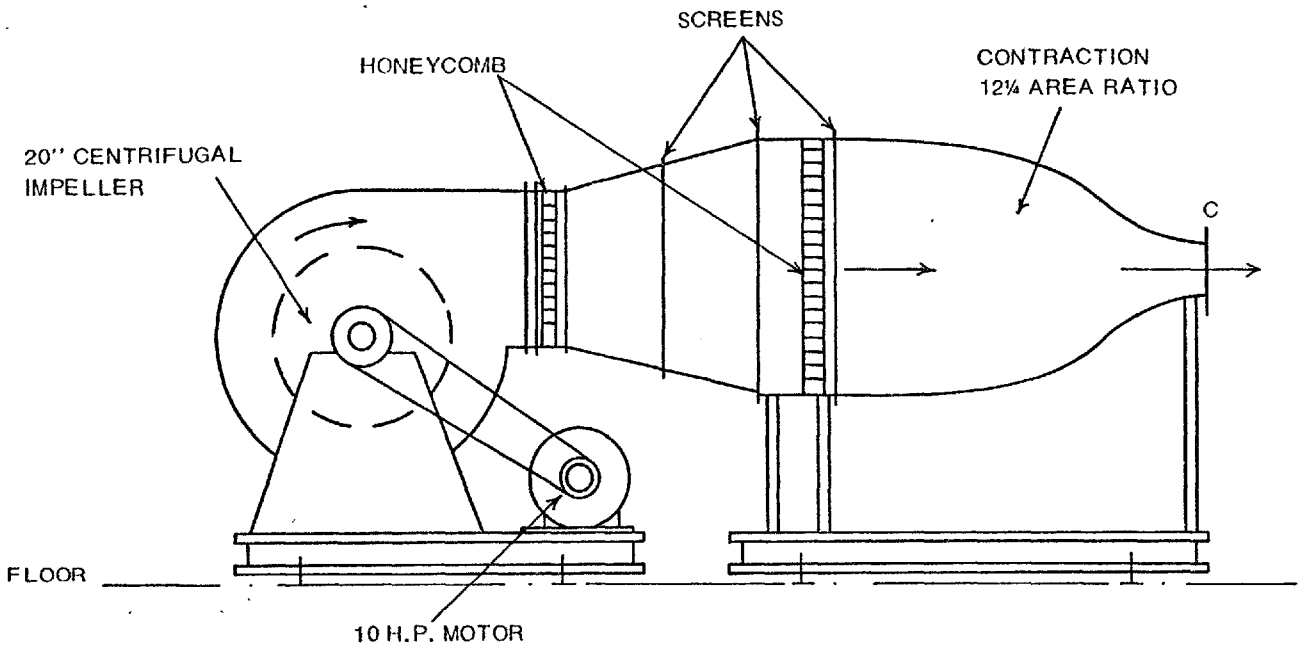

FIG. 3.1.1a DIAGRAM OF MAIN FLOW CIRCUIT

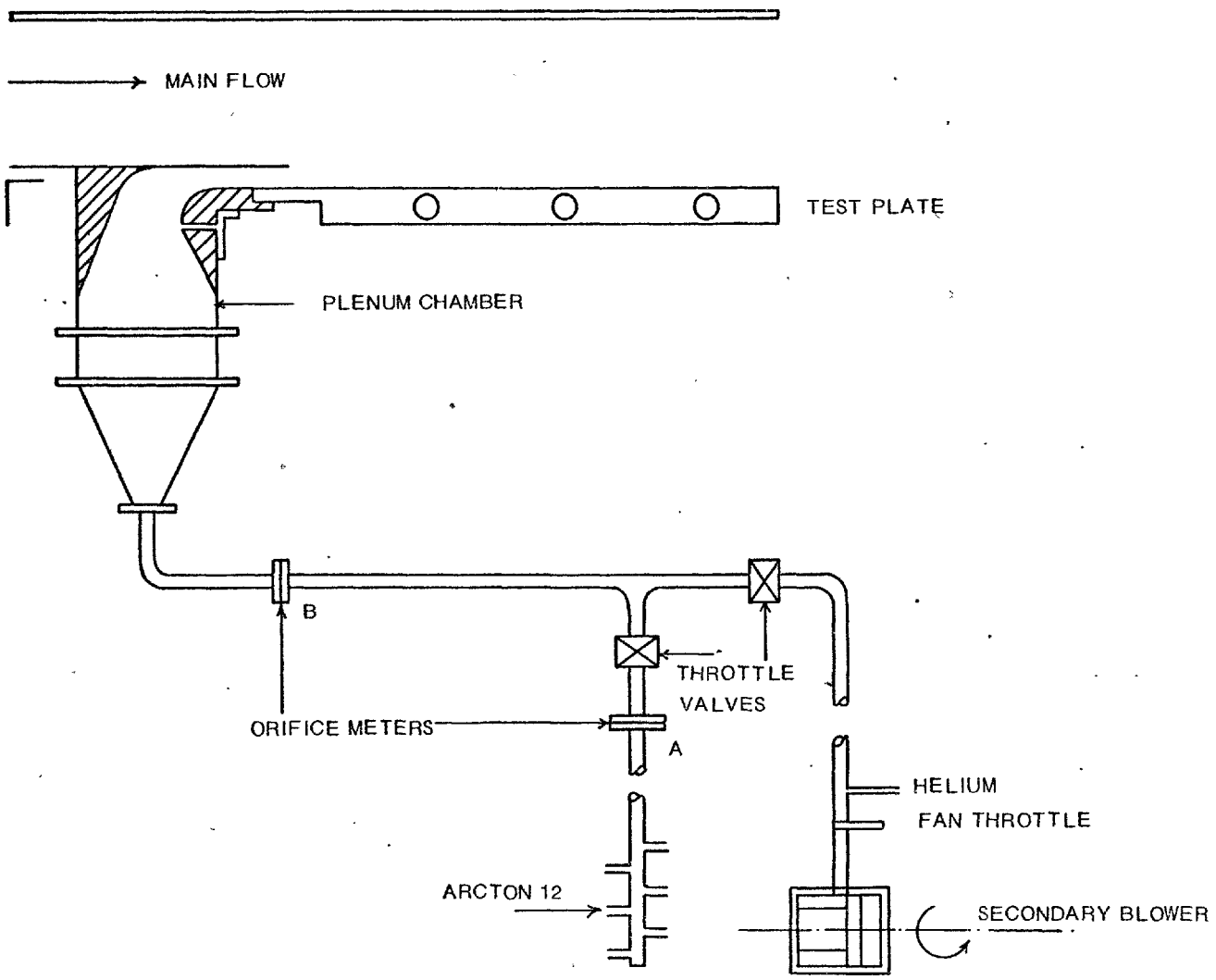

FIG. 3.1.1b DIAGRAM OF SECONDARY FLOW CIRCUIT

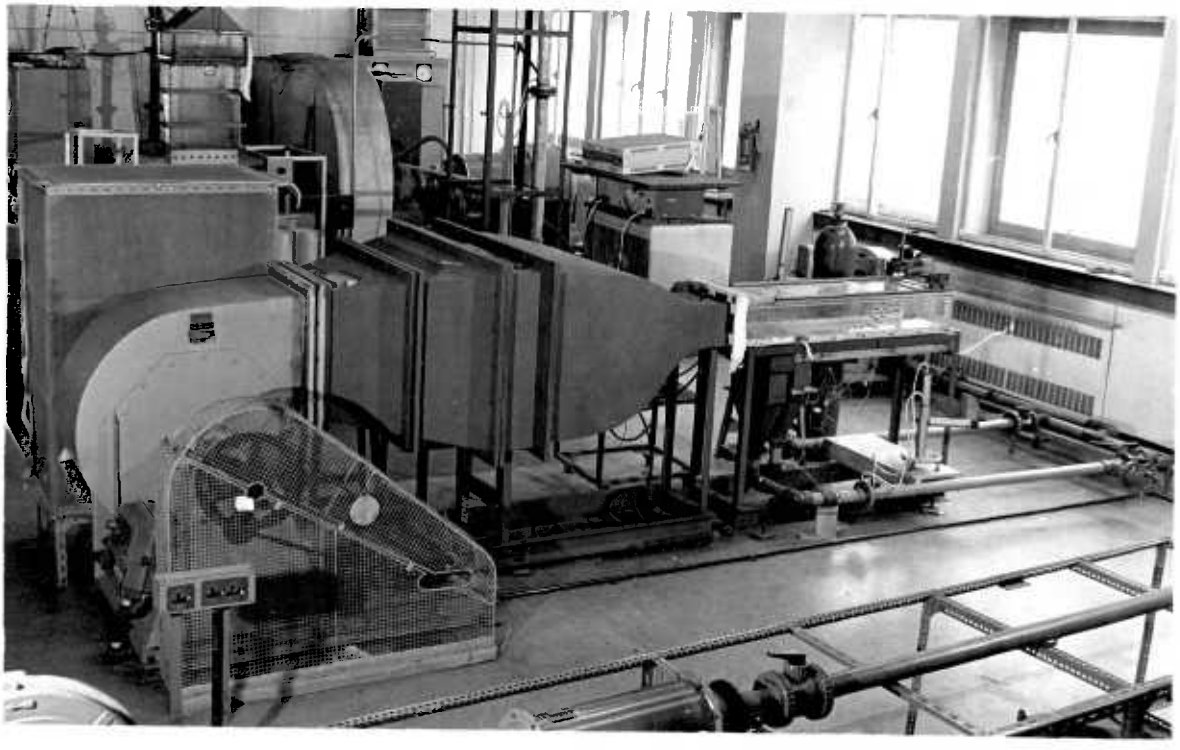

Plate 3.1.a Experimental flow arrangement

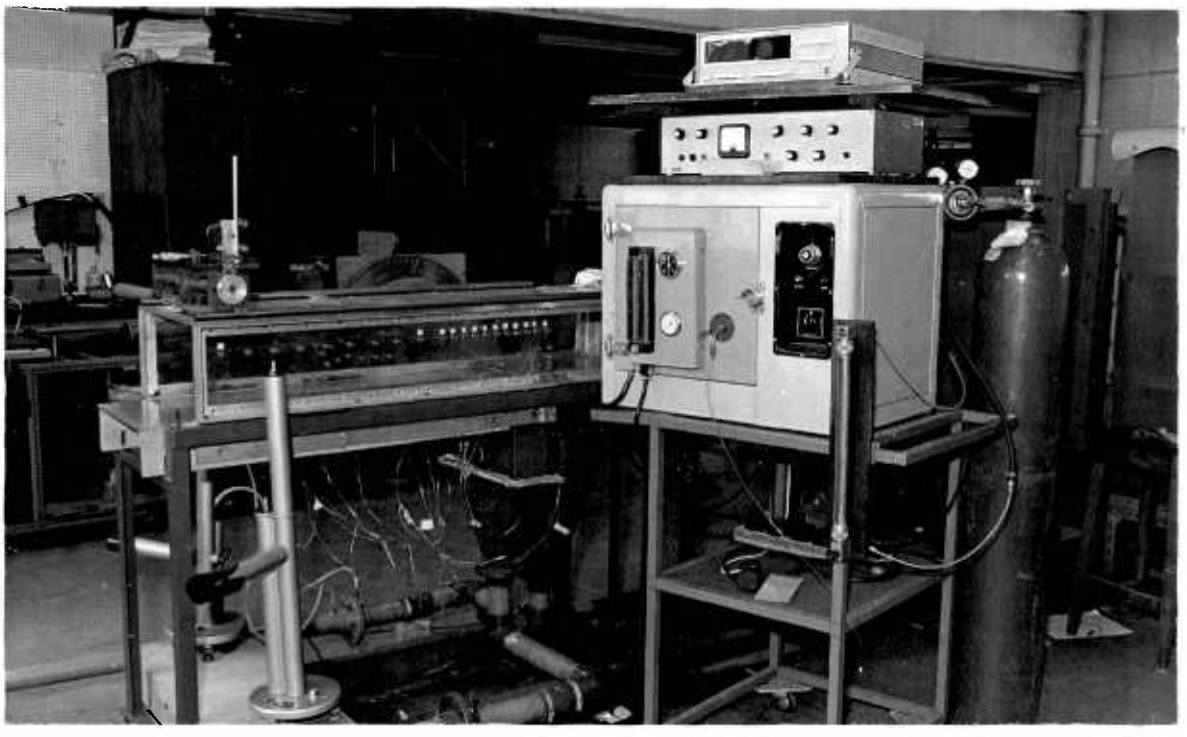

Plate 3.1.b Concentration measuring Instrumentation

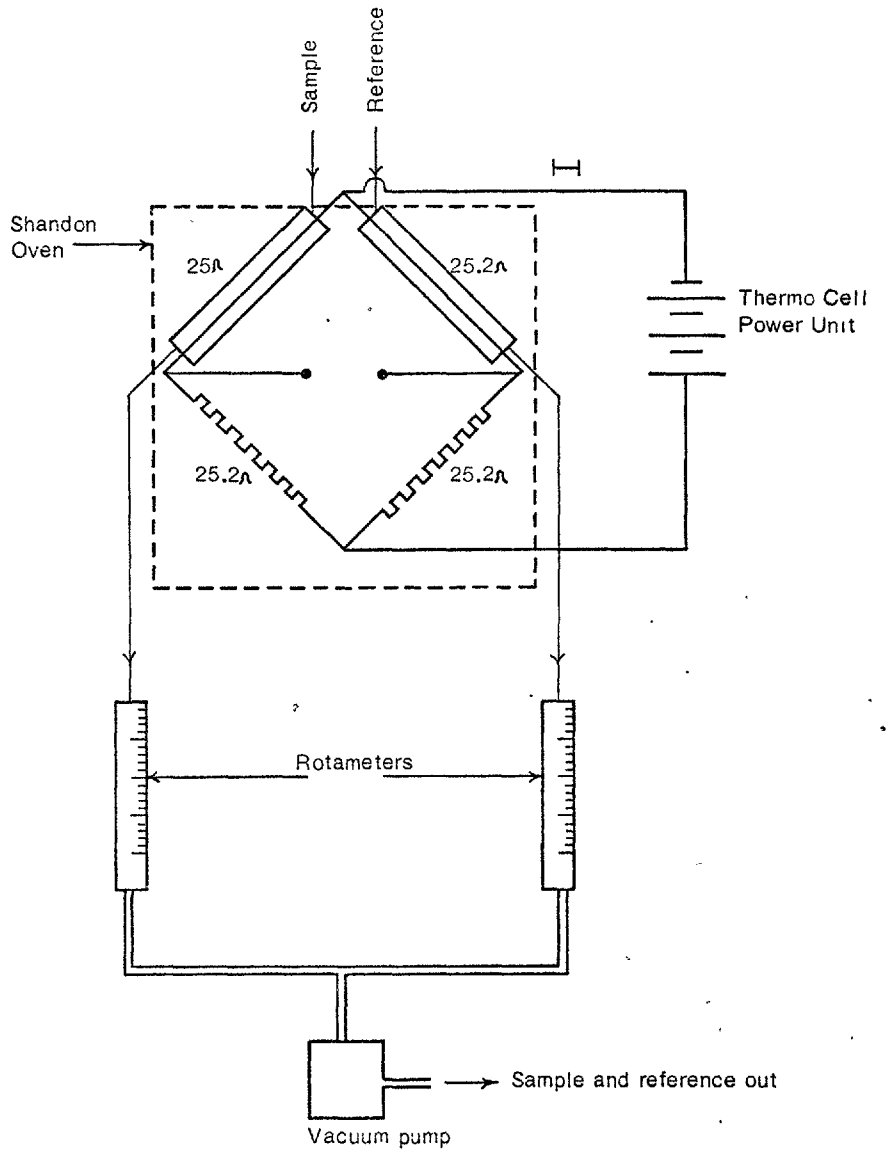

THERMAL CONDUCTIVITY CELL-SAMPLING
FLOW CIRCUIT

FIG. 3.1.2.

CALIBRATION CURVES FOR THE CELL
AT 100MA BRIDGE CURRENT

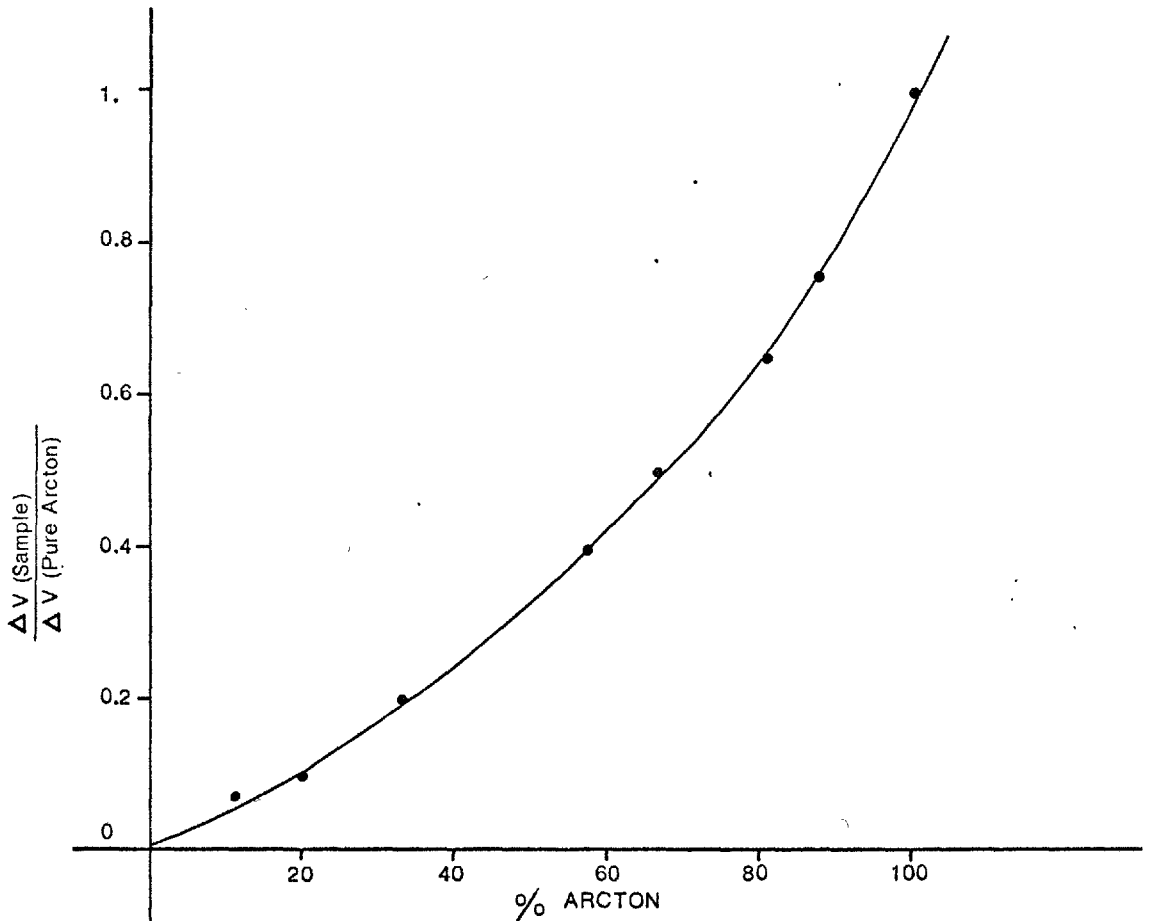

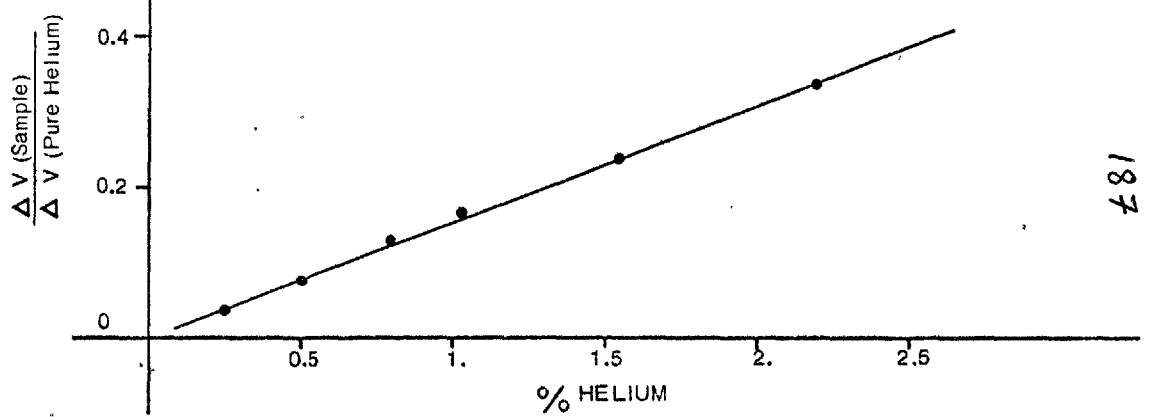

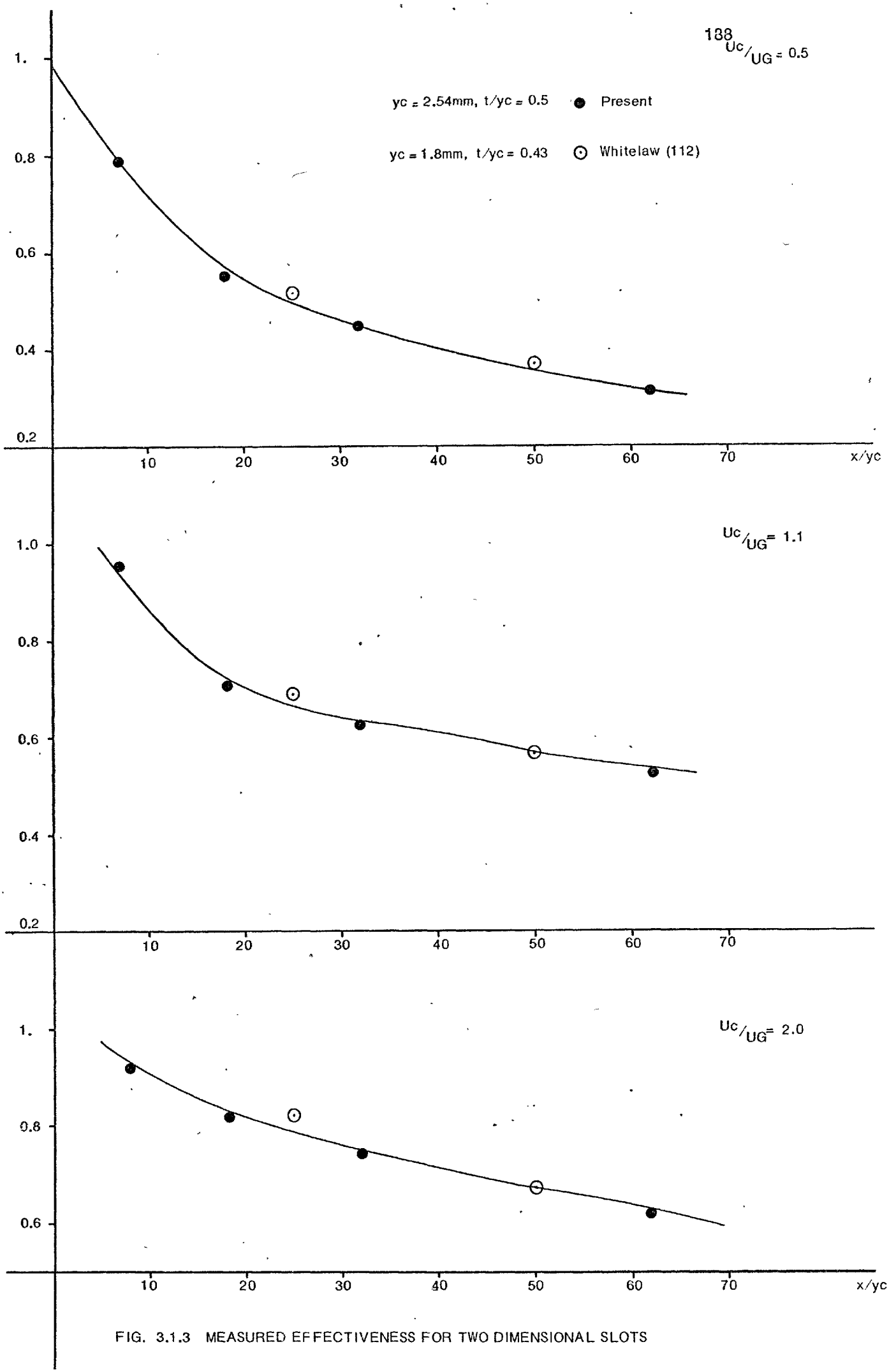

FIG. 3.1.3 MEASURED EFFECTIVENESS FOR TWO DIMENSIONAL SLOTS

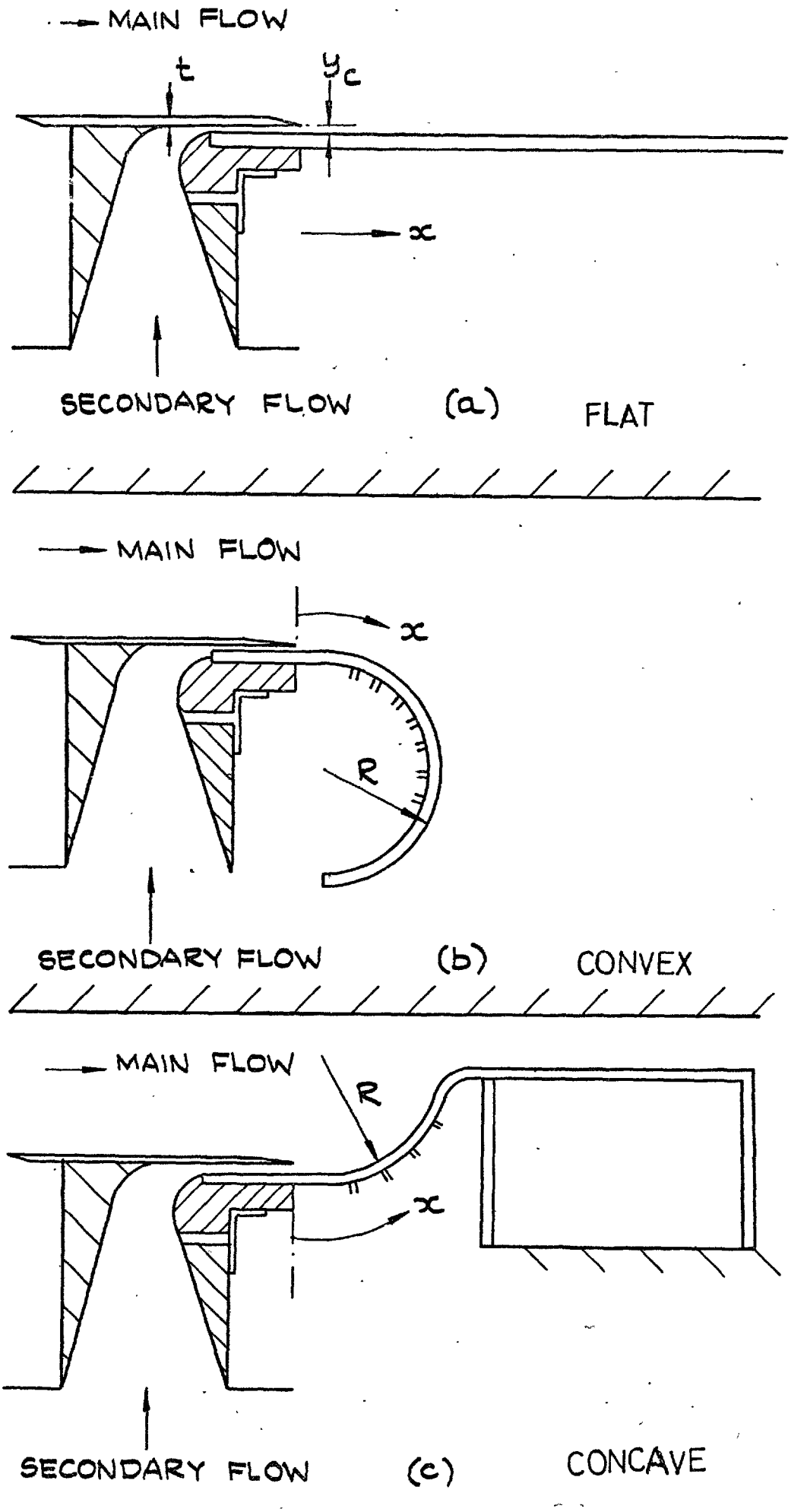

FIG. 3.1.4. FLOW CONFIGURATIONS

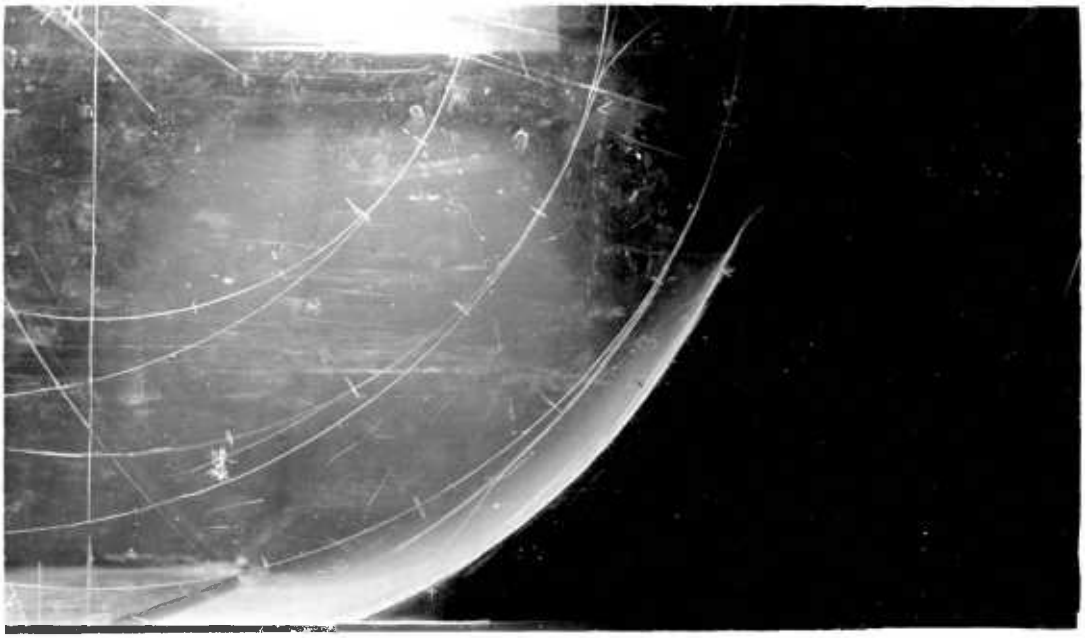

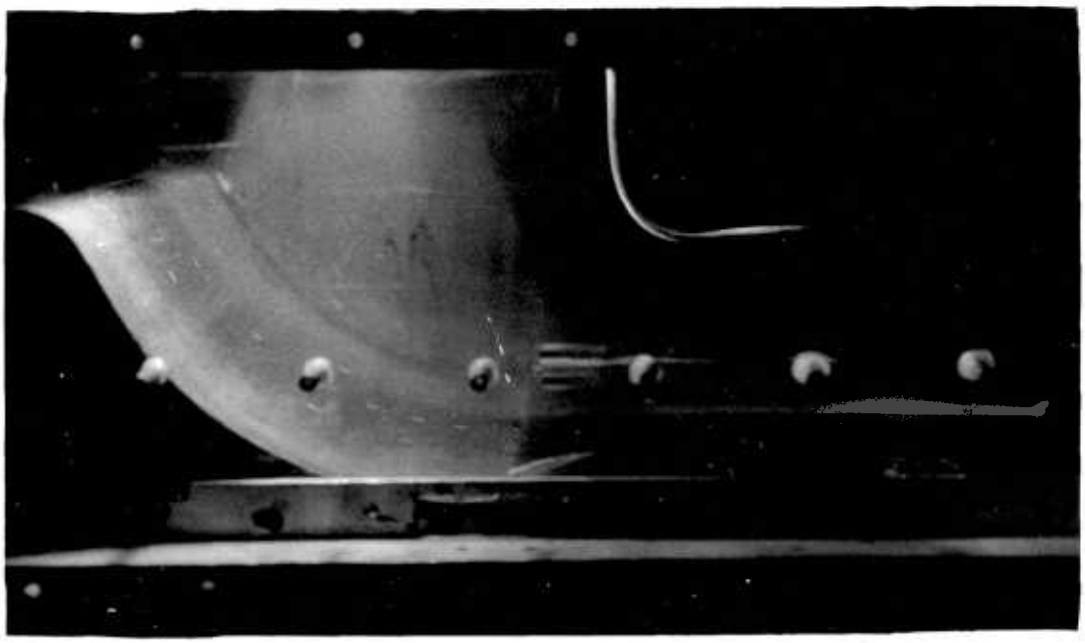

Plate 3.2 Smoke tests on the concave plates

TABLE 3.1. RANGE OF MEASUREMENTS

Symbol	R (mm)	Y_c (mm)	U_c/U_G	p_c/p_G
•	∞	2.54	0.5, 1.1, 1.6, 2.0	1.0, 2.25
⊙	+152.5	2.54	0.5, 1.1, 1.6, 2.0	1.0, 2.25
⊗	+76	2.54	0.5, 1.1, 1.6, 2.0	1.0, 2.25
□	+76	5.1	0.5, 1.1, 1.6,	1.0, 2.25
△	-152.5	2.54	0.5, 1.1, 1.6, 2.0	1.0, 2.25
⊡	-152.5	5.1	0.5, 1.1, 1.6, 2.0	1.0, 2.25

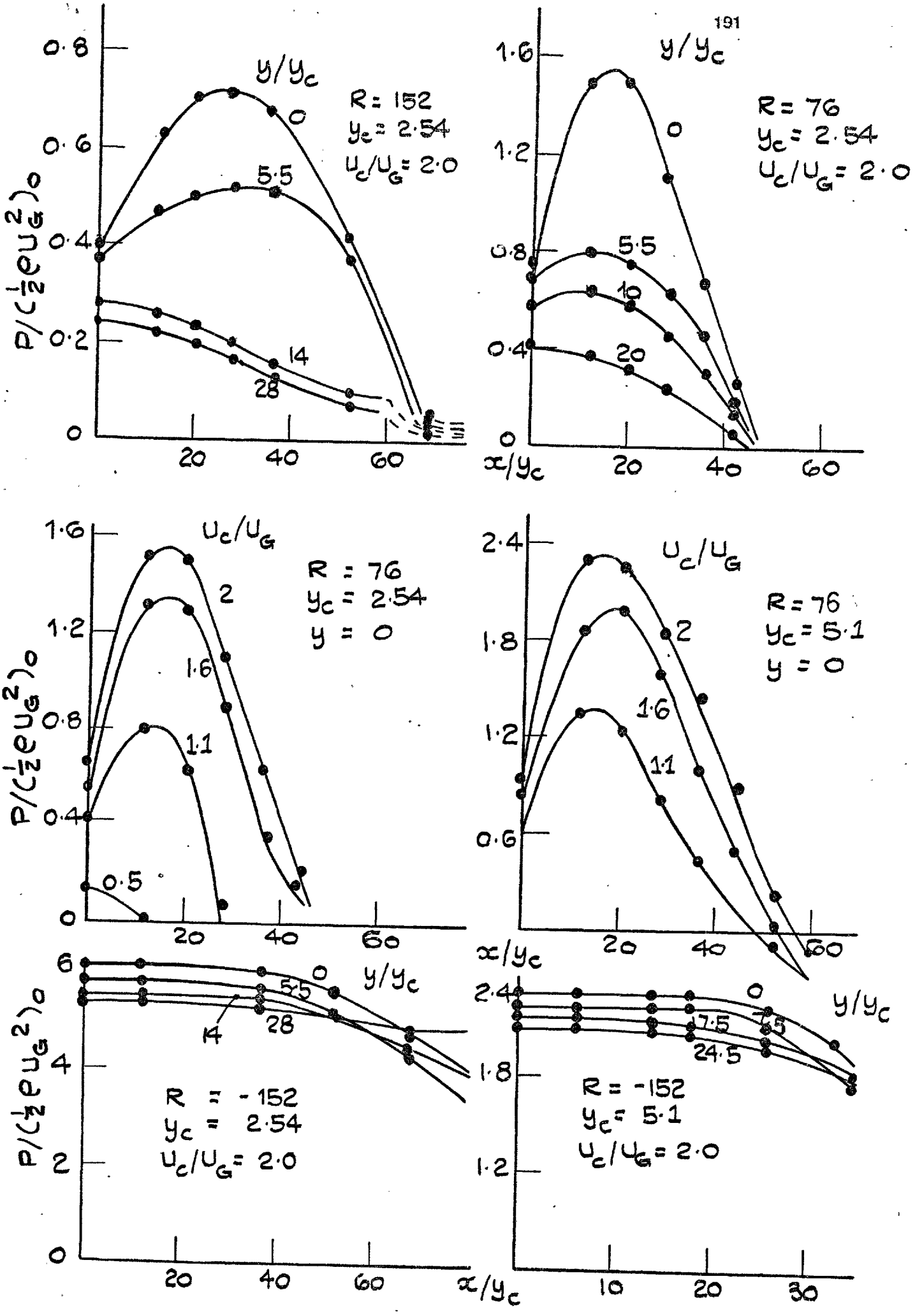

FIG 3.1.5. STATIC PRESSURES ON CONVEX AND CONCAVE SURFACES

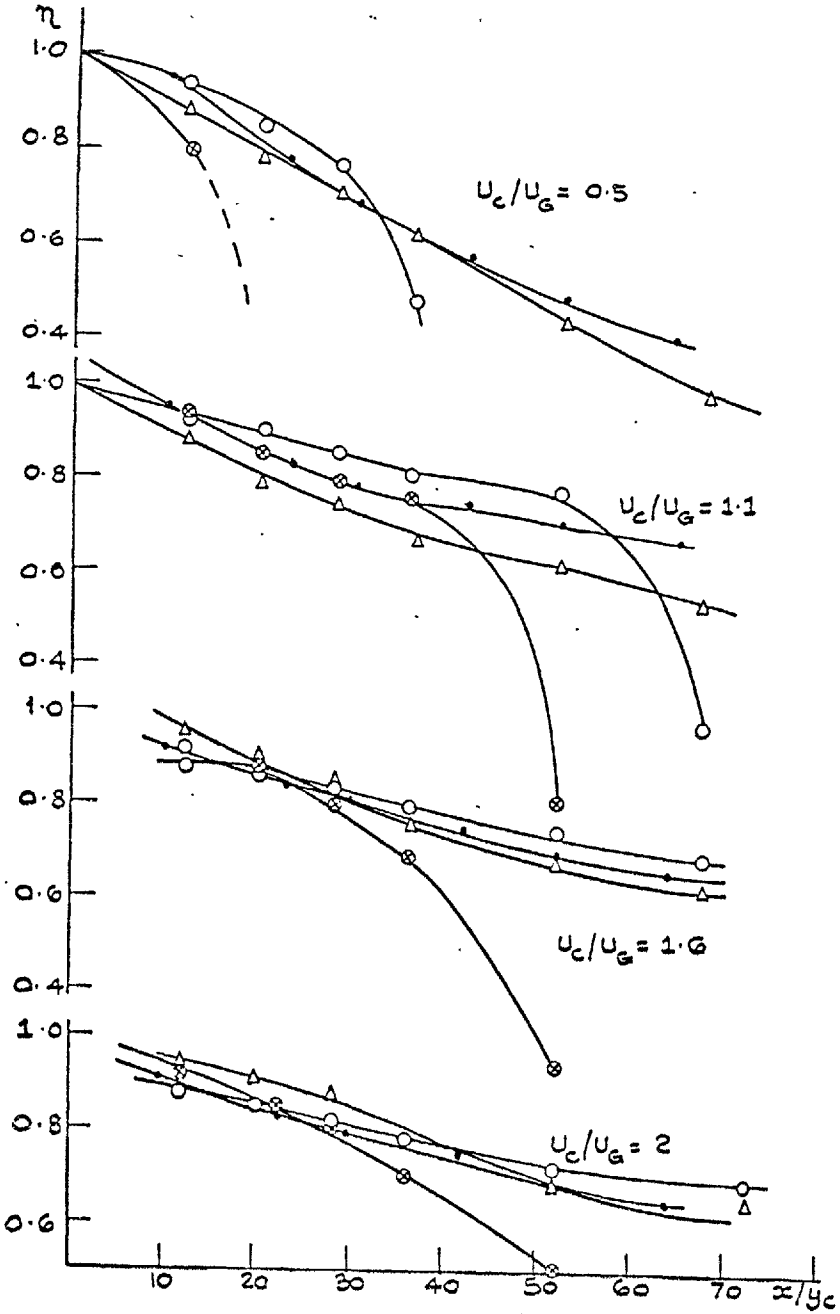

FIG. 3.1.6. IMPERVIOUS WALL EFFECTIVENESS ON FLAT, CONVEX AND CONCAVE SURFACES ρ_c/ρ_G = 1.0

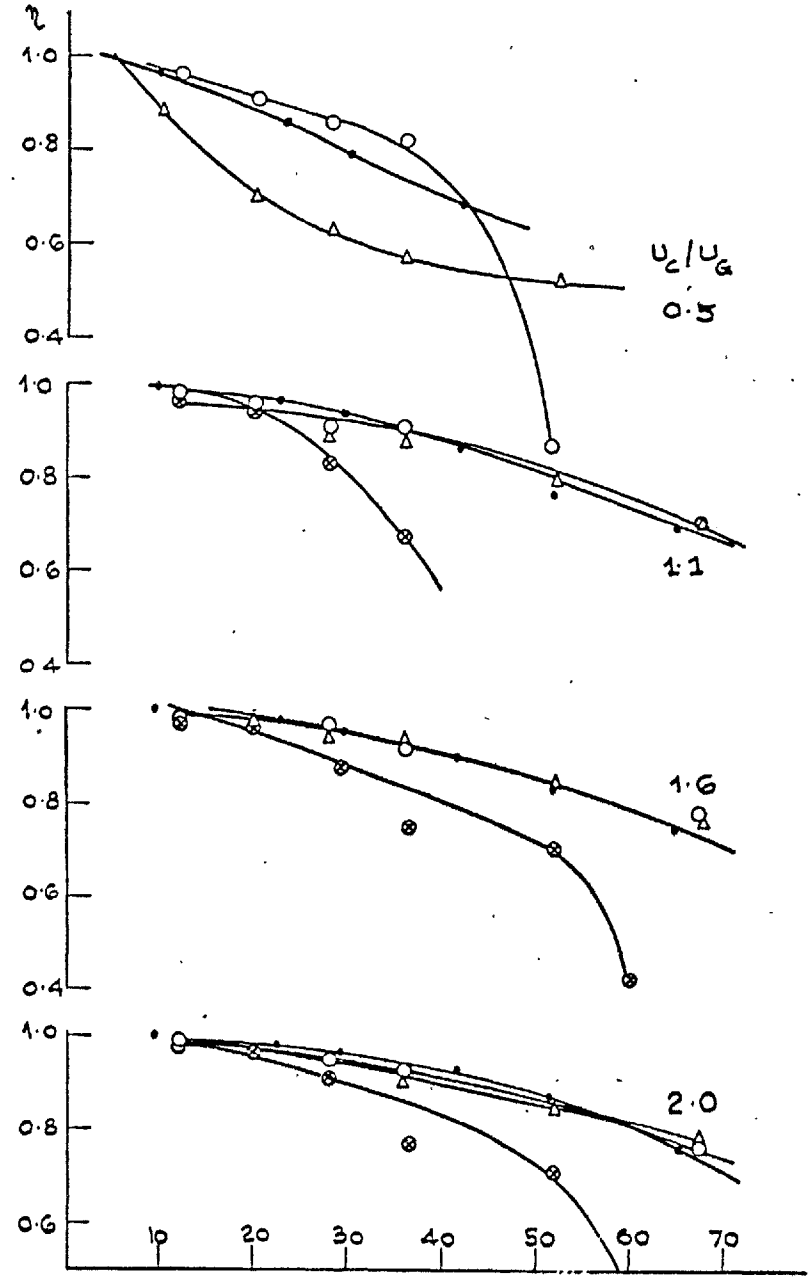

IMPERVIOUS WALL EFFECTIVENESS ON FLAT, CONVEX AND CONCAVE SURFACES ρ_c/ρ_G = 2.25

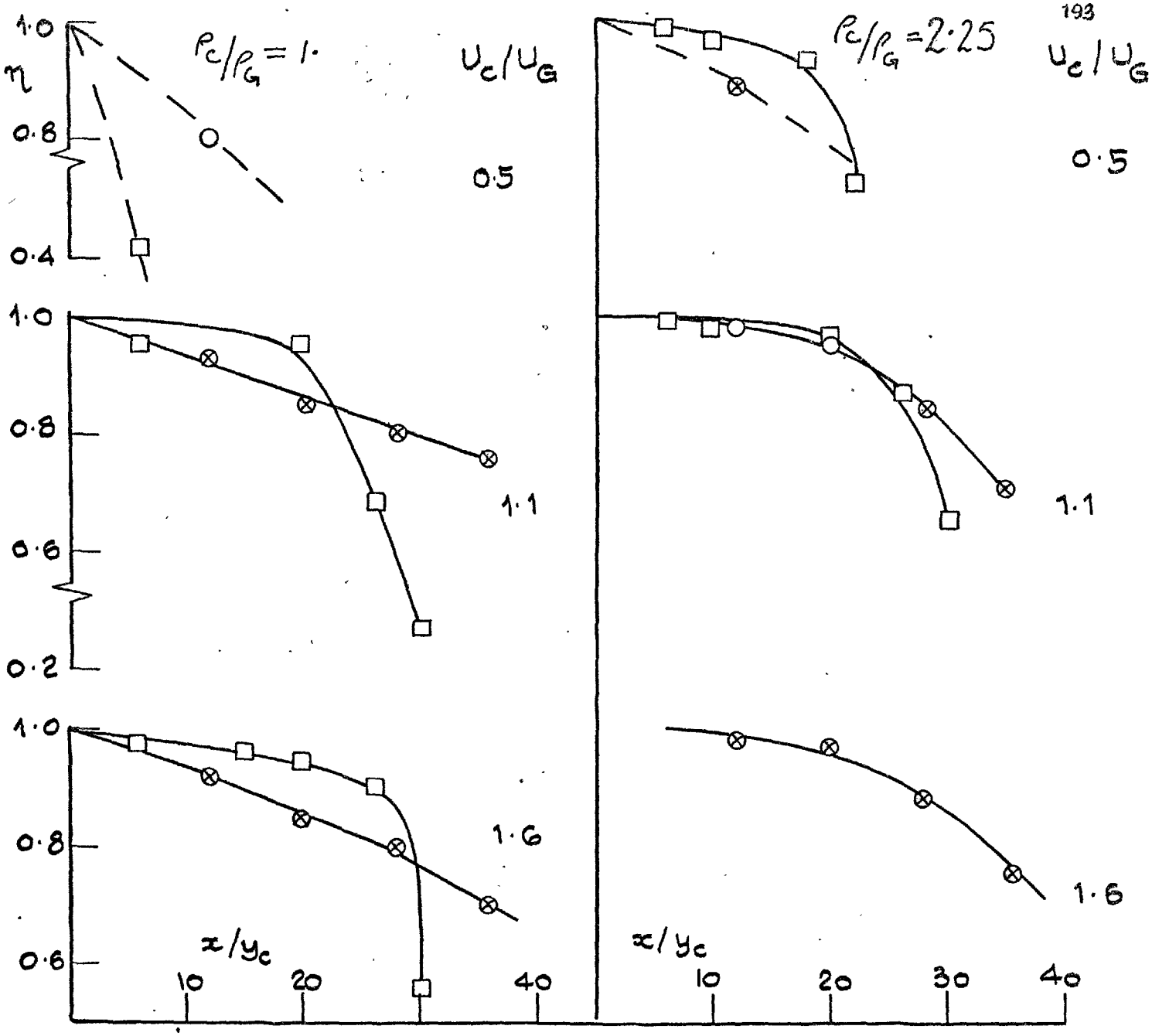

FIG. 3.1.7 INFLUENCE OF SLOT HEIGHT ON CONVEX SURFACE EFFECTIVENESS

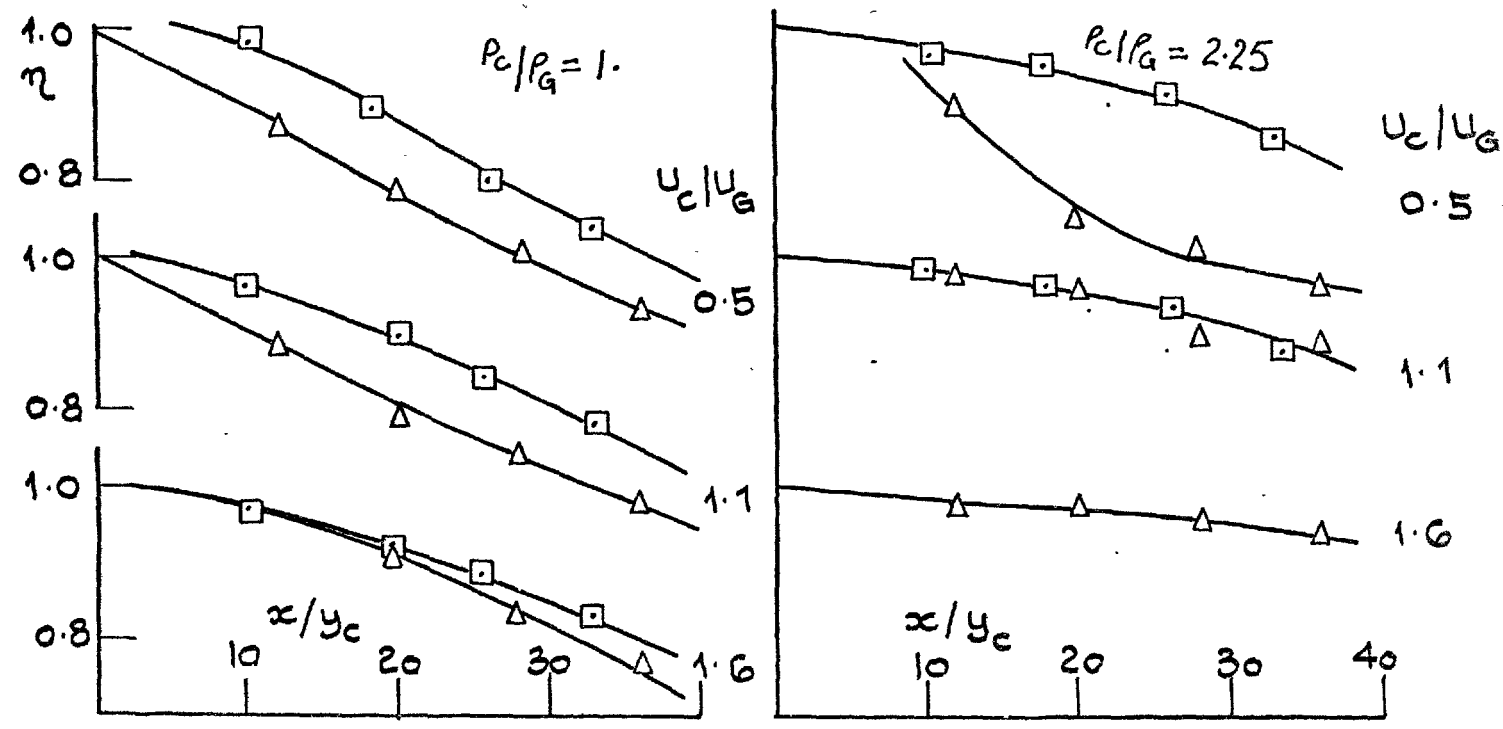

FIG. 3.1.7.b INFLUENCE OF SLOT HEIGHT ON CONCAVE SURFACE EFFECTIVENESS

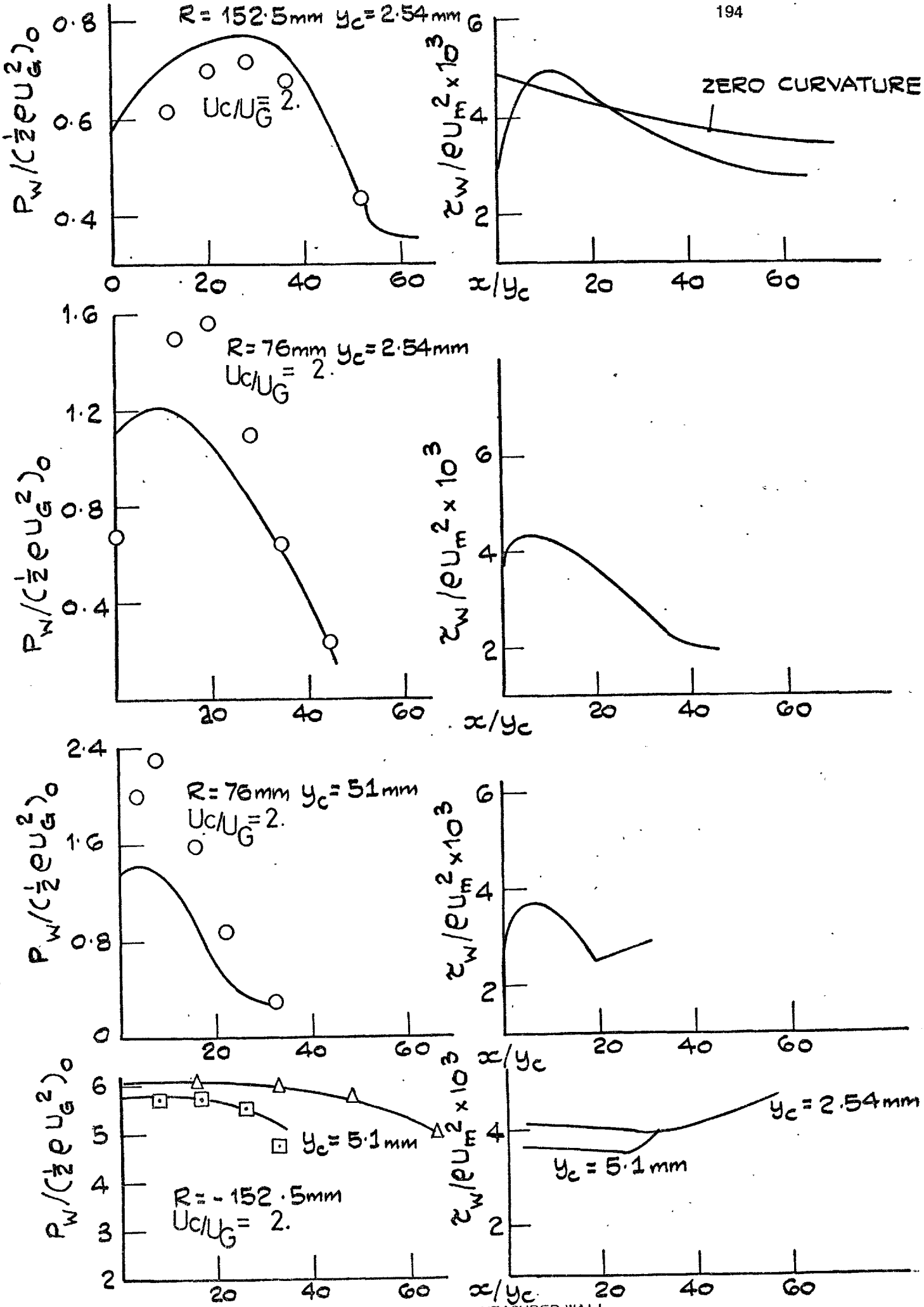

FIG. 3.2.1. COMPARISON OF CALCULATED AND MEASURED WALL

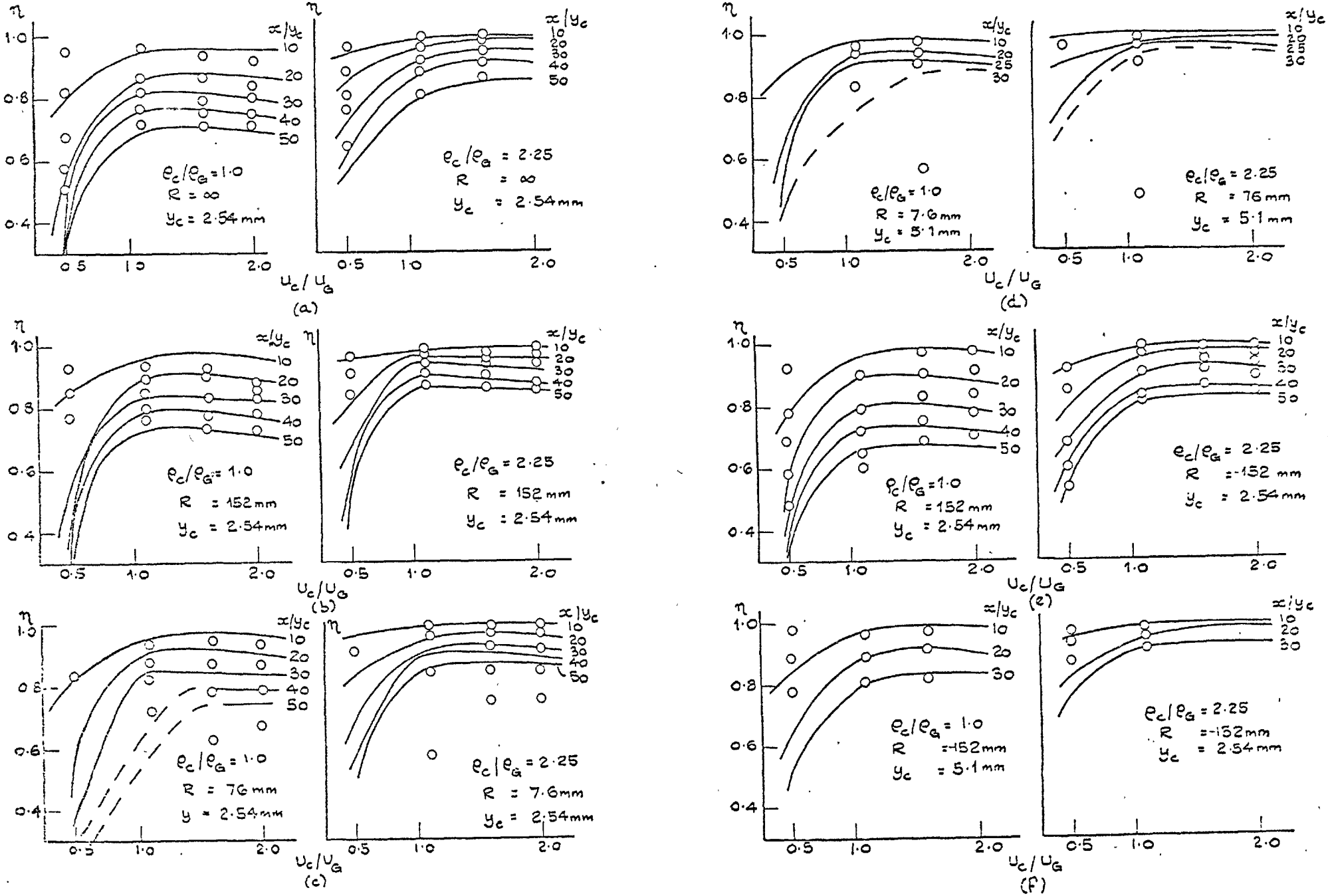

FIG. 3.2.2. COMPARISON OF MEASUREMENTS & CALCULATIONS

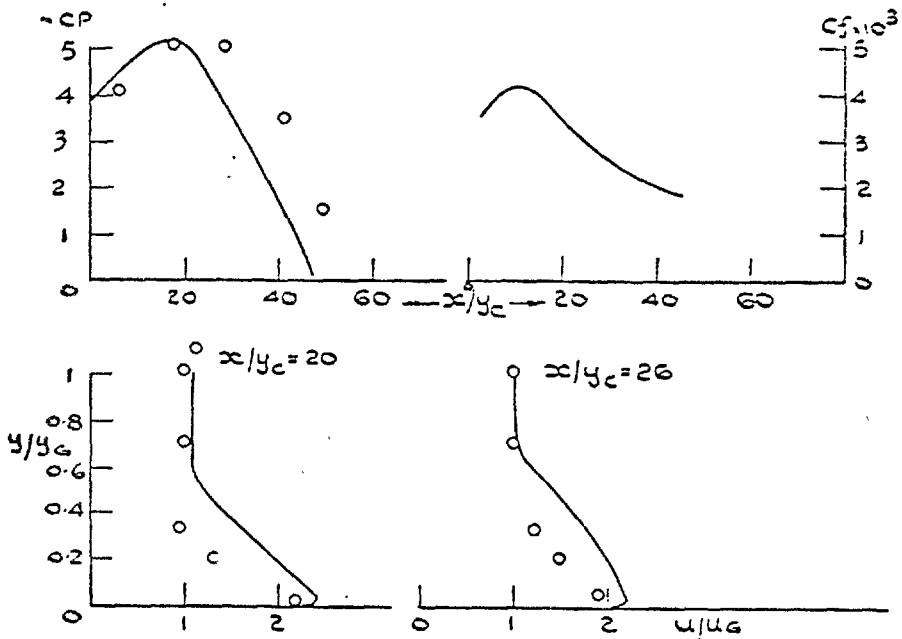

FIG. 3.2.3. COMPARISON OF CALCULATIONS AND MEASUREMENTS
(R = 0.014, yc/R = 0.031)

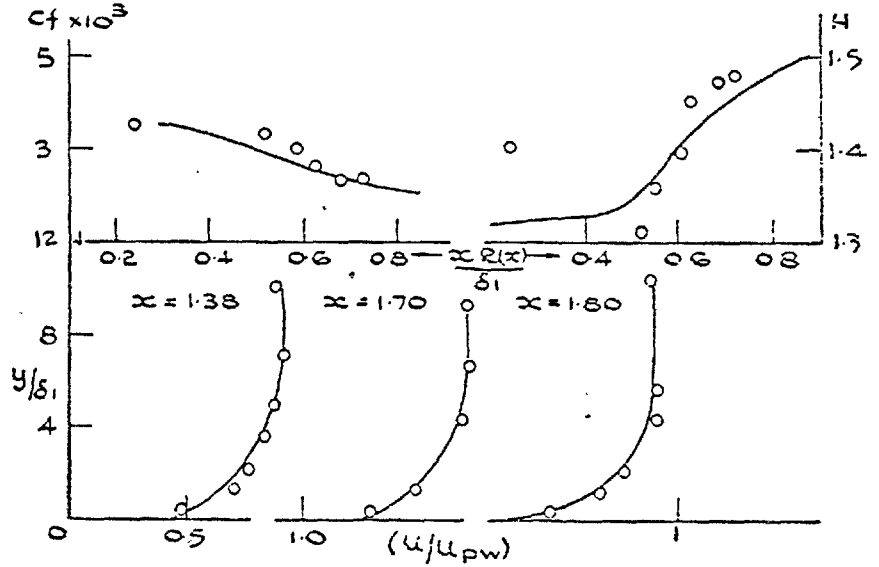

FIG. 3.2.4.. COMPARISON OF CALCULATIONS AND MEASUREMENTS
(δ_1/R = 0.01, CONVEX)

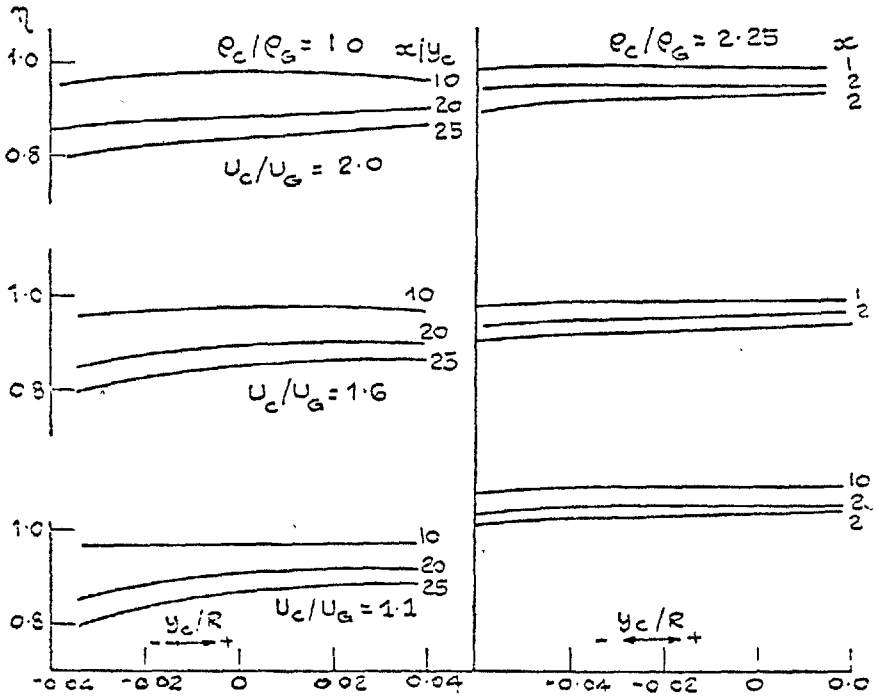

FIG. 3.2.5. CALCULATED INFLUENCE OF RADIUS OF CURVATURE

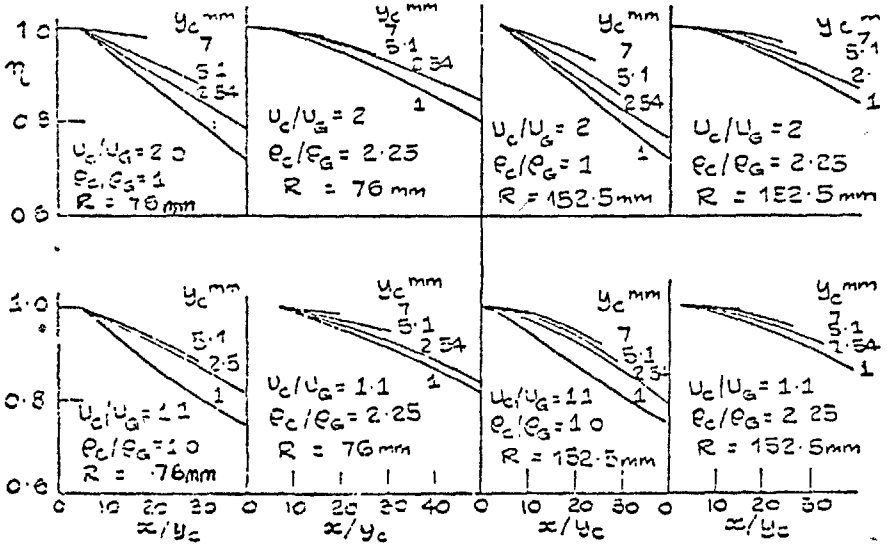

3.2.6. CALCULATED INFLUENCE OF yc

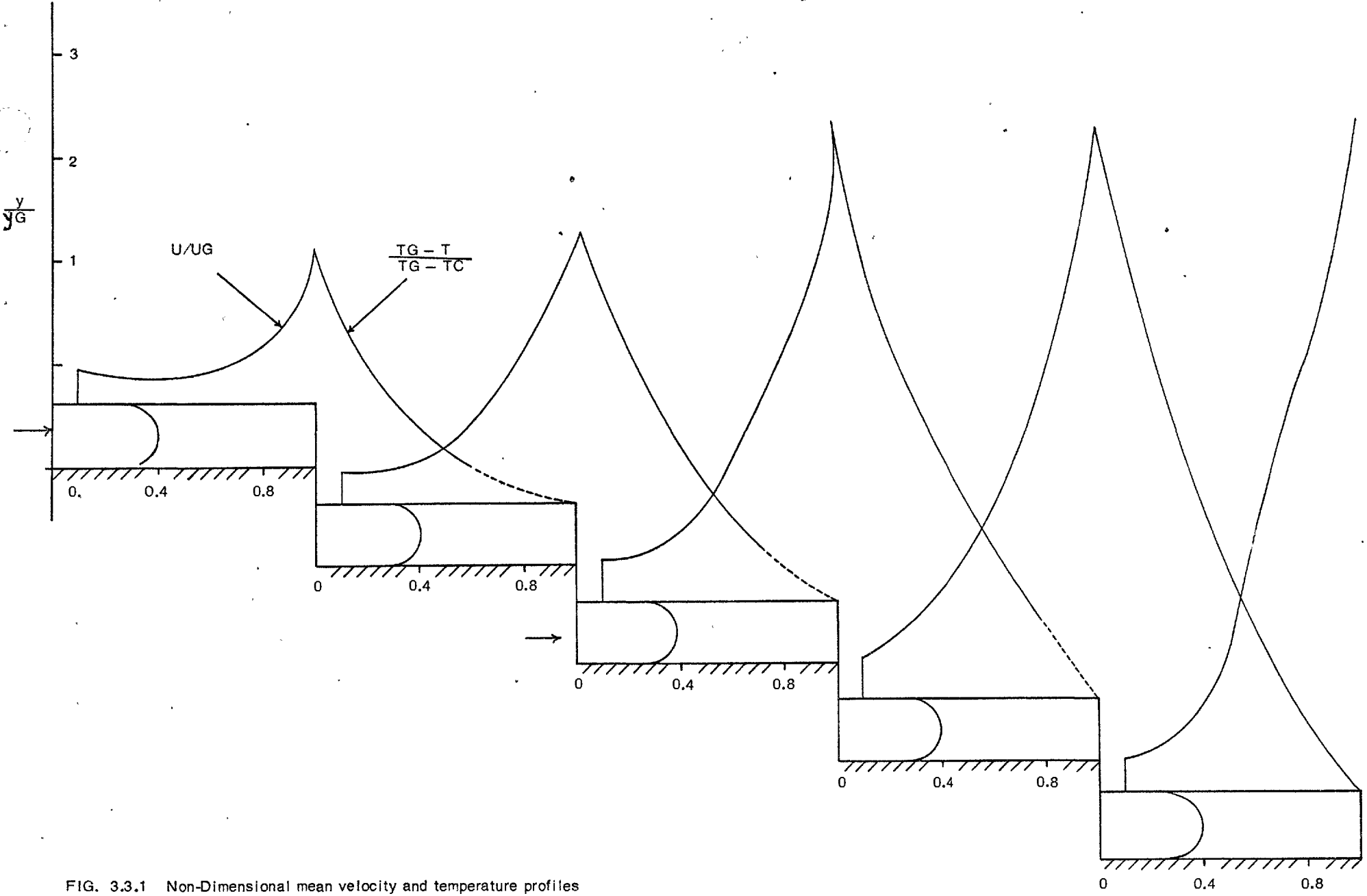

FIG. 3.3.1 Non-Dimensional mean velocity and temperature profiles

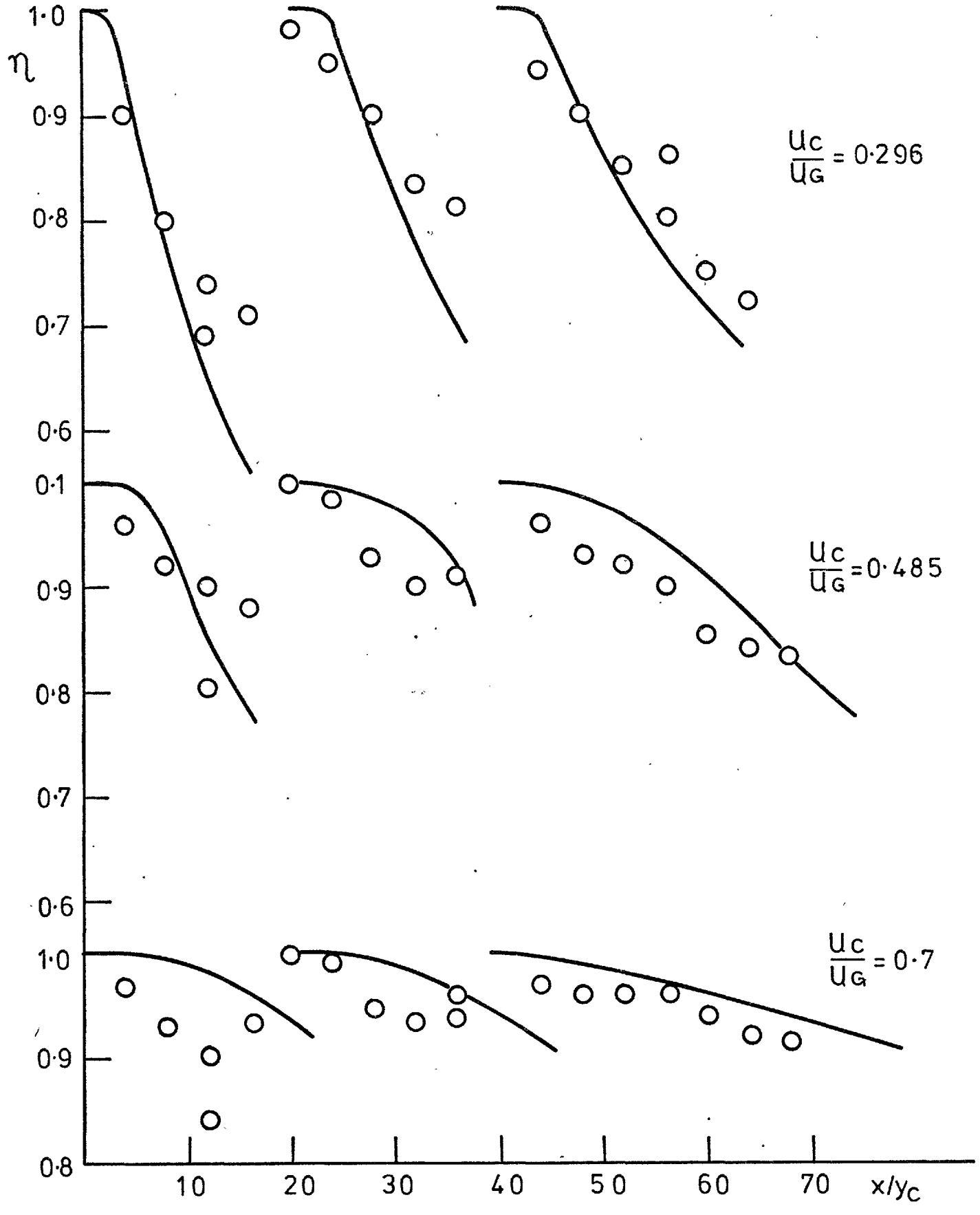

FIG. 3.3.2. COMPARISON BETWEEN MEASURED AND PREDICTED ADIABATIC WALL EFFECTIVENESS

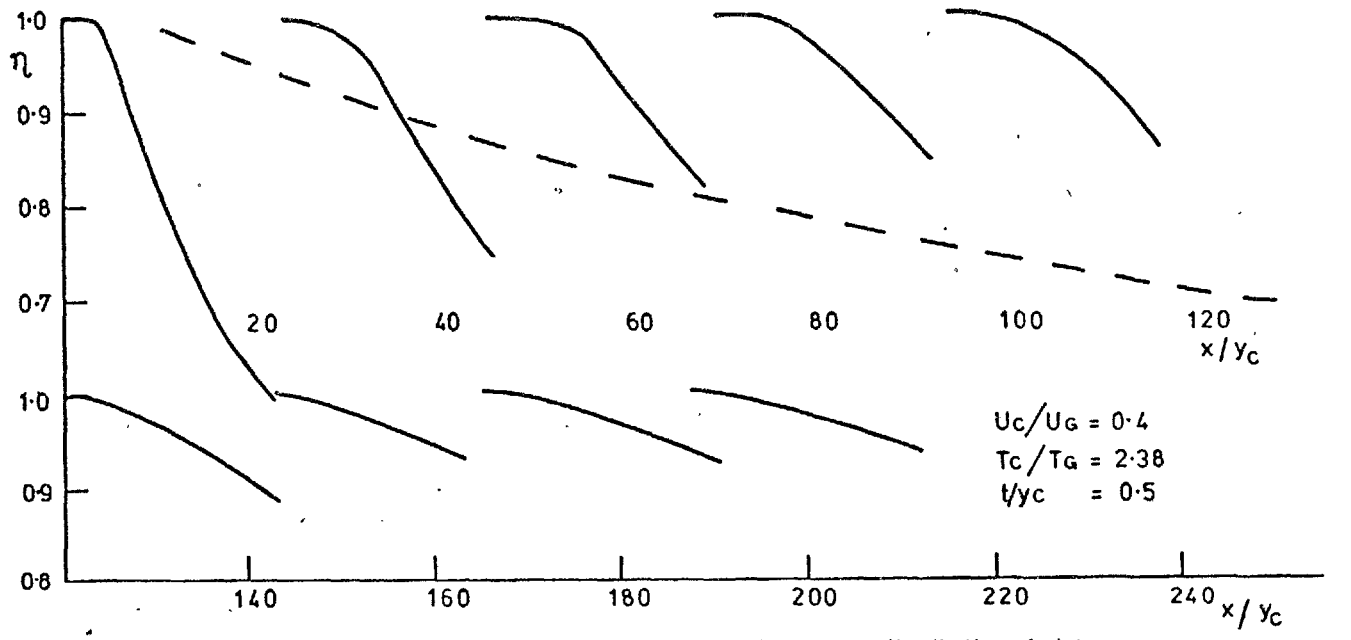

FIG. 3.3.3.a Predicted values of adiabatic wall effectiveness for an even distribution of slots

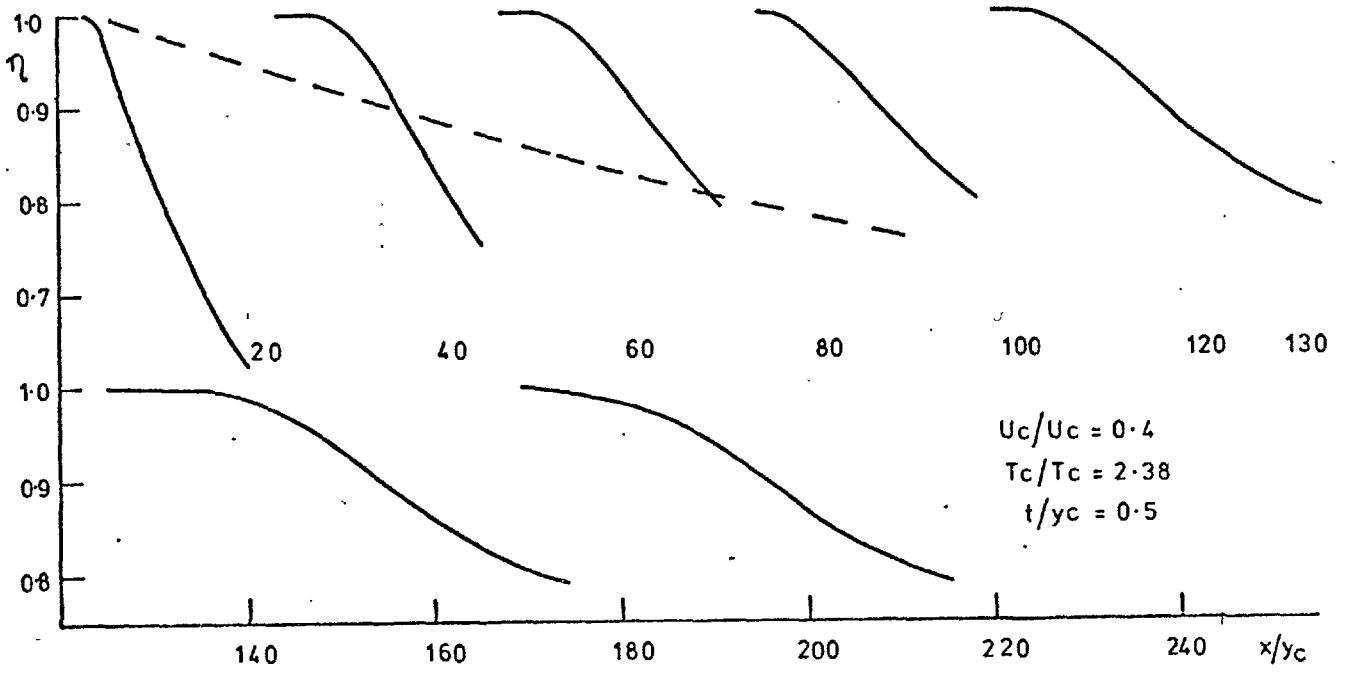

FIG. 3.3.3.b Predicted values of adiabatic wall effectiveness with slots located to provide a minimum effectiveness of 0.8

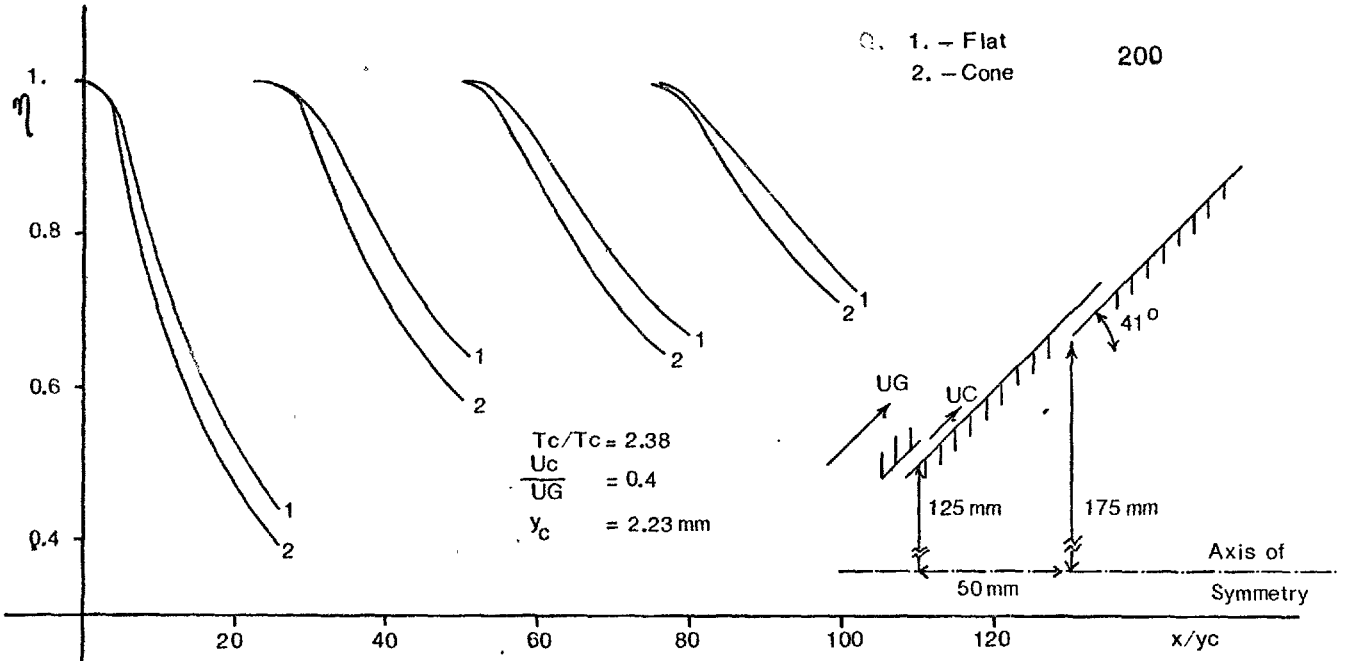

FIG. 3.4.1. Influence of film stretching at conical end

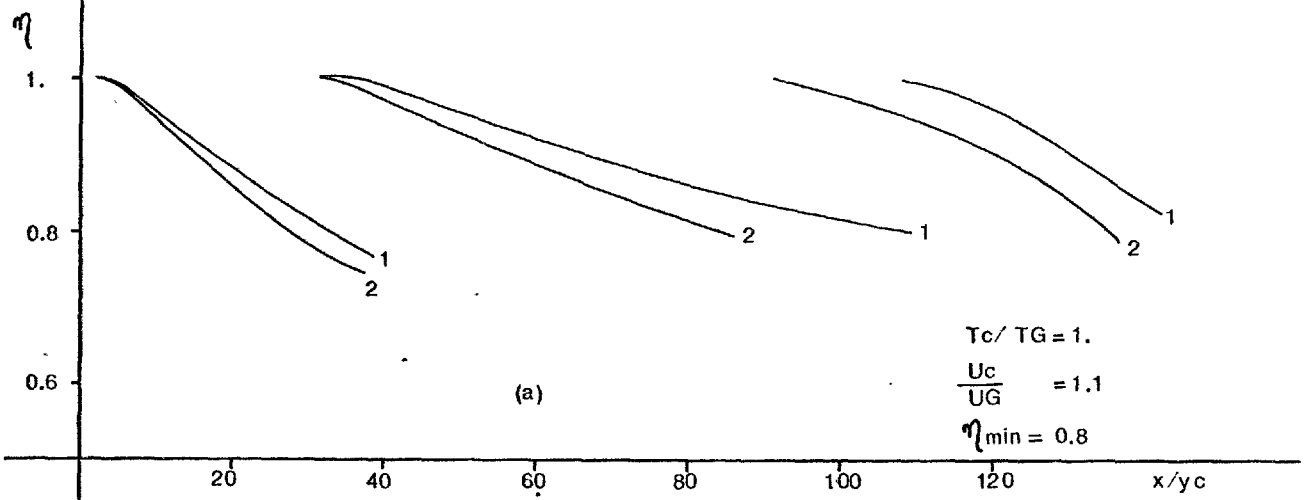

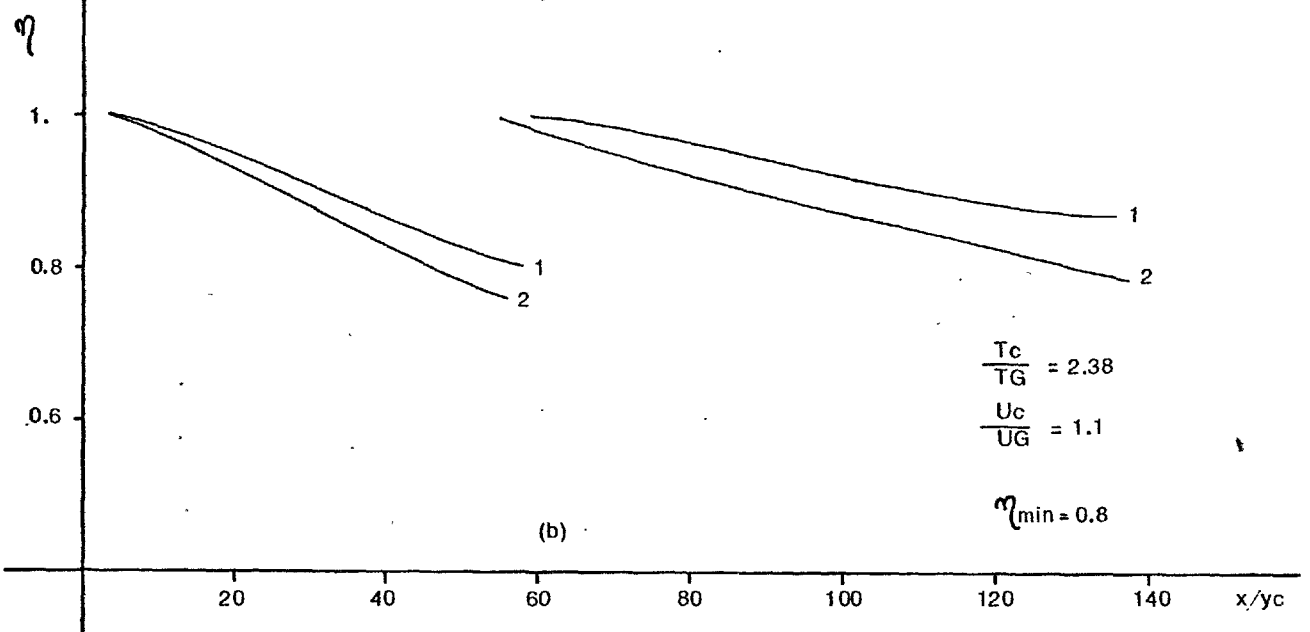

FIG. 3.4.2. Influence of density ratio on stretched film

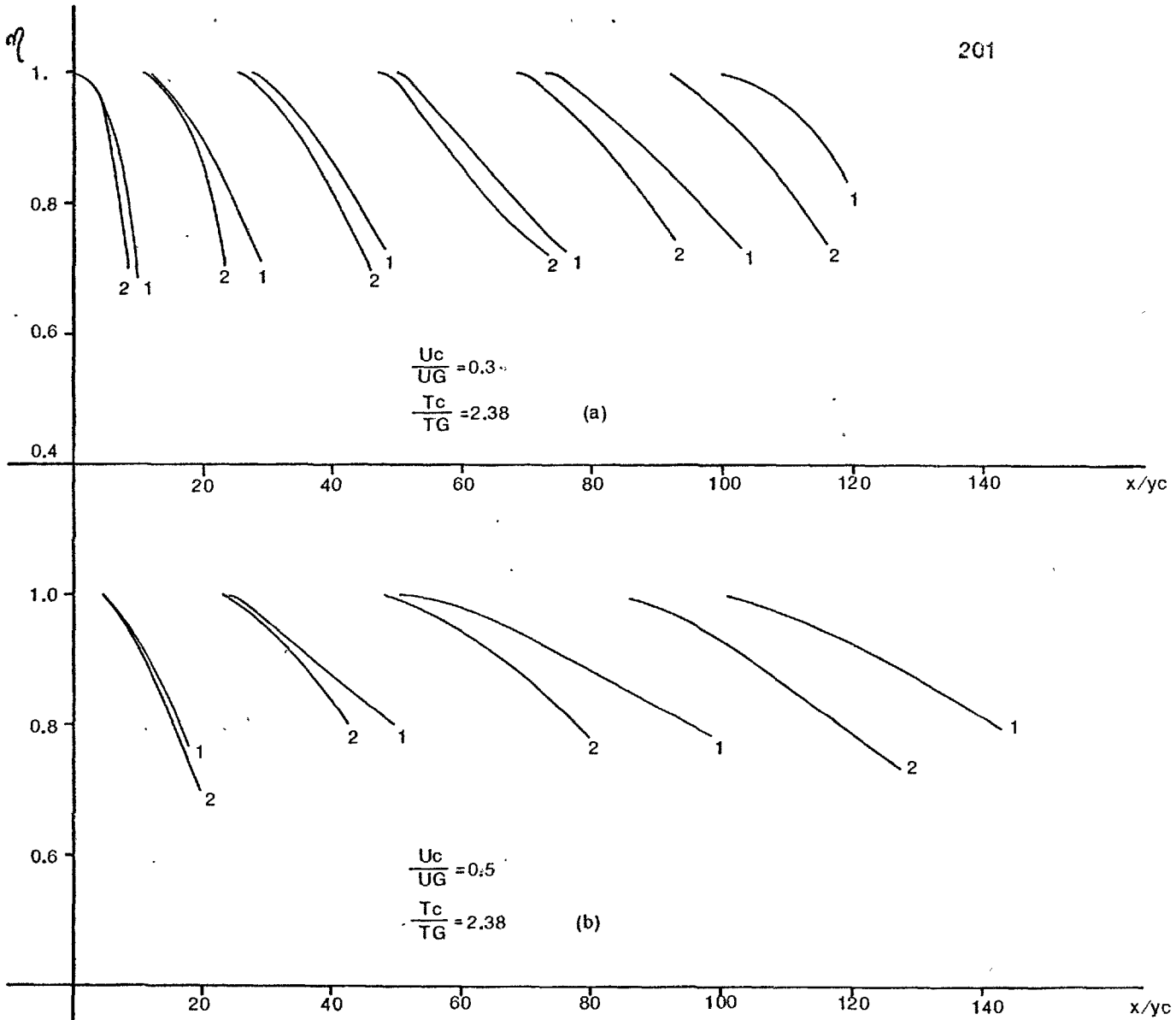

FIG. 3.4.3. Influence of velocity ratio

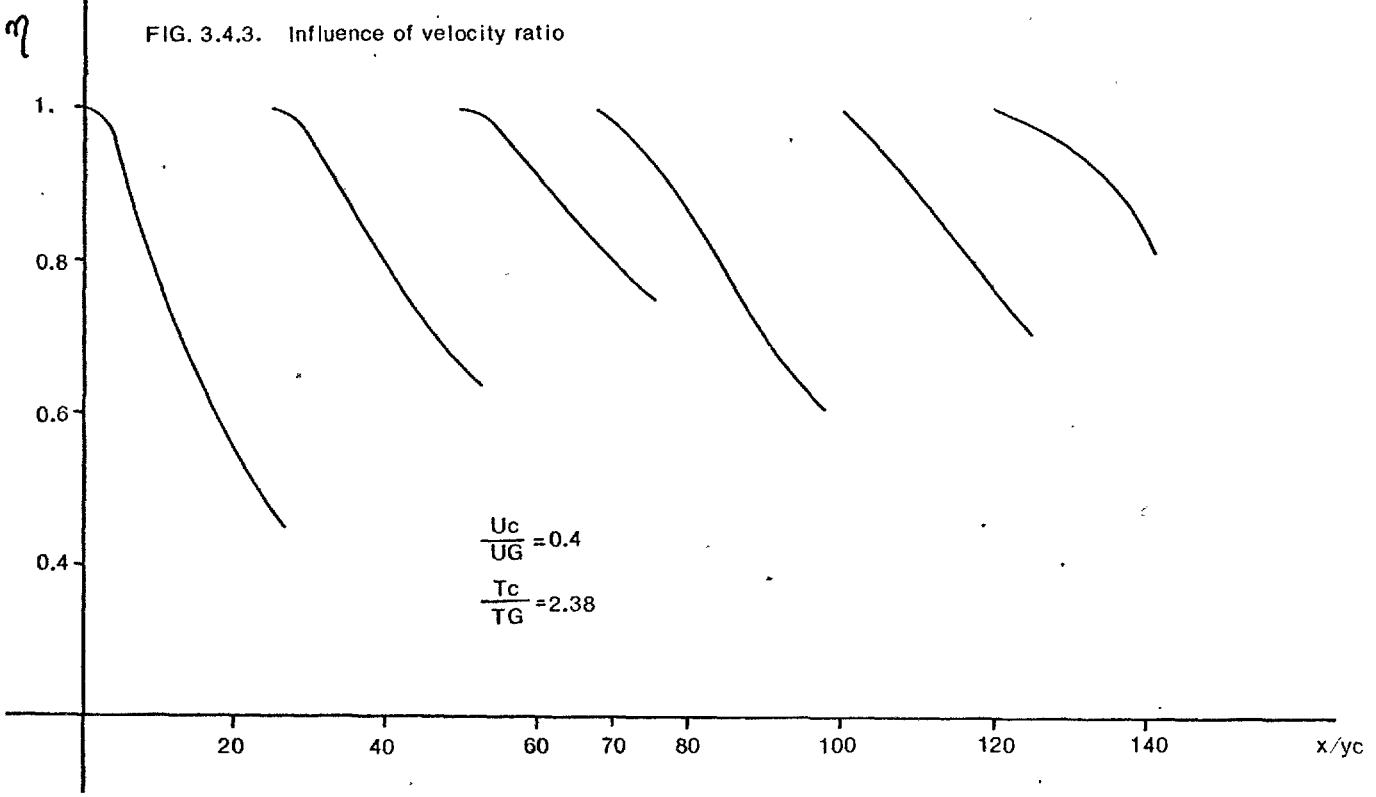

FIG. 3.4.4. Effectiveness of 3 flat and 3 flared slots

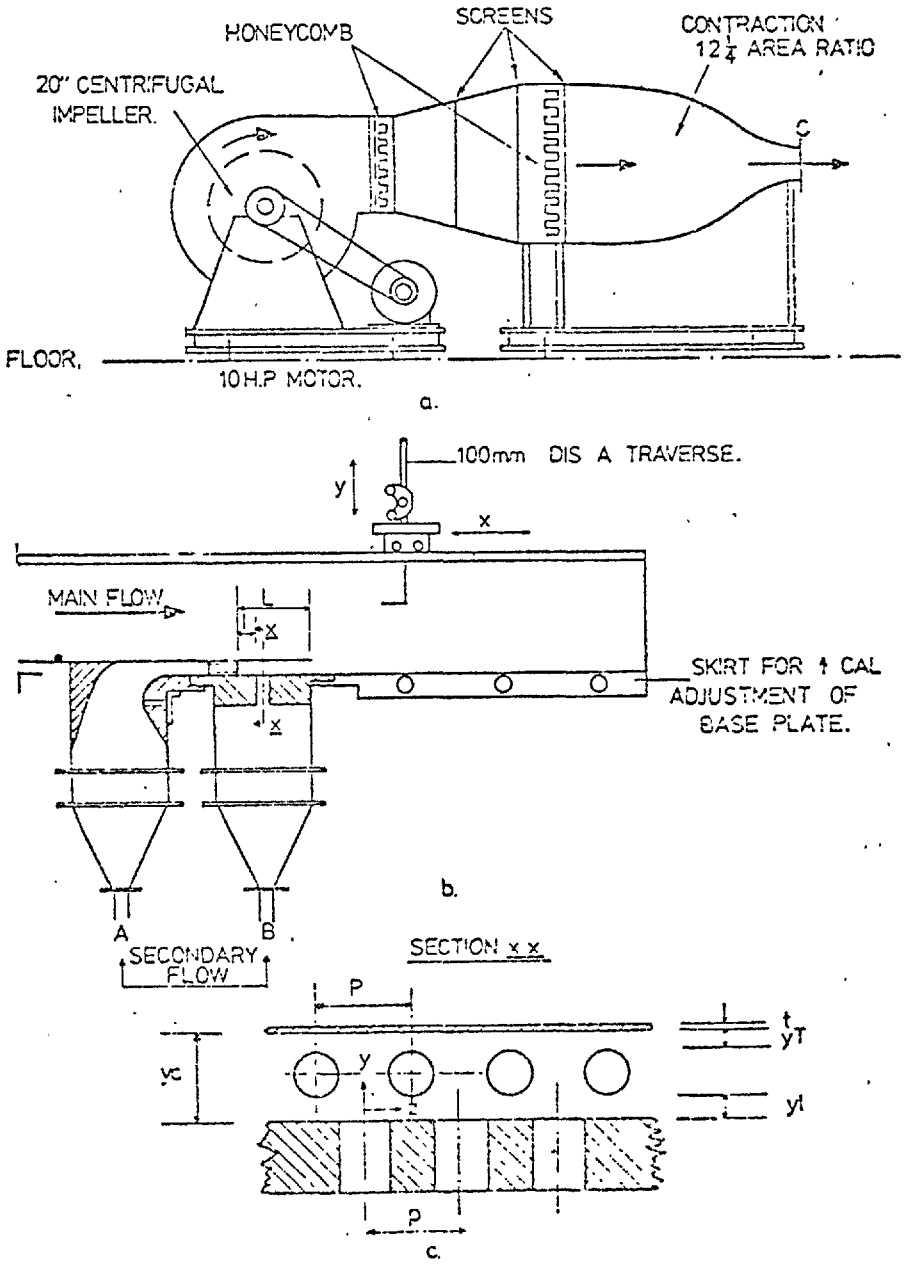

FIG. 4.1.1. FLOW CONFIGURATIONS

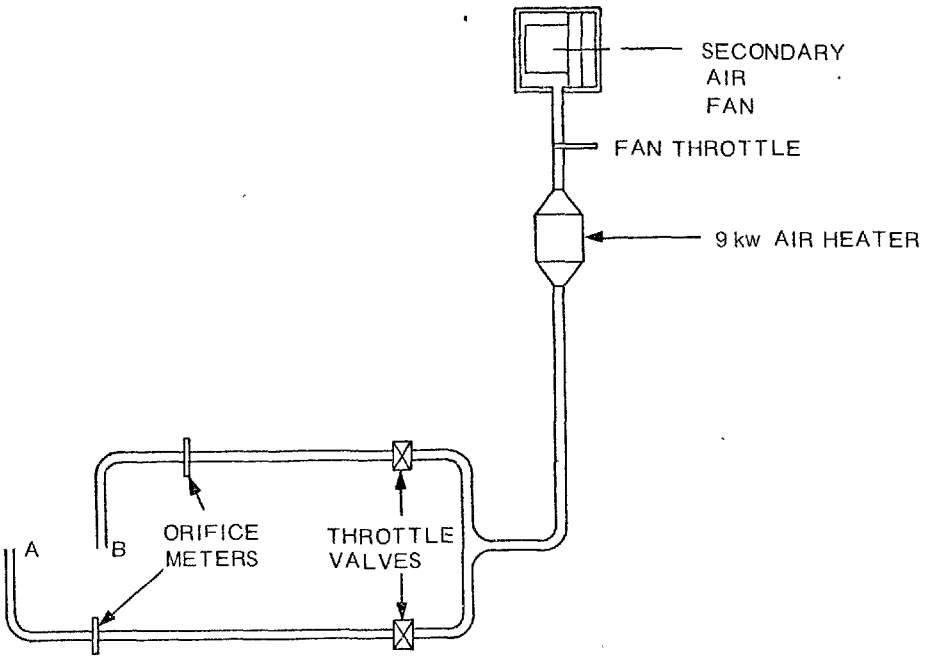

f.

Flow arrangements for heat transfer measurements

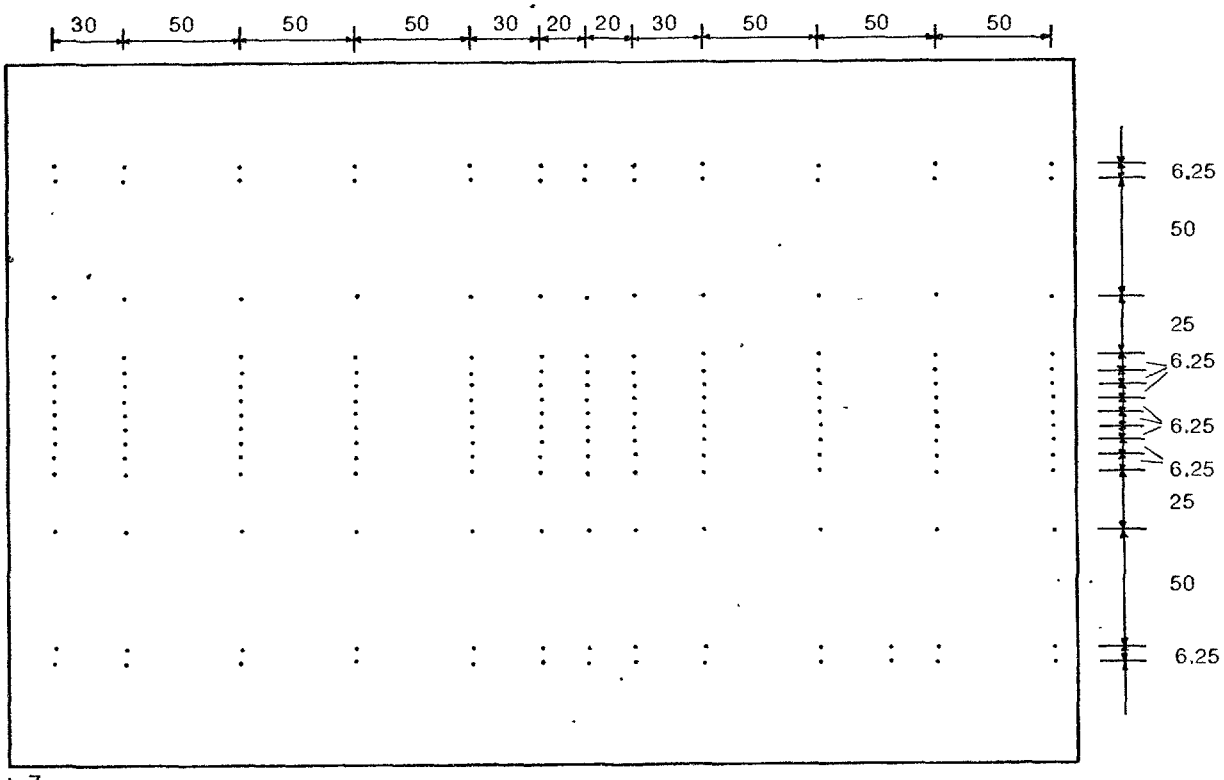

g. LAY OUT OF THERMO COUPLES ON HEAT TRANSFER PLATE

All dimensions in mm.

FIG. 4.1.1 Flow Configurations.

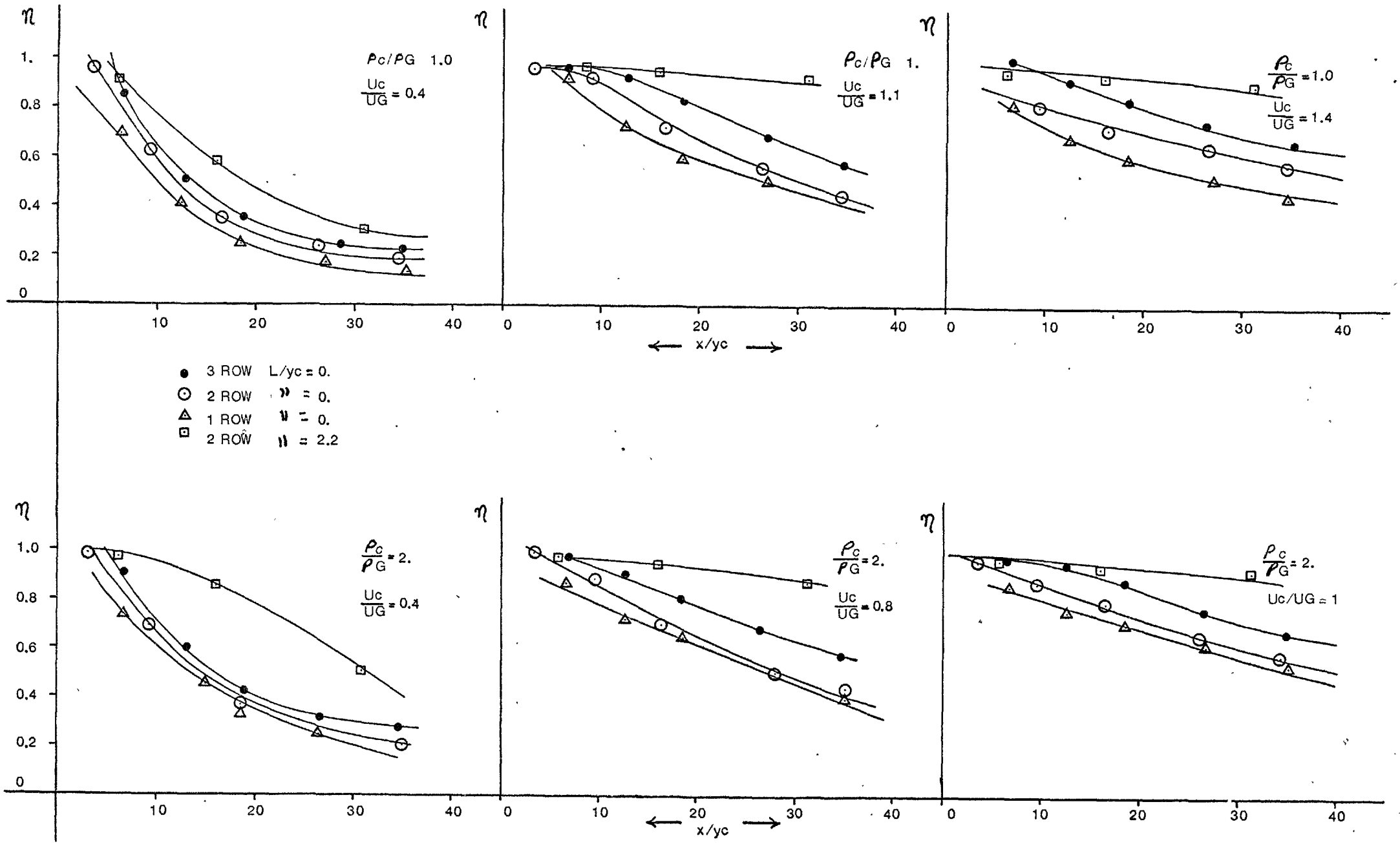

FIG. 4.2.1. Influence of number of rows on effectiveness of tangential holes.

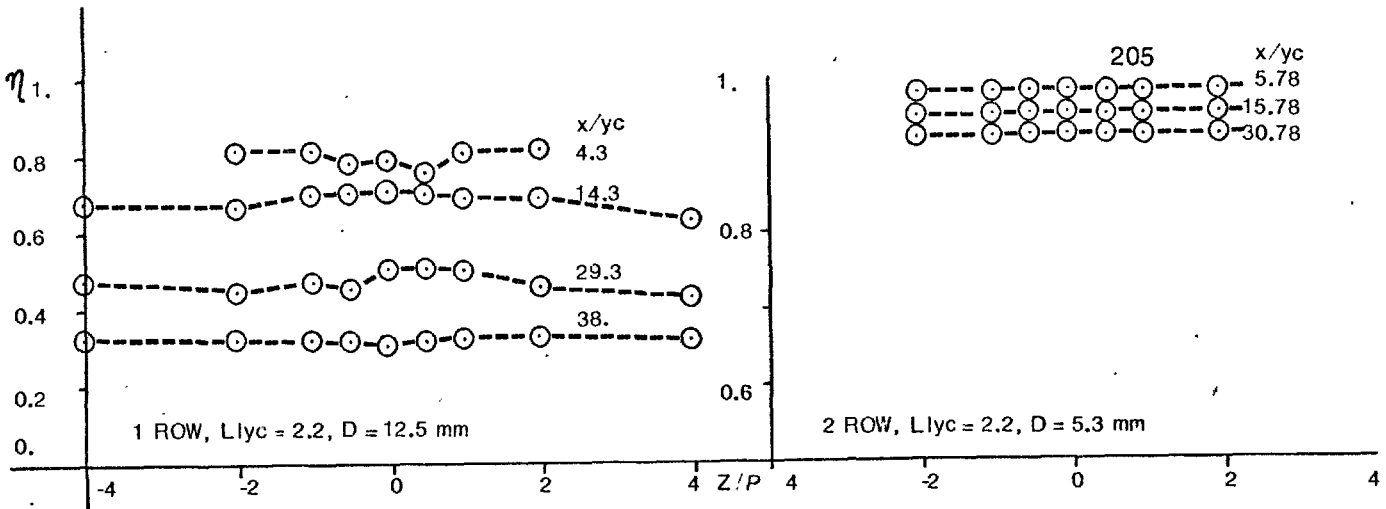

FIG. 4.2.2. x - stream effectiveness distributions.

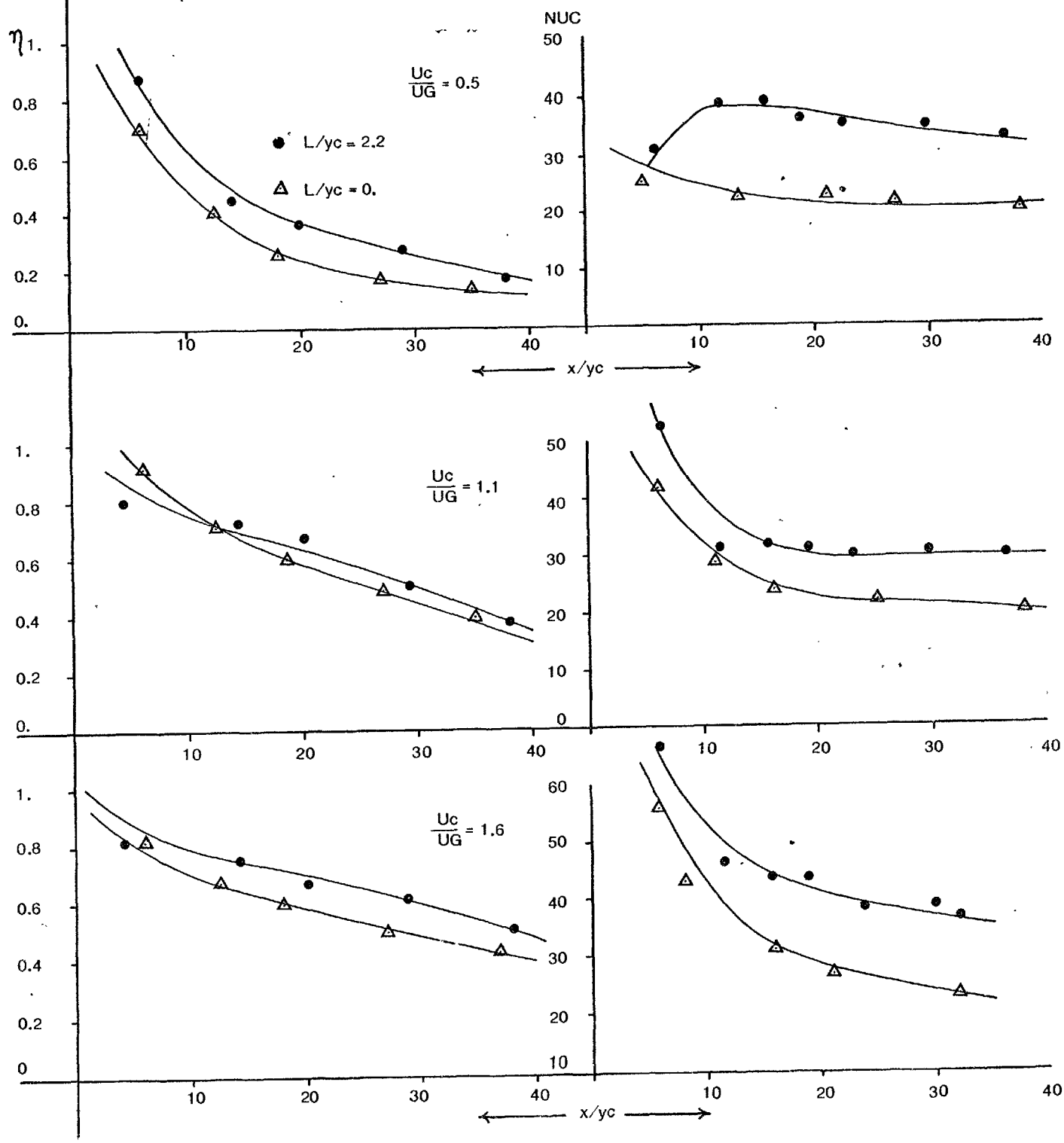

FIG. 4.2.3. Influence of lip length on efectiveness and heat transfer of tangential holes.

Experiment	P/D	D(mm)	H/D	L/D	y_c(mm)	ℓ/D	t(mm)	A_o(mm^2)	A_o/A	N	ρ_c/ρ_G	U_c/U_G
1	1.4	9	2	4.0	11	1	1.25	1530	0.458	1	1.0	0.8, 1.1, 1.6, 2.0
2	1.4	9	2	2.5	11	1	1.25	1530	0.458	1	1.0	0.8, 1.1, 1.6, 2.0
3	1.4	9	2	2.5	11	0.2	1.25	1530	0.458	1	1.0	0.8, 1.1, 1.6, 2.0
4	1.4	9	2	4.0	11	1	1.25	1530	0.458	1	2.25	0.8, 1.1, 1.6, 2.0
5	1.4	9	2	2.5	11	1	1.25	1530	0.458	1	2.25	0.8, 1.1, 1.6, 2.0
6	2.0	12.5	2	4.0	11	1	1.25	1530	0.458	1	1.0	0.8, 1.1, 1.6, 2.0
7	2.0	12.5	2	2.5	11	1	1.25	1530	0.458	1	1.0	0.8, 1.1, 1.6, 2.0
8	2.0	12.5	2	4.0	11	1	1.25	1530	0.458	1	2.25	0.8, 1.1, 1.6, 2.0
9	2.0	6.25	2	4	11	1	1.25	765	0.23	1	1.0	0.8, 1.1, 1.6, 2.0
10	2.0	6.25	2	2.5	11	1	1.25	765	0.23	1	1.0	0.8, 1.1, 1.6, 2.0
11	2.0	6.25	2	4	11	1	1.25	765	0.23	1	2.25	0.8, 1.1, 1.6, 2.0
12	2.0	6.25	2	2.5	11	1	1.25	765	0.23	1	2.25	0.8, 1.1, 1.6, 2.0
13	2.0	6.25	2	4.0	11	1	6.25	765	0.23	1	1.0	0.8, 1.1, 1.6, 2.0
14	2.0	6.25	2	4.0	11	1	1.25	1530	0.458	2	1.0	0.8, 1.1, 1.6, 2.0
15	2.0	6.25	2	2.5	11	1	1.25	1530	0.458	2	1.0	0.8, 1.1, 1.6, 2.0
16	2.0	6.25	2	4.0	6.25	1	1.25	765	0.40	1	1.0	0.8, 1.1, 1.6, 2.0

TABLE 4.2.2

Values of parameters for which measurements of effectiveness were obtained for for normal injection slots.

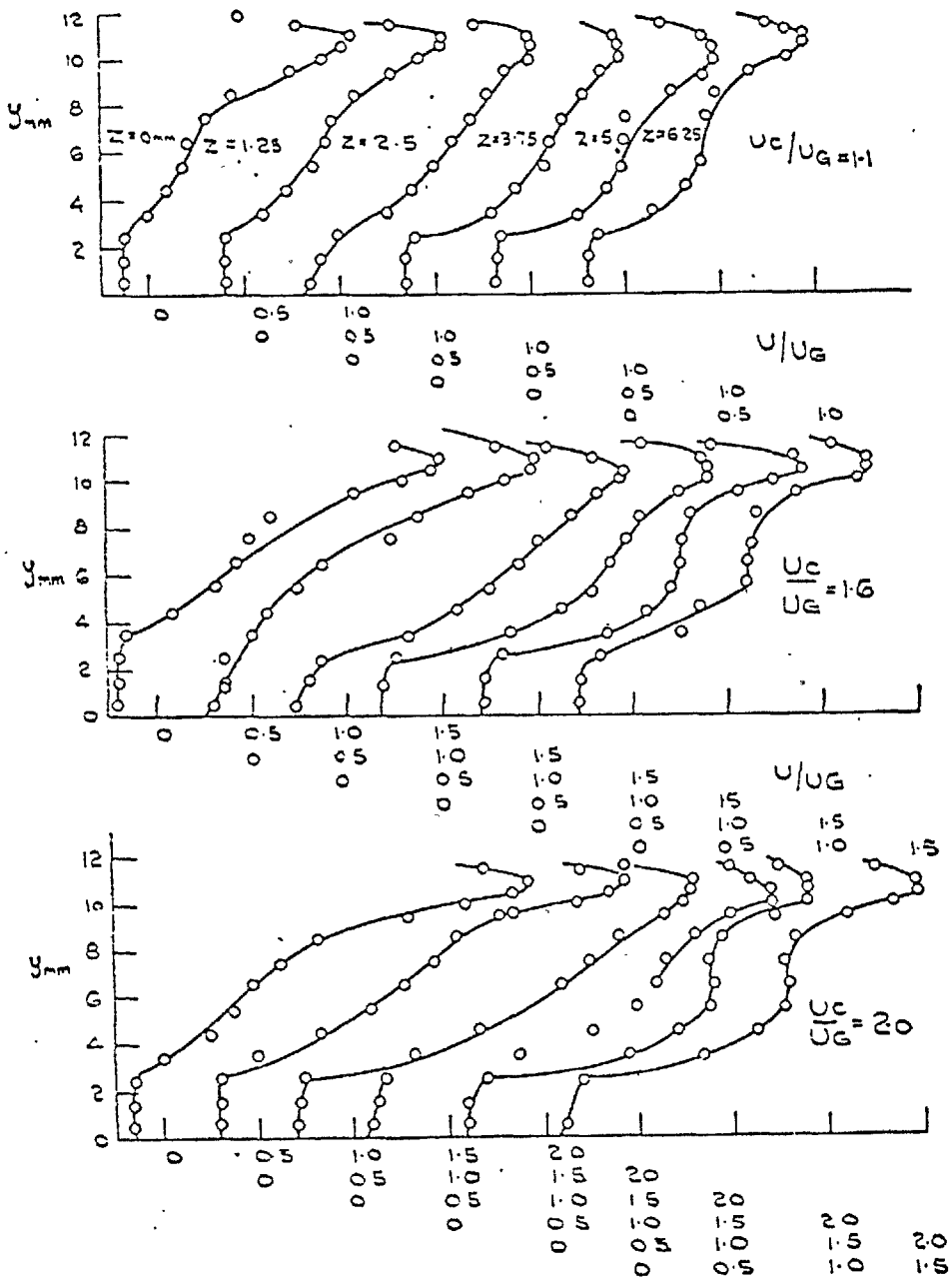

FIG. 4.2.4. MEAN VELOCITY PROFILES AT LIP EXIT EXPERIMENT 6

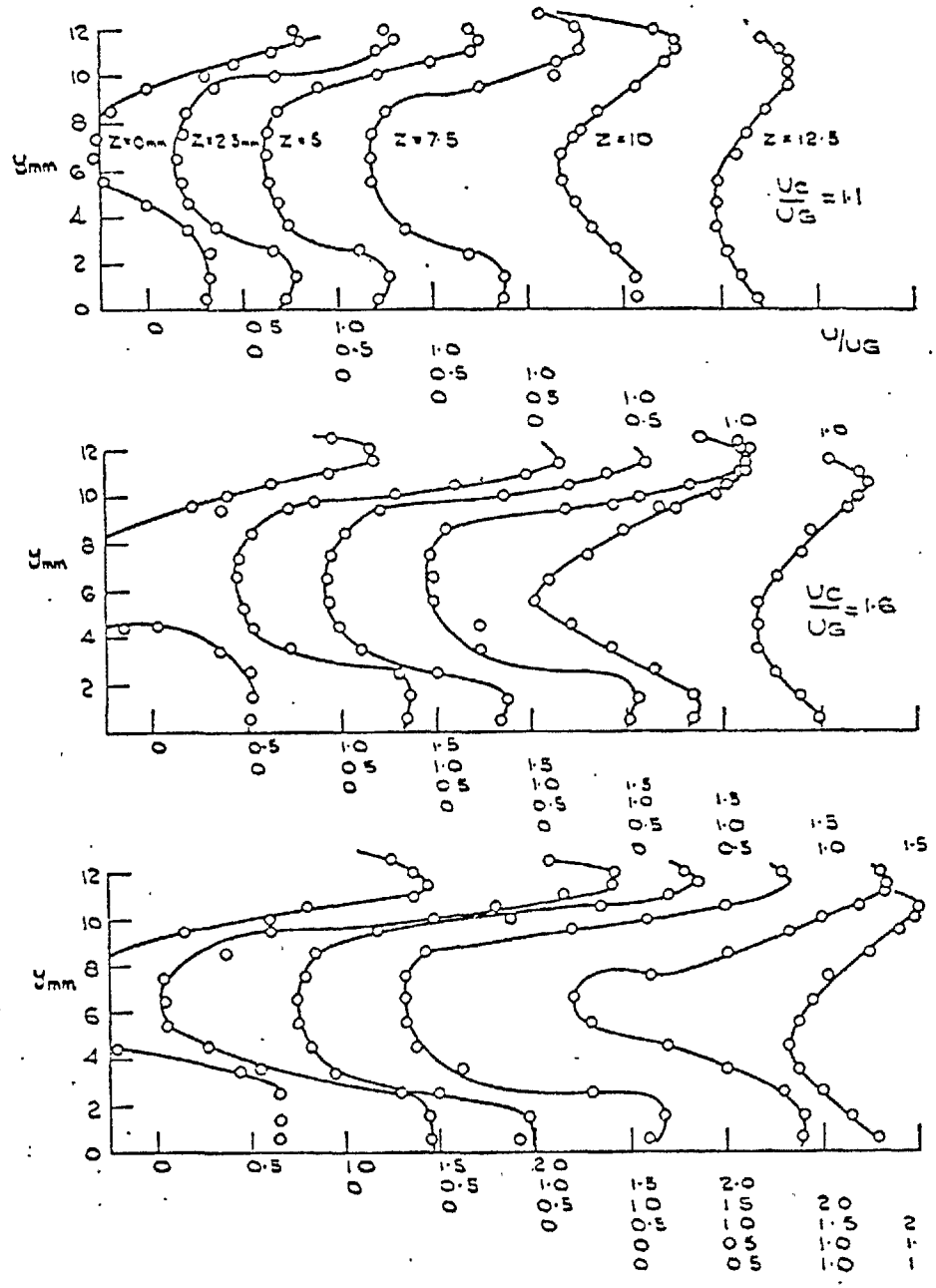

MEAN VELOCITY PROFILES AT LIP EXIT EXPERIMENT 7

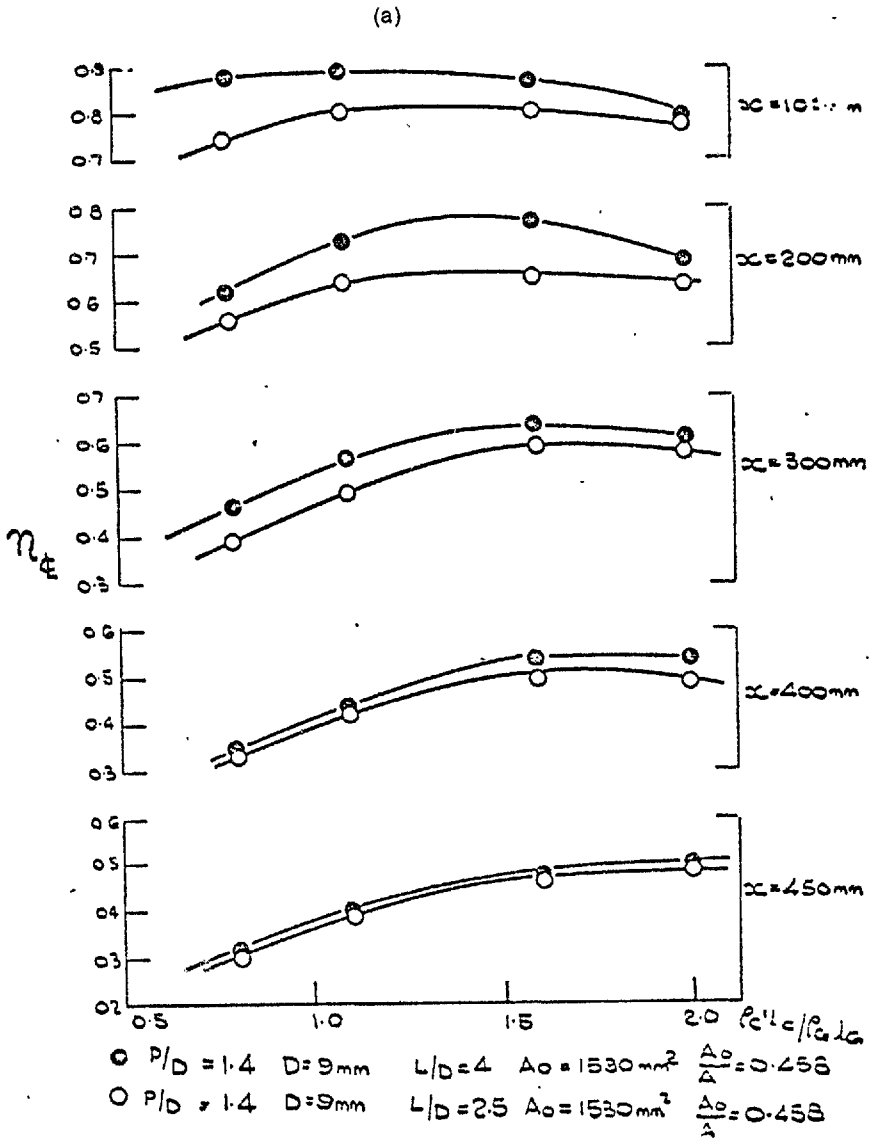

FIG. 4.2.5 INFLUENCE OF LIP LENGTH EXPERIMENTS 1 and 2

(a) Expts 1 and 2

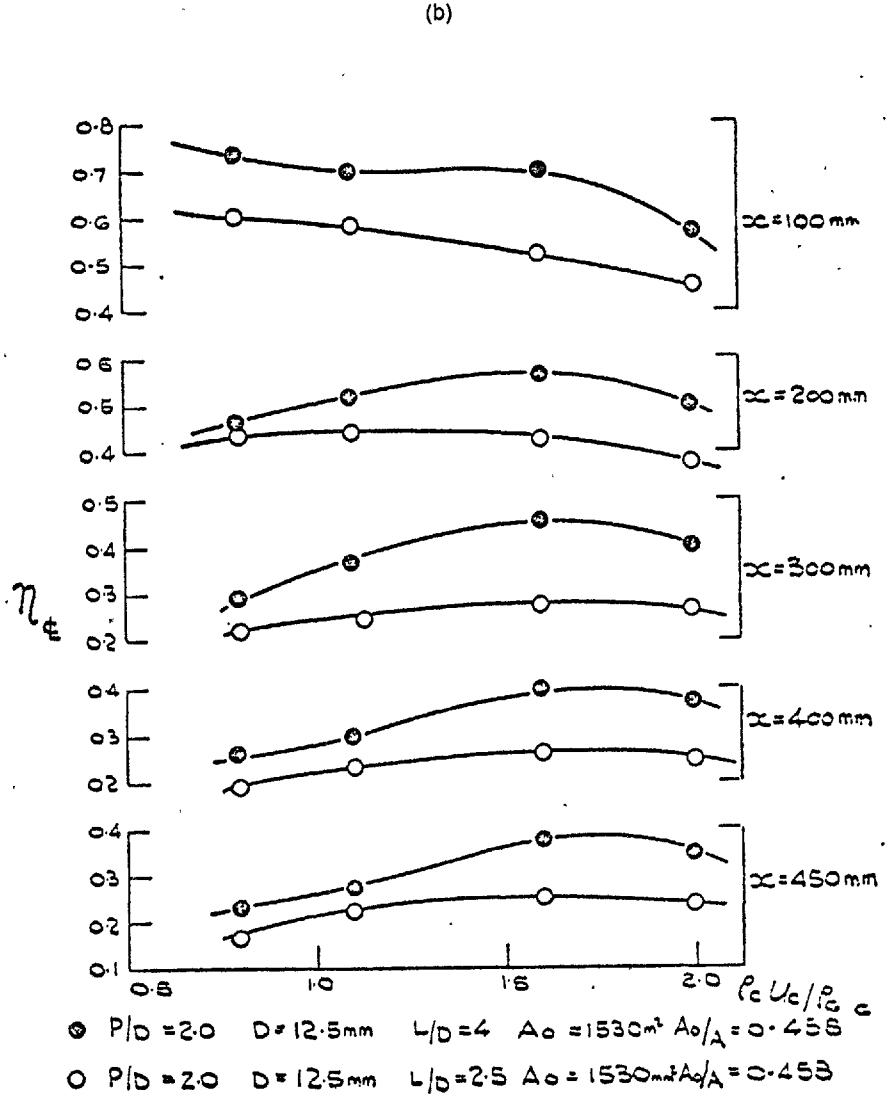

(b) Expts (6 and 7)

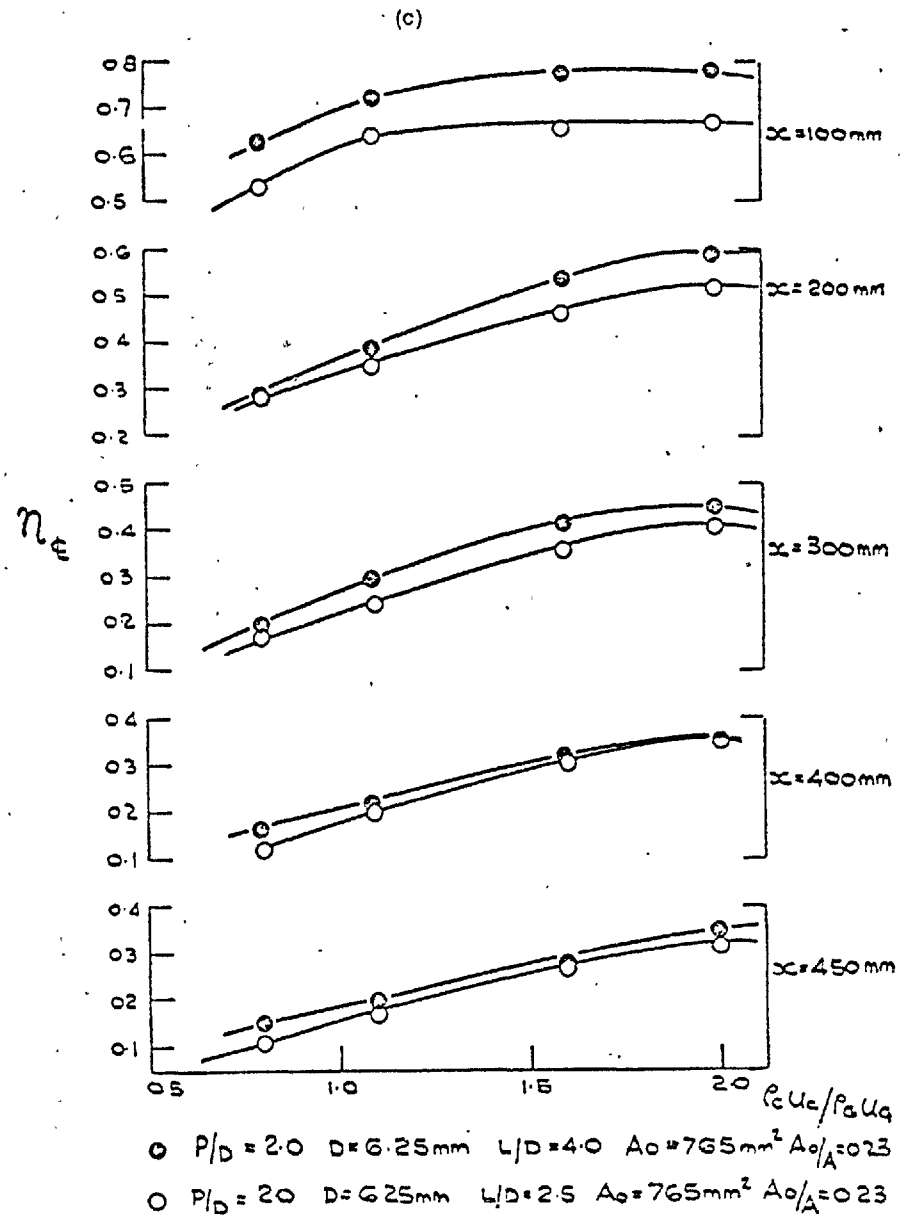

FIG. 4.2.5 INFLUENCE OF LIP LENGTH EXPERIMENTS
(c) Expts 9 & 10

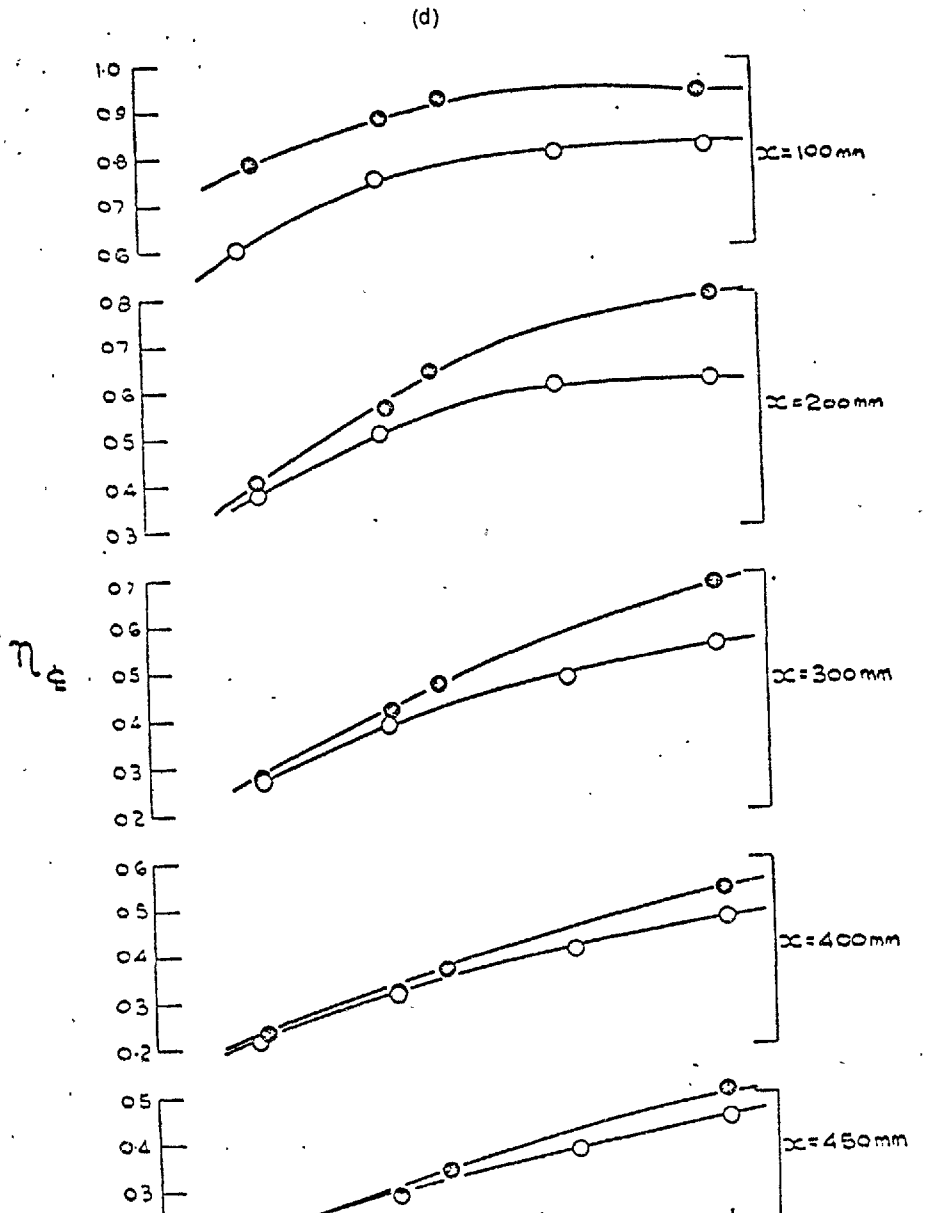

(d) Expts 4 & 5

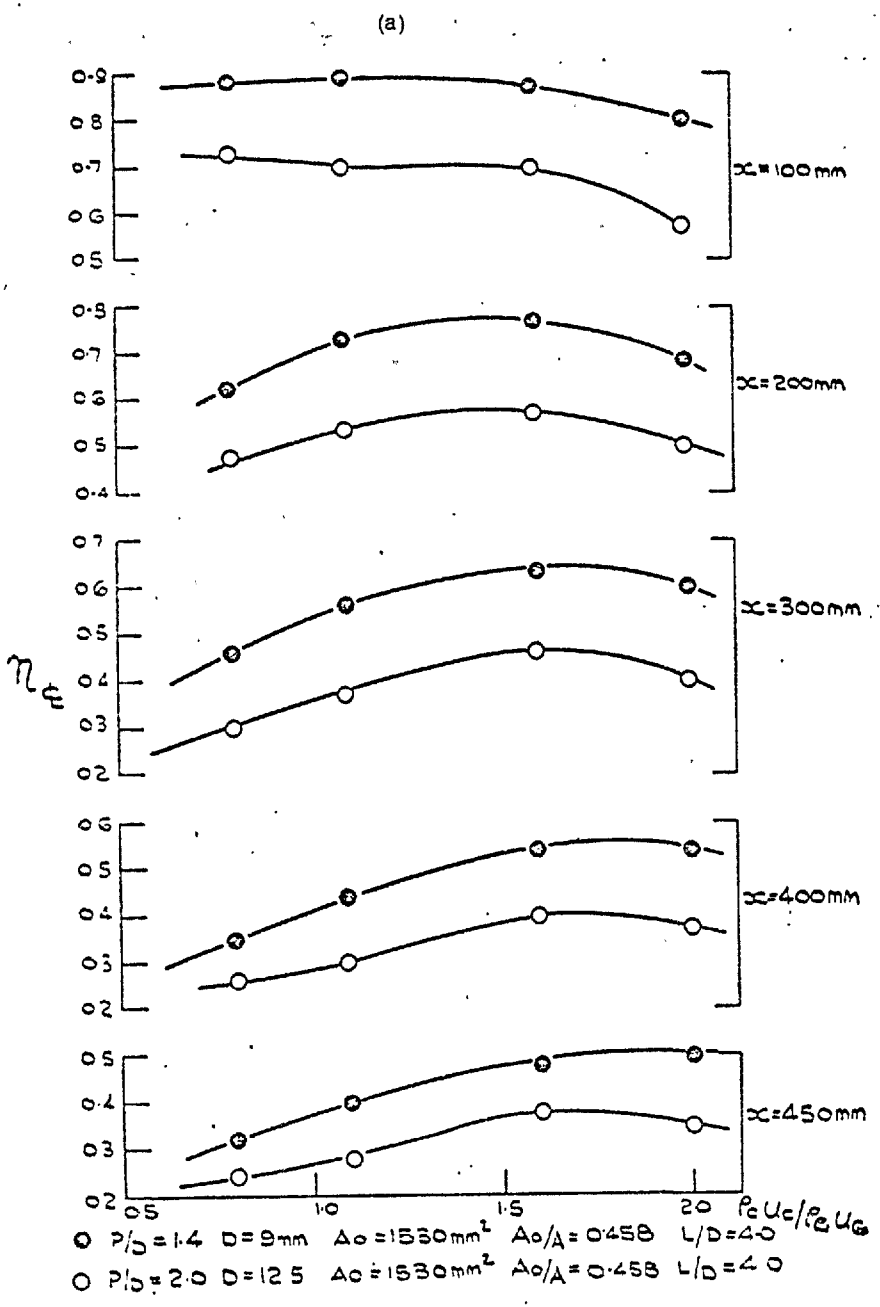

FIG. 4.2.6. INFLUENCE OF PITCH-DIAMETER RATIO:

(a) Expts 1 & 6

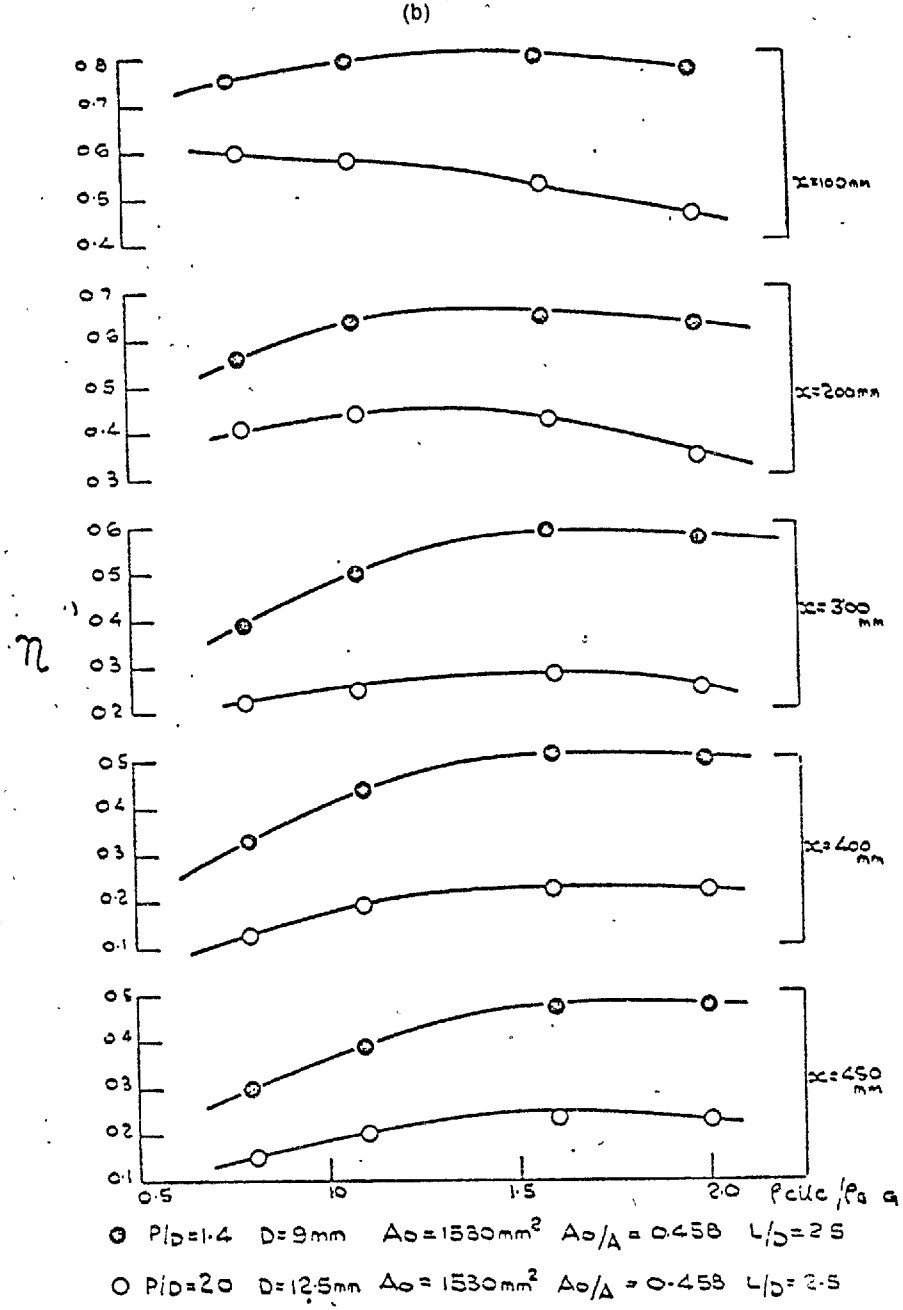

(b) Expts 2 & 7

(a)

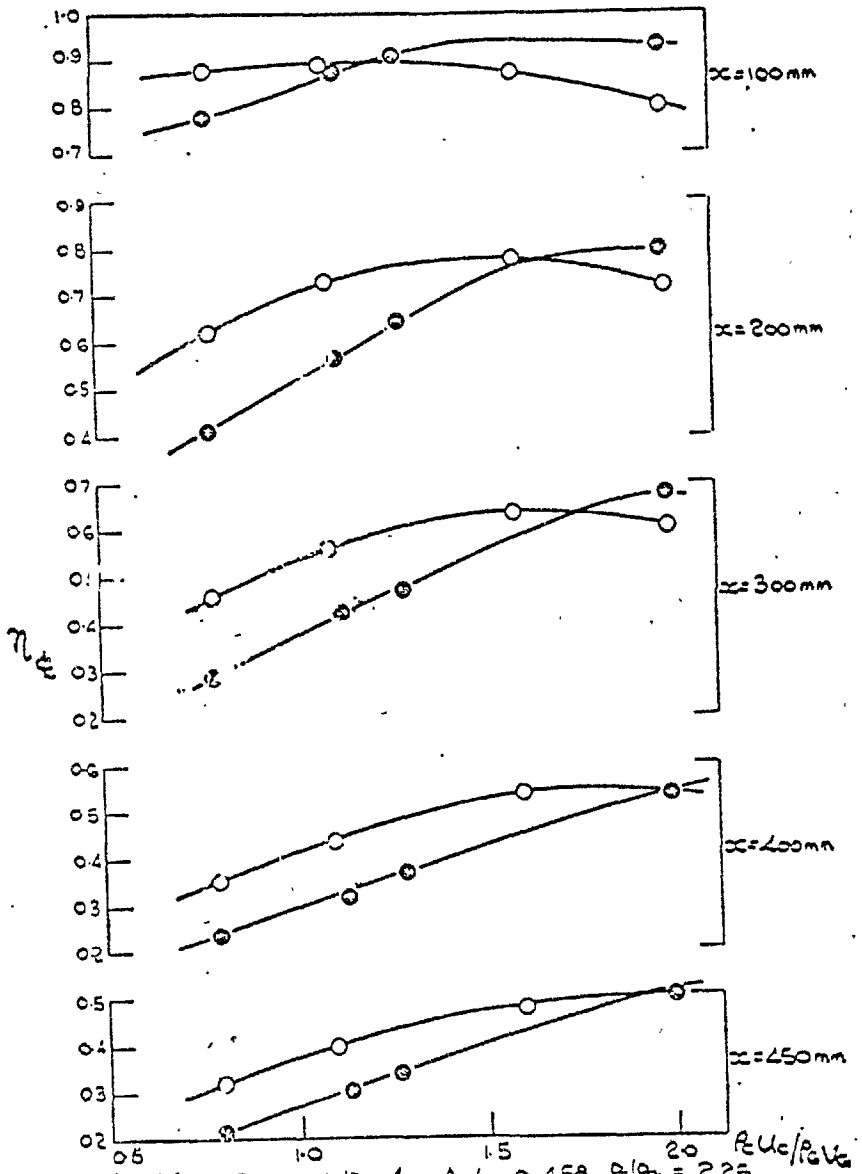

FIG. 4.2.7. INFLUENCE OF DENSITY RATIO

(a) Expts 4 & 5

(b)

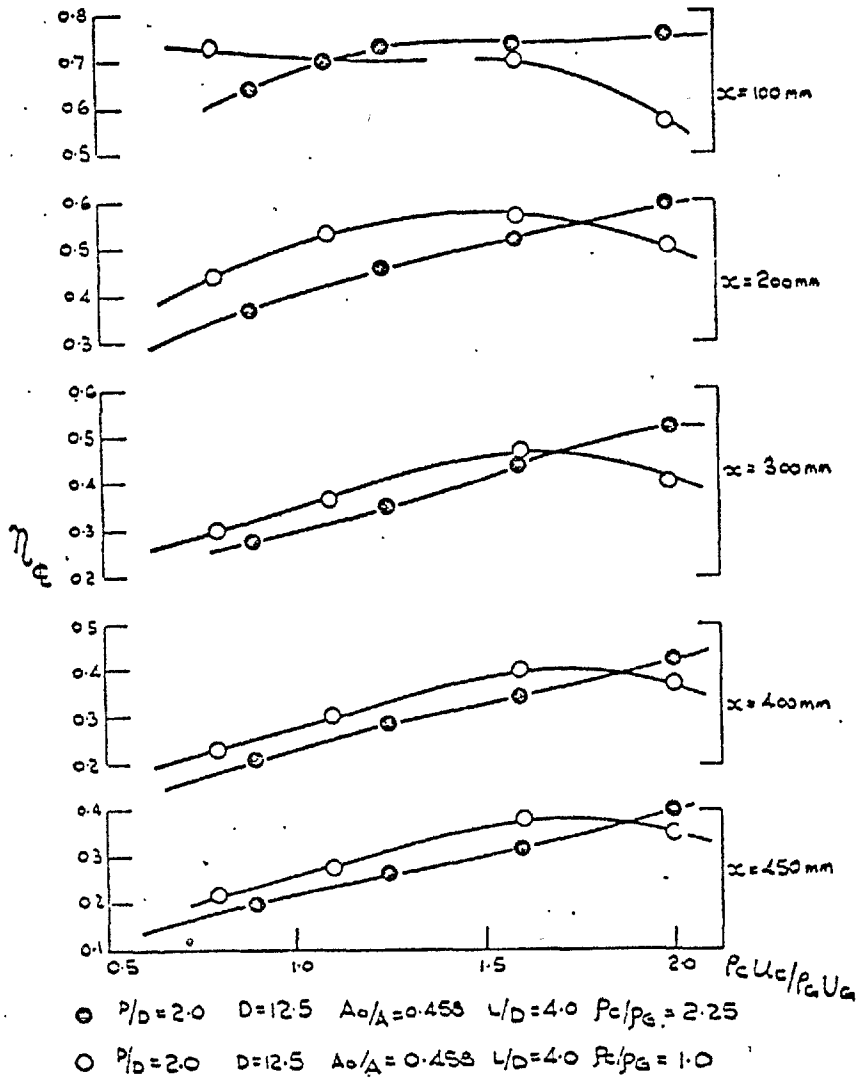

(b) Expts 6 & 8

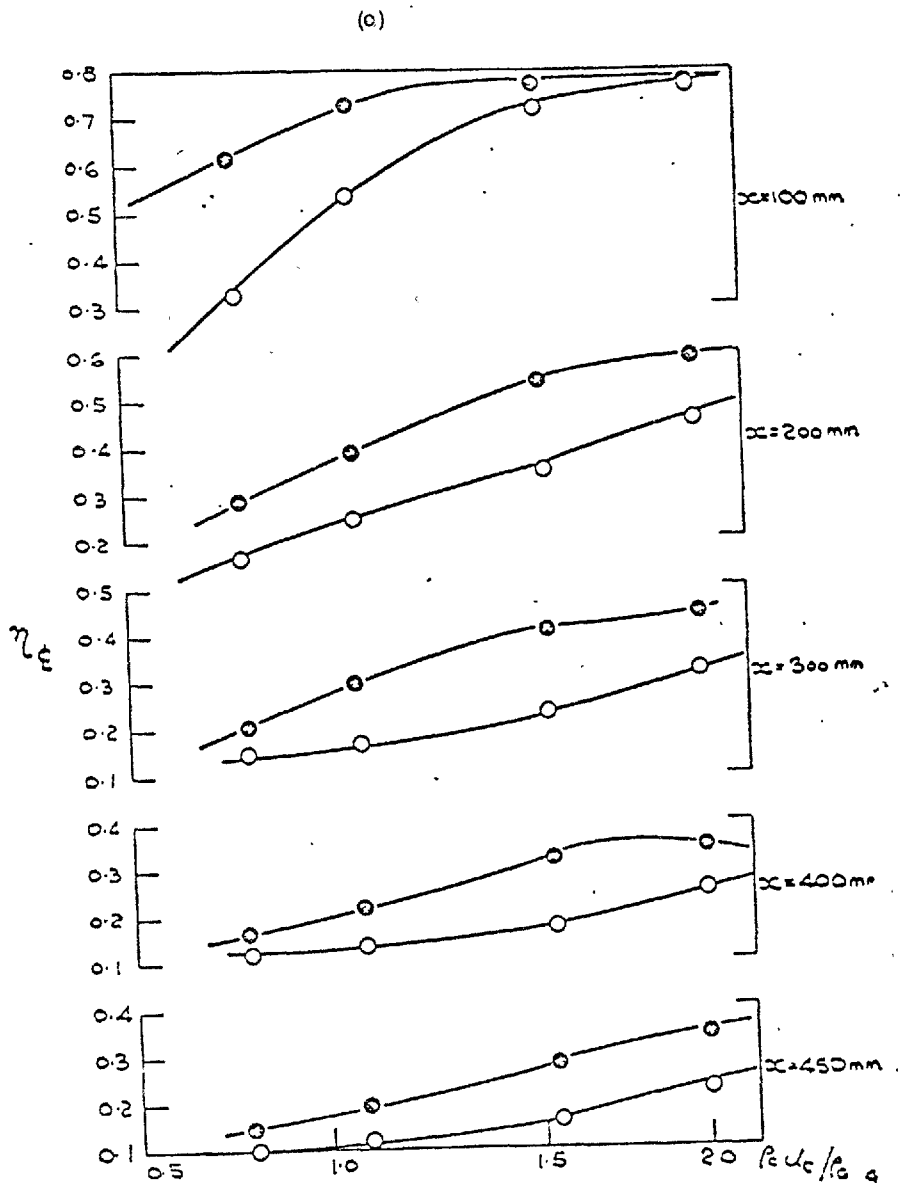

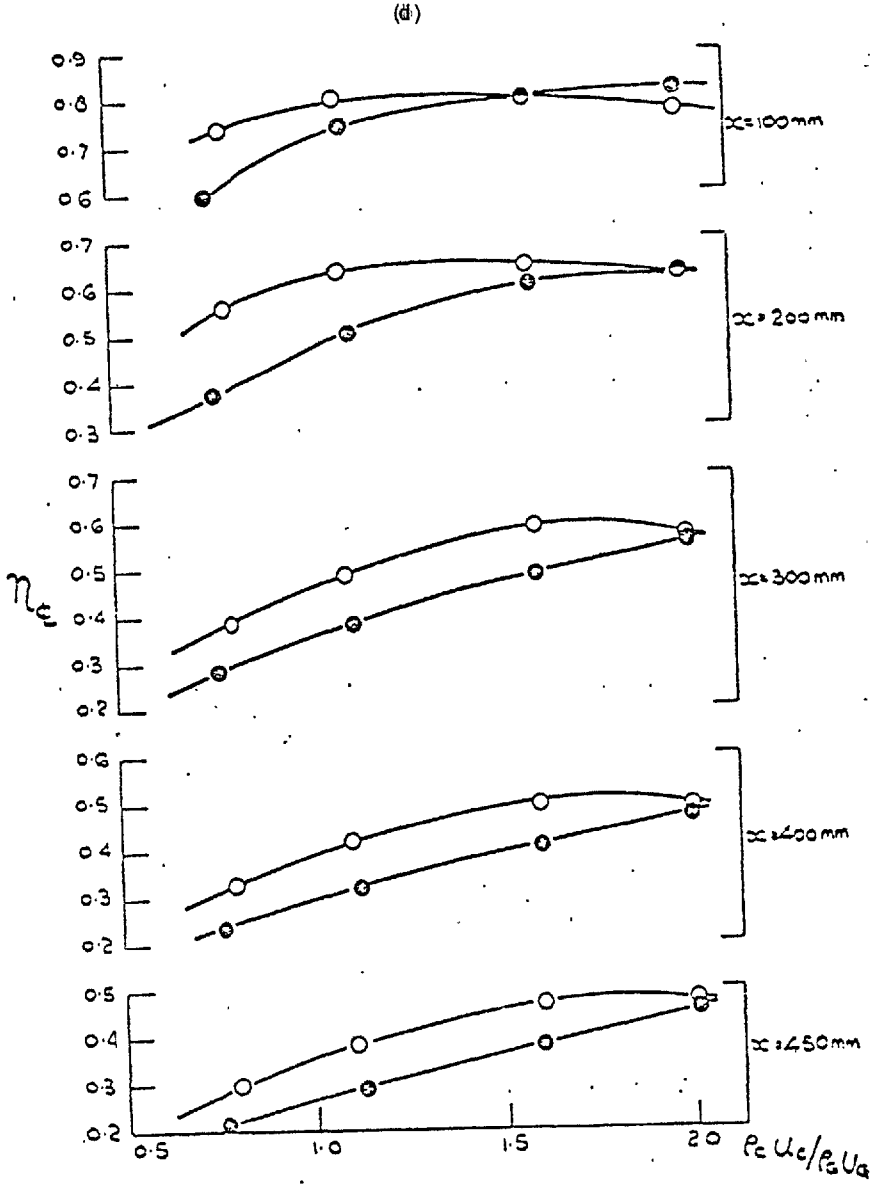

FIG. 4.2.7. INFLUENCE OF DENSITY RATIO

(c) Expts 9 & 11

(d) Expts 2 & 5

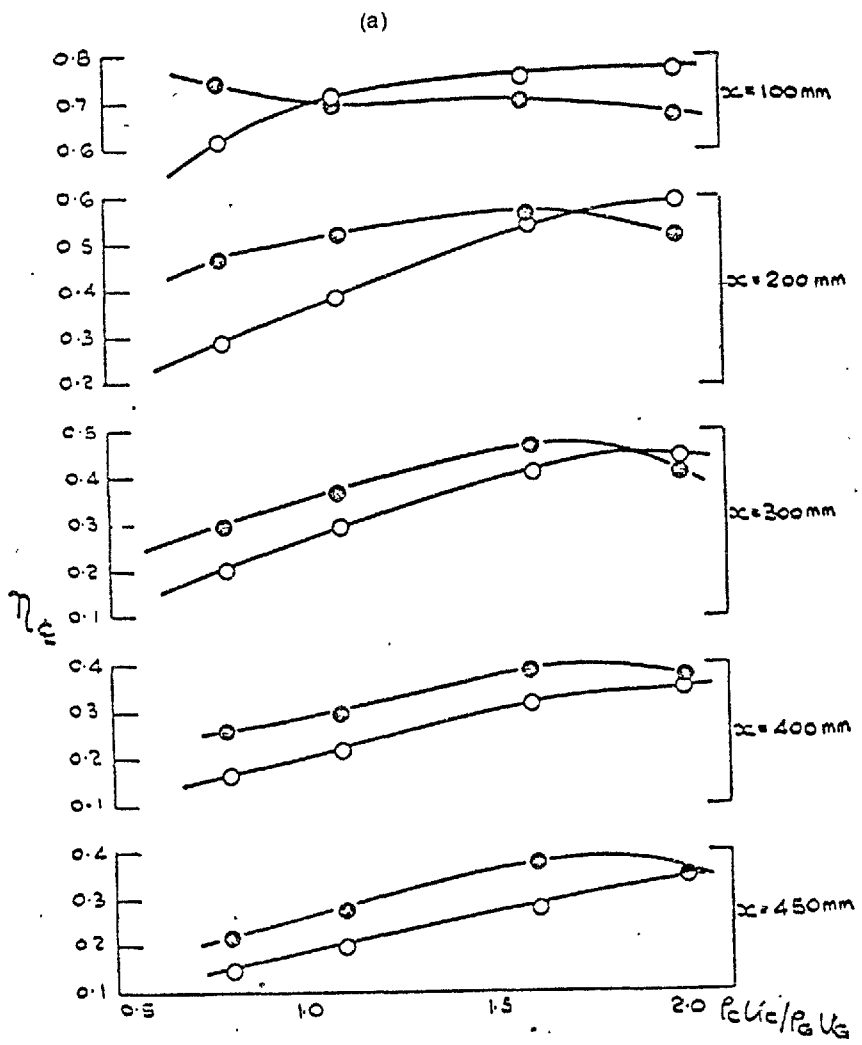

⊙ P/D=2·0 D=12·5mm A_o=1530mm² A_o/A=0·458 L/D=4·0

○ P/D=2·0 D=6·25mm A_o=765mm² A_o/A=0·23 L/D=4·0

FIG. 4.2.8. INFLUENCE OF OPEN AREA RATIO & OPEN AREA:

(a) Expts 6 & 9

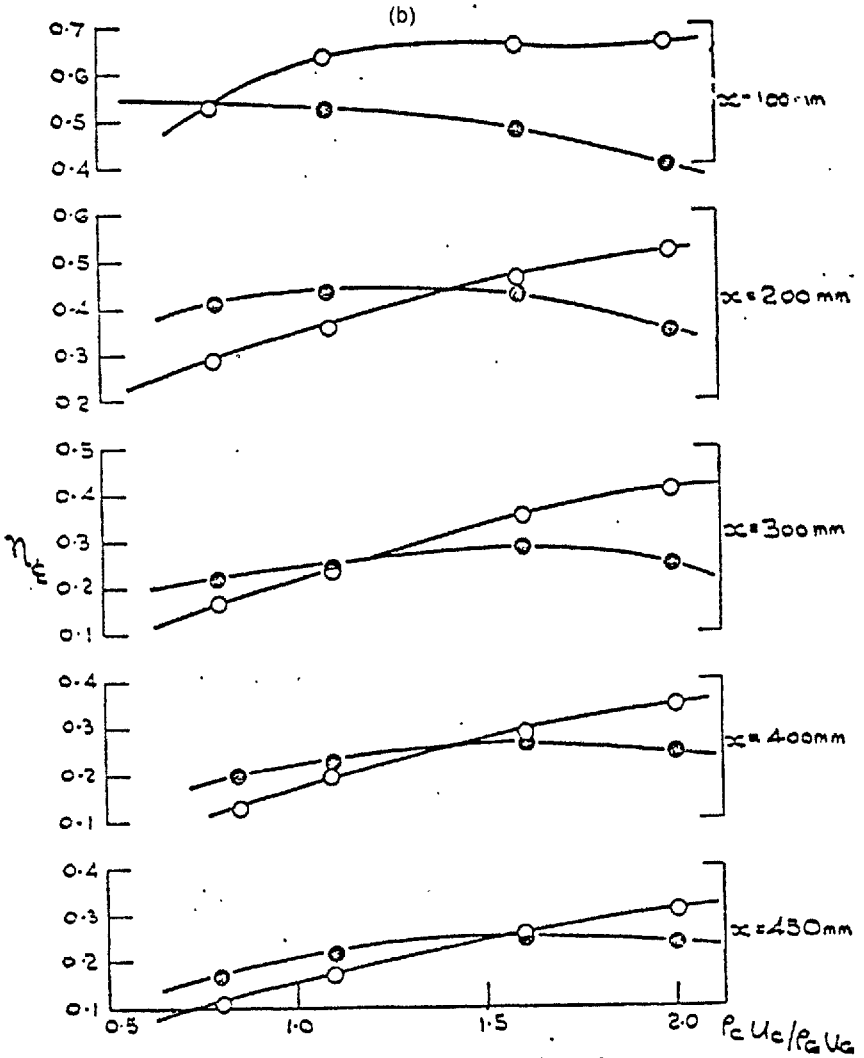

⊙ P/D=2·0 D=12·5 L/D=2·5 A_o=1530mm² A_o/A=0·458

○ P/D=2·0 D=6·25 L/D=2·5 A_o=765mm² A_o/A=0·23

(b) Expts 7 & 10

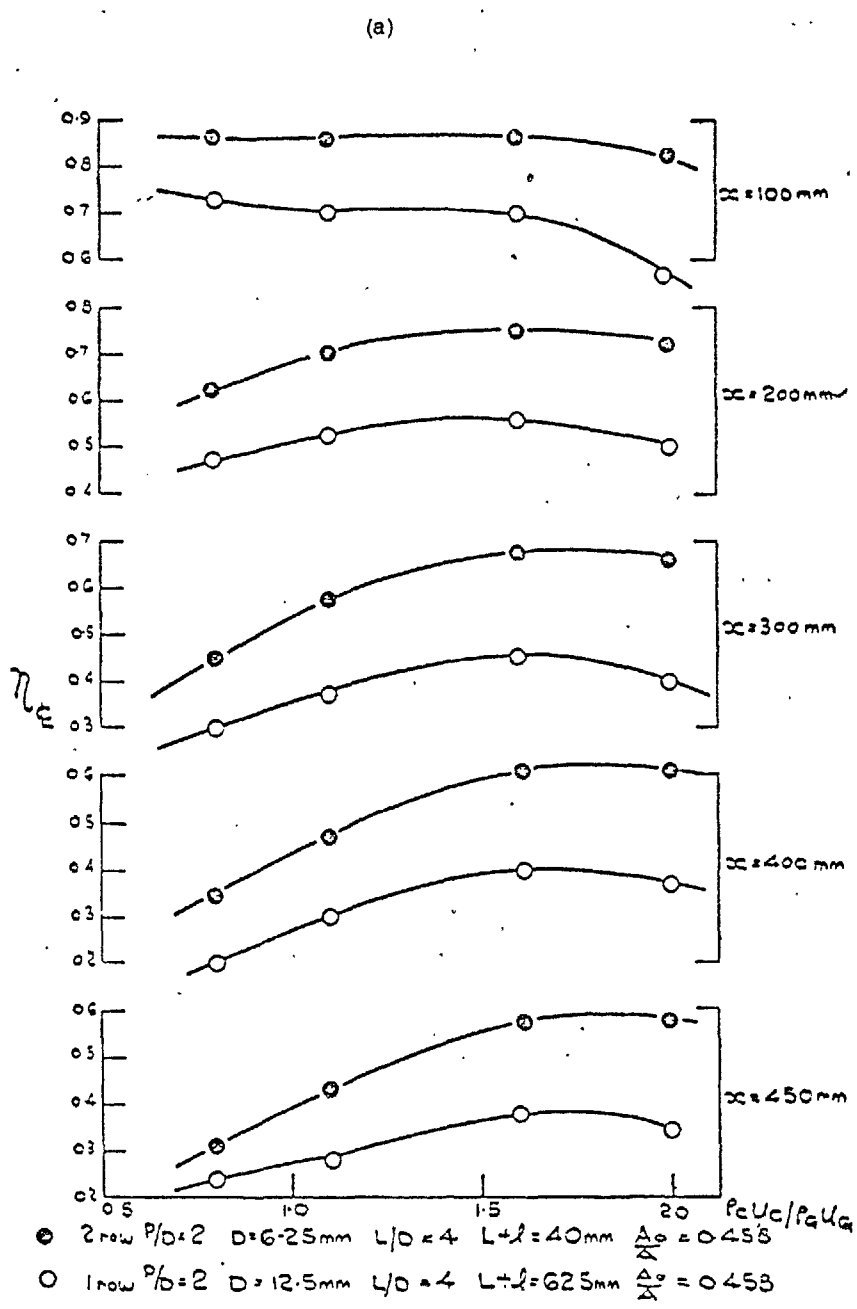

FIG. 4.2.9. INFLUENCE OF NUMBER OF ROWS OF HOLES

(a) Expts 14 & 6

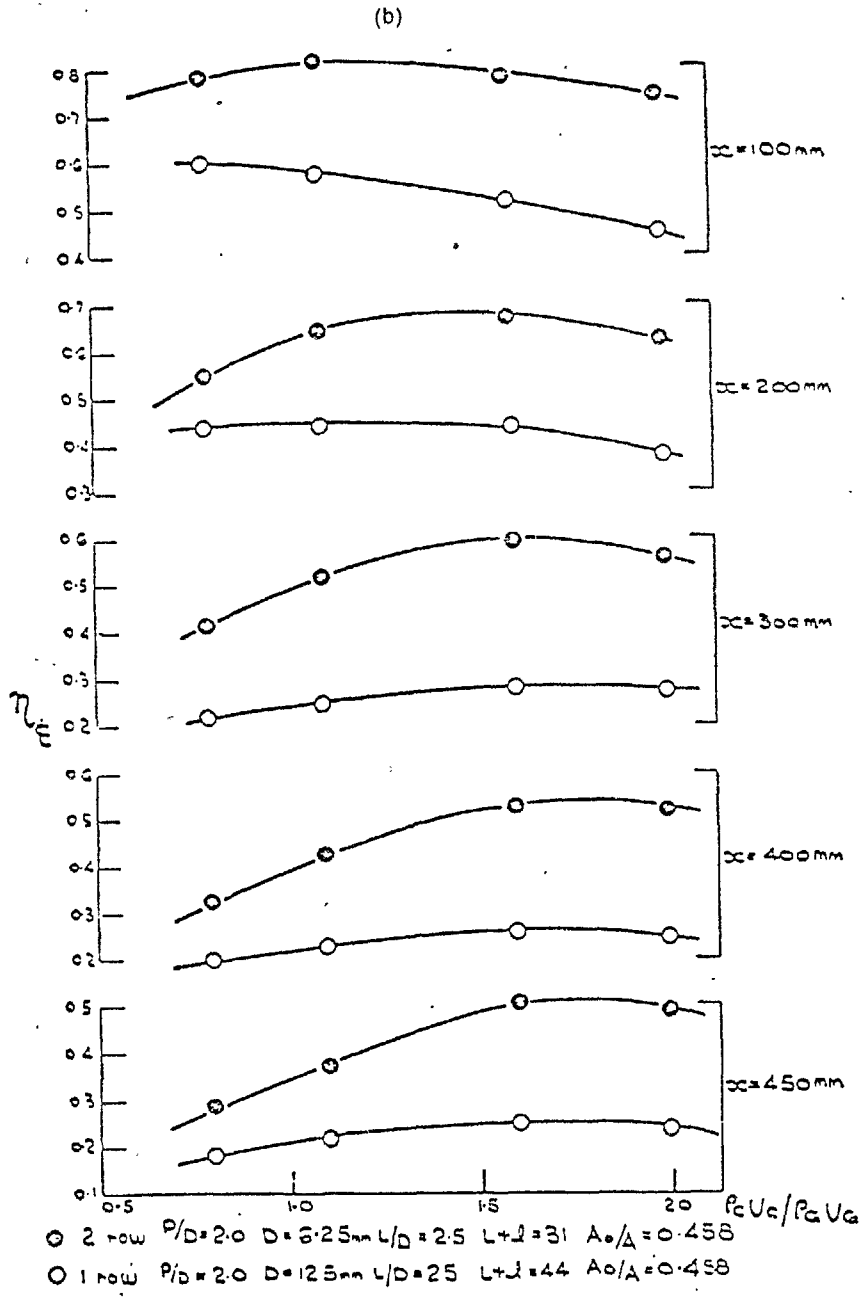

(b) Expts 15 & 7

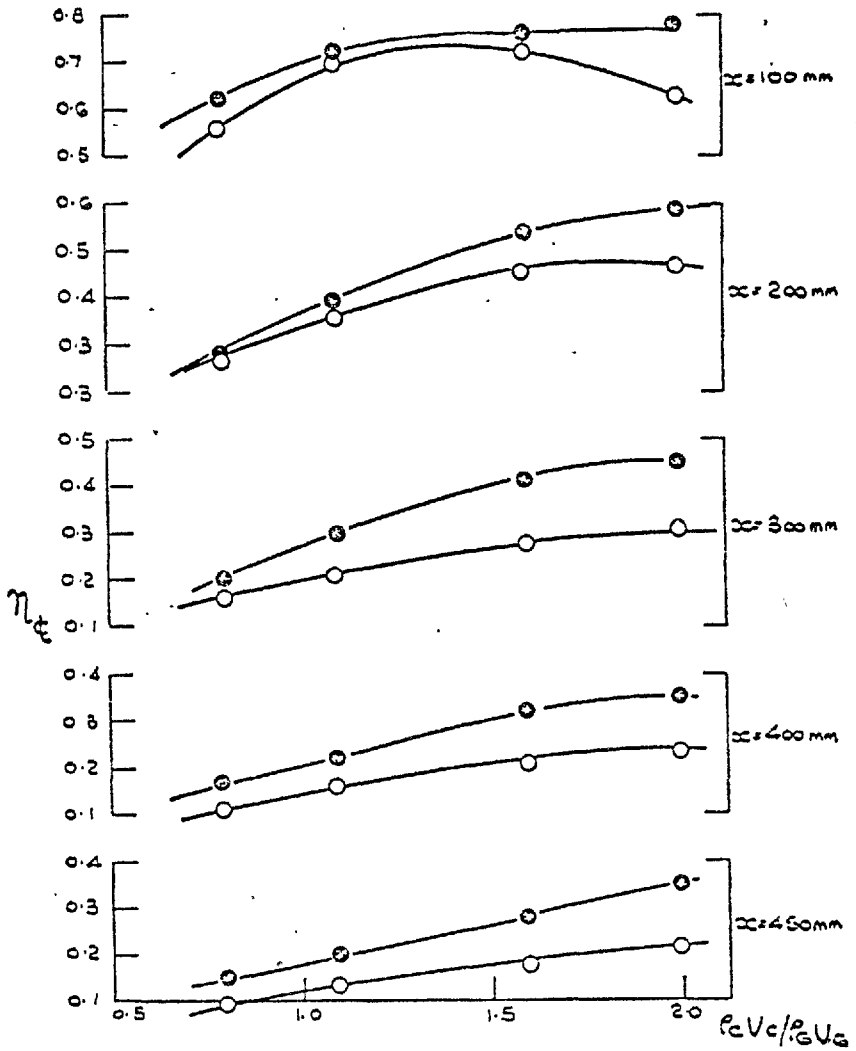

FIG. 4.2.10 INFLUENCE OF LIP THICKNESS:
EXPERIMENTS 9 & 13

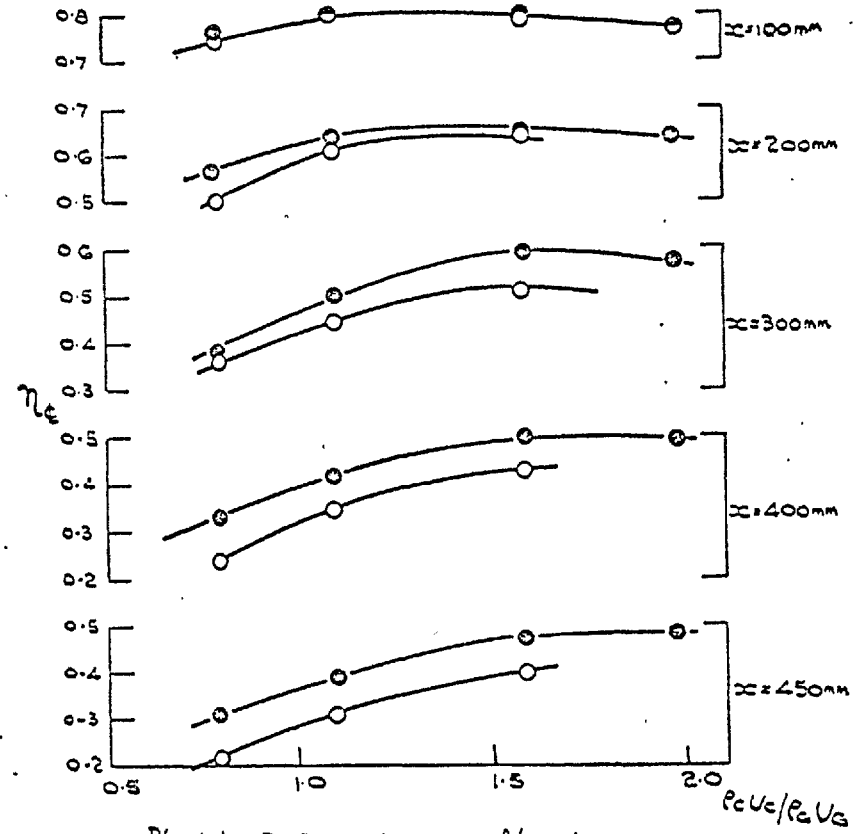

FIG. 4.2.11 INFLUENCE OF HOLE POSITION
EXPERIMENTS 2 & 3

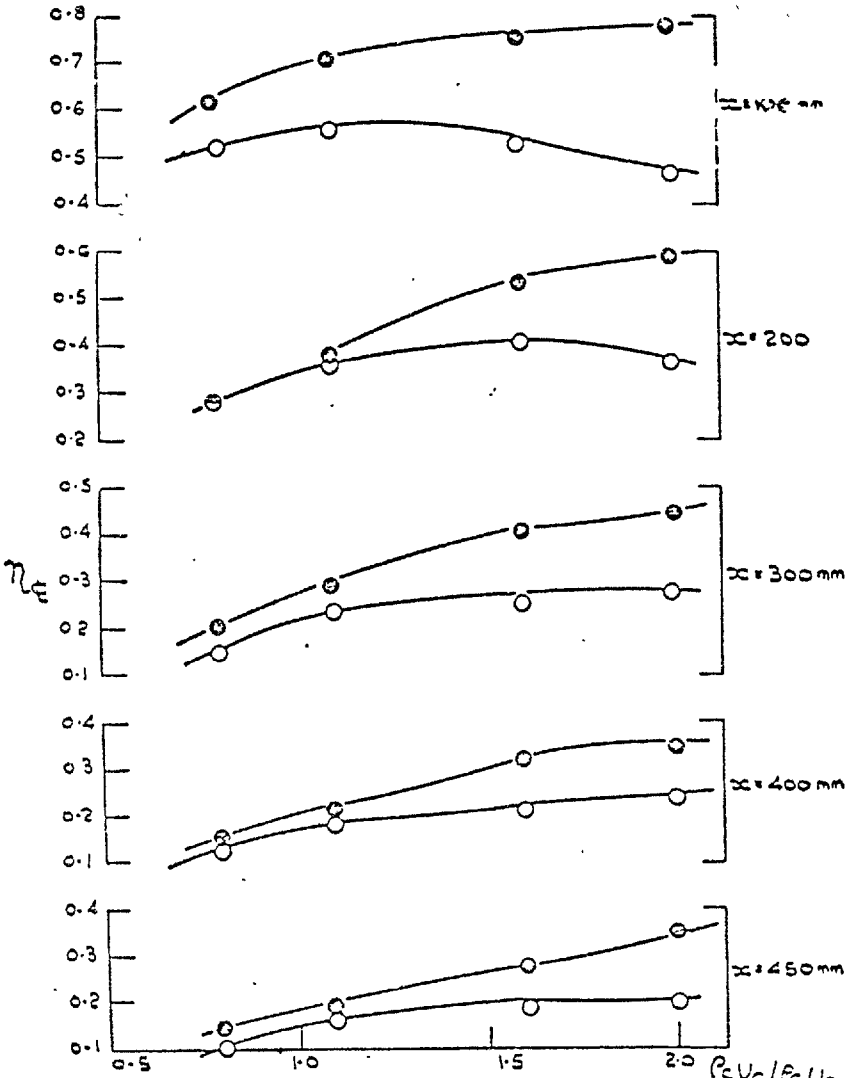

● P/D = 2·0 D = 6·25mm A_o = 7·65mm² L/D = 4 y_c = 11 ρ_c/ρ_G = 1·0

○ P/D = 2·0 D = 6·25mm A_o = 7·65mm² L/D = 4 y_c = 6·25 ρ_c/ρ_G = 1·0

FIG. 4.2.12 INFLUENCE OF SLOT HEIGHT.
EXPERIMENTS 9 & 16

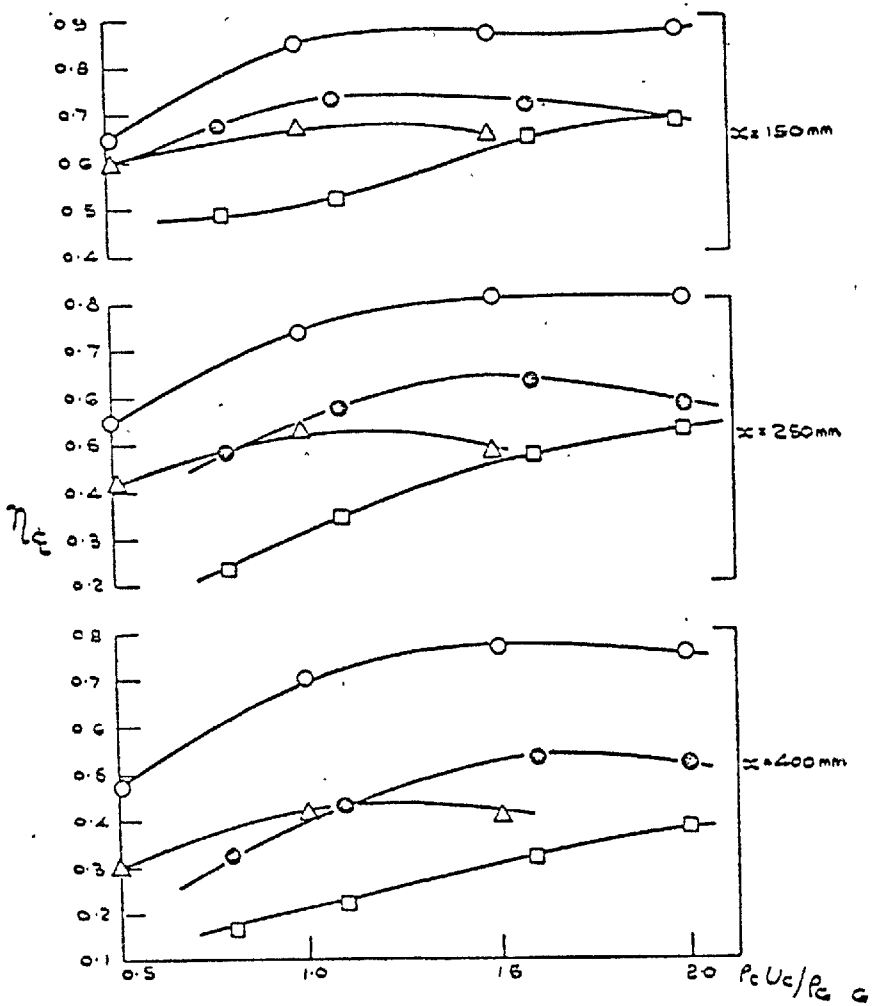

○ 2-D, t/y_c = 0·126 y_c = 6·25mm L/ℓ = 25mm KACKER & WHITELAW

● 3-D 2 ROW NORMAL INJECTION, P/D = 2 D = 6·25mm PRESENT
y_c = 11, A_o/A = 0·253, L/ℓ = 3·1mm

△ 3-D, SINGLE ROW, TANGENTIAL INJECTION NIGAM & WHITELAW
P/D = 1·8 D = 7·3mm, A_o/A = 0·264, L/ℓ = 30mm, y_c = 12·5mm

□ 3-D, SINGLE ROW NORMAL INJECTION PRESENT
P/D = 2·0 D = 6·25 A_o/A = 0·23 L/ℓ = 3·1mm, y_c = 11mm.

FIG. 4.2.13 COMPARISON OF HOLE ARRANGEMENTS

Table 4.2.3

Values of parameters for which effectiveness were obtained for combined normal and tangential jets

Experiment	P/D	t (mm)	D (mm)	y_T (mm)	y_l (mm)	y_c (mm)	l/D	L/y_c	A_o (mm^2)	A_o/A	ρ_c/ρ_G	U_t/U_n	U_t/U_G
1	2	1.25	6.25	0.5	0.5	7.25	1	4.4	1530	0.67	1	1	0.5,1.1,1.6,2
2	2	1.25	6.25	0.5	0.5	7.25	1	4.4	1530	0.67	2	1	0.5,1.1,1.6
3	2	1.25	6.25	0.5	0.5	7.25	1	4.4	1530	0.67	1	2	0.5,1.1,1.6
4	2	1.25	6.25	0.5	0.5	7.25	1	4.4	1530	0.67	2	2	0.5,1.1,1.6
5	2	1.25	6.25	0.5	0.5	7.25	1	2.2	1530	0.67	1	1	0.5,1.1,1.6
6		1.25	6.25	0.5	0.5	7.25	1	2.2	1530	0.67	2	1	0.5,1.1,1.6
7	2	1.25	6.25	0.5	0.5	7.25	1	2.2	1530	0.67	1	2	0.5,1.1,1.6
8	2	1.25	6.25	0.5	0.5	7.25	1	2.2	1530	0.67	2	2	0.5,1.1,1.6
9	2	1.25	6.25	7.25	0.5	14.0	1	2.2	1530	0.356	1	1	0.5,1.1,1.6
10	2	1.25	6.25	7.25	0.5	14.0	1	2.2	1530	0.356	2	1	0.5,0.8,1.2
11	2	1.25	6.25	7.25	0.5	14.0	1	2.2	1530	0.356	1	2	0.5,1.1,1.6
12	2	1.25	6.25	7.25	0.5	14.0	1	2.2	1530	0.356	2	2	0.5,0.8,1.2
13	2.8	1.25	9	3.5	0.5	14.0	1	2.2	1530	0.356	1	1	0.5,1.1,1.6
14	2.8	1.25	9	3.5	0.5	14.0	1	2.2	1530	0.356	2	1	0.5,0.8,1.4
15	2.8	1.25	9	3.5	0.5	14.0	1	2.2	1530	0.356	1	2	0.5,1.1,1.6
16	2.8	1.25	9	3.5	0.5	14.0	1	2.2	1530	0.356	2	2	0.4,0.8,1.3
17	4	1.25	12.5	1	0.5	14.0	1	2.2	1530	0.356	1	1	0.5,1.1,1.6
18	4	1.25	12.5	1	0.5	14.0	1	2.2	1530	0.356	2	1	0.5,1.1,1.5
19	4	1.25	12.5	1	0.5	14.0	1	2.2	1530	0.356	1	2	0.5,1.1,1.5
20	2	1.25	12.5	1	0.5	14.0	1	2.2	3060	0.67	1	1	0.5,1.1
21	2	1.25	12.5	1	0.5	14.0	1	2.2	3060	0.67	1	2	0.5,1.1
22	2	1.25	12.5	1	0.5	14.0	00	2.2	1530	0.356	1	00	0.5,1.1,1.6
23	2	1.25	12.5	1	0.5	14.0	00	2.2	1530	0.356	1	00	0.5,0.8,1.1 Tangential Injection
24	2	1.25	5.3	1	0.5	14.0	00	2.2	1530	0.356	1	00	0.5,0.8,1.1,2 row
25	2	1.25	5.3	1	0.5	14.0	00	2.2	1530	0.356	2	00	0.5,1.1,1.6 injection Injection
26	2	1.25	9	1	0.5	10.5	1	4.4	2200	0.67	1	1	0.5,1.1,1.6
27	2	1.25	9	1	0.5	10.5	1	4.4	2200	0.67	2	1	0.5,1.1,1.6
28	2	1.25	9	1	0.5	10.5	1	4.4	2200	0.67	1	2	0.5,1.1,1.6
29	2	1.25	9	1	0.5	10.5	1	2.2	2200	0.67	1	1	0.5,1.1,1.6
30	2	1.25	9	1	0.5	10.5	1	2.2	2200	0.67	2	1	0.5,1.1,1.6
31	2	1.25	9	1	0.5	10.5	1	2.2	2200	0.67	1	2	0.5,1.1,1.6
32	2	1.25	12.5	0	0	11	1	2.2	1530	0.458	1	0	0.8,1.1,1.6 2 normal injection from ref.5
33	2	1.25	9	0.35	0.35	10.95	-	0	1530	0.458	1		Slot 3, ref.1
34	2	1.25	6.25	7.25	0.5	14	0	2.2	1530	0.356	1	1	0.5,1.1,1.6

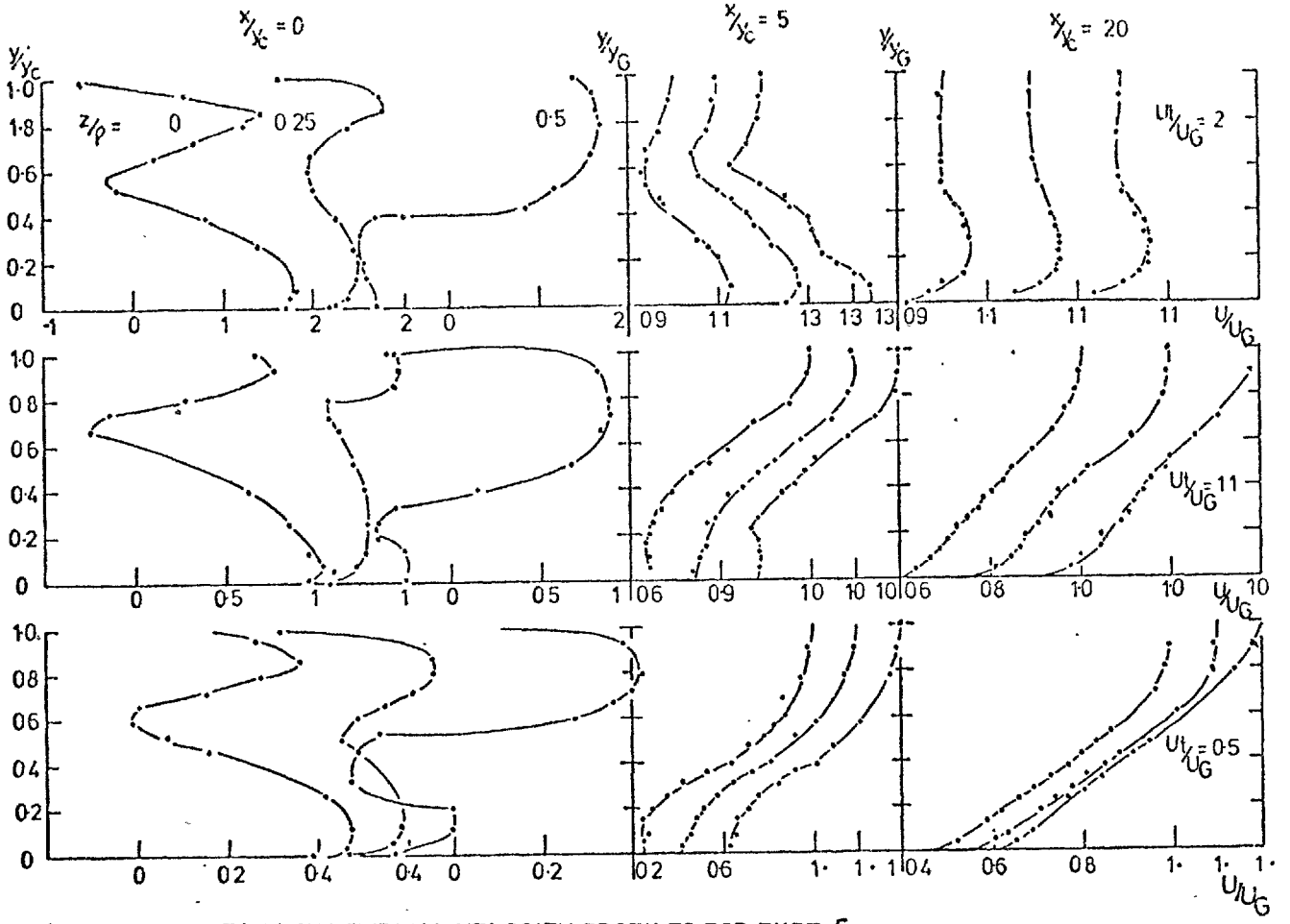

FIG. 4.2.14a MEAN LONGITUDINAL VELOCITY PROFILES FOR EXPT. 5

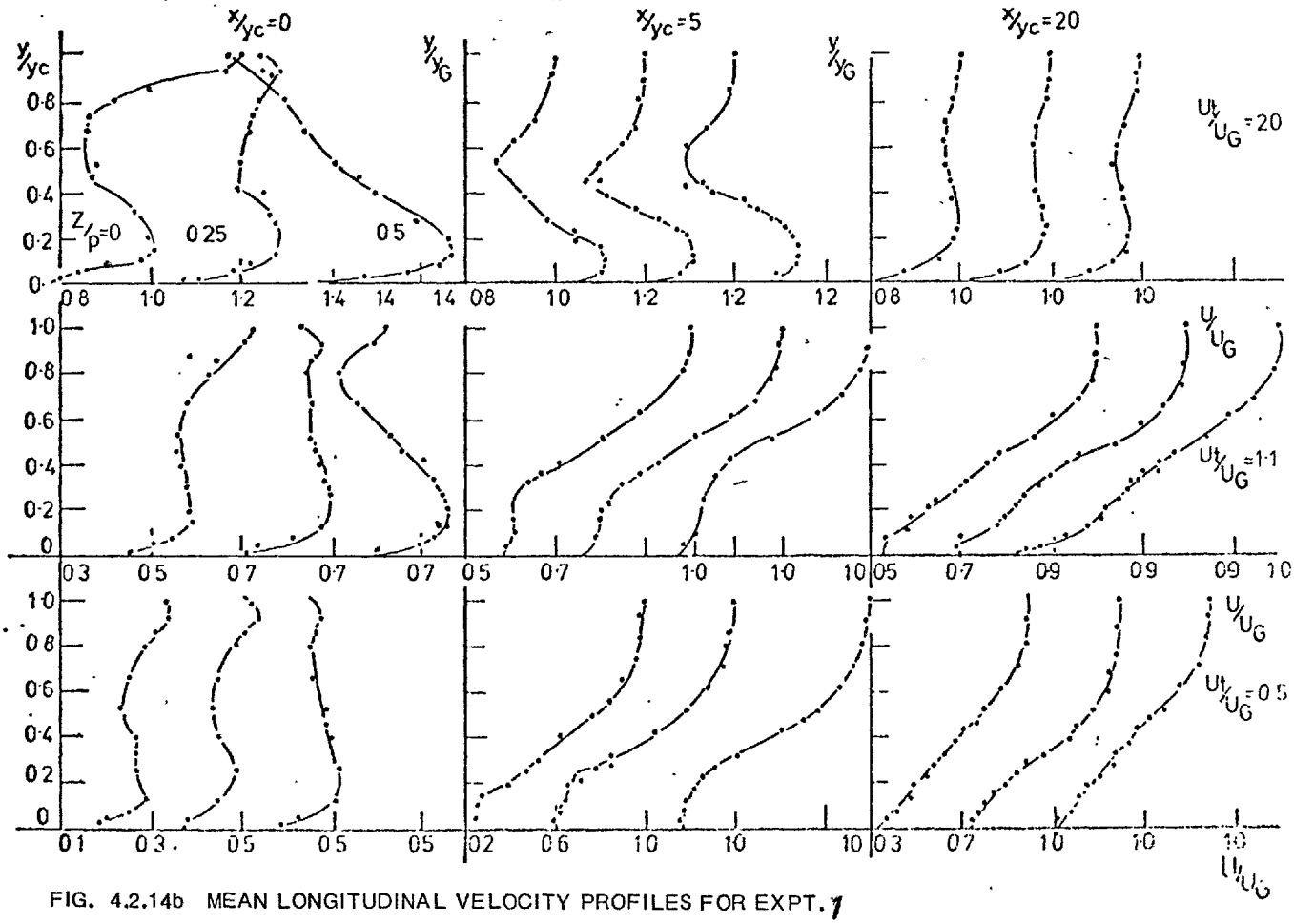

FIG. 4.2.14b MEAN LONGITUDINAL VELOCITY PROFILES FOR EXPT. 1

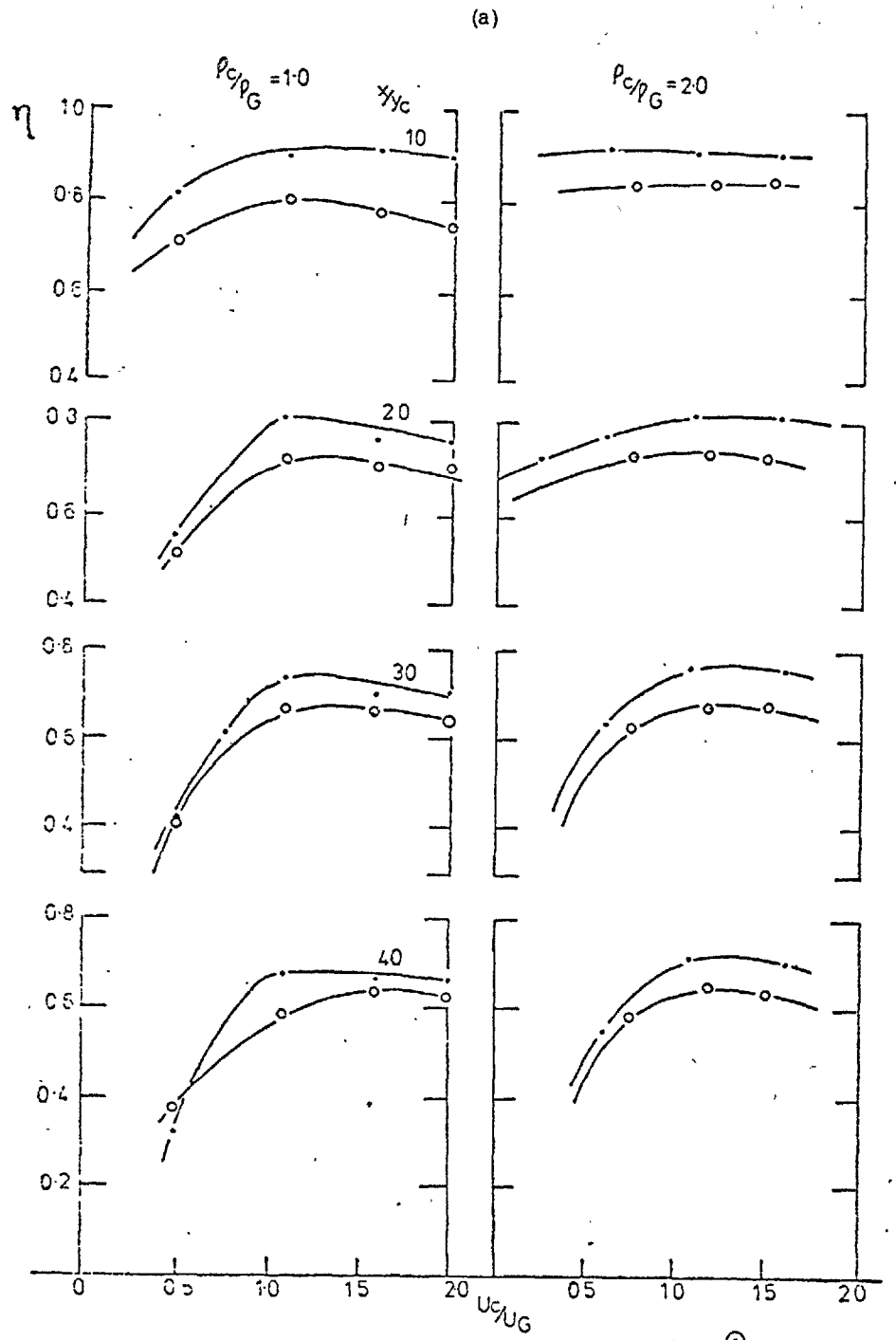

FIG. 4.2.15 INFLUENCE OF LIP LENGTH (a) Expts 1 and 5 ⊙
2 and 6

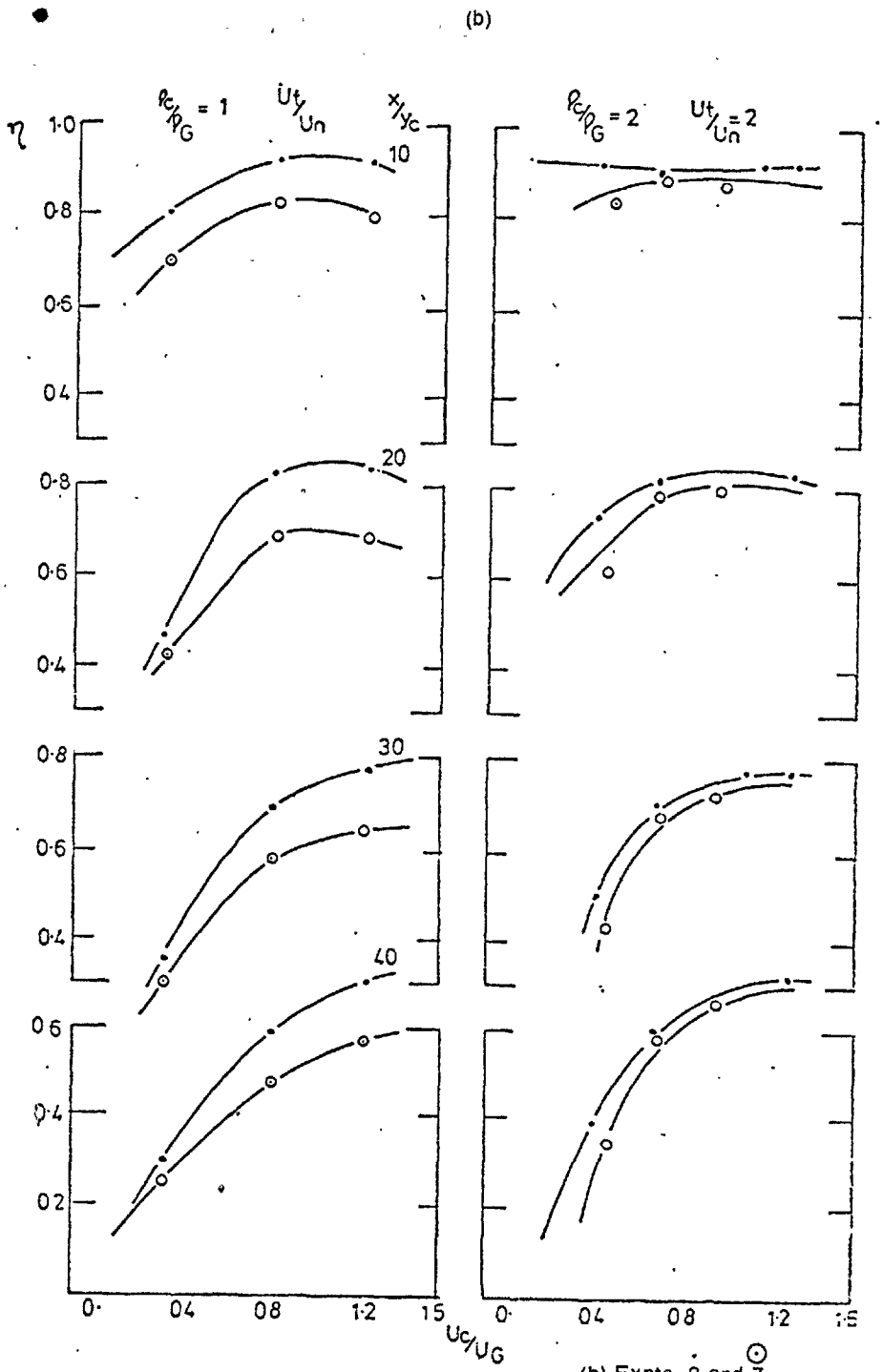

(b) Expts 3 and 7 ⊙
4 and 8

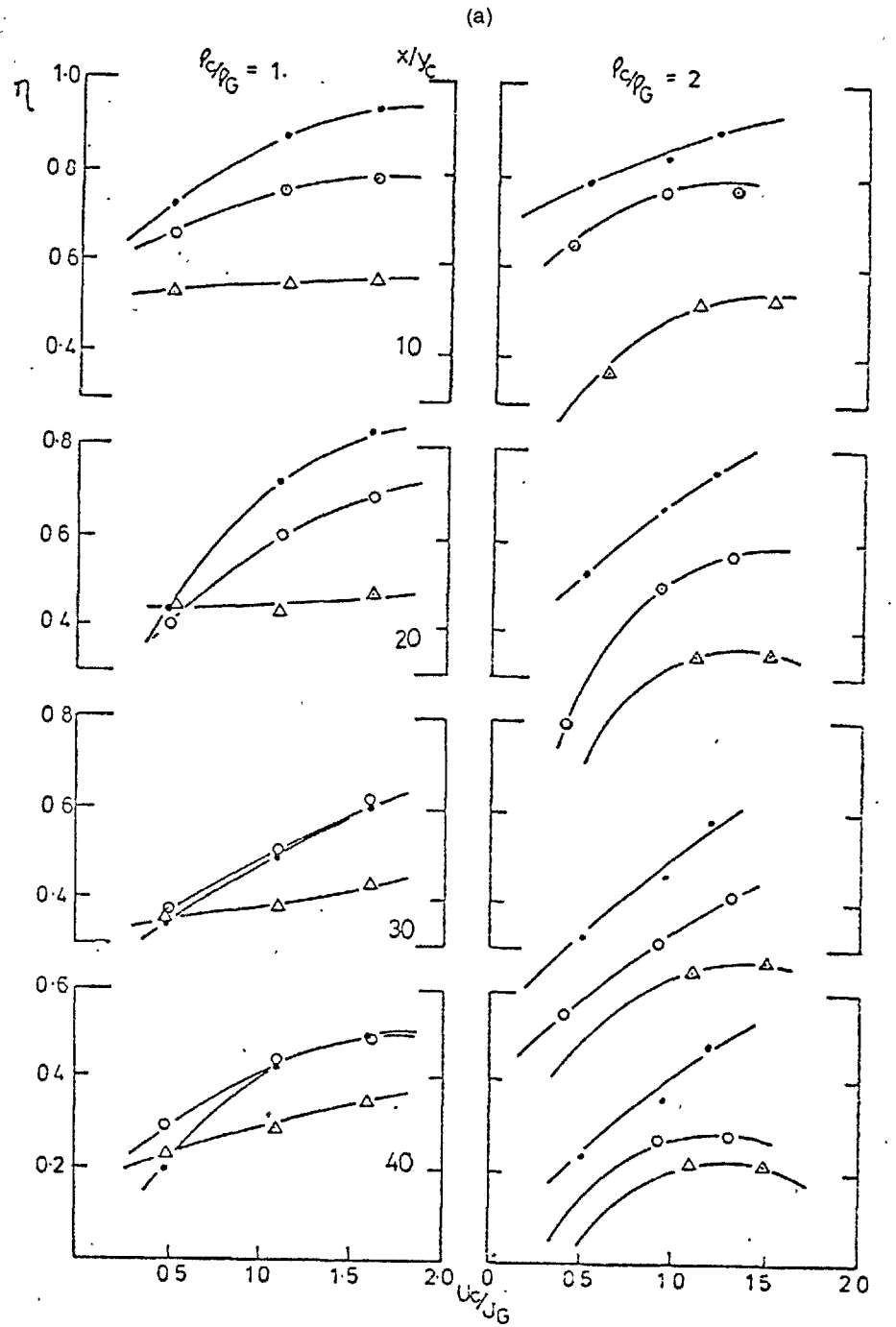

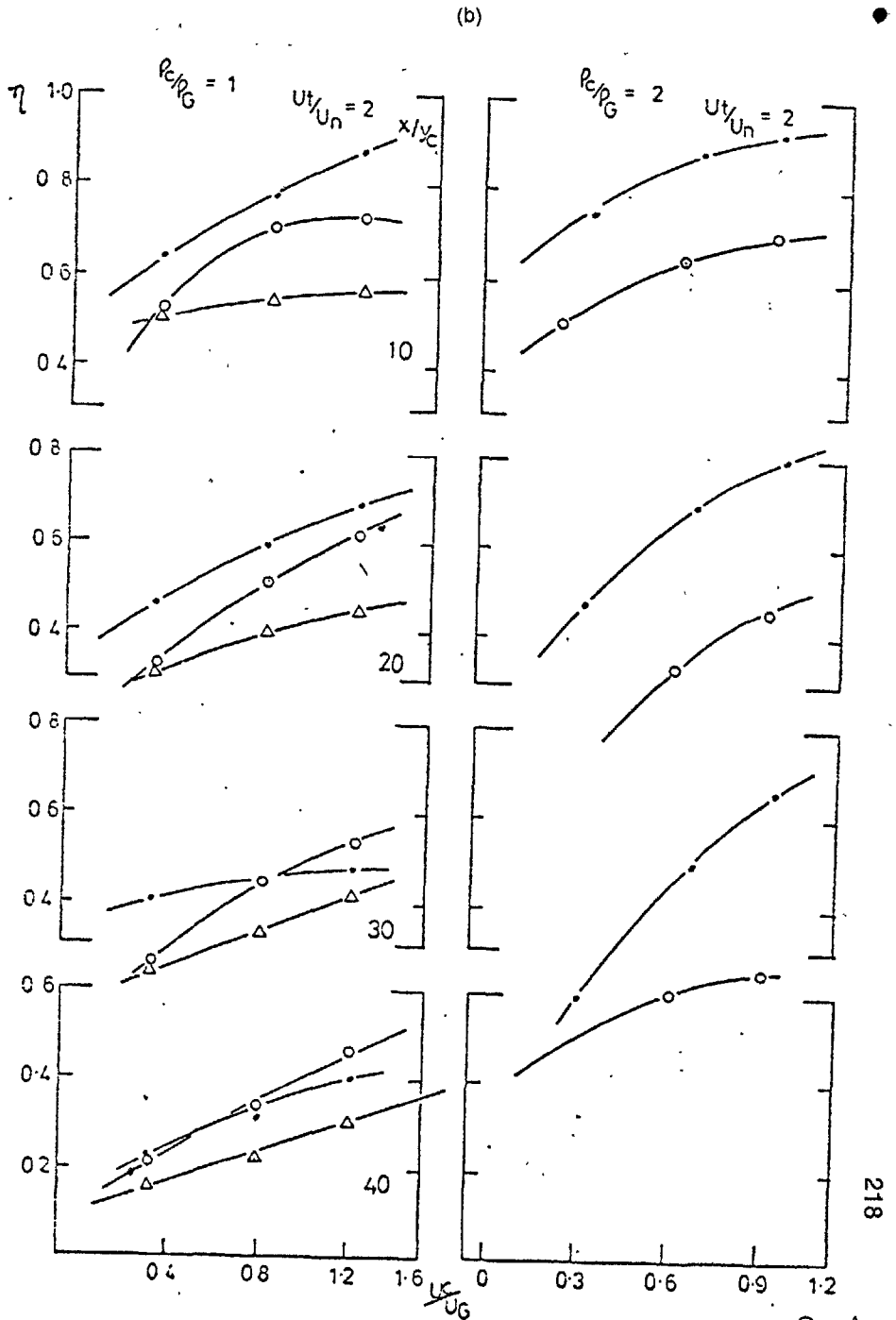

FIG. 4.2.16 INFLUENCE OF PITCH-DIAMETER-RATIO (a) Expts • 9, ⊙ 13, △ 17
10, 14, 18

(b) Expts • 11, ⊙ 15, △ 19
12, 16,

(a)

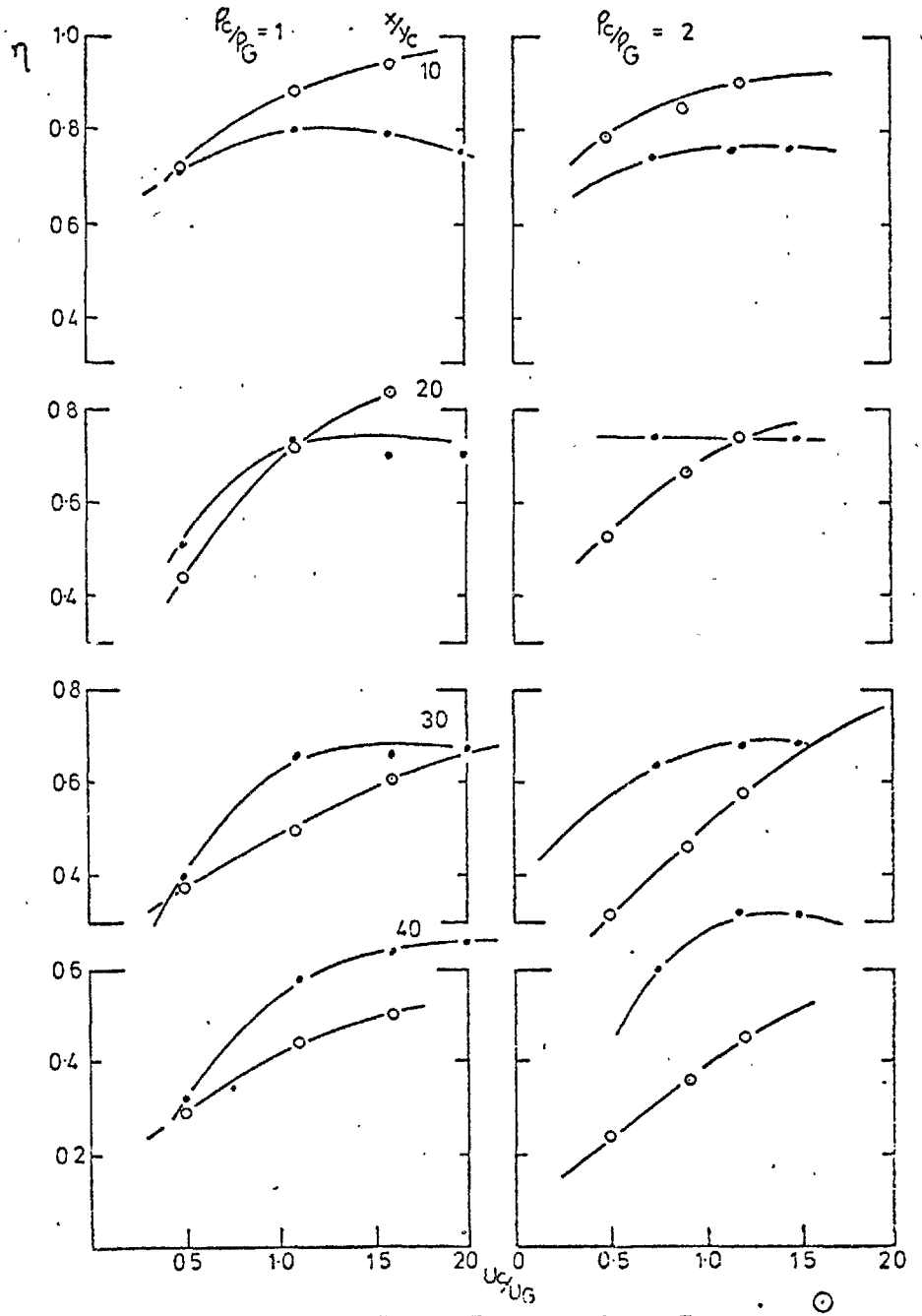

FIG. 4.2.17. INFLUENCE OF OPEN AREA RATIO: Expts • 5 and 9 ⊙ 6 and 10

(b).

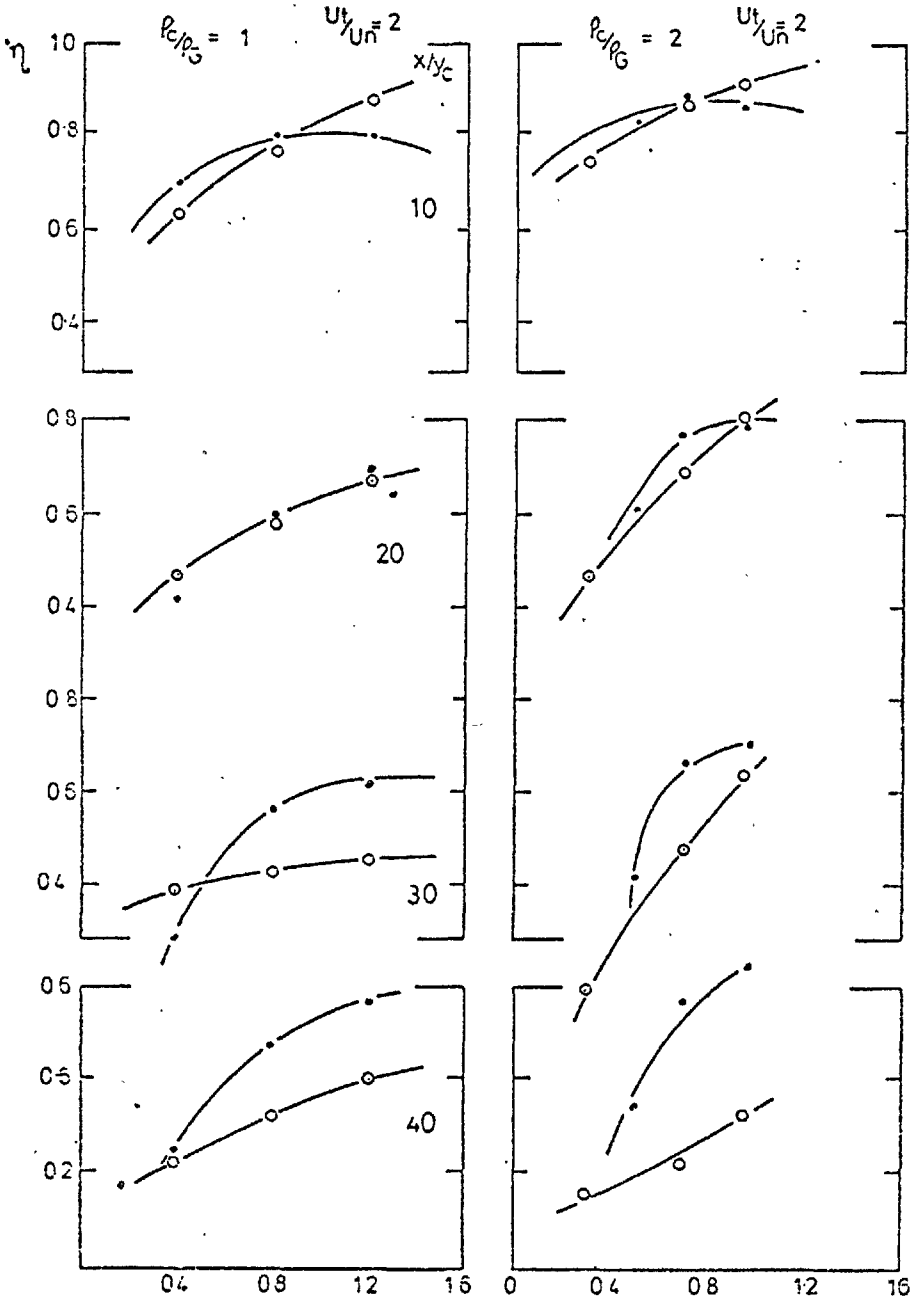

(b) Expts • 7 and 11 ⊙ 8 and 12

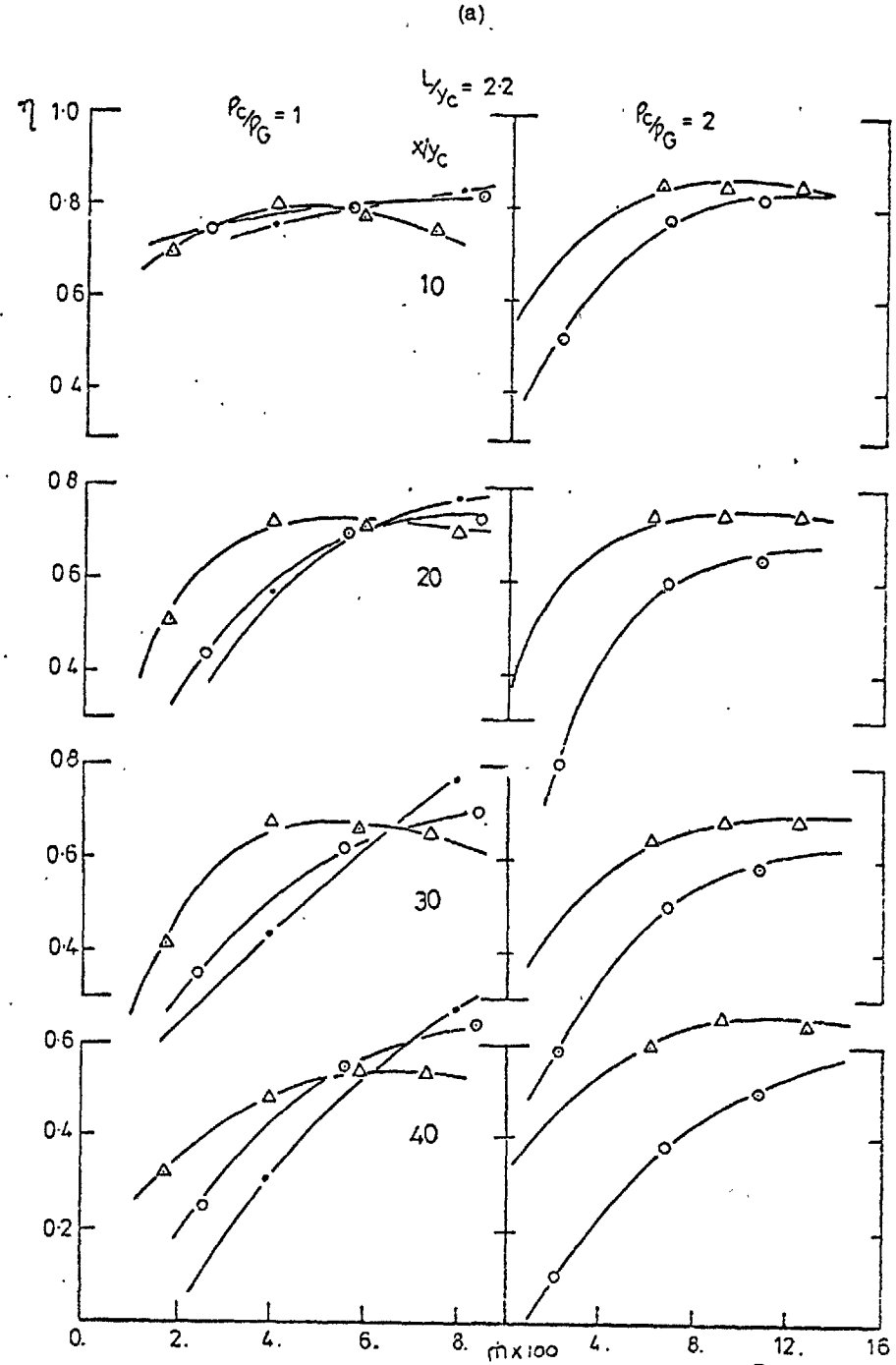

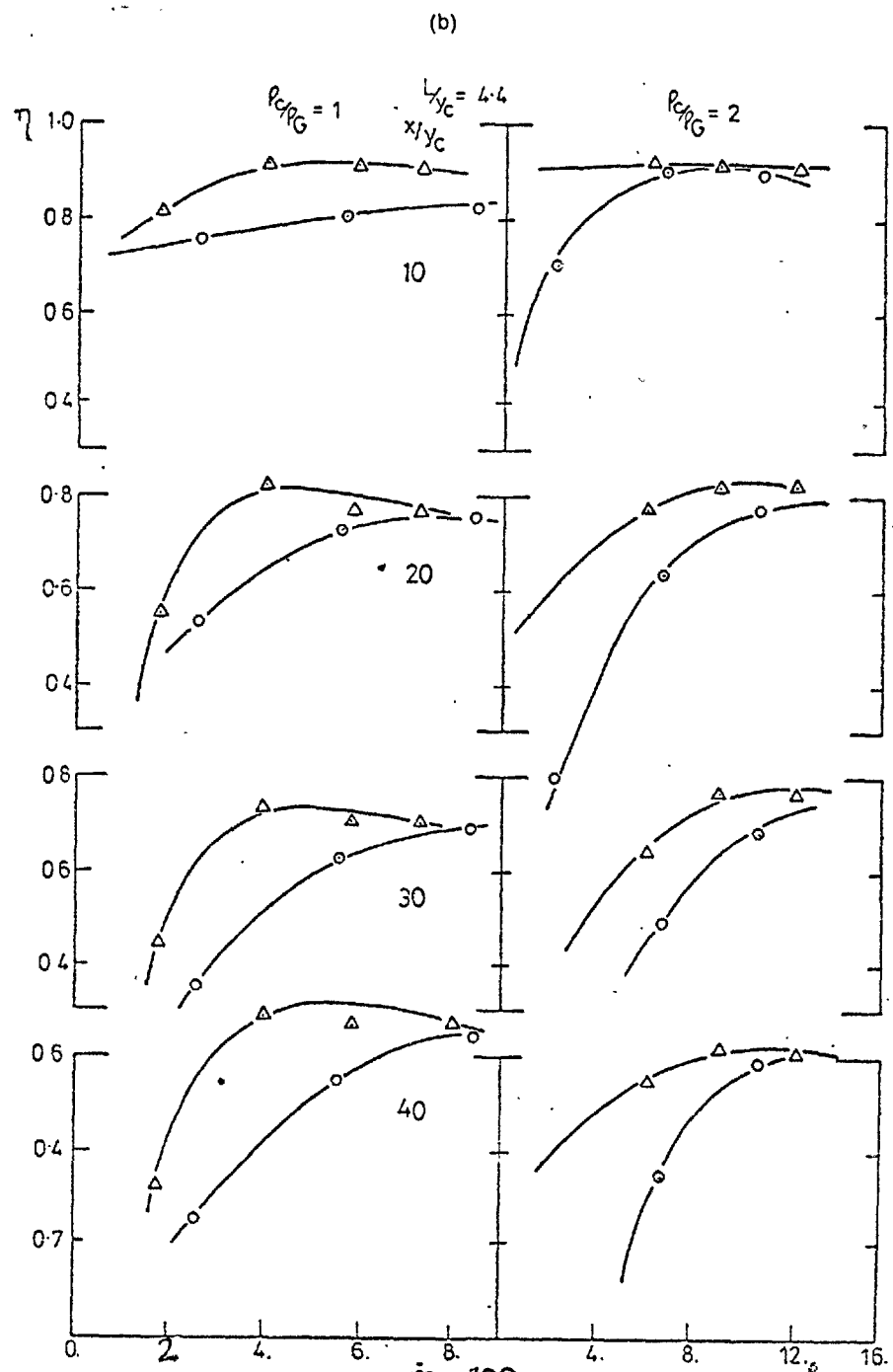

FIG. 4.2.18. INFLUENCE OF OPEN AREA: (a) Expts 20, 29 and 5 ⊙ △
30 and 6

(b) Expts 26 and 1 ⊙ △
27 and 2

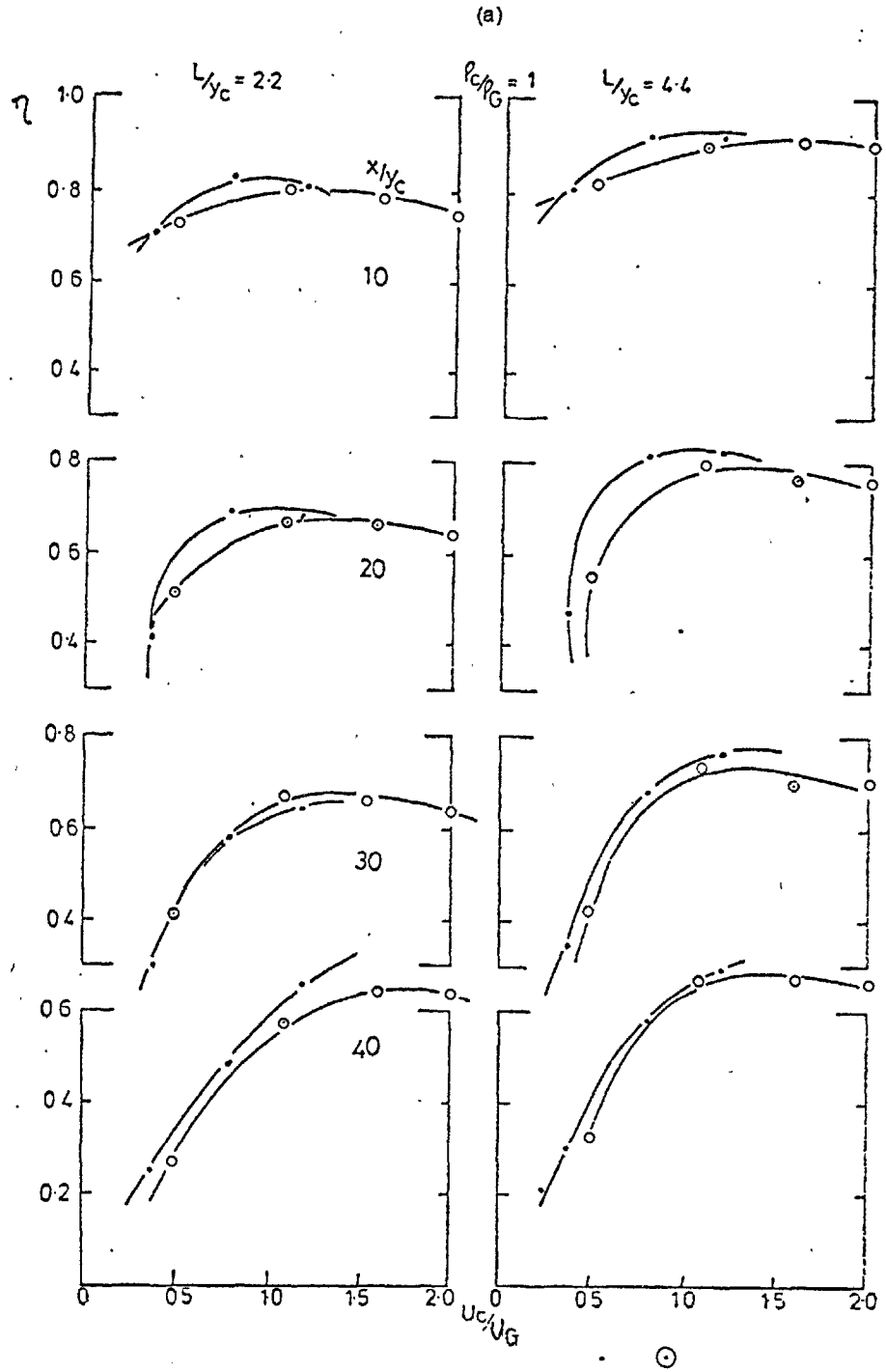

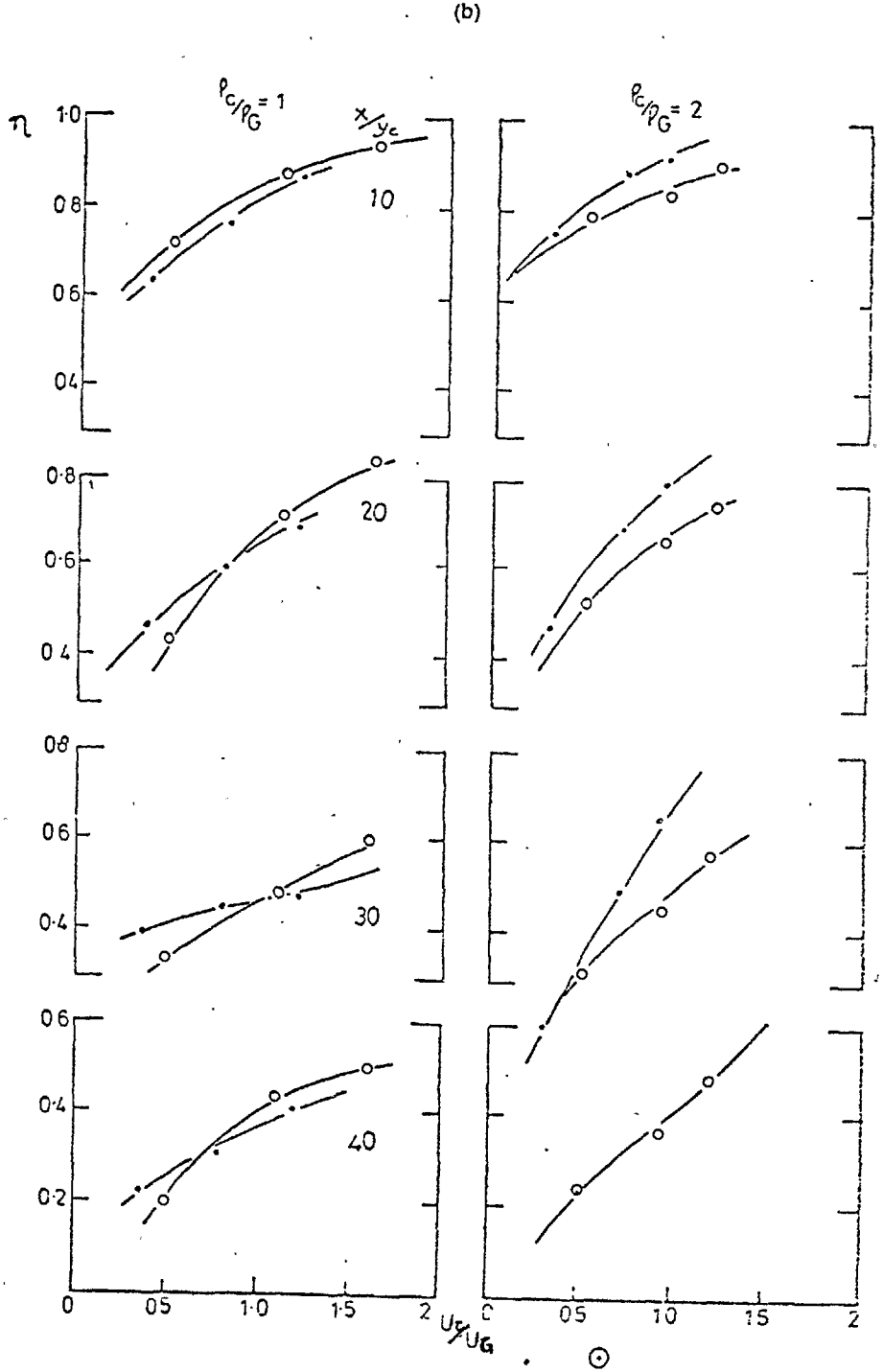

FIG. 4.2.19. INFLUENCE OF Ut/Un (a) Expts 5 and 7
1 and 3

(b) Expts 11 and 9
12 and 10

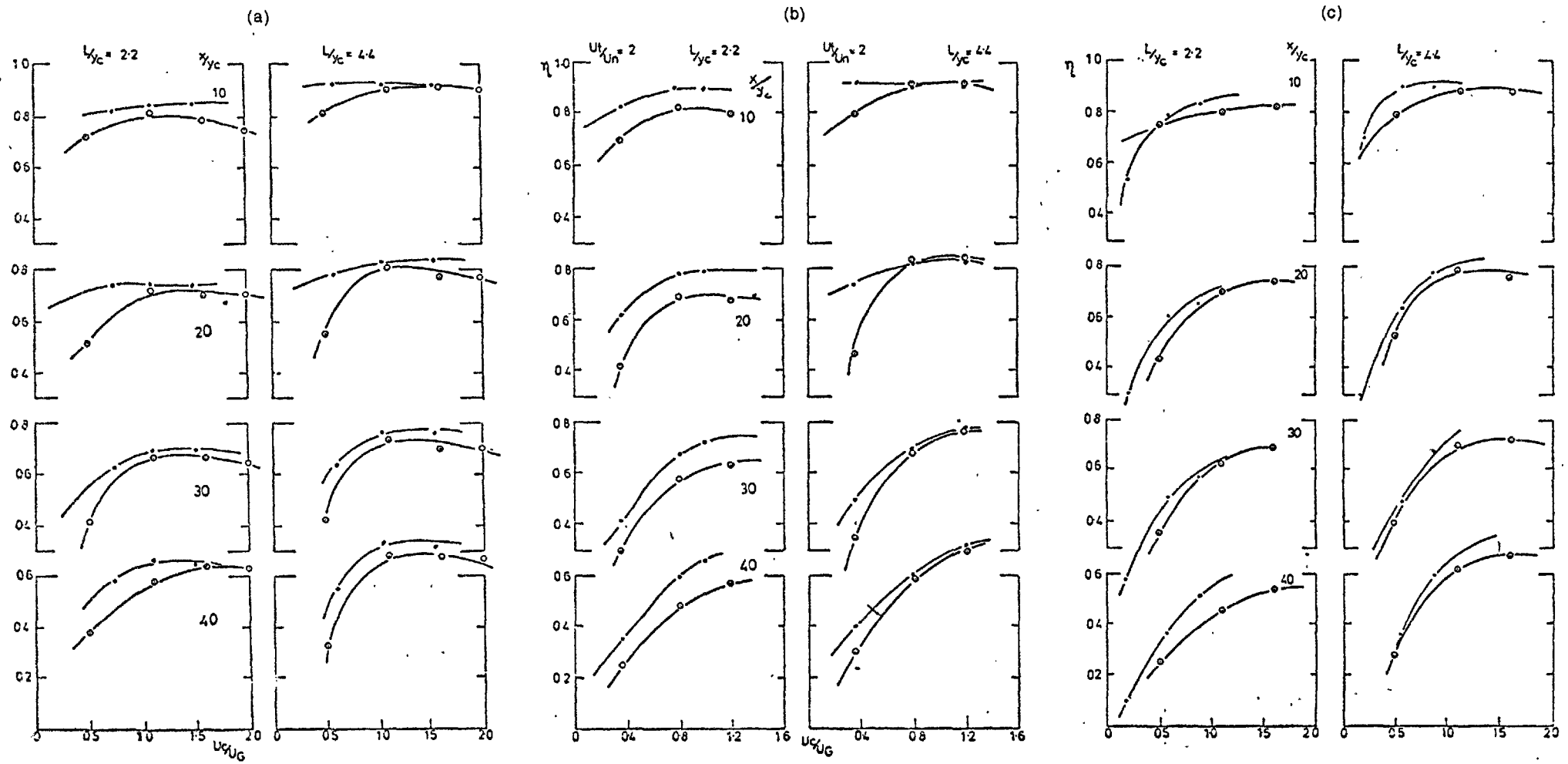

FIG. 4.2.20 INFLUENCE OF DENSITY RATIO: (a) Expts 6 and 5 (b) Expts 8 and 7
2 and 1 4 and 3
(c) Expts 30 and 29
27 and 26

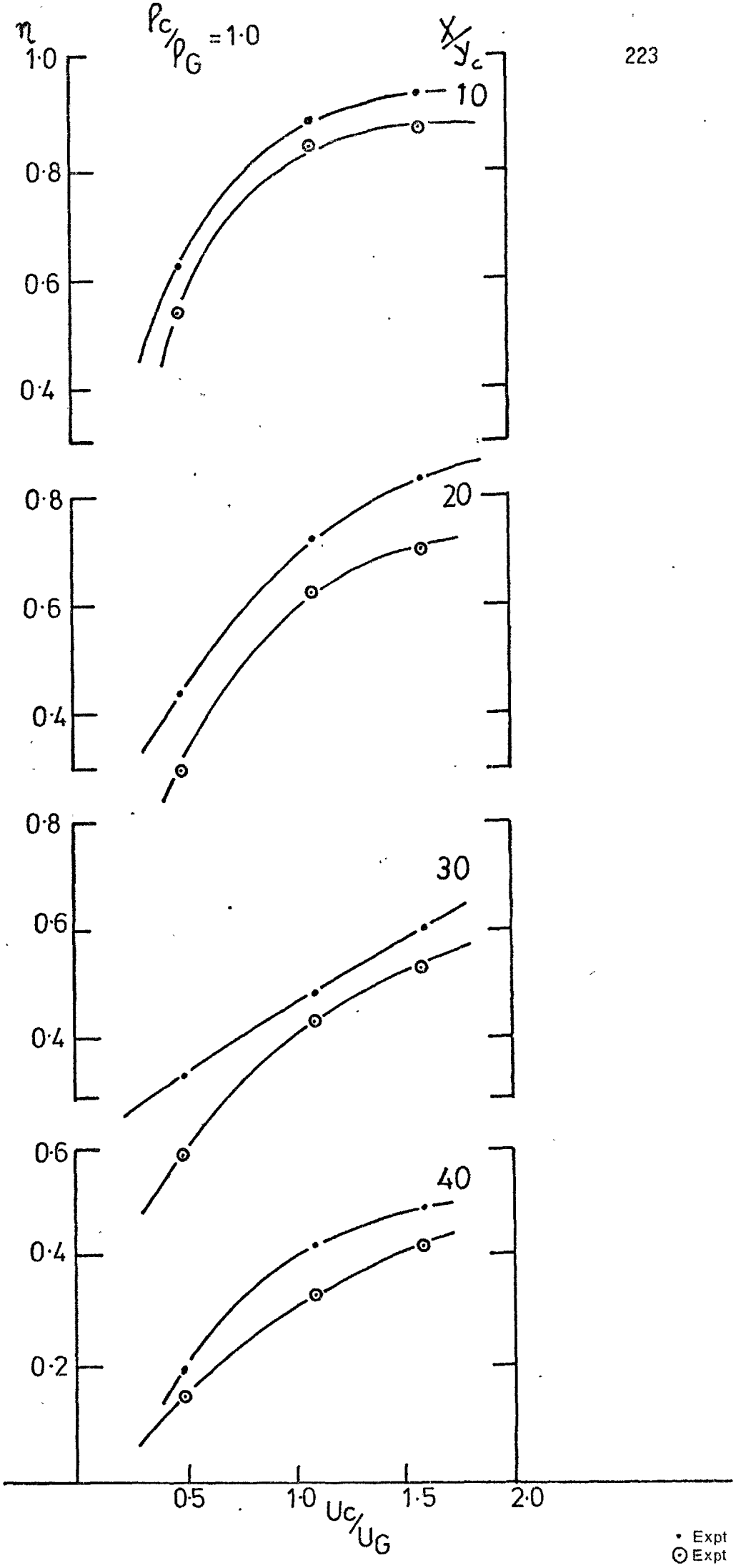

FIG. 4.2.23 INFLUENCE OF DISTANCE OF TANGENTAL HOLES EXI

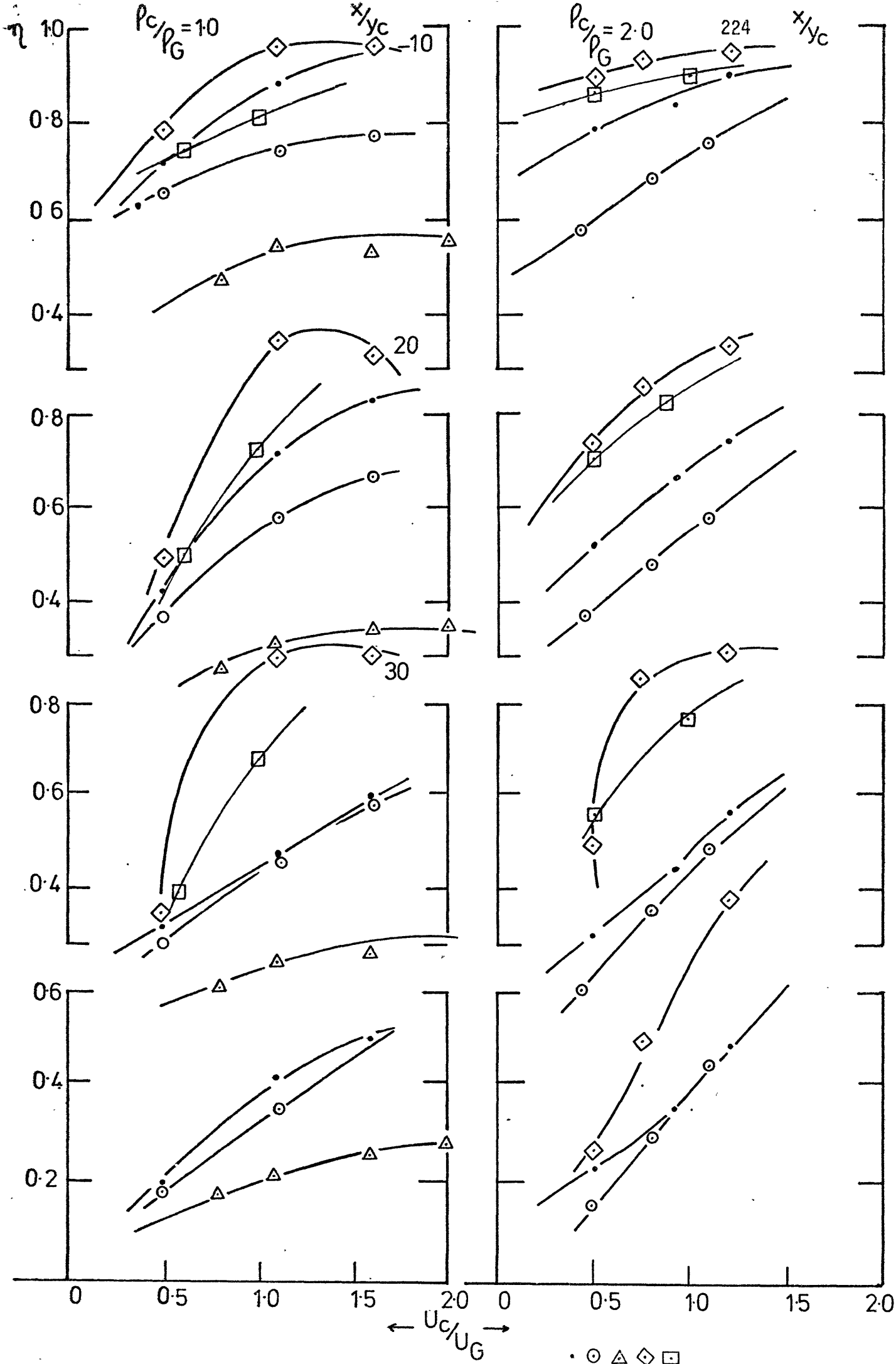

FIG. 3.2.21. INFLUENCE OF INJECTION GEOMETRY

Expts	•	⊙	△	◇	□
	9	22	32	24	33
	10	23		25	

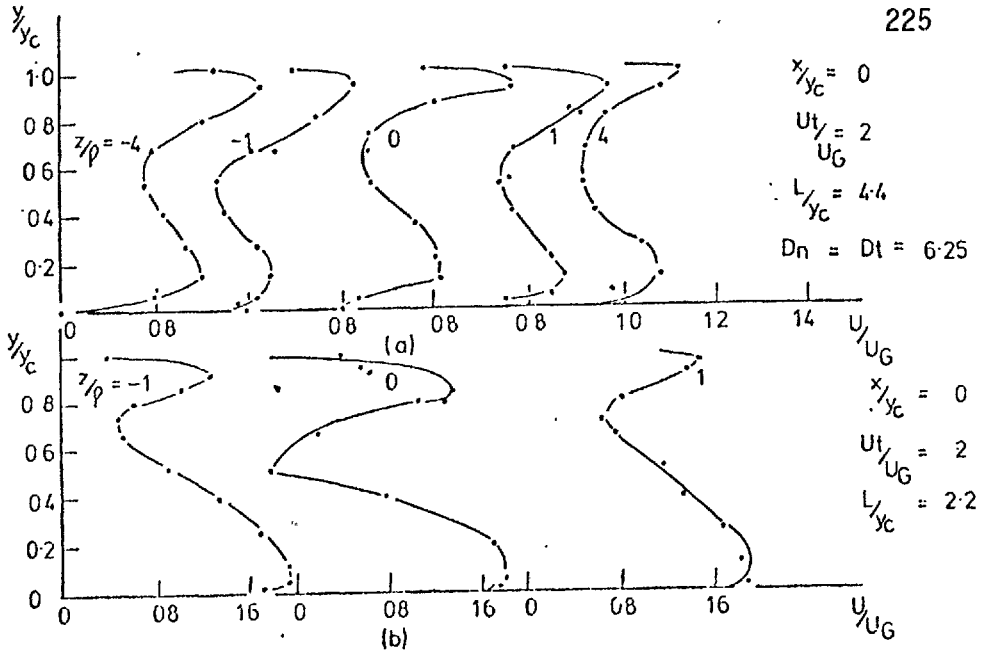

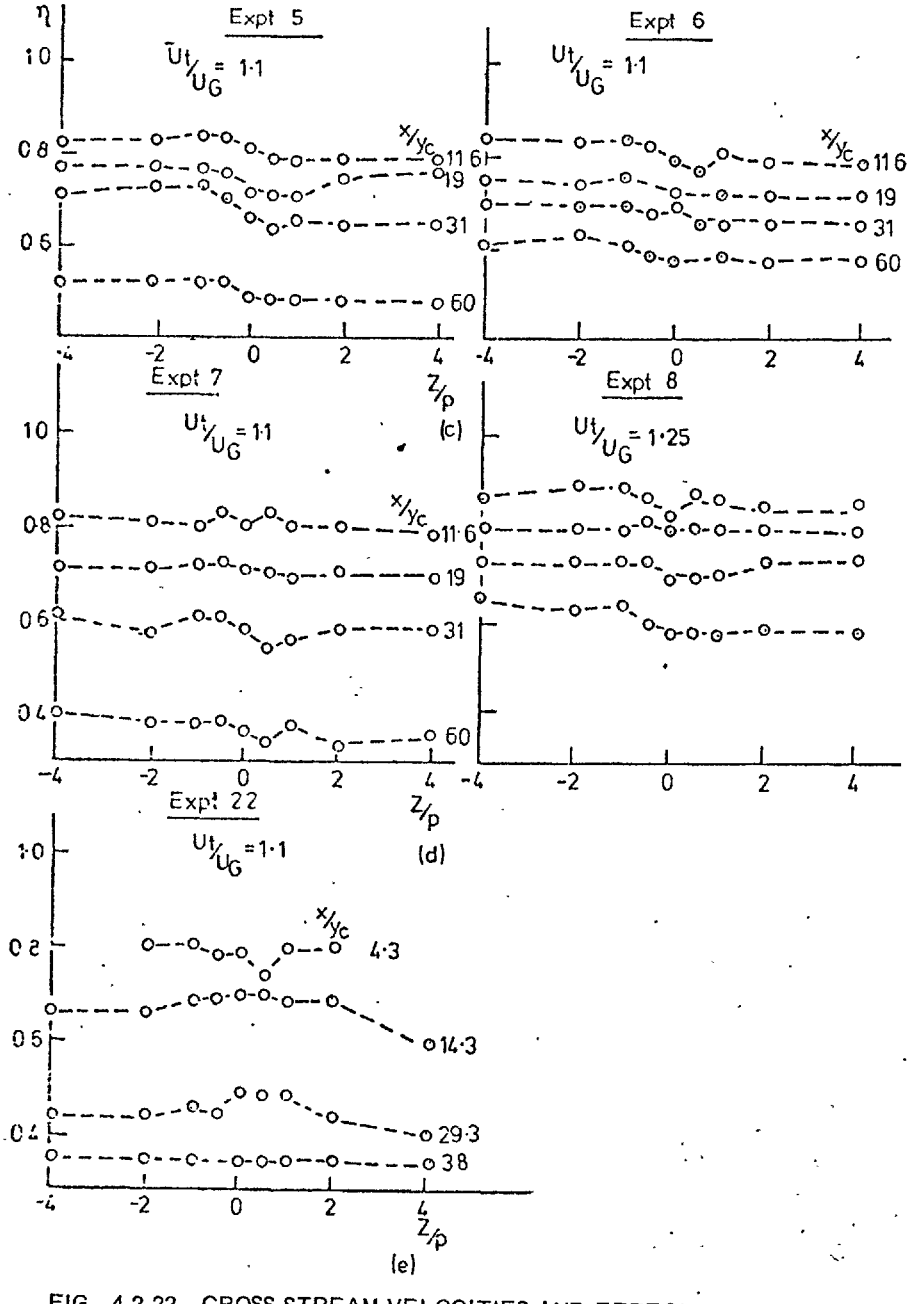

FIG. 4.2.22 CROSS STREAM VELOCITIES AND EFFECTIVENESS

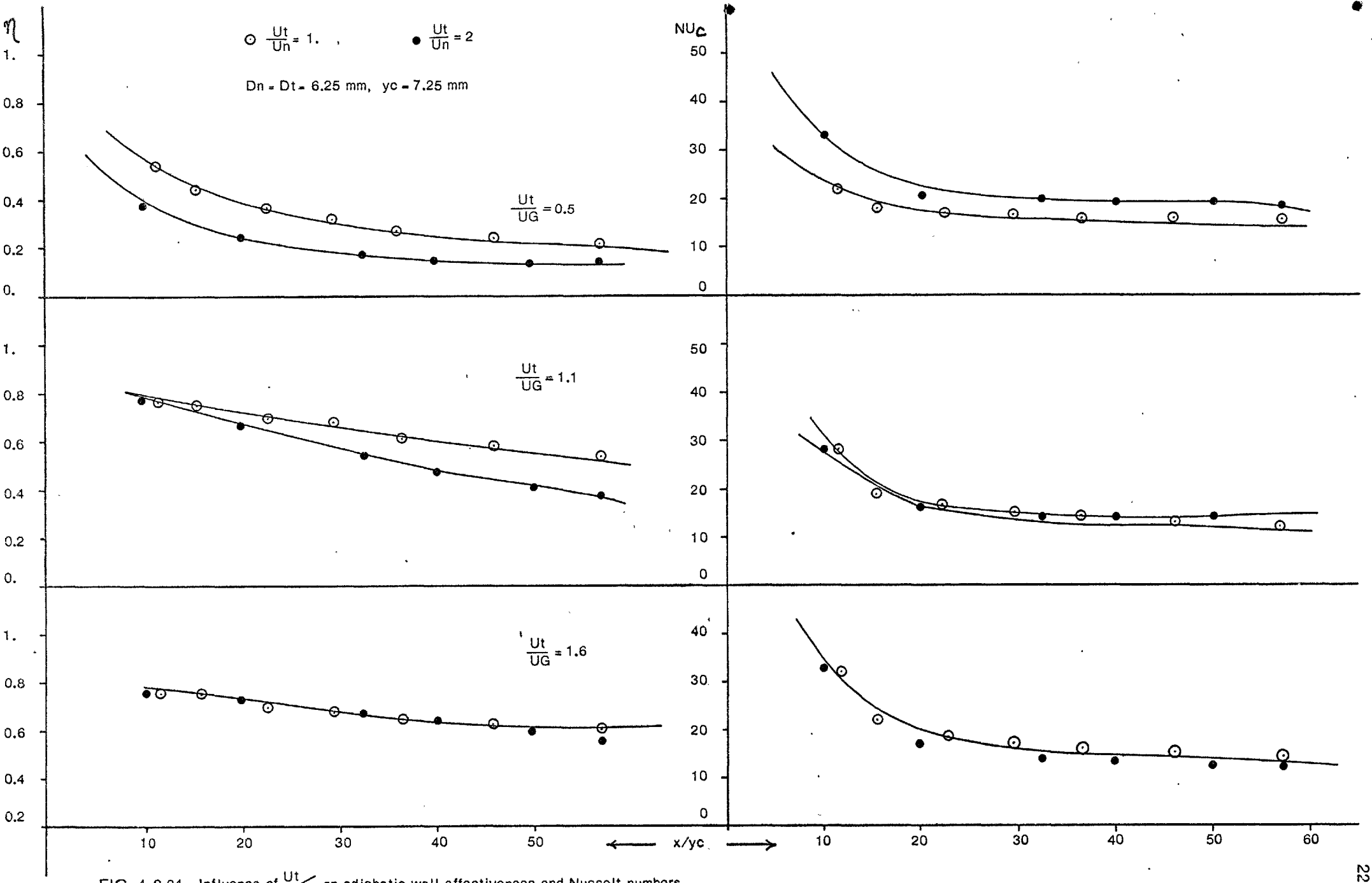

FIG. 4.2.24 Influence of $\frac{Ut}{Un}$ on adiabatic wall effectiveness and Nusselt numbers.

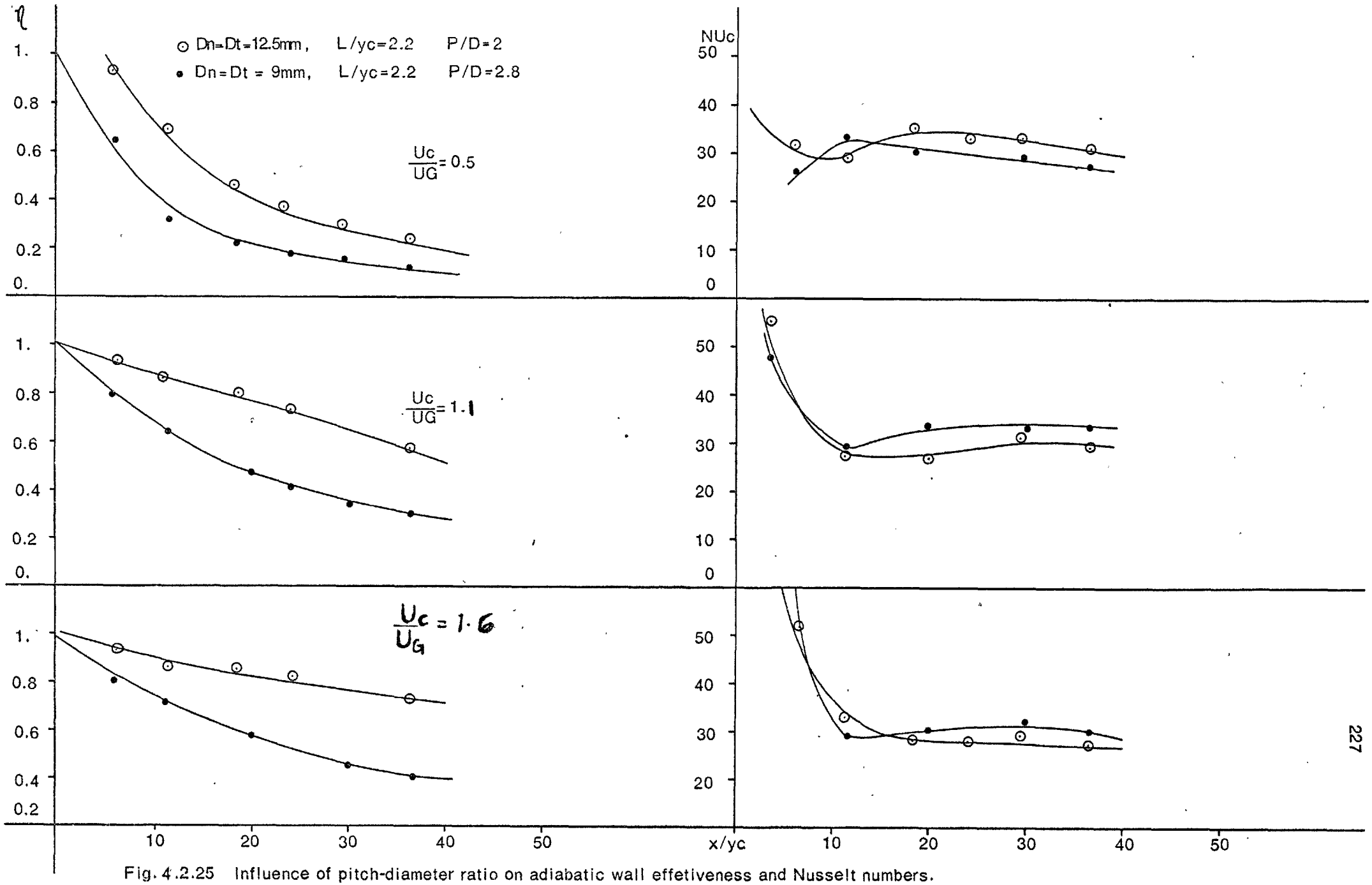

Fig. 4.2.25 Influence of pitch-diameter ratio on adiabatic wall effetiveness and Nusselt numbers.

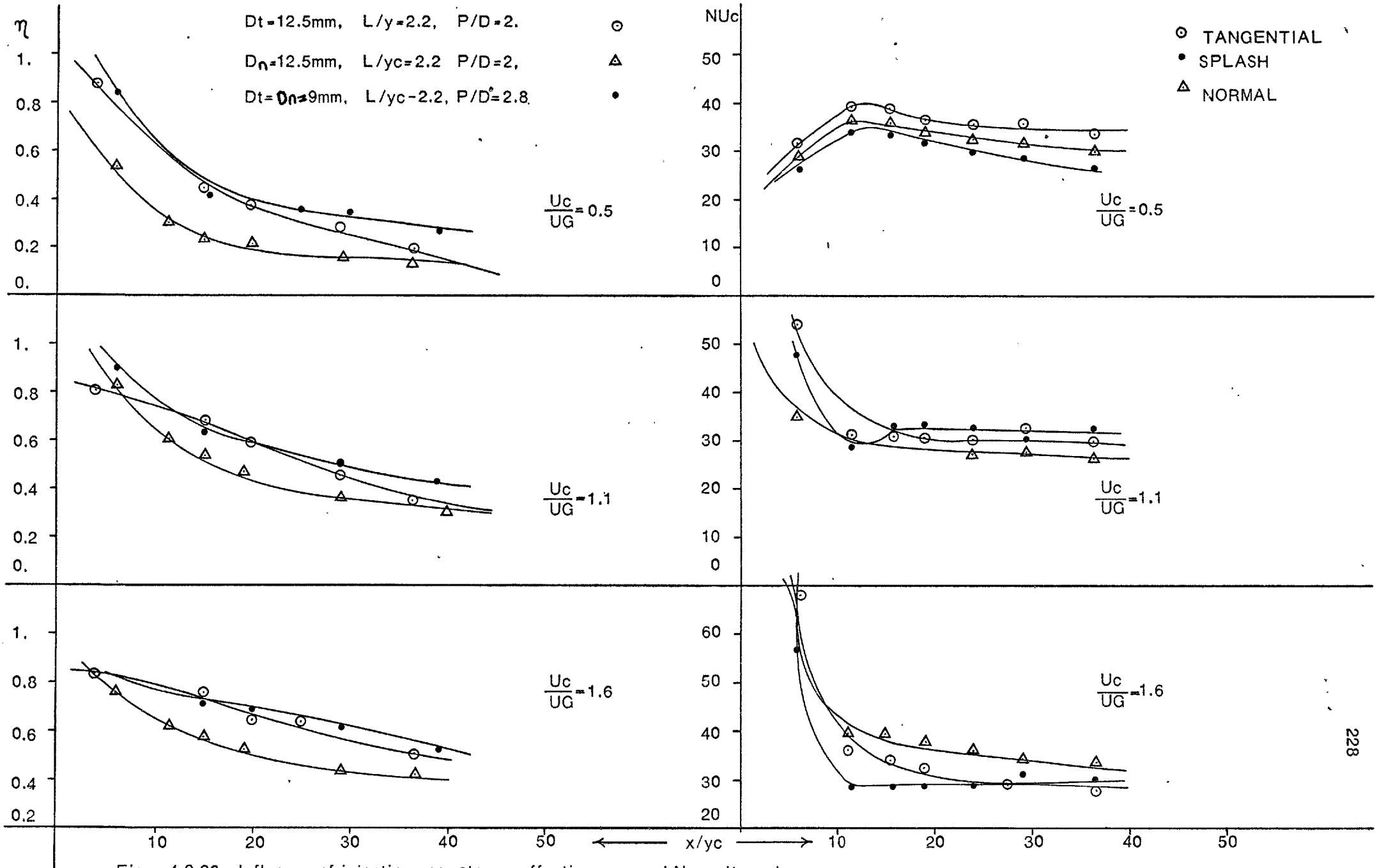

Fig. 4.2.26 Influence of injection geometry on effectiveness and Nusselt numbers.

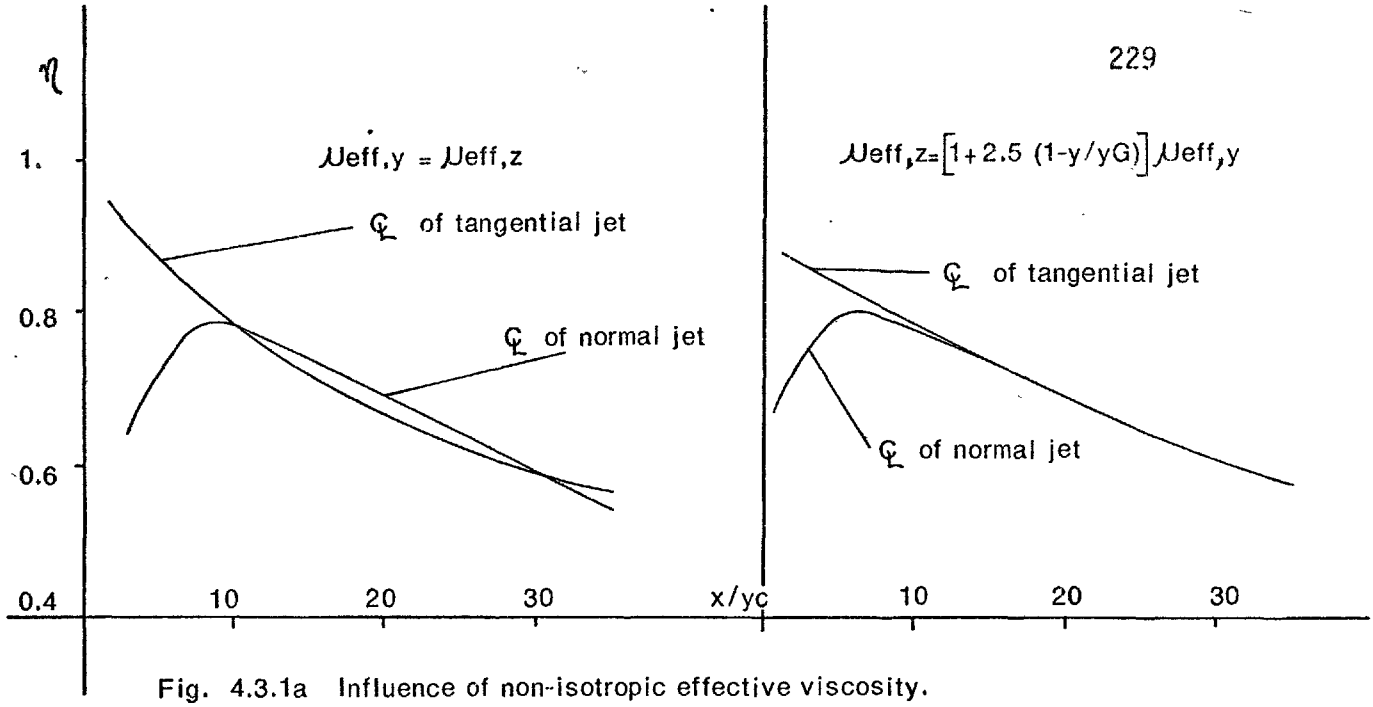

Fig. 4.3.1a Influence of non-isotropic effective viscosity.

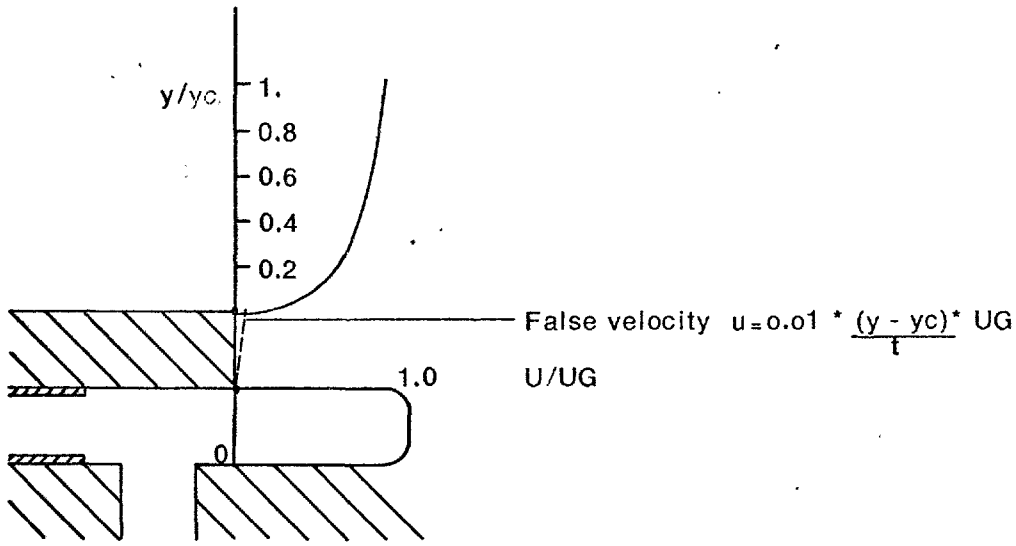

Fig. 4.3.1 b. Mainstream and lip velocity profiles at slot exit for thick lipped slots

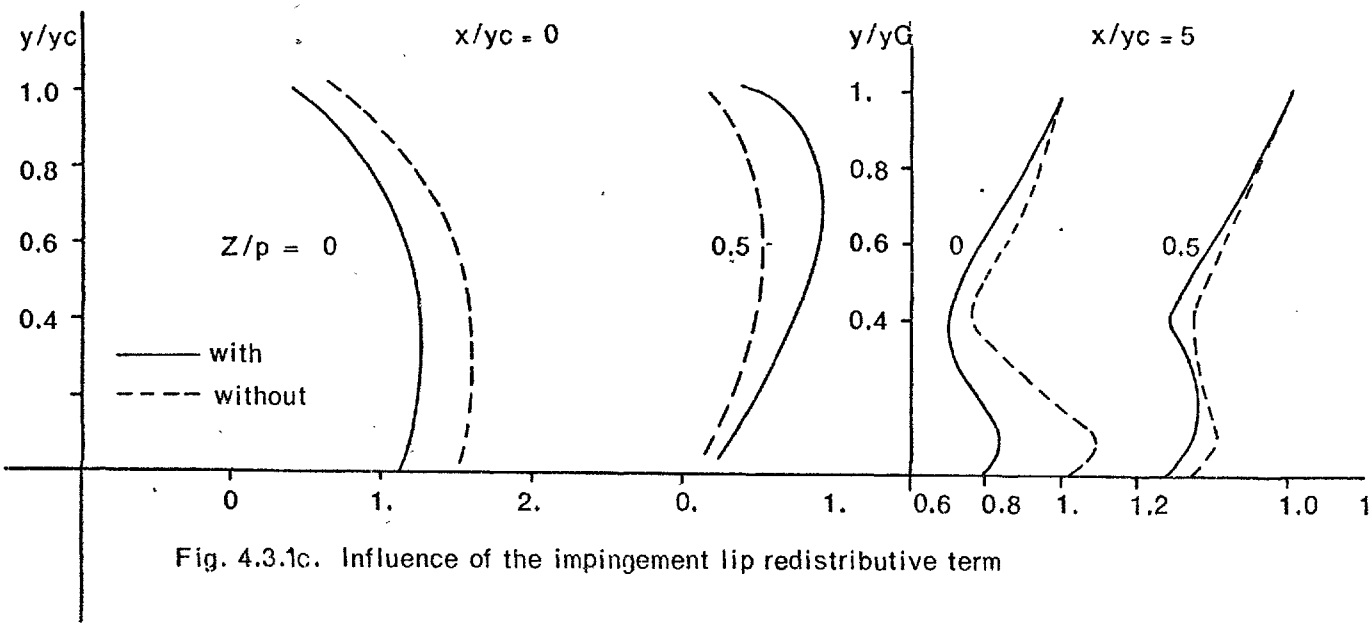

Fig. 4.3.1c. Influence of the impingement lip redistributive term

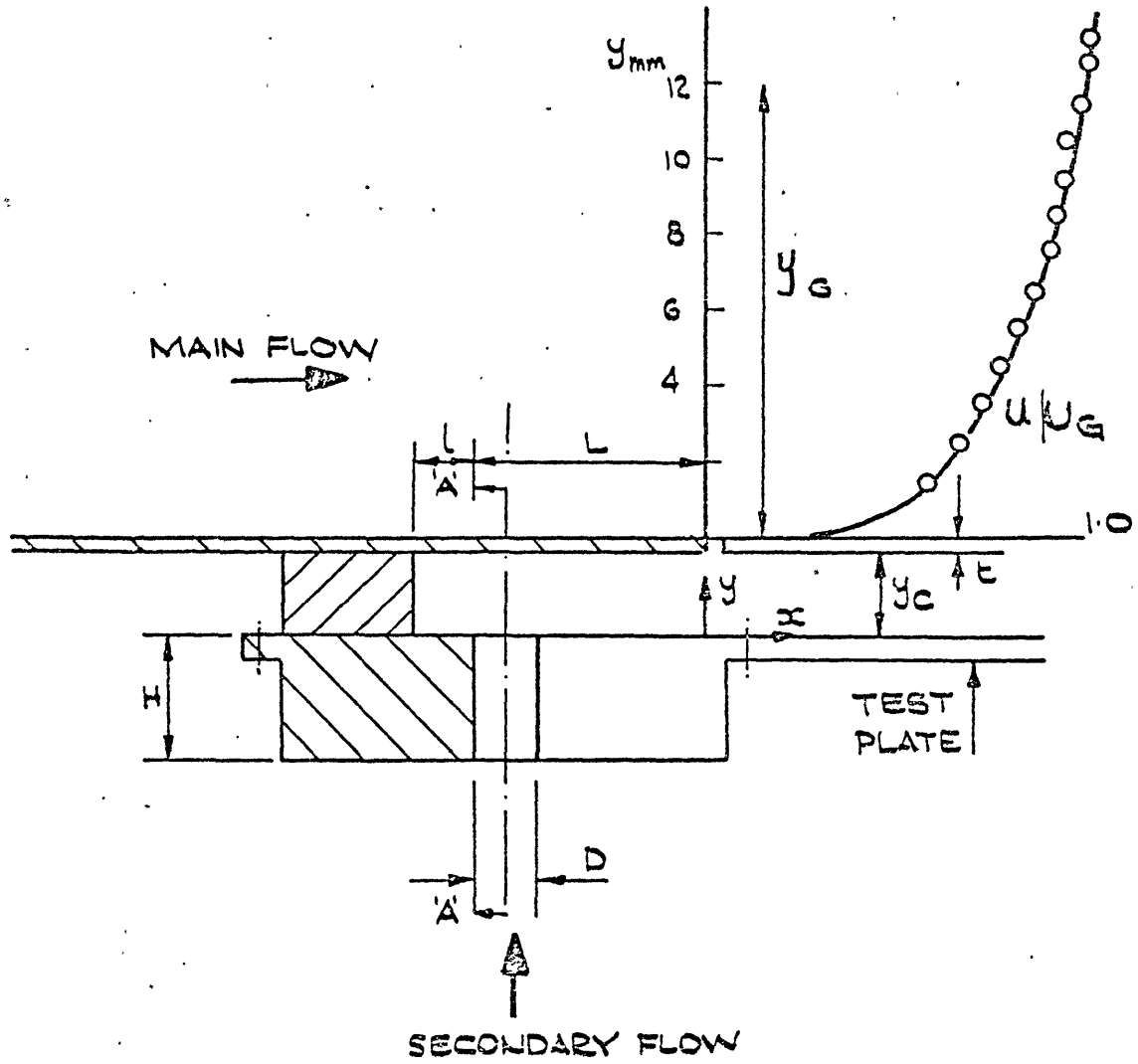

FIG. 4.4.1. SLOT CONFIGURATION FOR NORMAL HOLES CALCULATIONS

SECTION 'A'A'

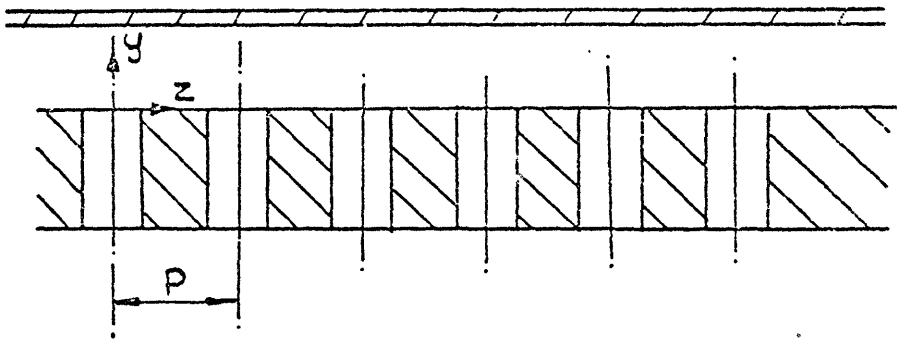

PLAN OF TWO ROW SLOT

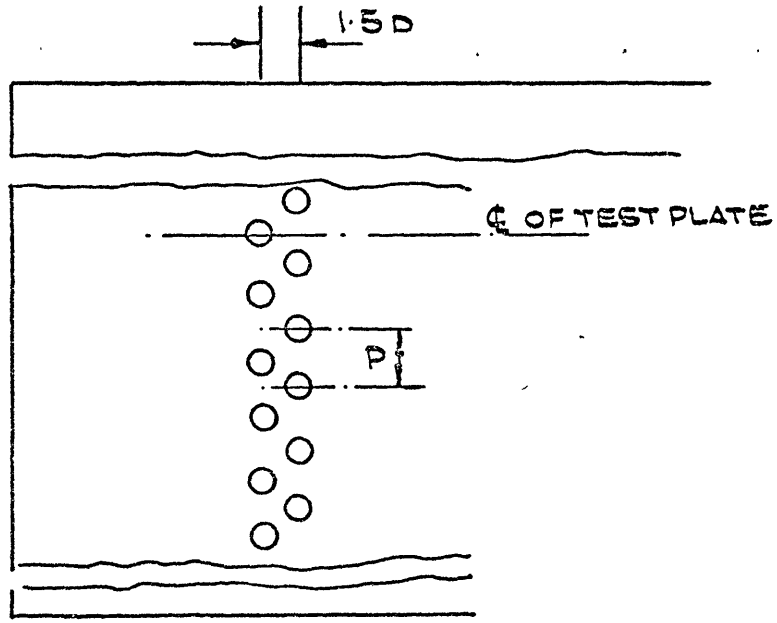

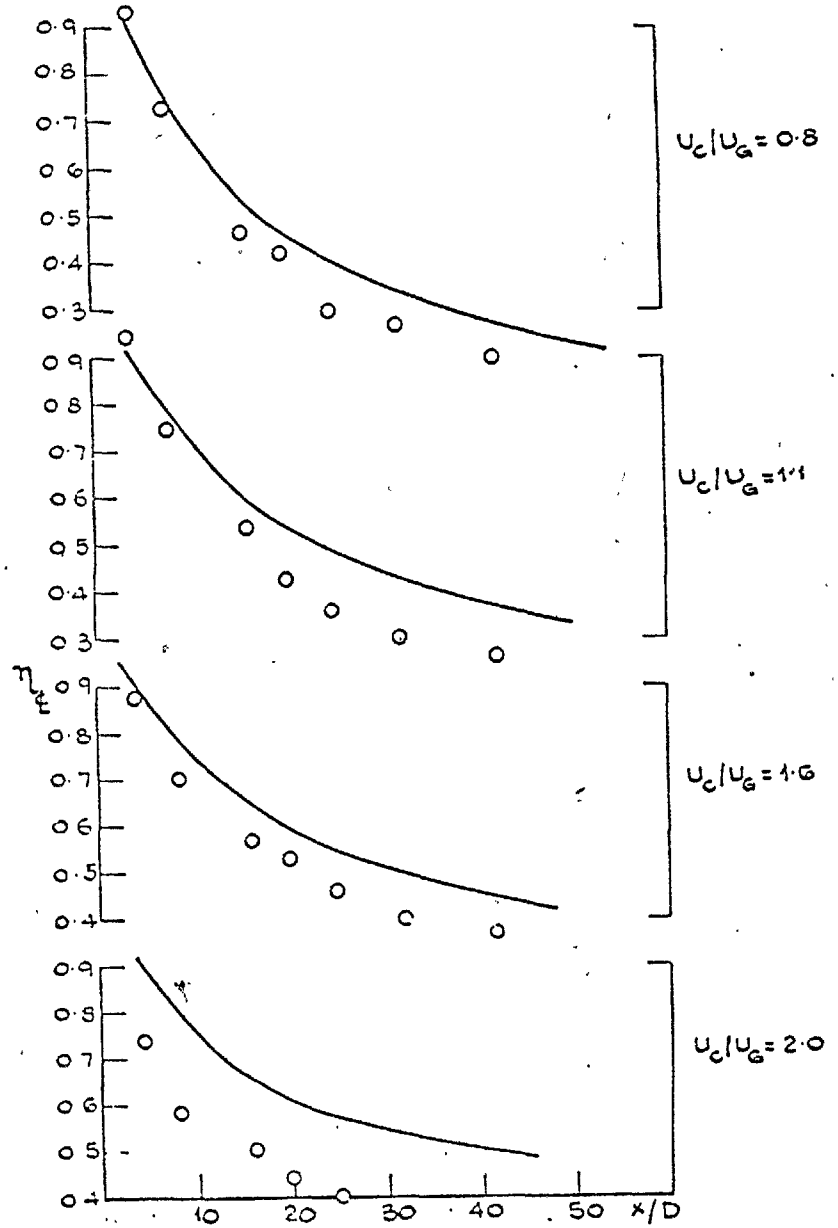

FIG. 4.4.2a COMPARISON OF CALCULATED AND MEASURED IMPERVIOUS-WALL EFFECTIVENESS
P/D = 2, D = 12.5, L/D = 4

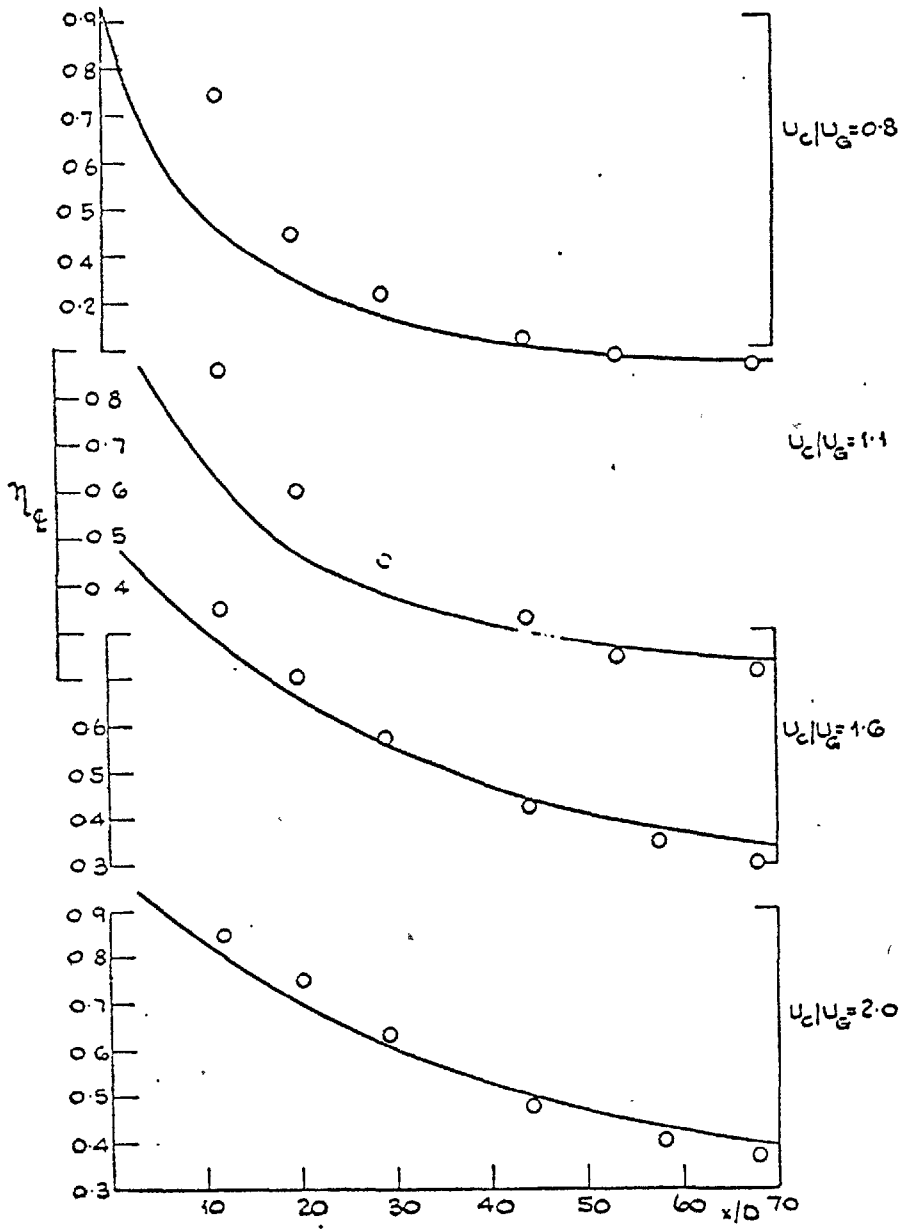

FIG. 4.4.2b COMPARISON OF CALCULATED AND MEASURED IMPERVIOUS-WALL EFFECTIVENESS
P/D = 2.0, D = 6.25, L/D = 4

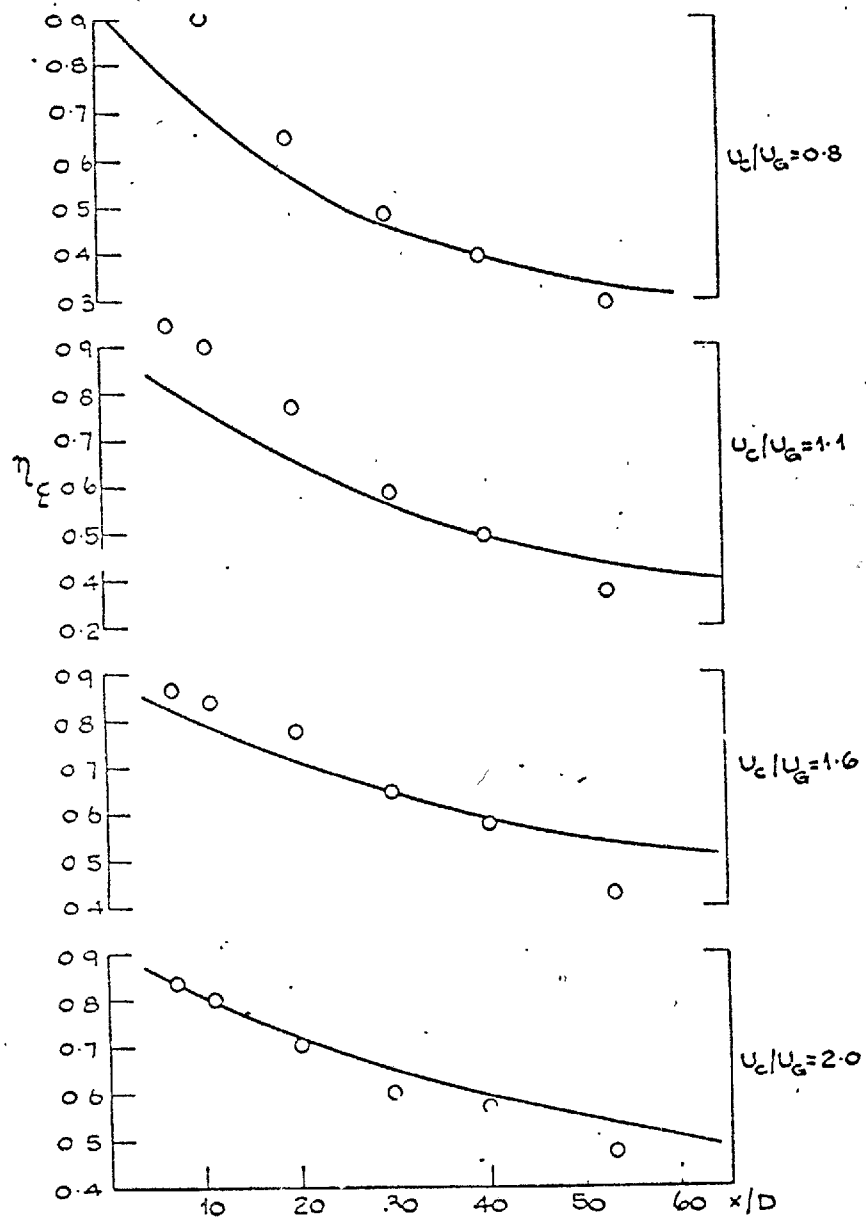

FIG. 4.4.3. COMPARISON OF MEASURED AND CALCULATED IMPERVIOUS WALL EFFECTIVENESS
P/D = 1.4, D = 9, L/D = 4

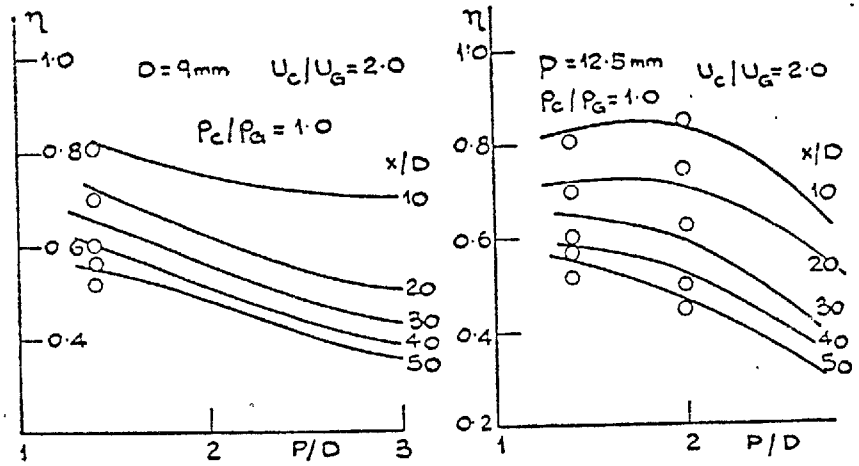

FIG. 4.4.4 INFLUENCE OF PITCH DIAMETER RATIO

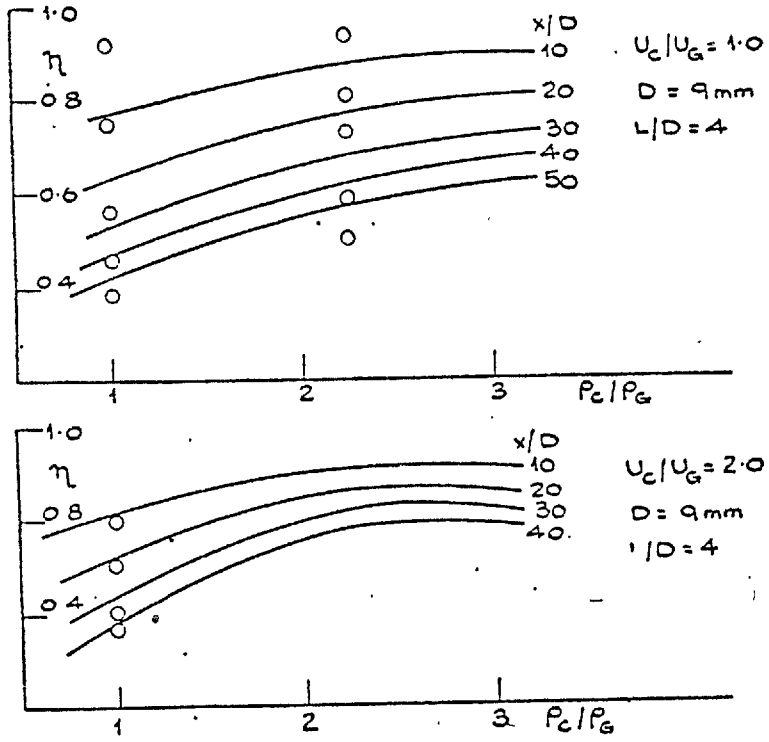

FIG. 4.4.5 INFLUENCE OF DENSITY RATIO

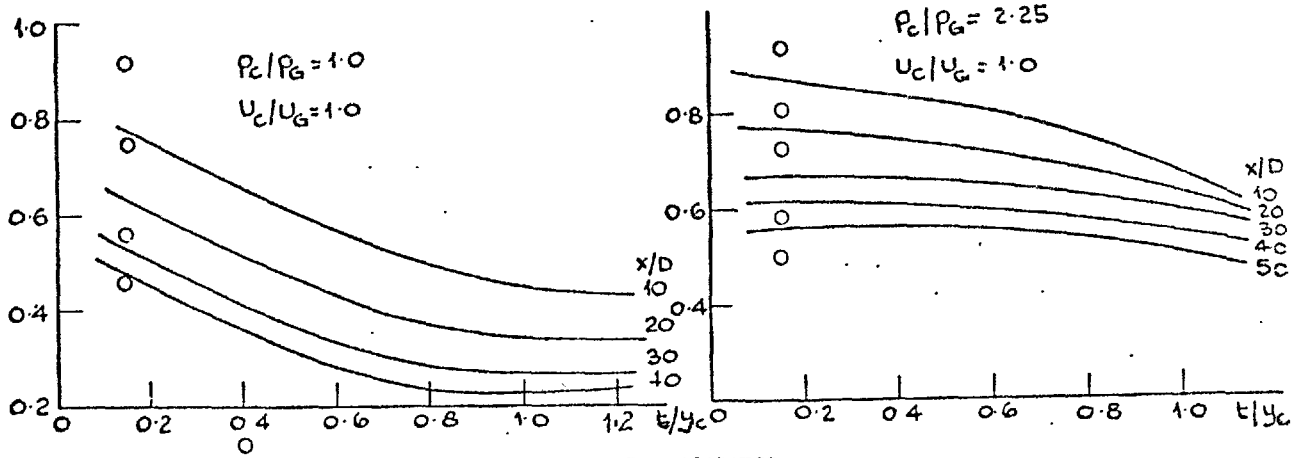

FIG. 4.4.6 INFLUENCE OF LIP THICKNESS

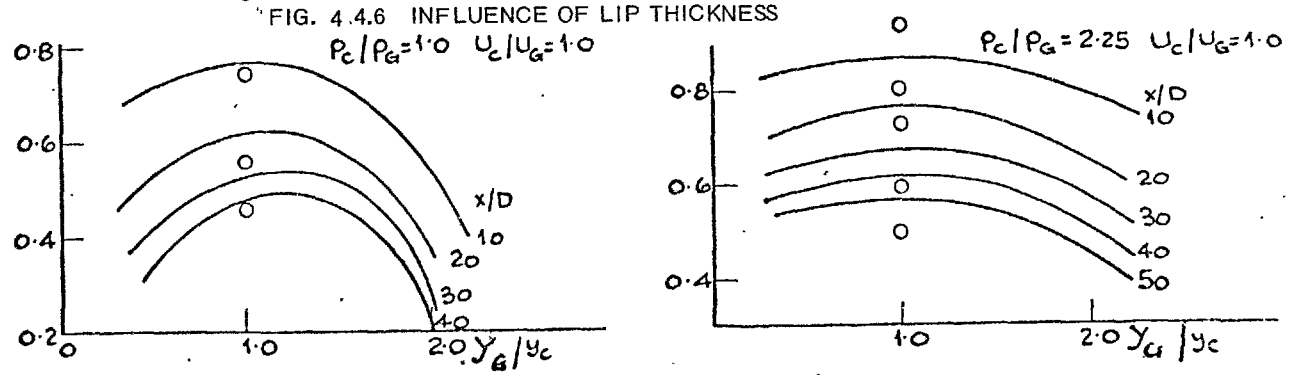

FIG. 4.4.7. INFLUENCE OF $y_{G/yc}$

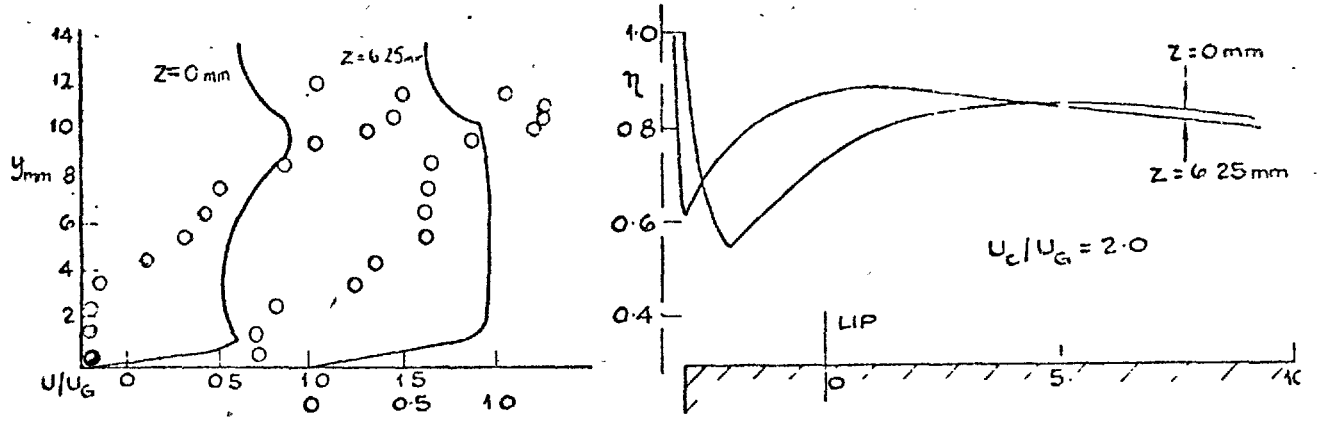

a). MEAN VELOCITY PROFILES AT X = 0

b). EFFECTIVENESS IN INJECTION REGION

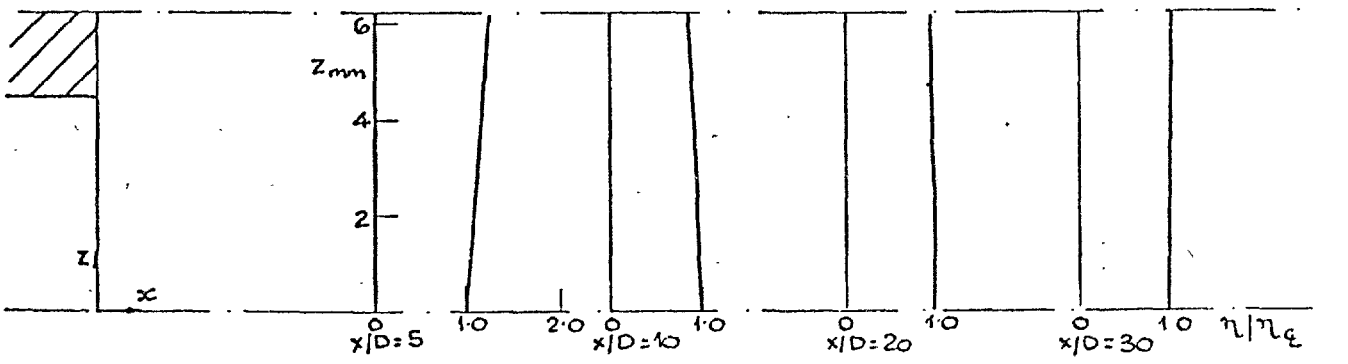

c). VARIATION OF EFFECTIVENESS IN CROSS-STREAM PLANES

FIG. 4.4.8. SOME IMPORTANT FEATURES

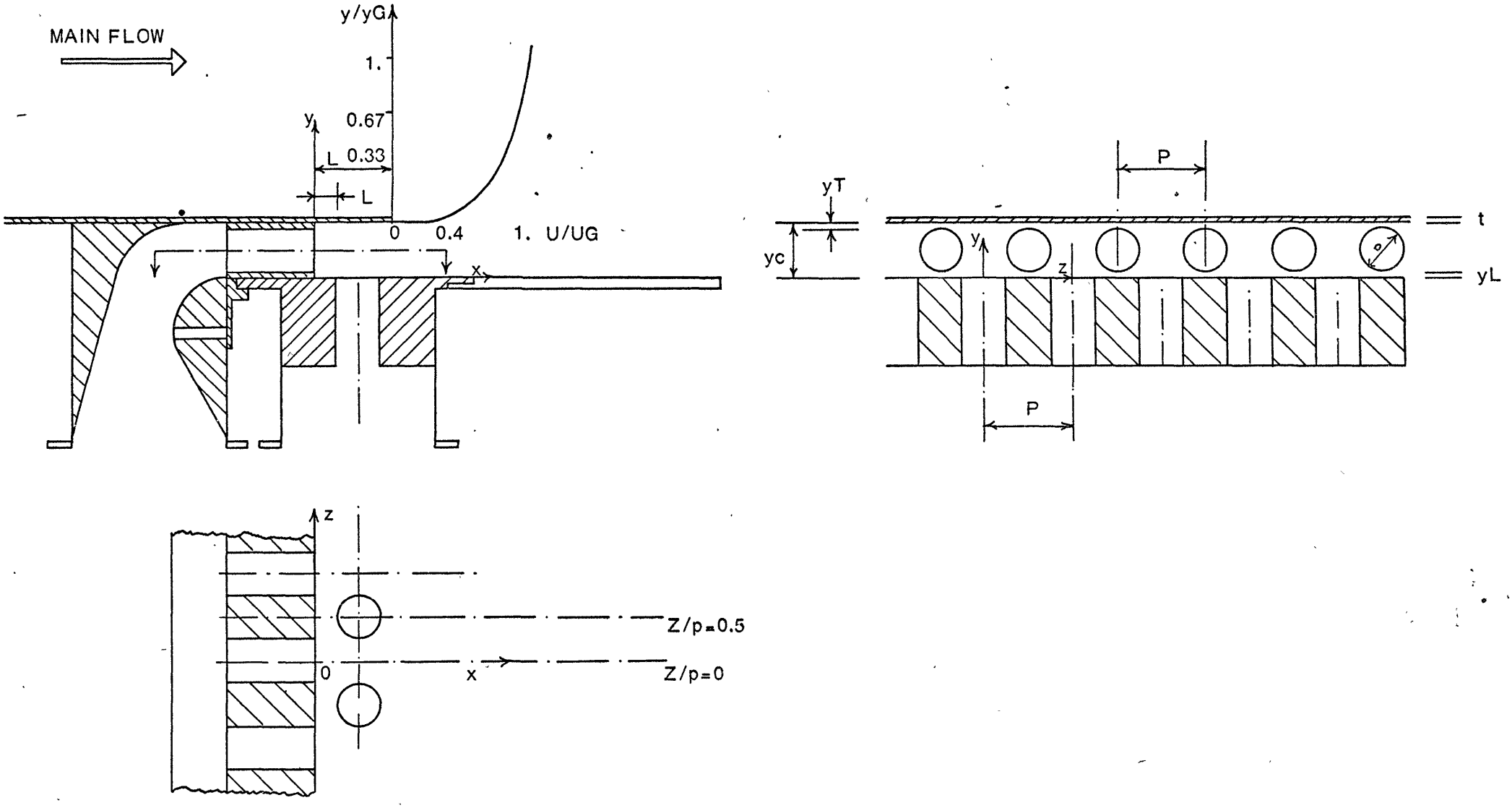

Fig. 4.4.9 Flow configurations for combined normal and tangential holes calculations.

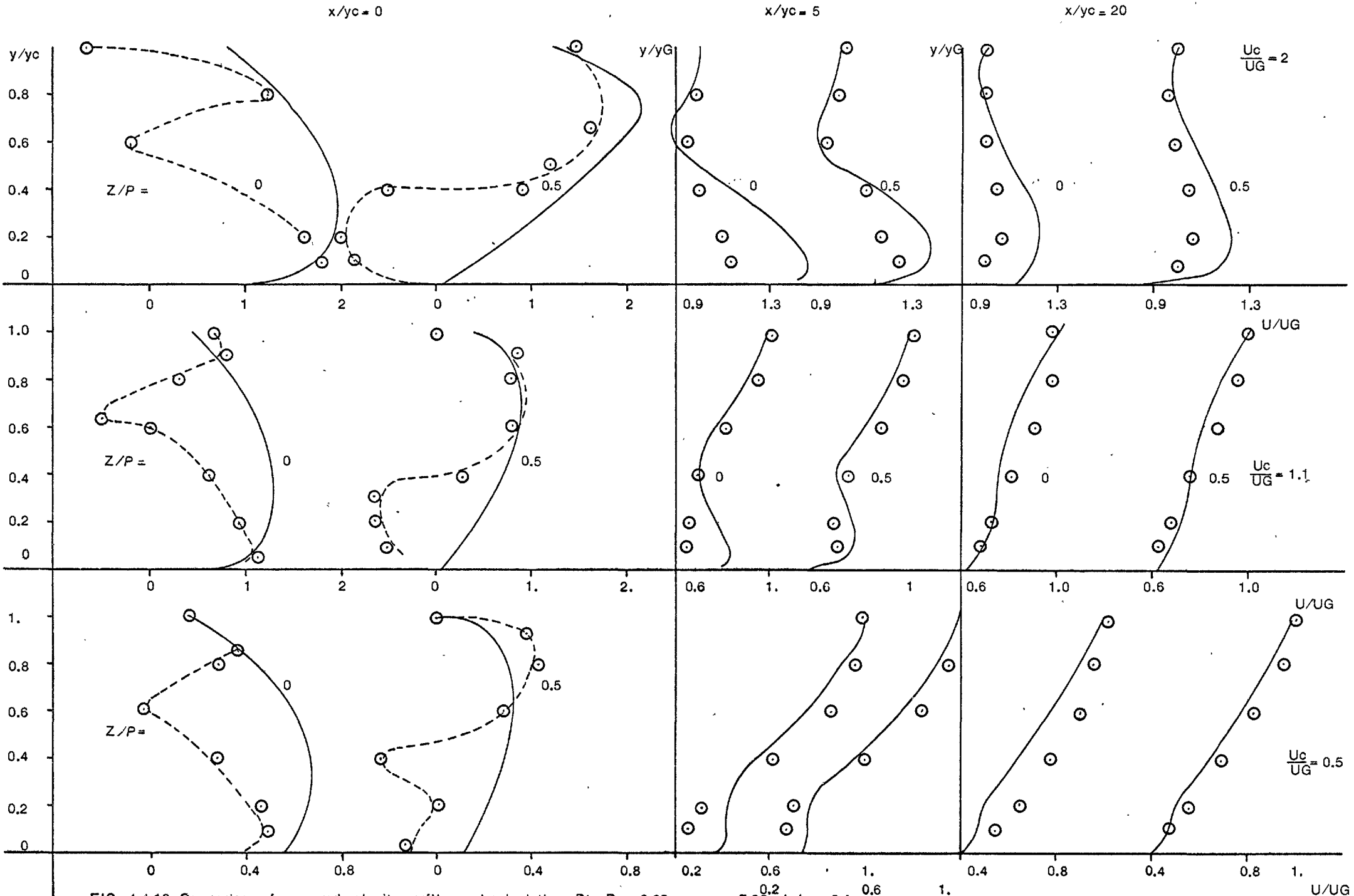

FIG. 4.4.10 Comparison of measured velocity profiles and calculations Dt = Dn = 6.25 mm, yc = 7.25 L/yc = 2.2.

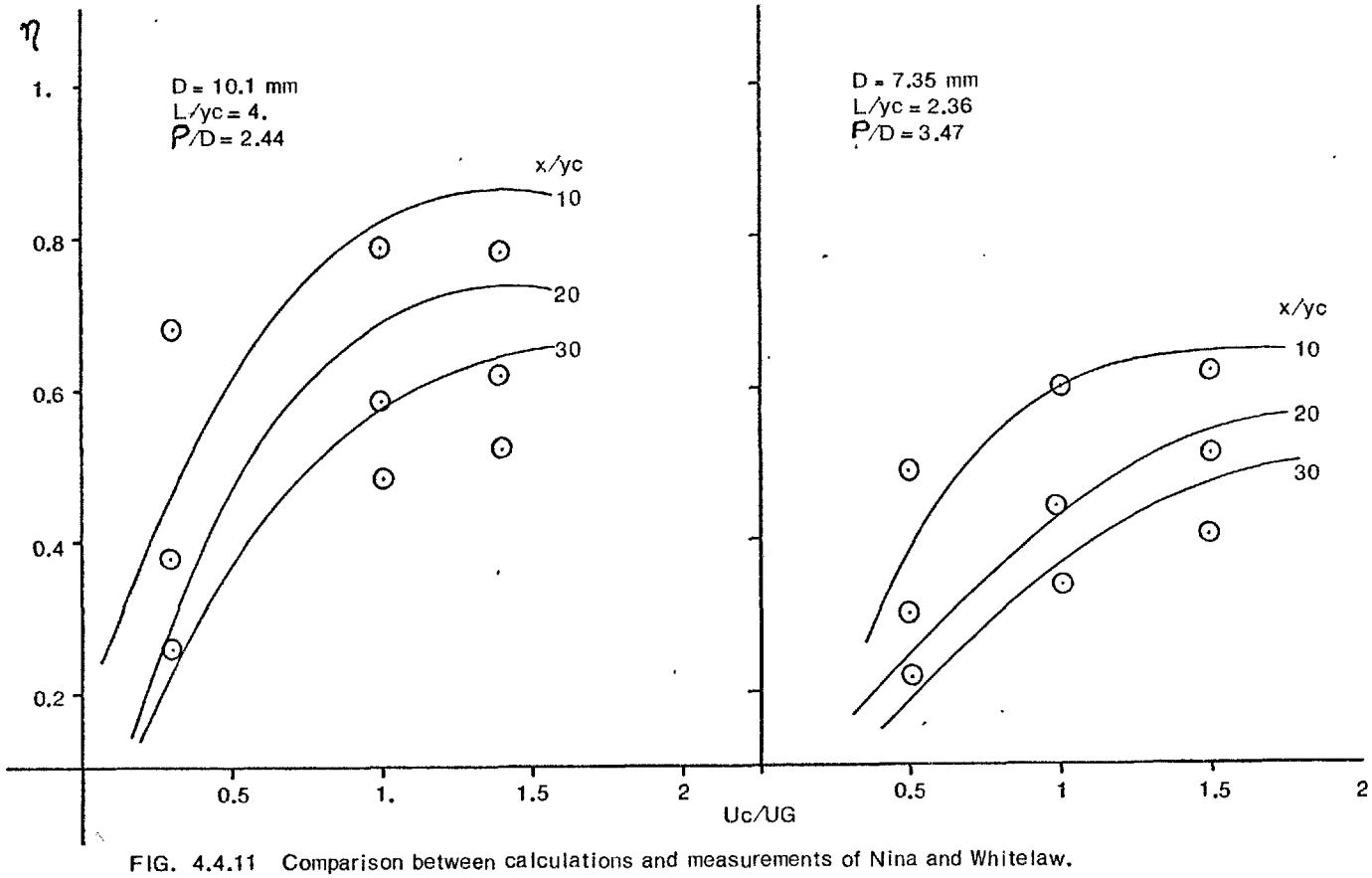

FIG. 4.4.11 Comparison between calculations and measurements of Nina and Whitelaw.

(a)

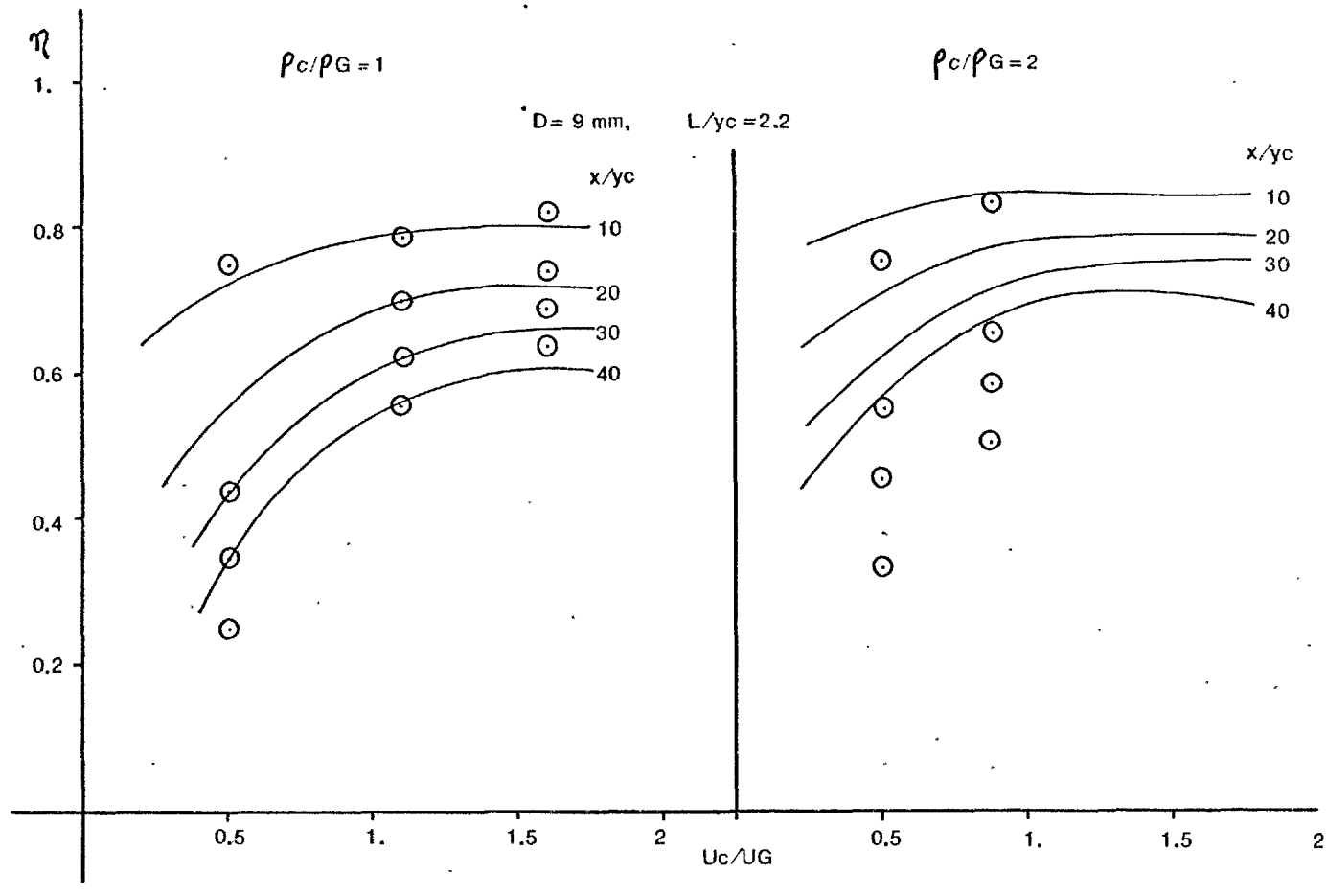

FIG. 4.4.11 Comparison between calculations and present measurements

(b)

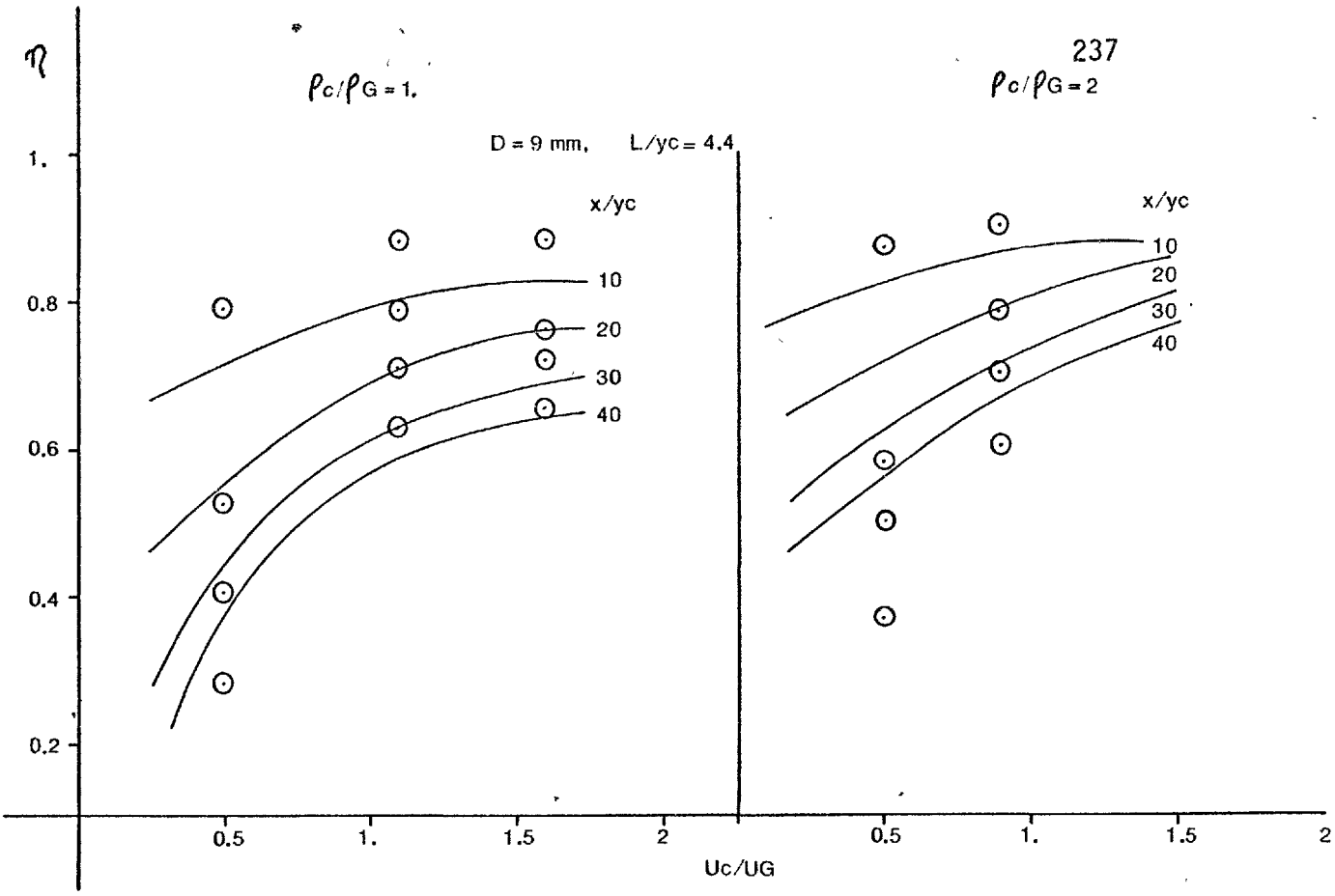

FIG. 4.4.11 Comparison between calculations and present measurements

(c)

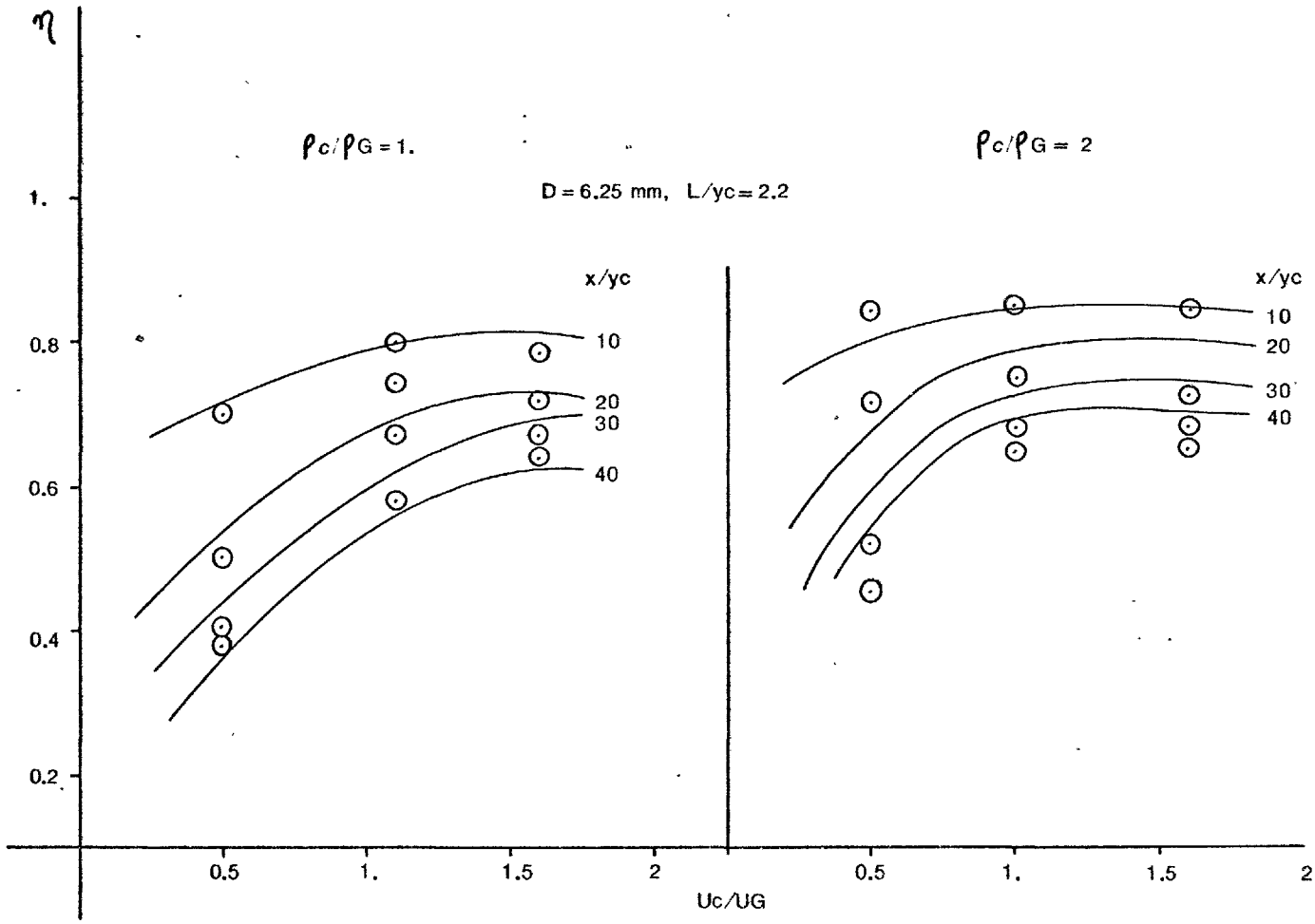

FIG. 4.4.11 Comparison between calculations and present measurements

(d)

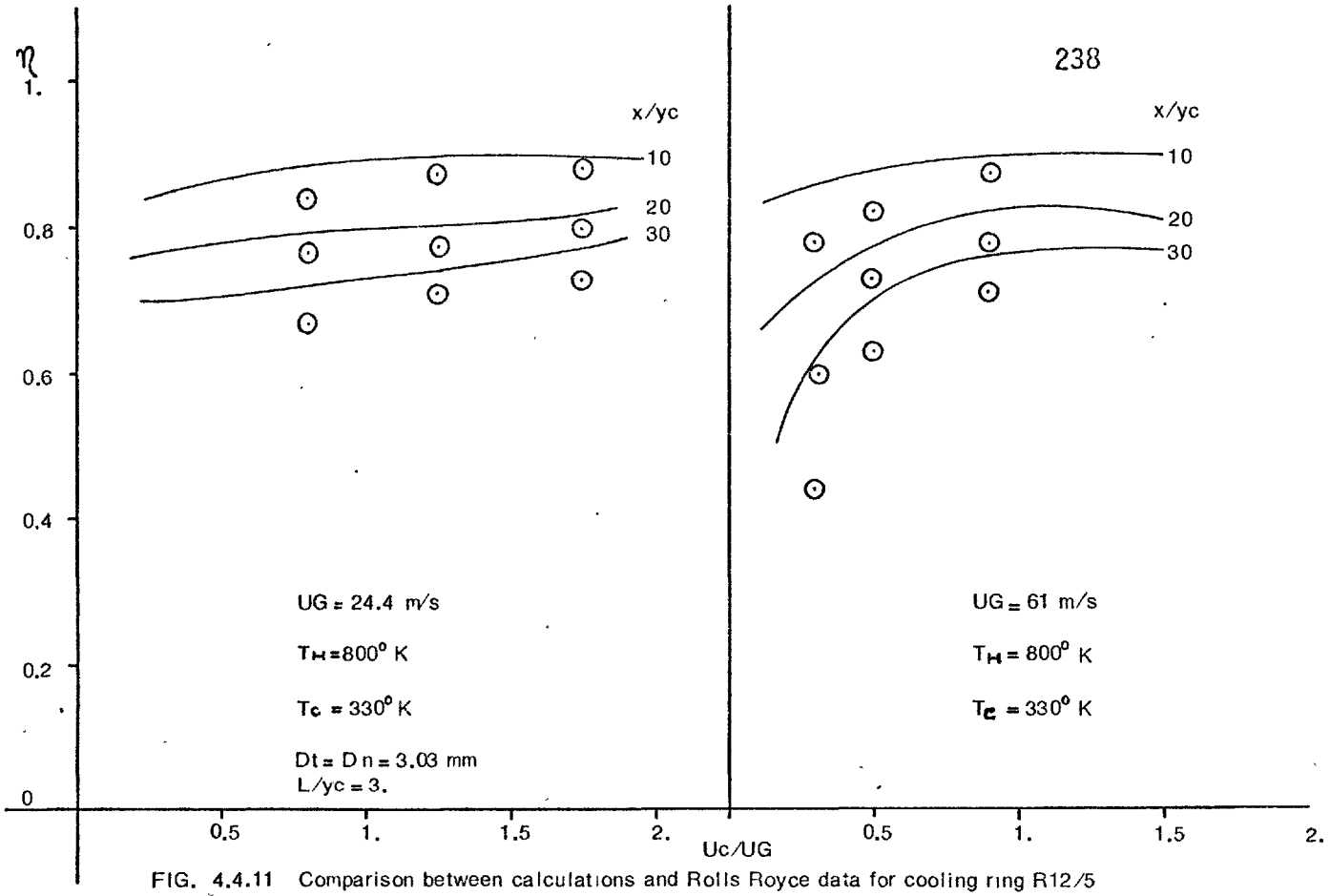

FIG. 4.4.11 Comparison between calculations and Rolls Royce data for cooling ring R12/5

(e)

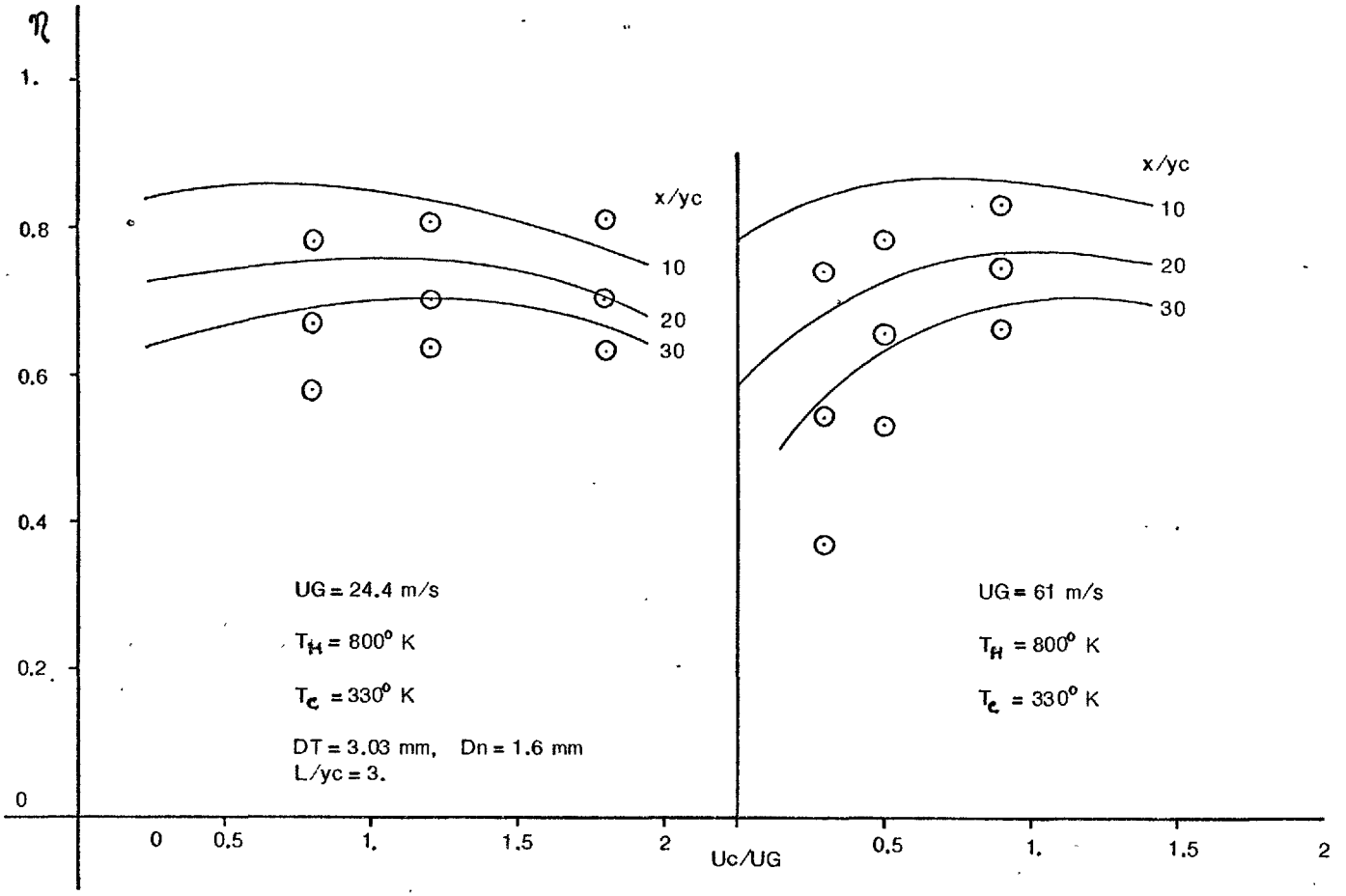

FIG. 4.4.11 Comparison between calculations and Rolls Royce data for cooling ring R12/3

(f)

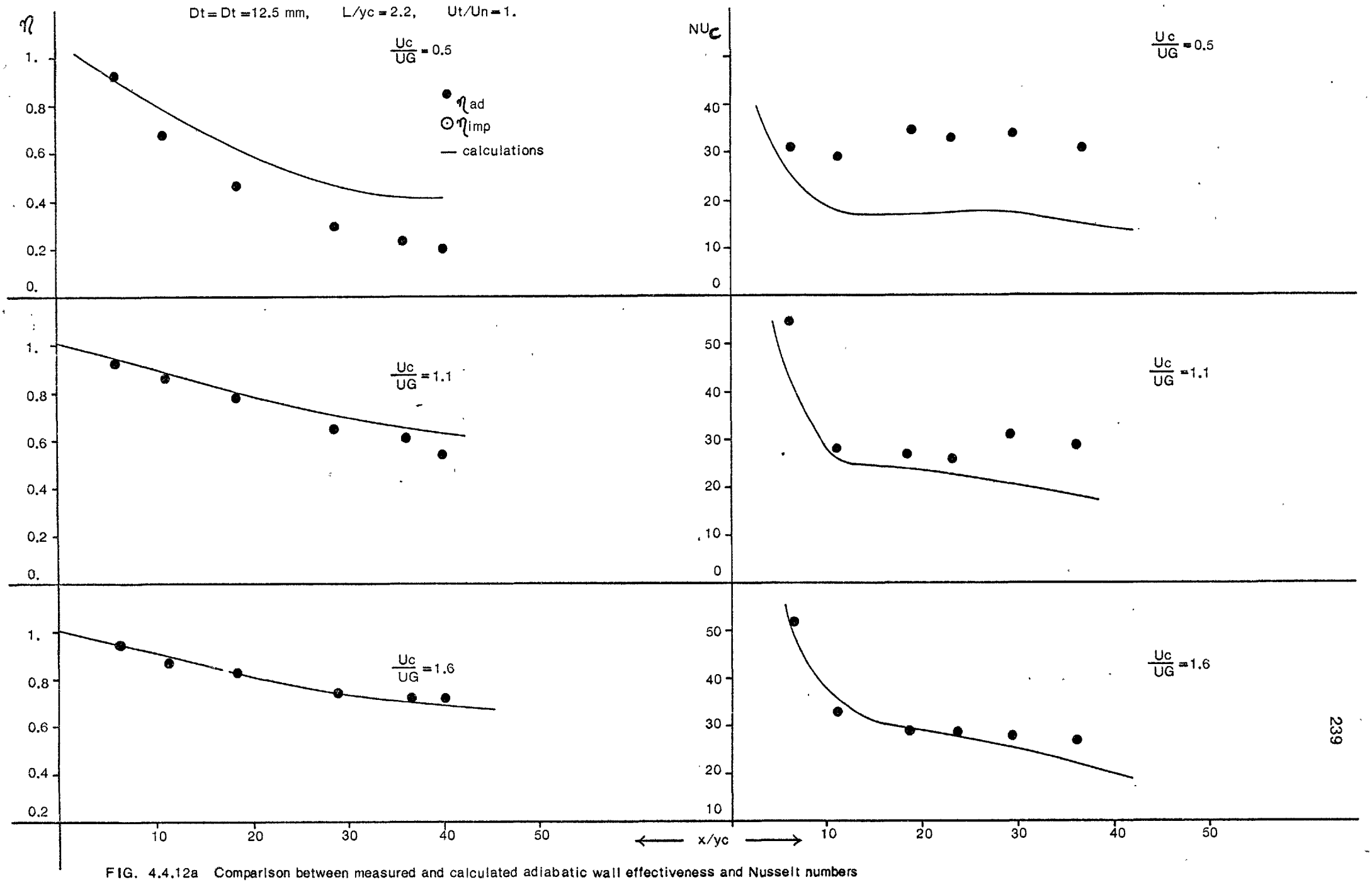

FIG. 4.4.12a Comparison between measured and calculated adiabatic wall effectiveness and Nusselt numbers

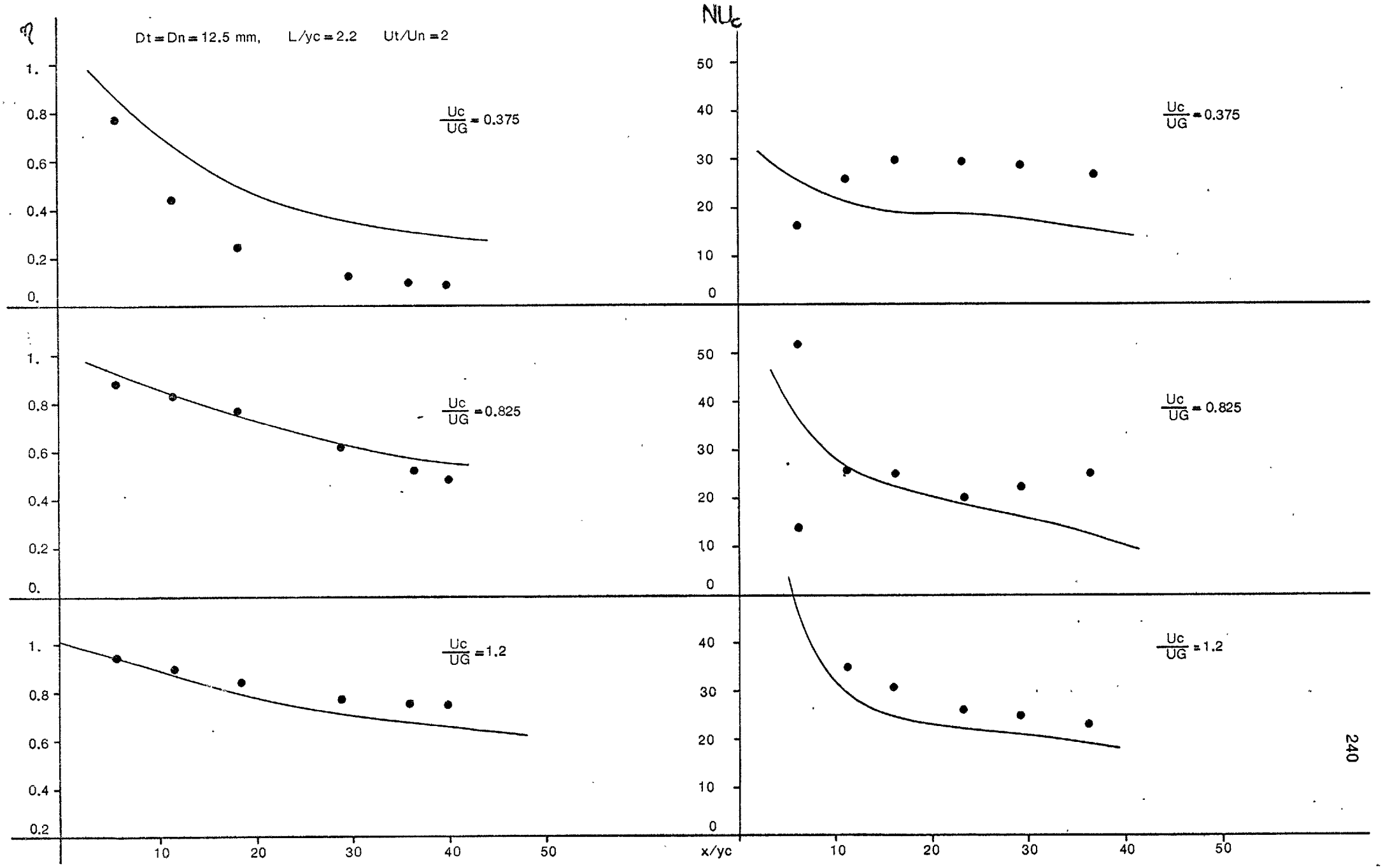

FIG. 4.4.12b Comparison between measured and calculated adiabatic wall effectiveness and Nusselt numbers.

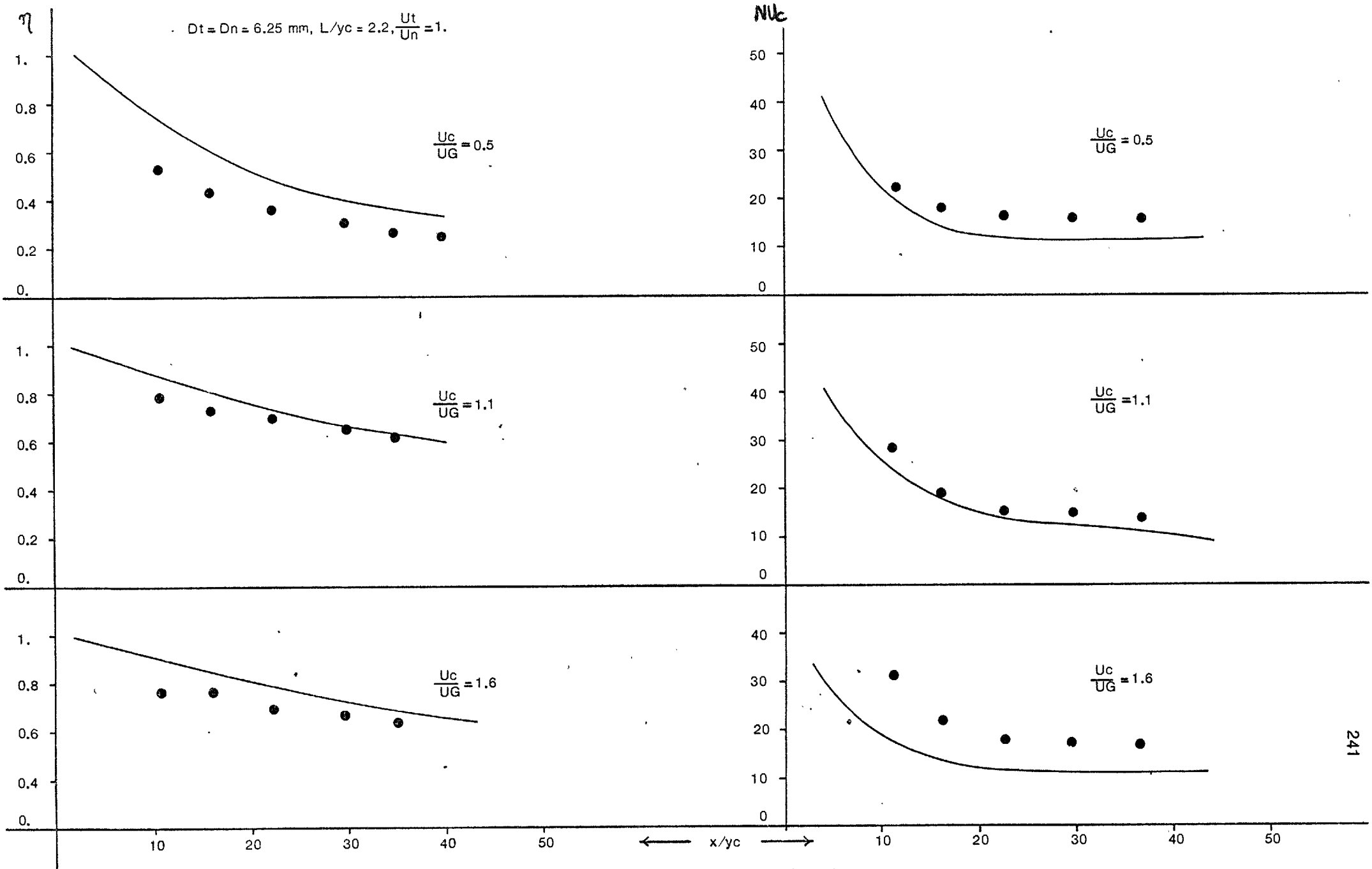

FIG. 4.4.12c Comparison between measured and calculated adiabatic wall effectiveness and Nusselt numbers.

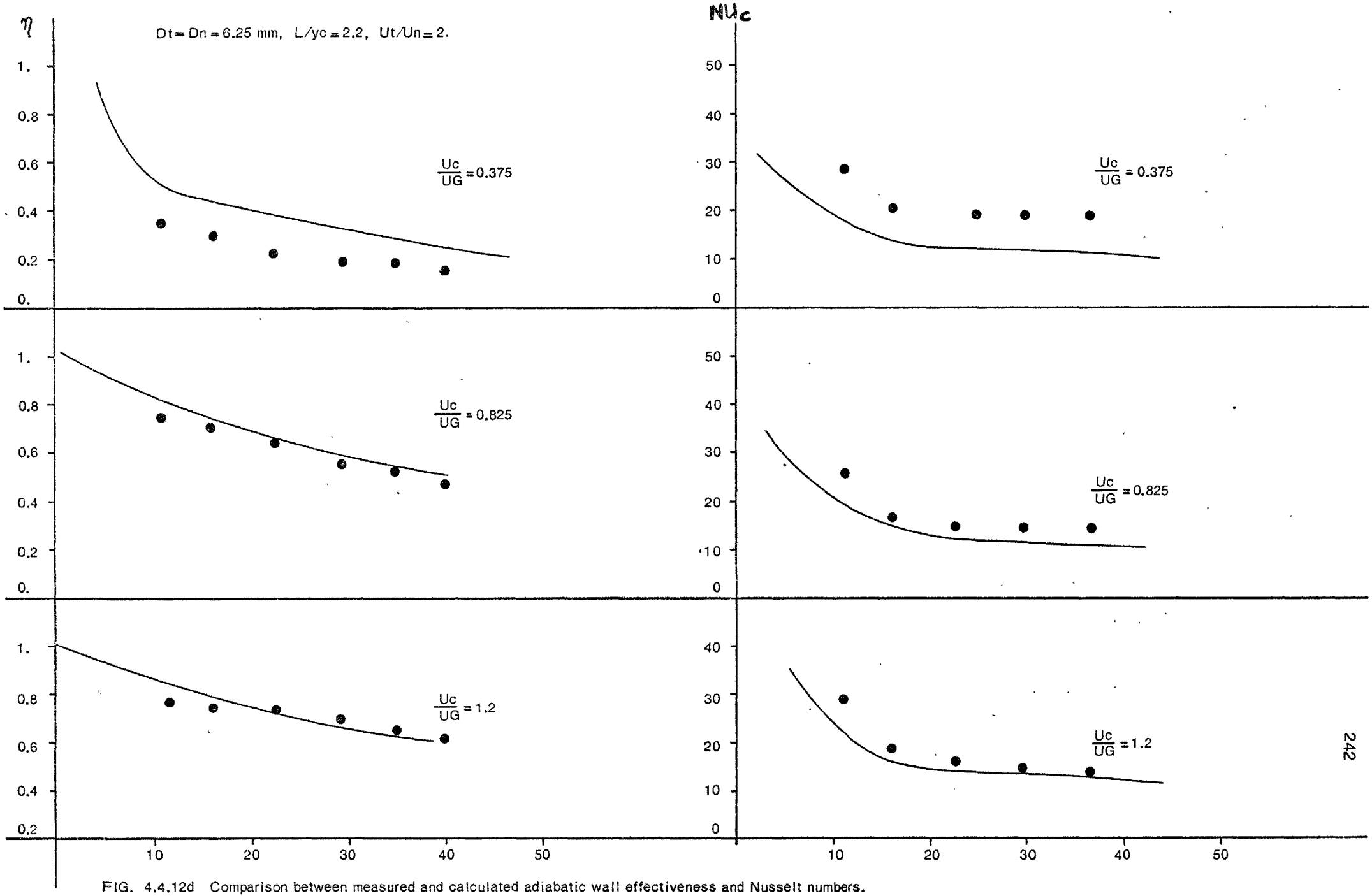

FIG. 4.4.12d Comparison between measured and calculated adiabatic wall effectiveness and Nusselt numbers.

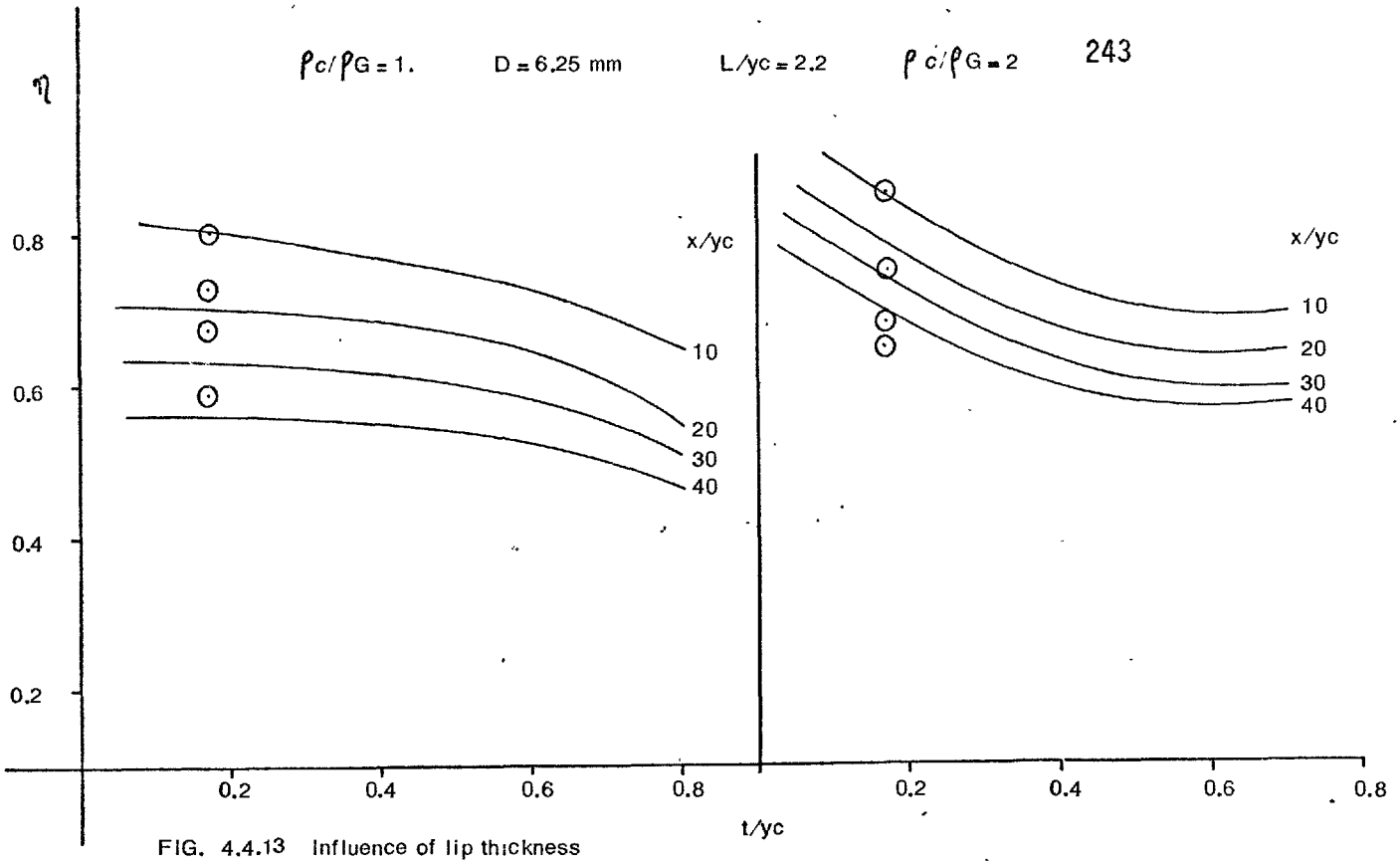

FIG. 4.4.13 Influence of lip thickness

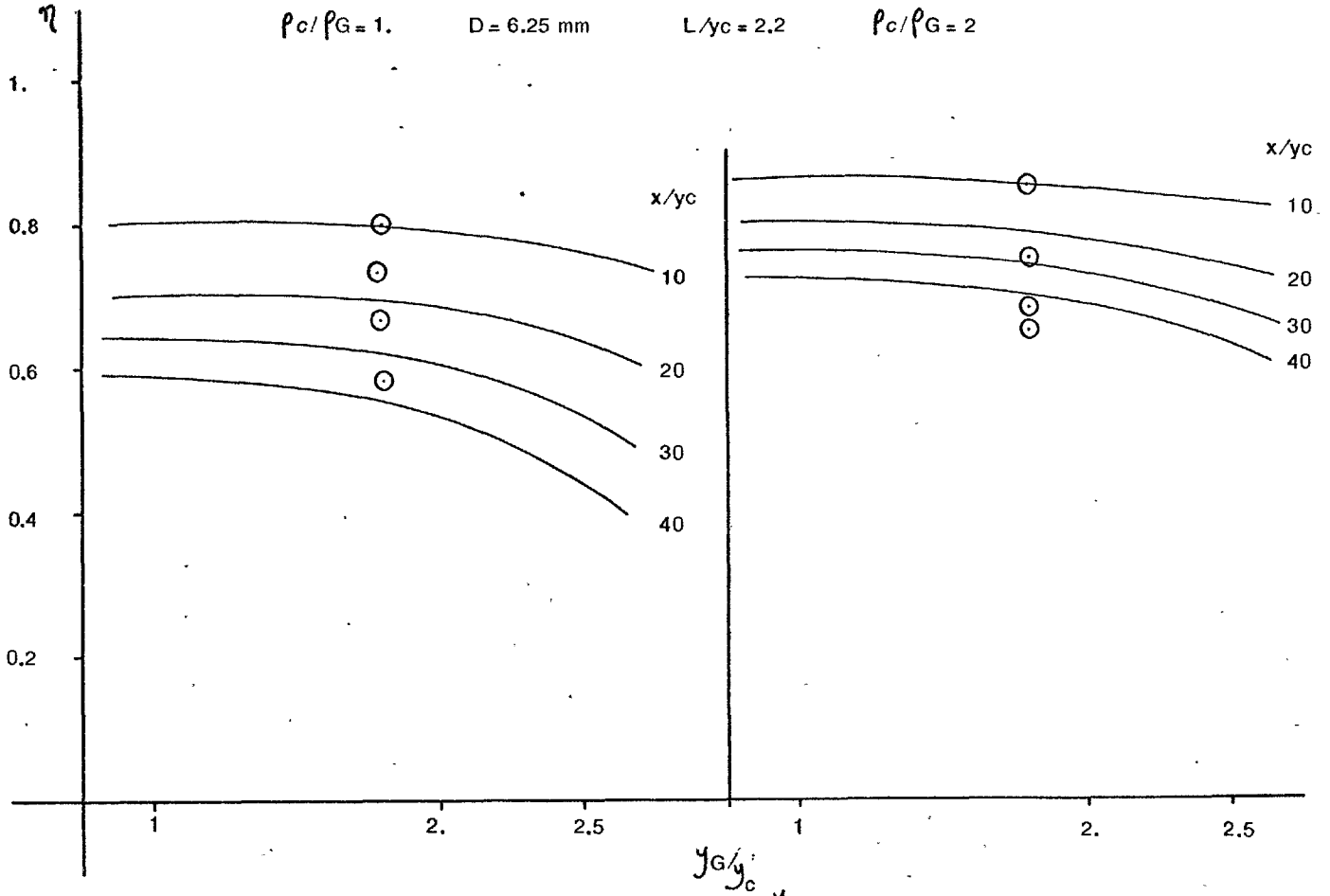

FIG. 4.4.14 Influence of upper boundary layer thickness (y_G/y_c)

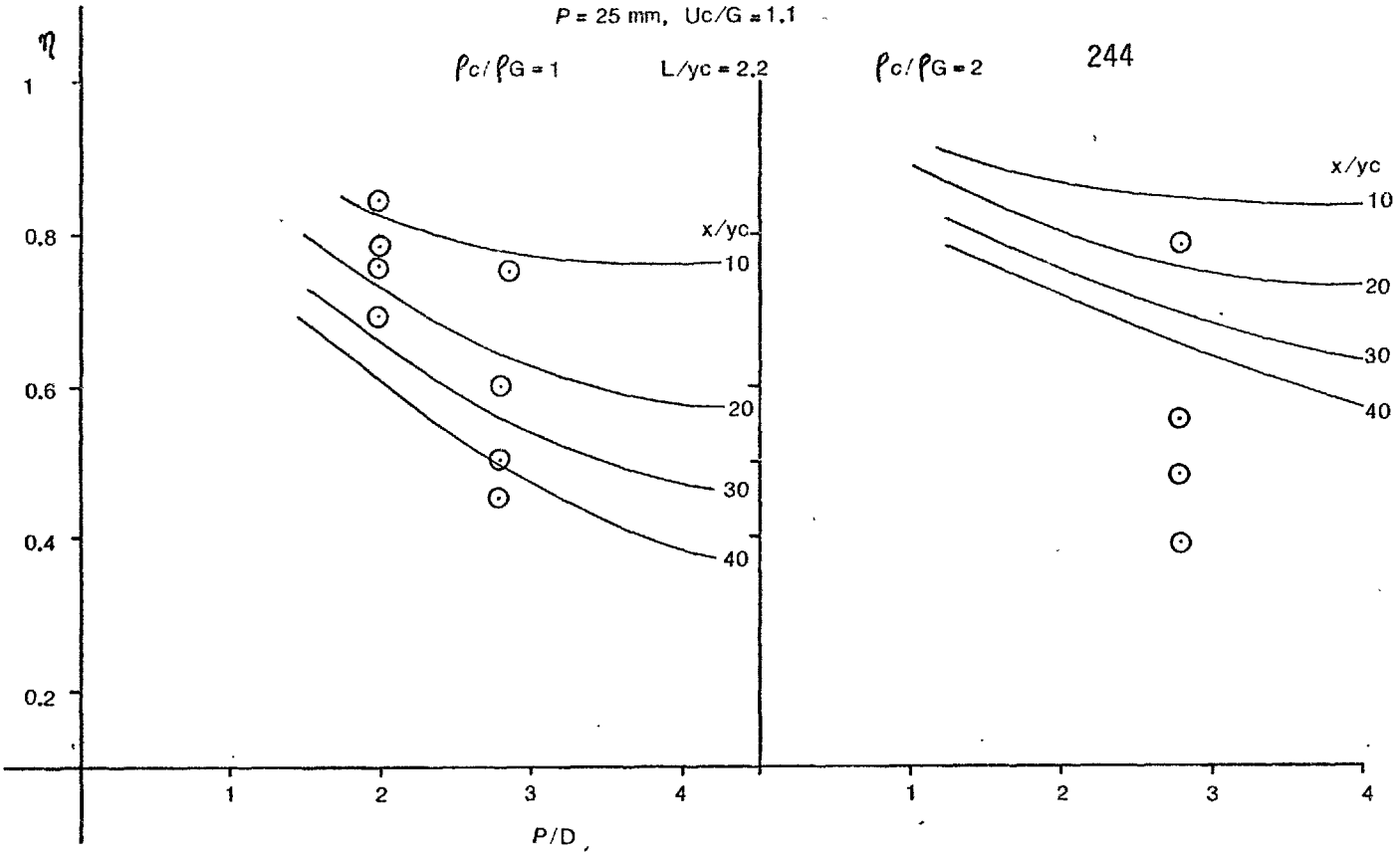

FIG. 4.4.15 Influence of pitch-diameter ratio for fixed pitch (a)

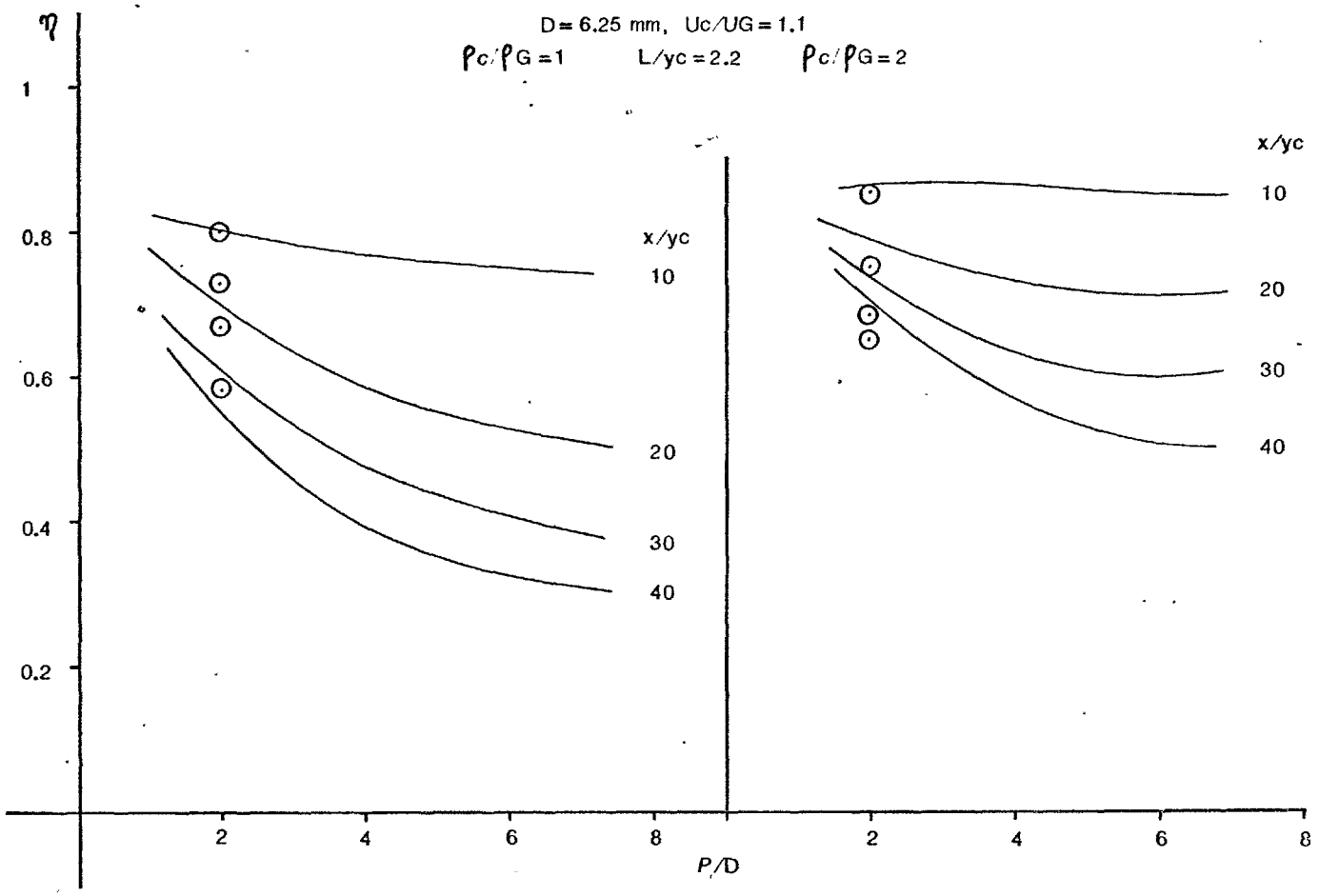

FIG. 4.4.15 Influence of pitch-diameter ratio for fixed diameter. (b)

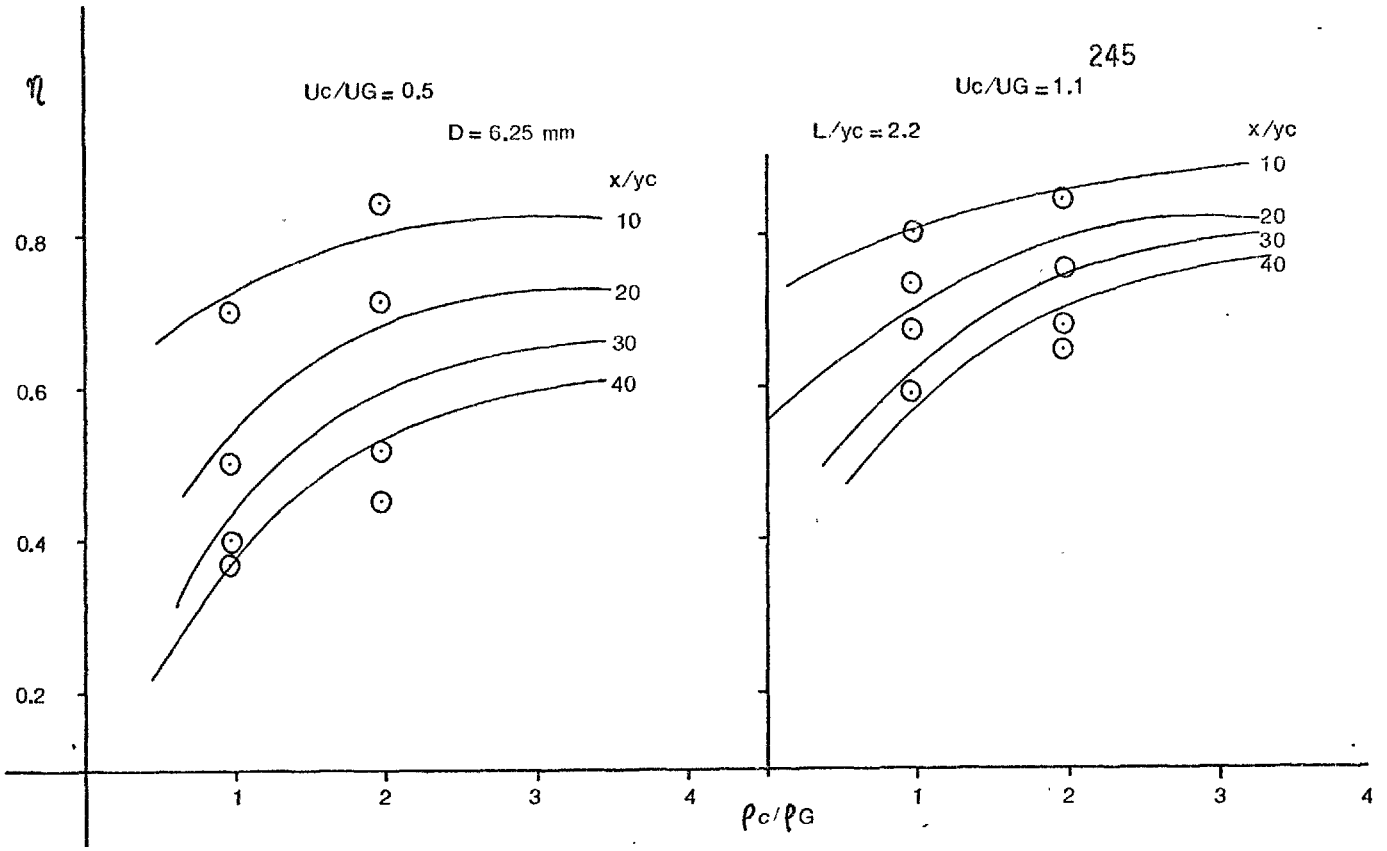

FIG. 4.4.16 Influence of density ratio

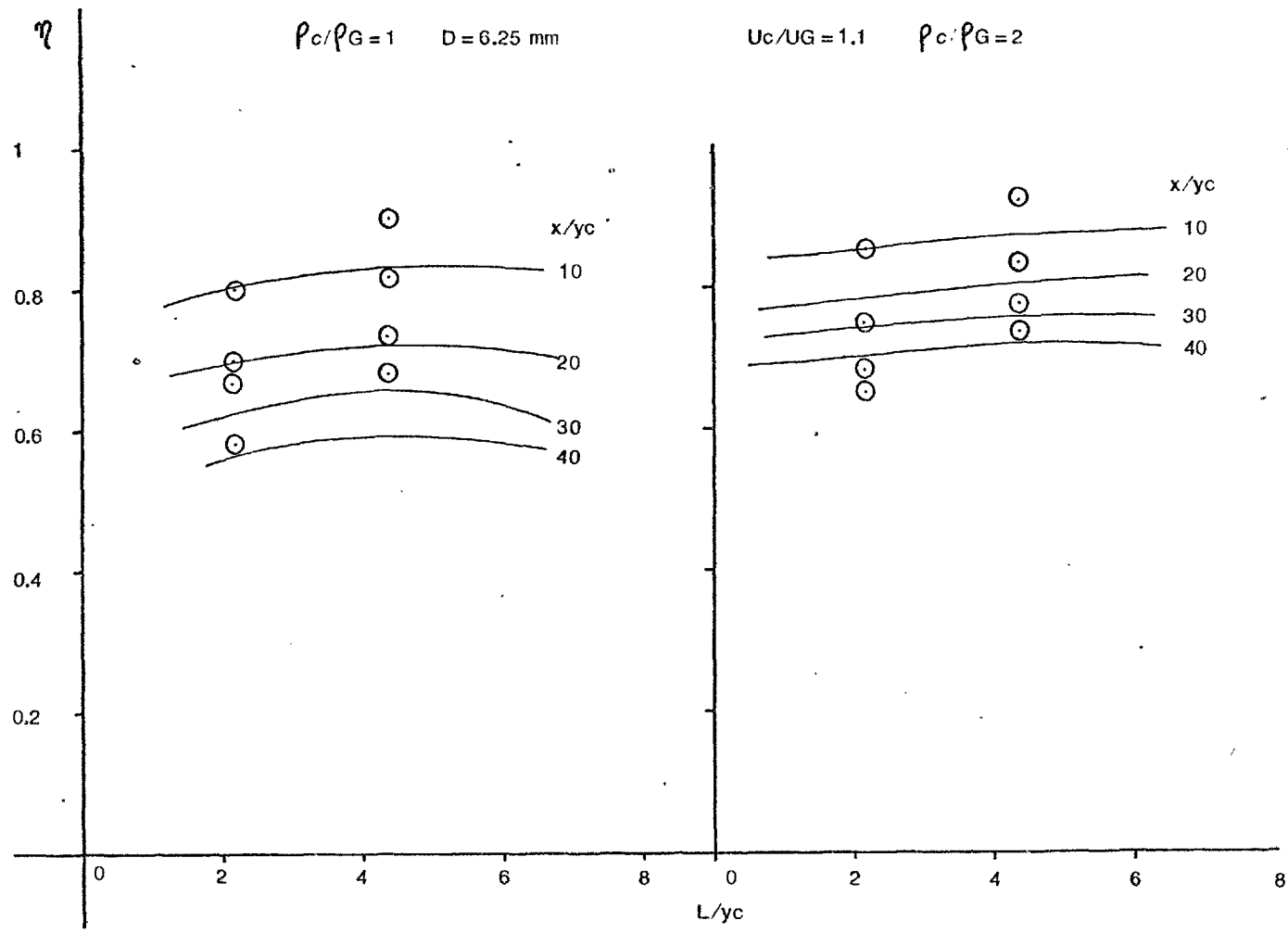

FIG. 4.4.17 Influence of lip length

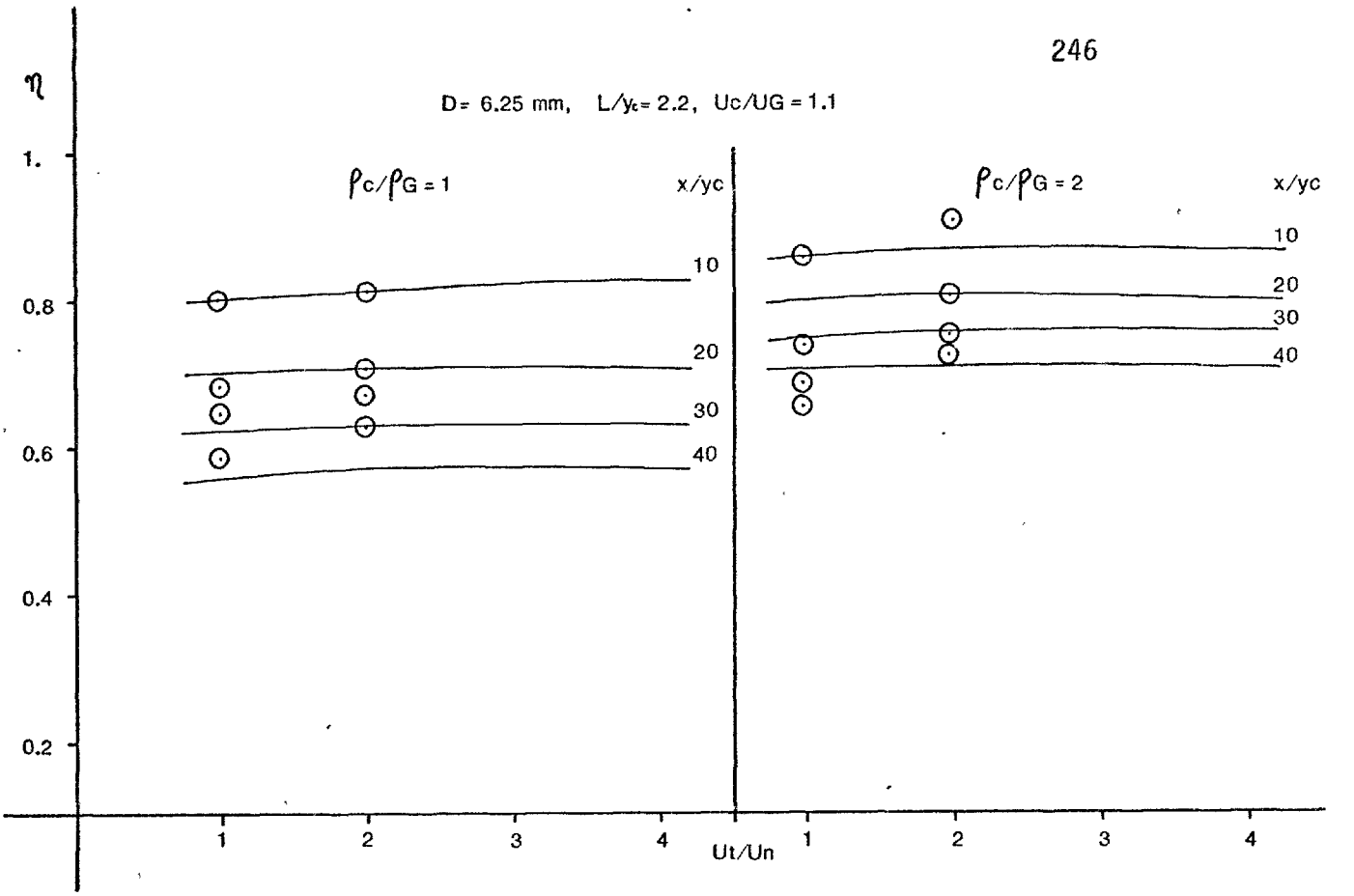

FIG. 4.4.18 Influence of tangential-normal momentum ratio for a fixed coolant flow rate.

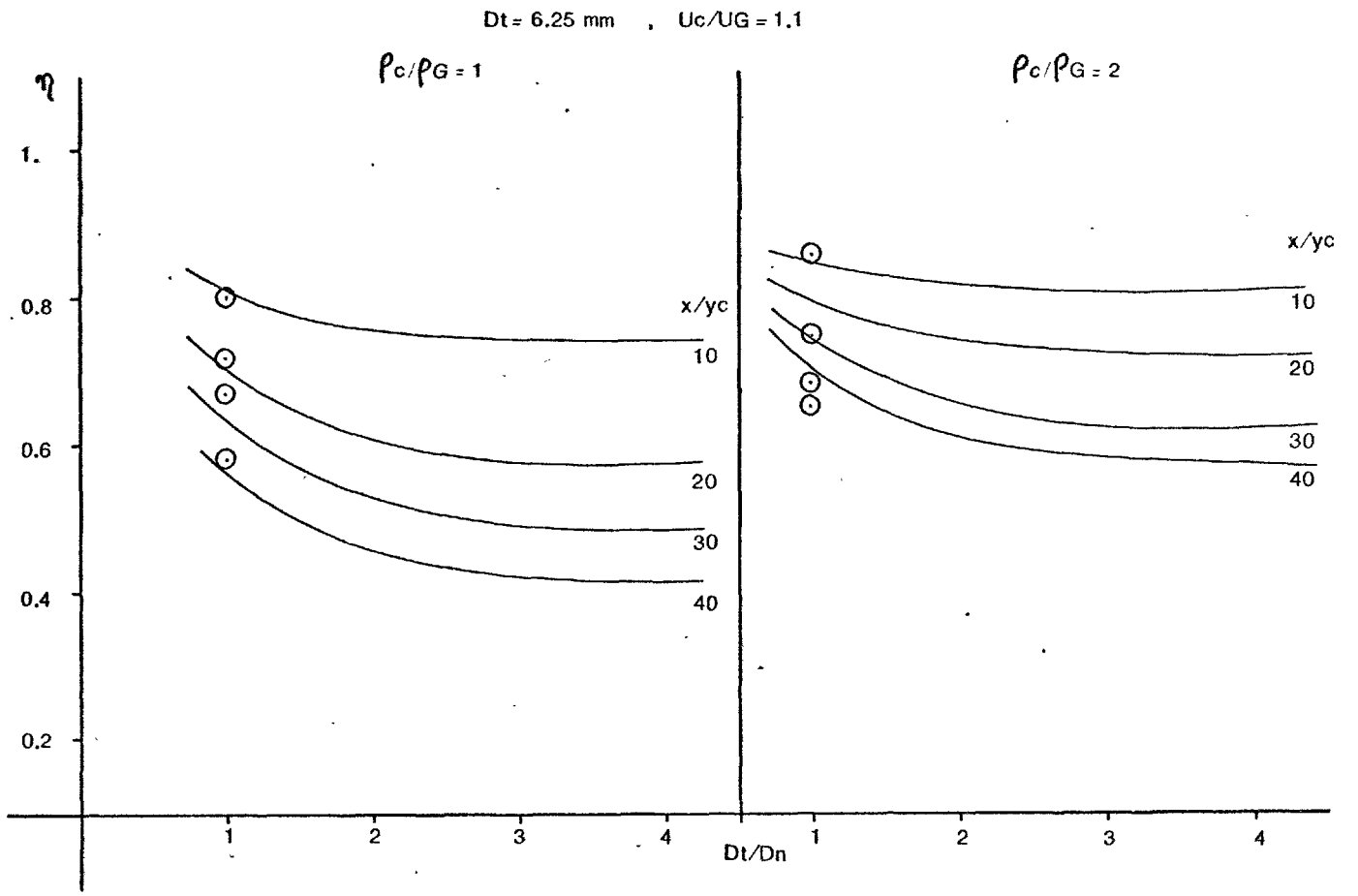

FIG. 4.4.19 Influence of diameter ratios.

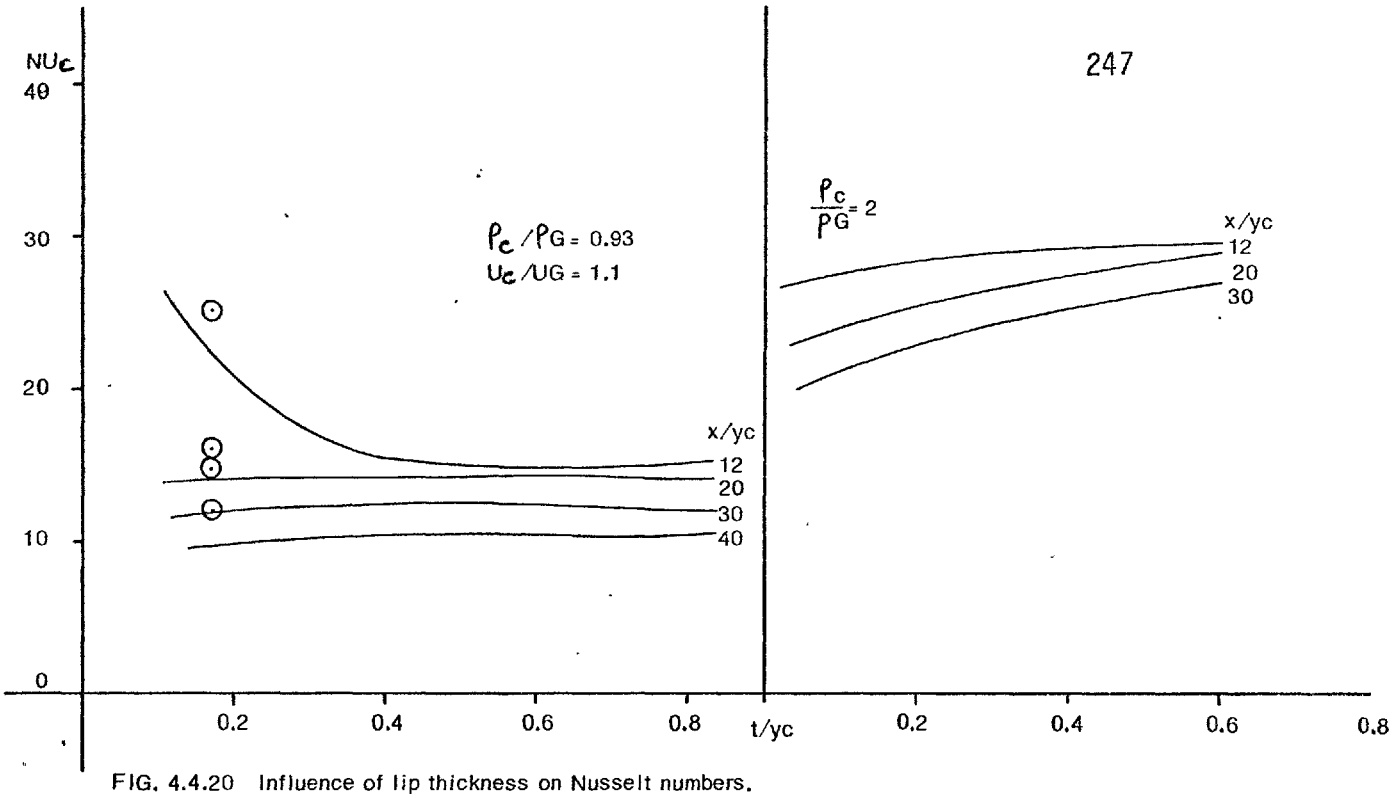

FIG. 4.4.20 Influence of lip thickness on Nusselt numbers.

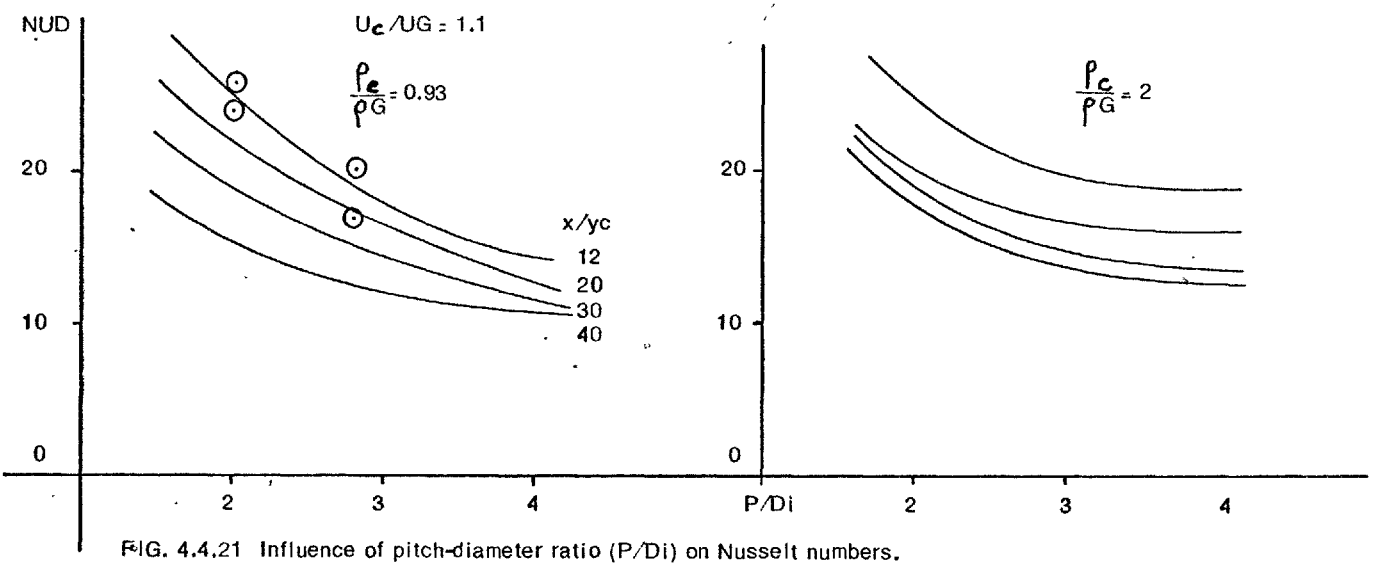

FIG. 4.4.21 Influence of pitch-diameter ratio (P/Di) on Nusselt numbers.

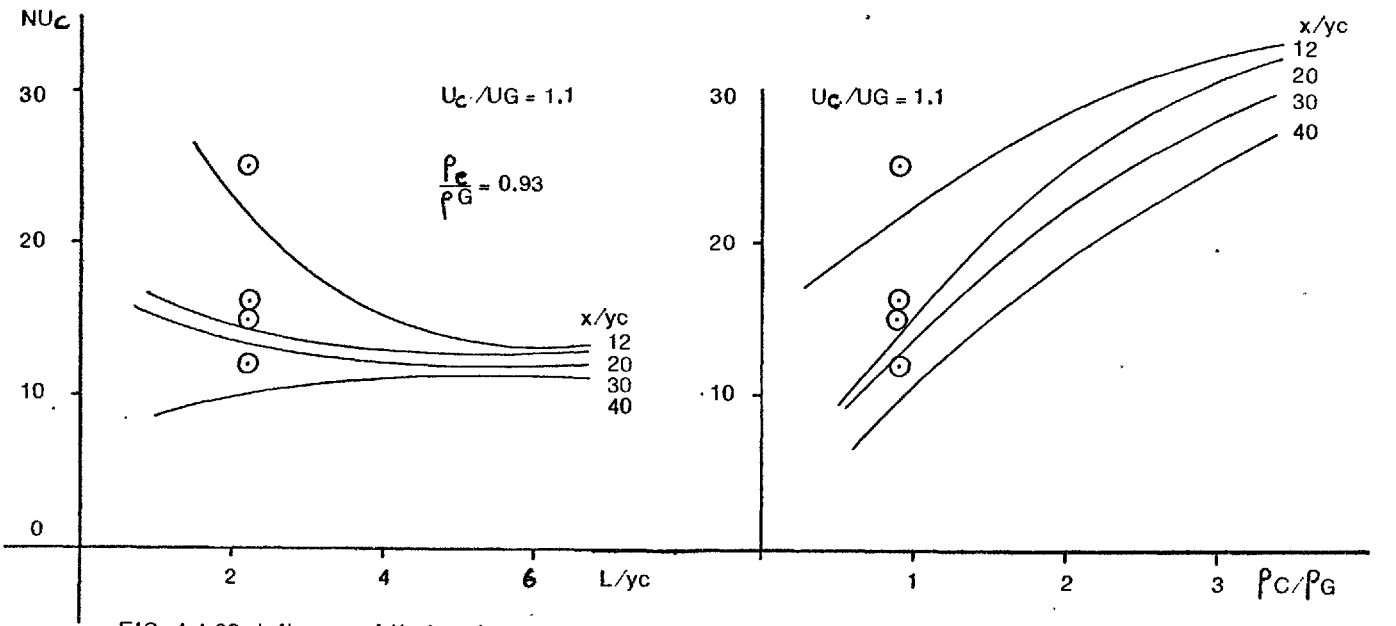

FIG. 4.4.22 Influence of lip length on Nusselt numbers

FIG. 4.4.27 Influence of density ratio on Nusselt numbers

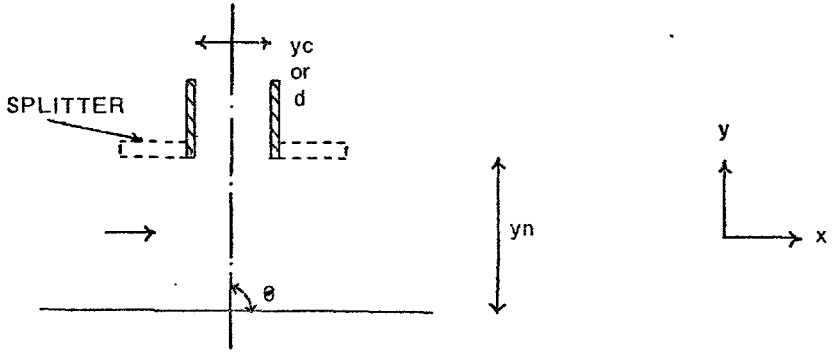

(a) Single slot/circular jet with/without cross flow with/without splitter plate

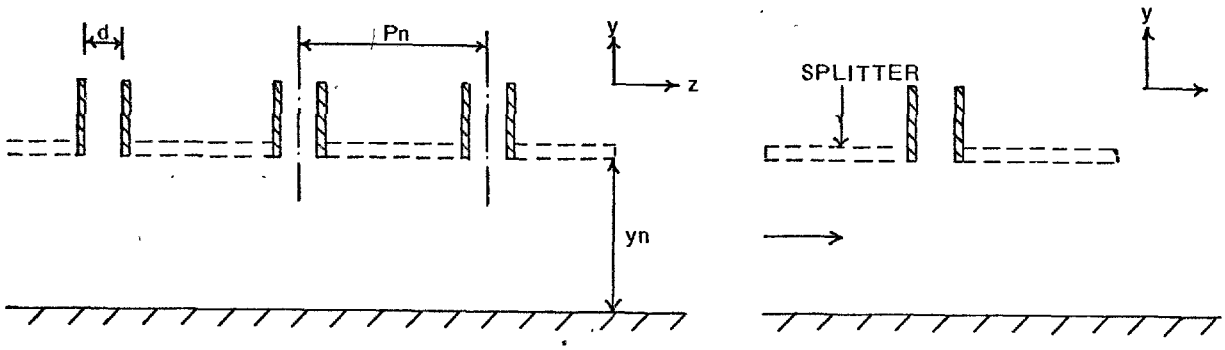

(b) Row of circular jets with or without cross flow (with/without splitter plate).

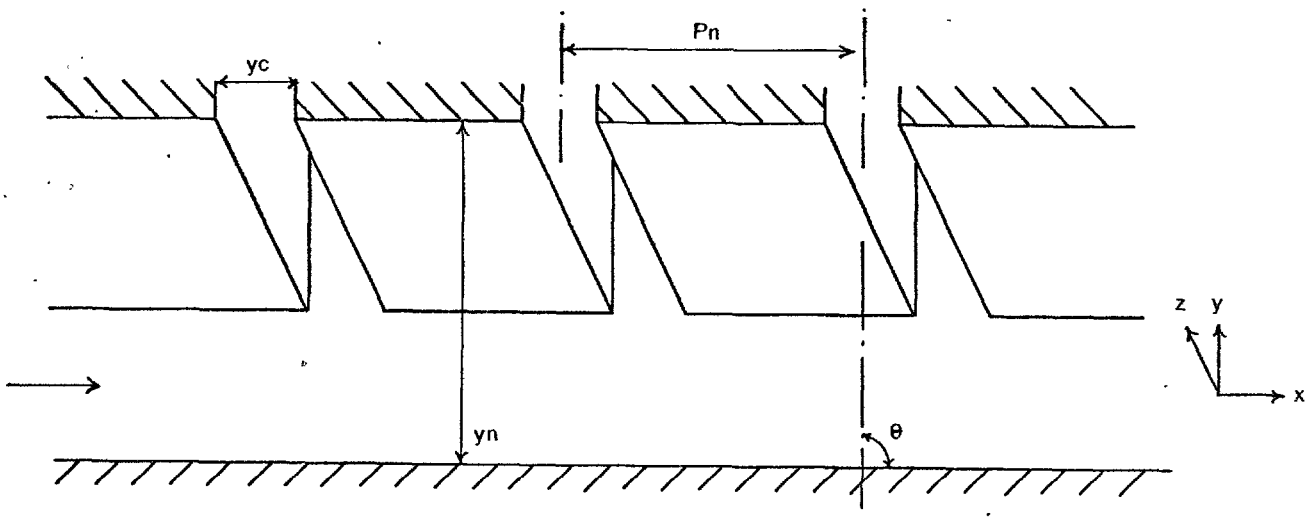

(c) Row of slot jets with/without cross flow.

FIG. 5.1.2 Impinging jets geometry.

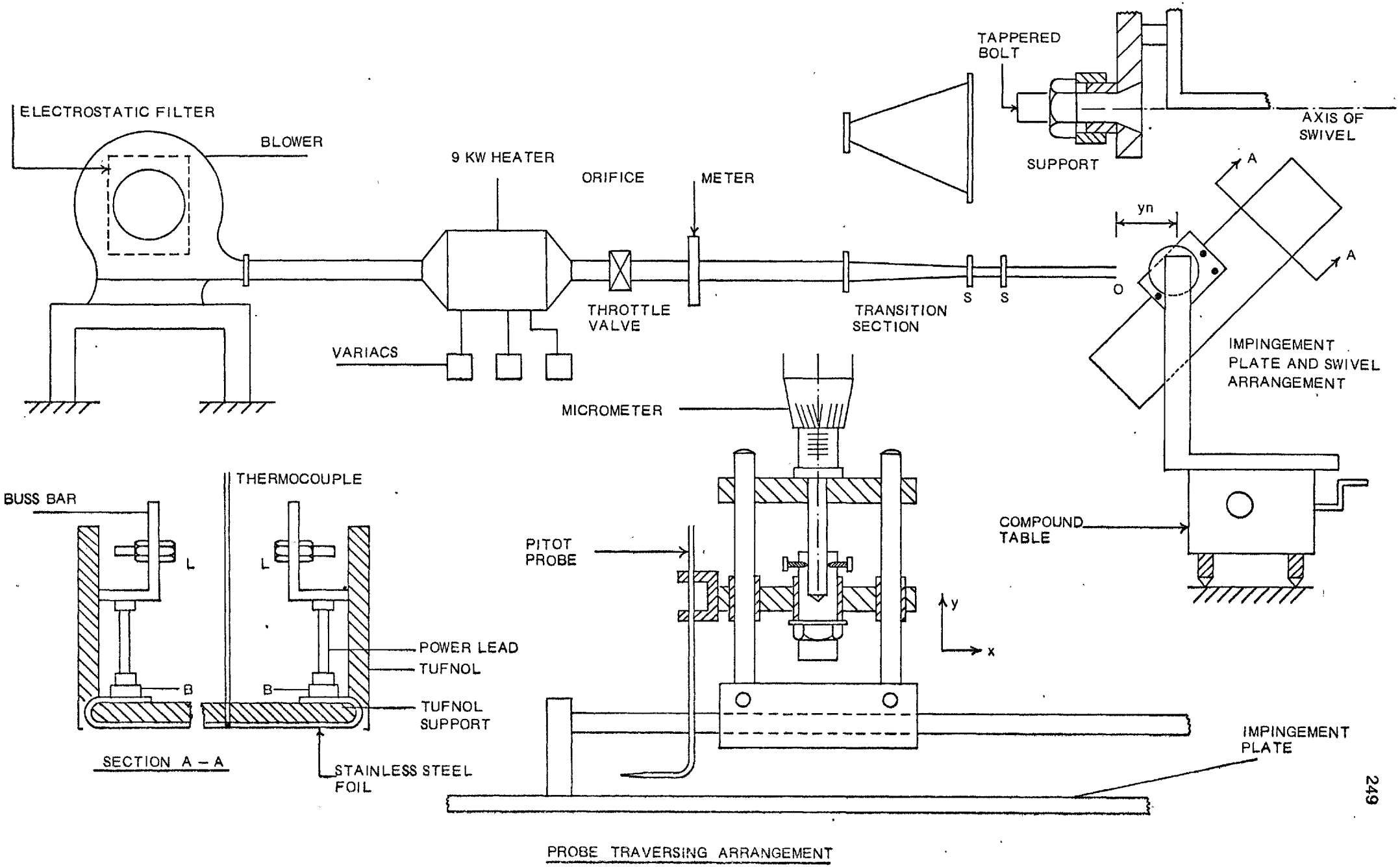

FIG. 5.2.1. FLOW Configurations

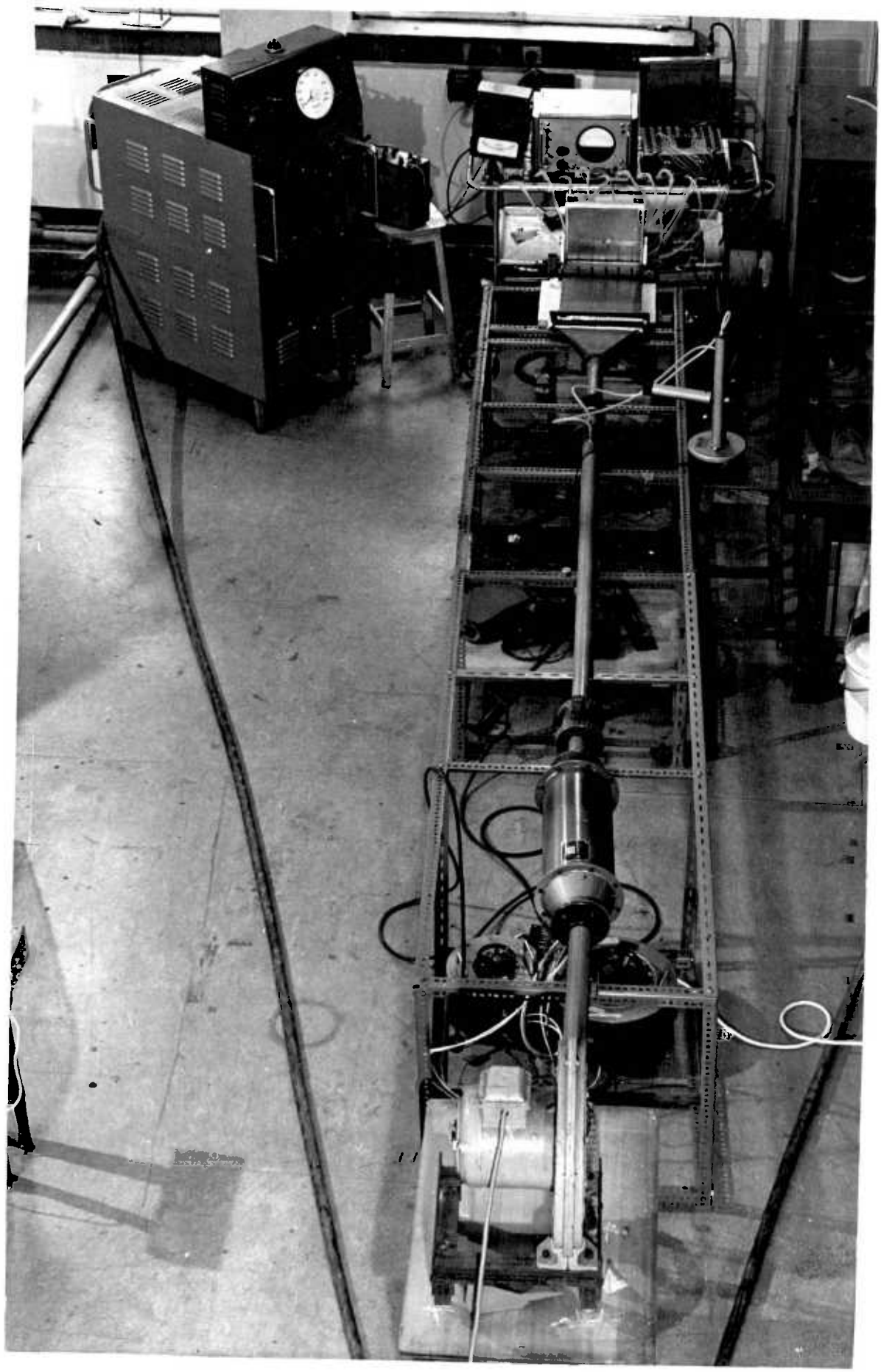

Plate 5.2.1 Flow arrangement for impingement heat transfer

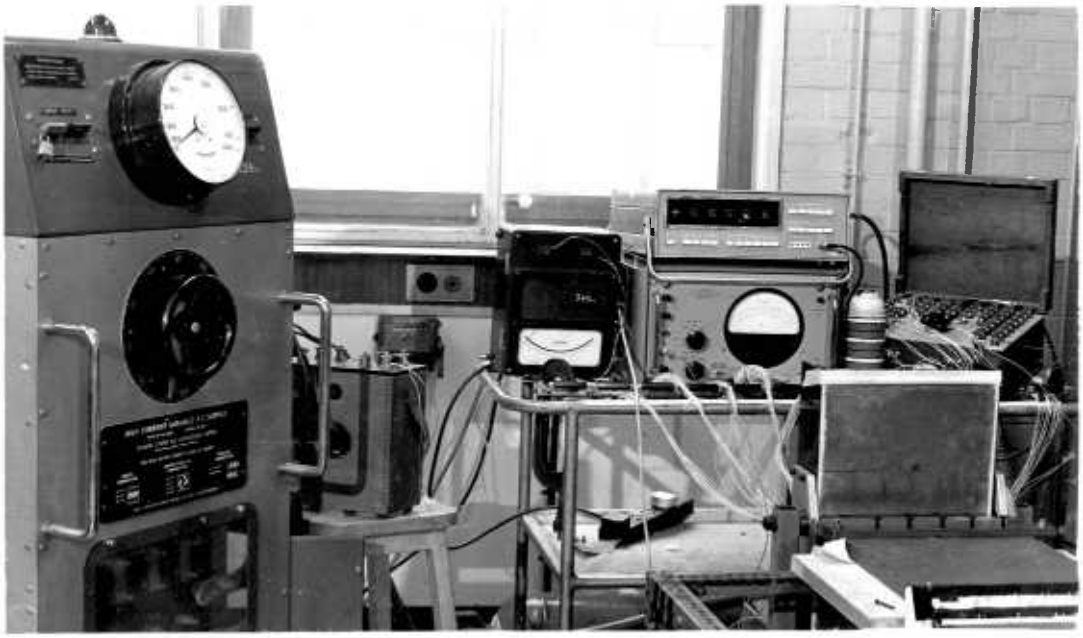

Plate 5.2.2.a Instruments for heat transfer measurement

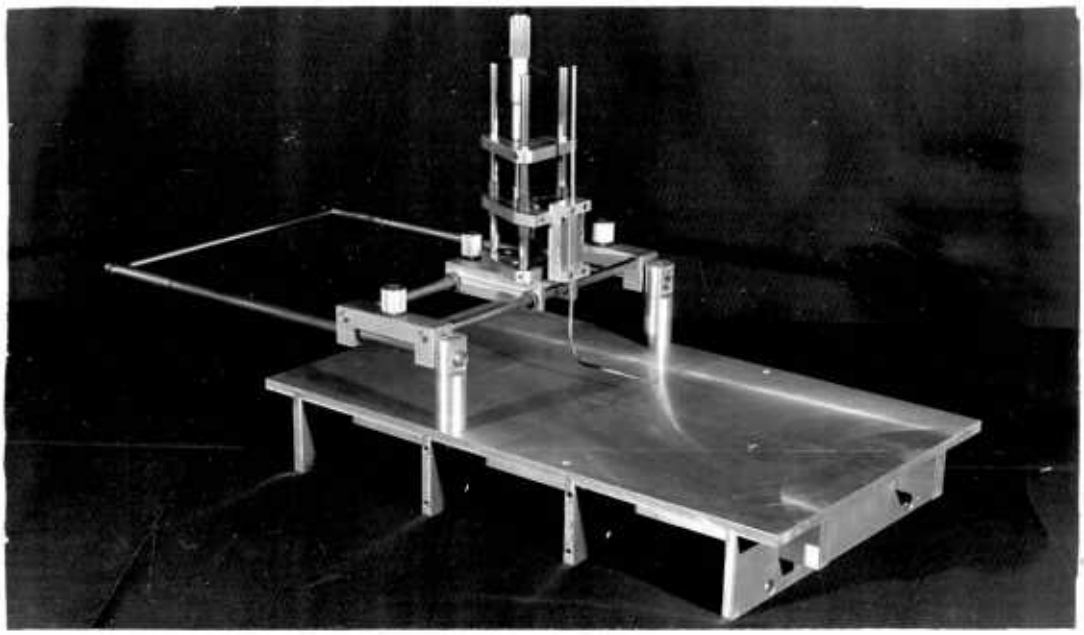

Plate 5.2.2.b Impingement plate for velocity measurements

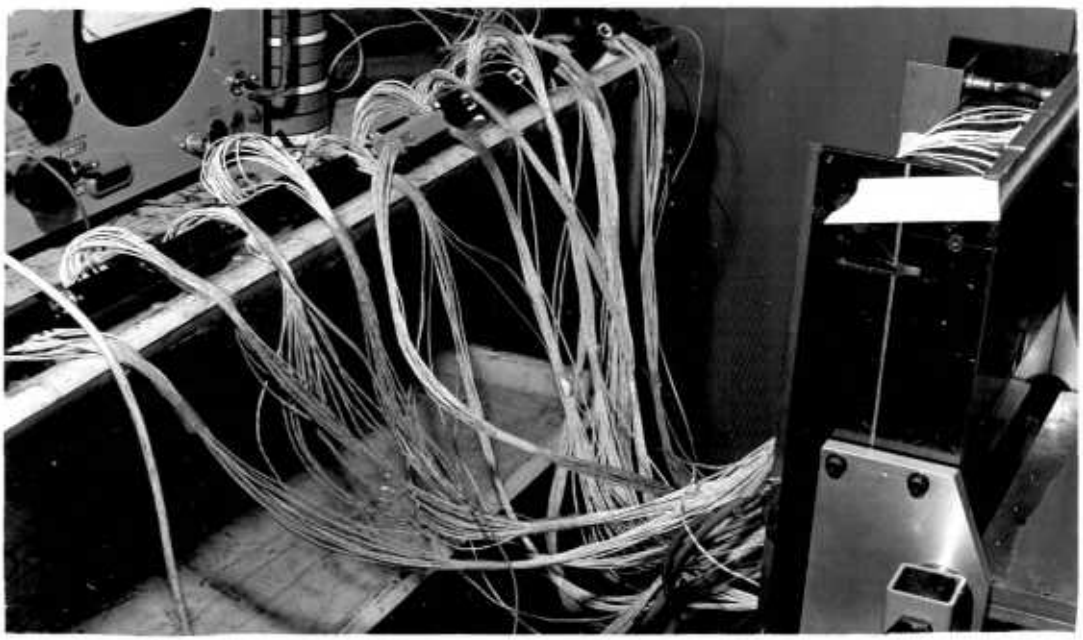

Plate 5.2.2.c Thermocouple arrangements

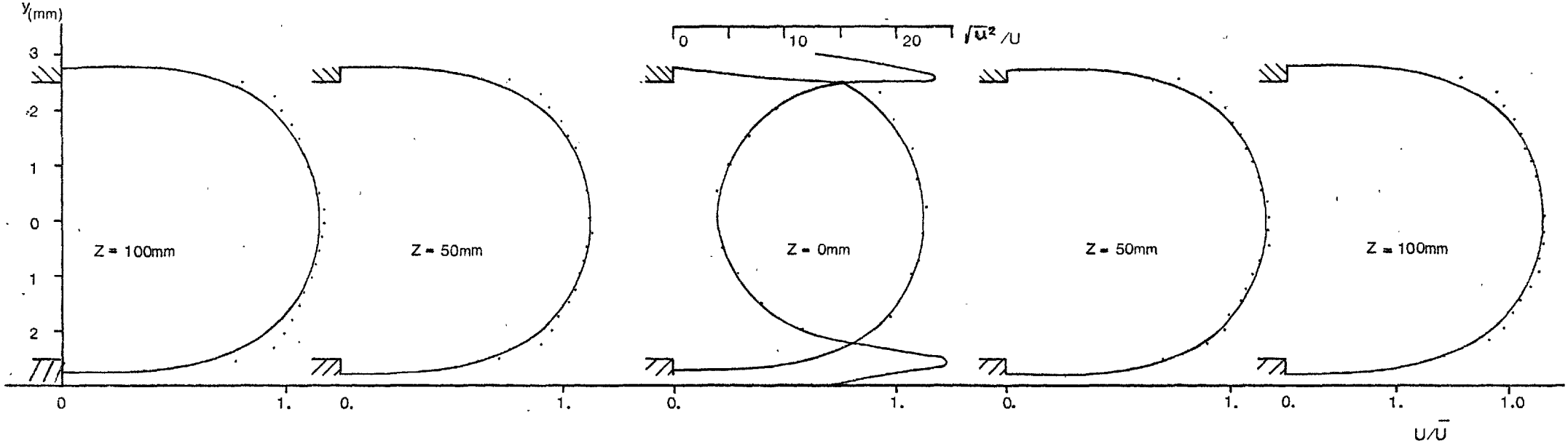

MEAN AND FLUCTUATING VELOCITY PROFILES IN CENTRAL 200mm

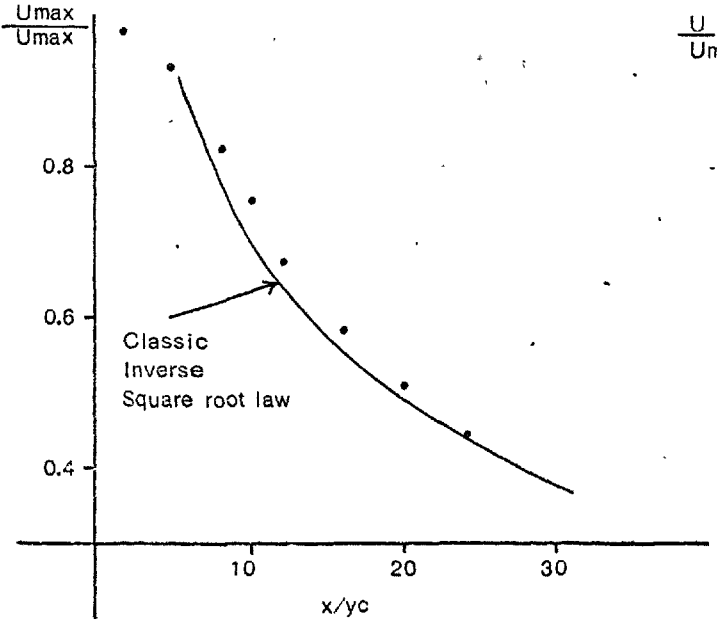

VELOCITY DECAY

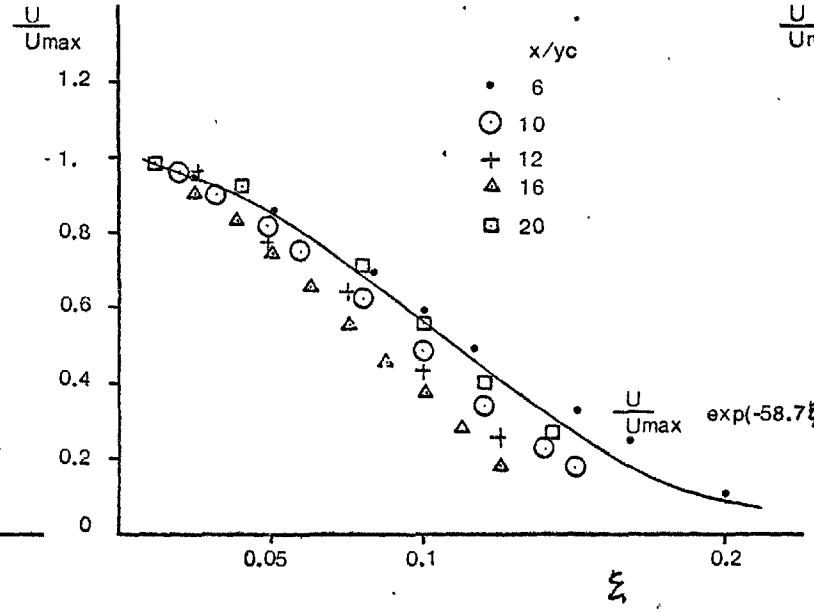

NORMALIZED VELOCITY

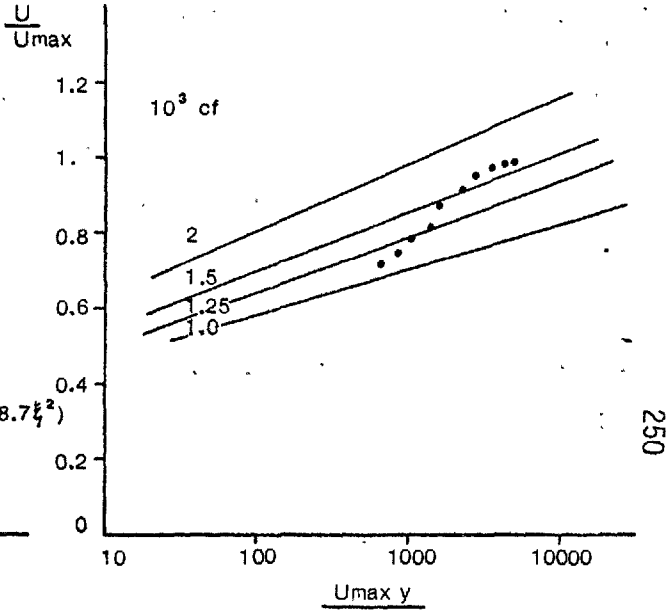

SKIN FRICTION NEAR EXIT

FIG. 5.2.2

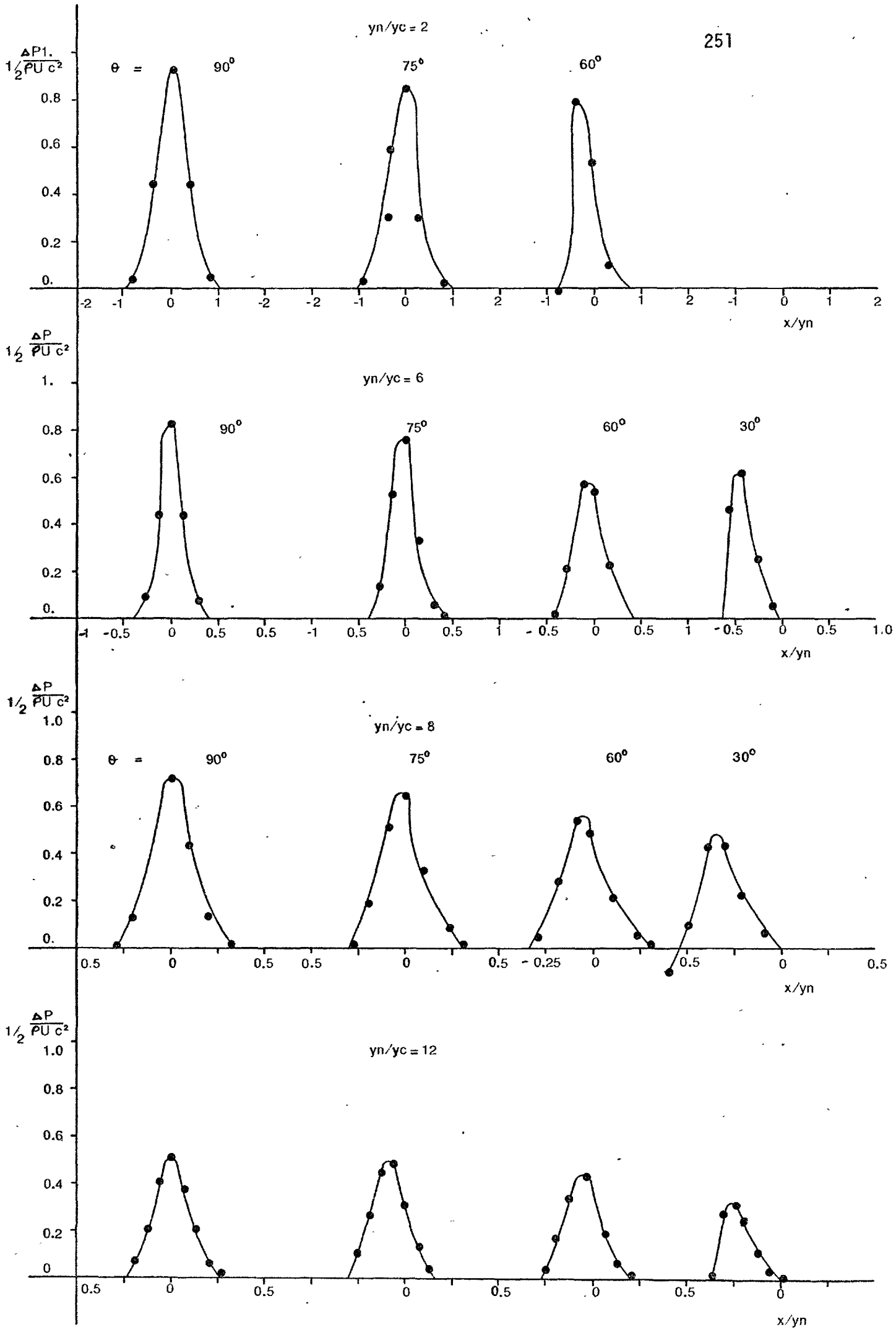

FIG. 5.2.3. Wall Static pressures

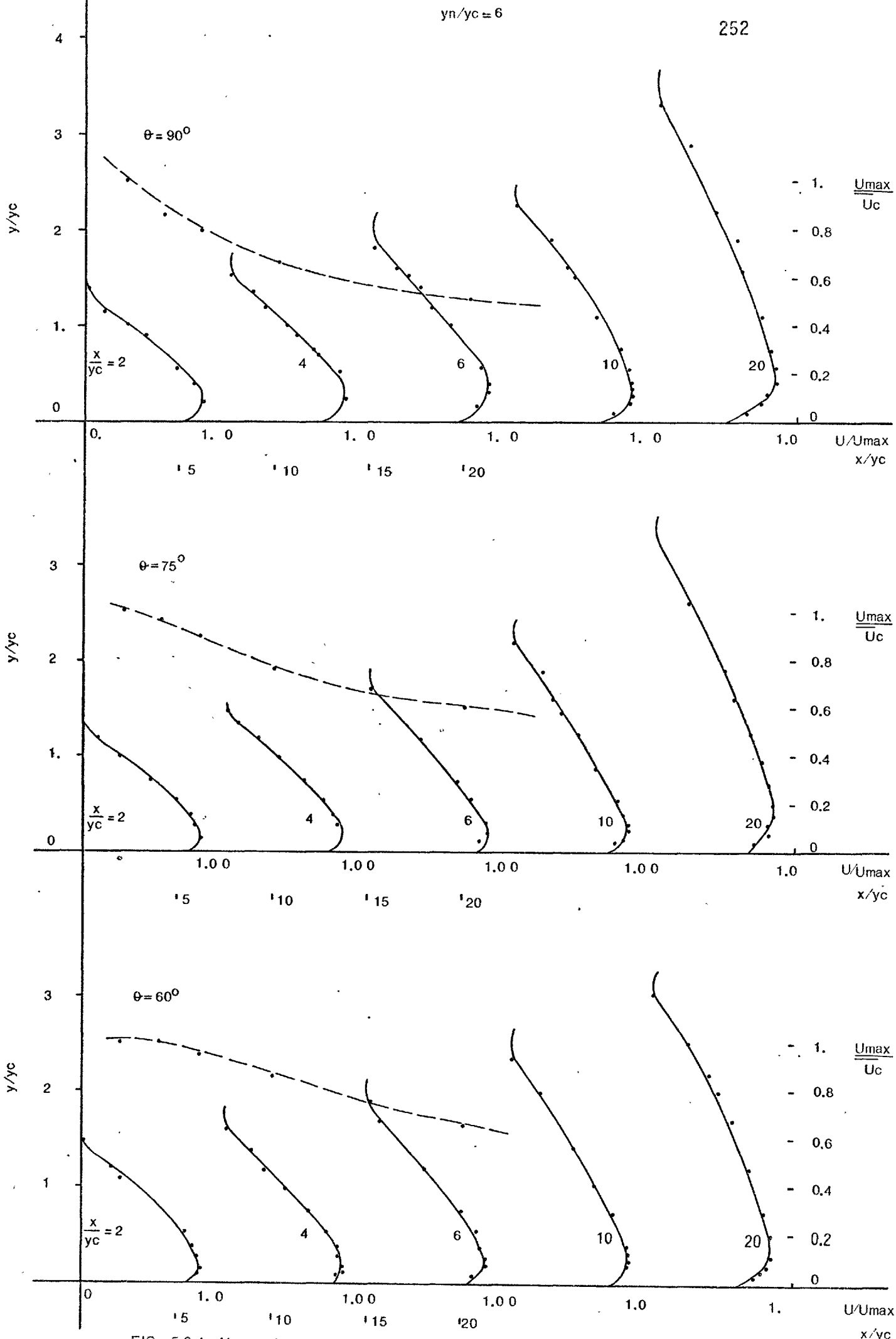

FIG. 5.2.4. Mean velocity parallel to impingement wall

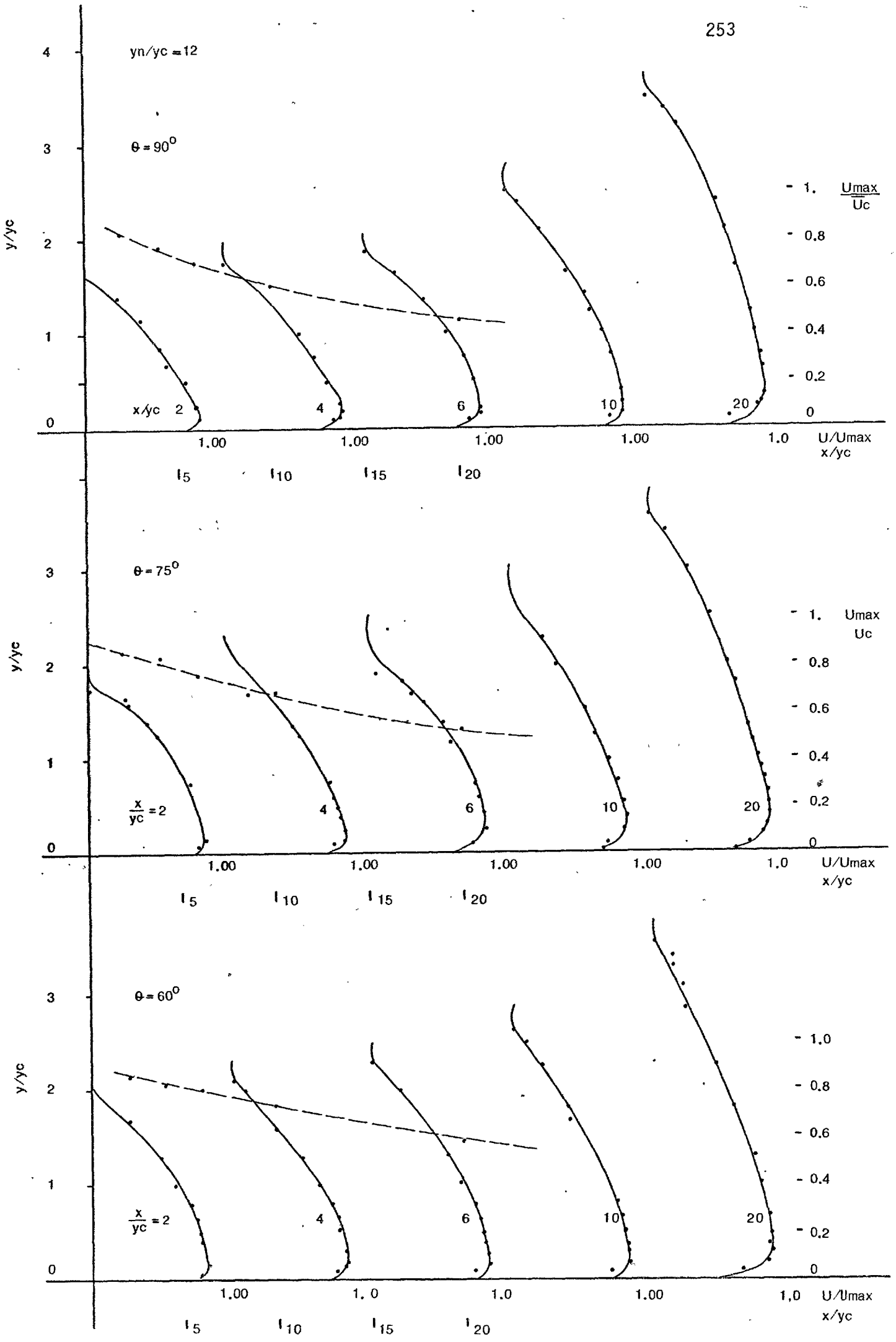

FIG. 5.2.4. Mean velocity parallel to impingement wall

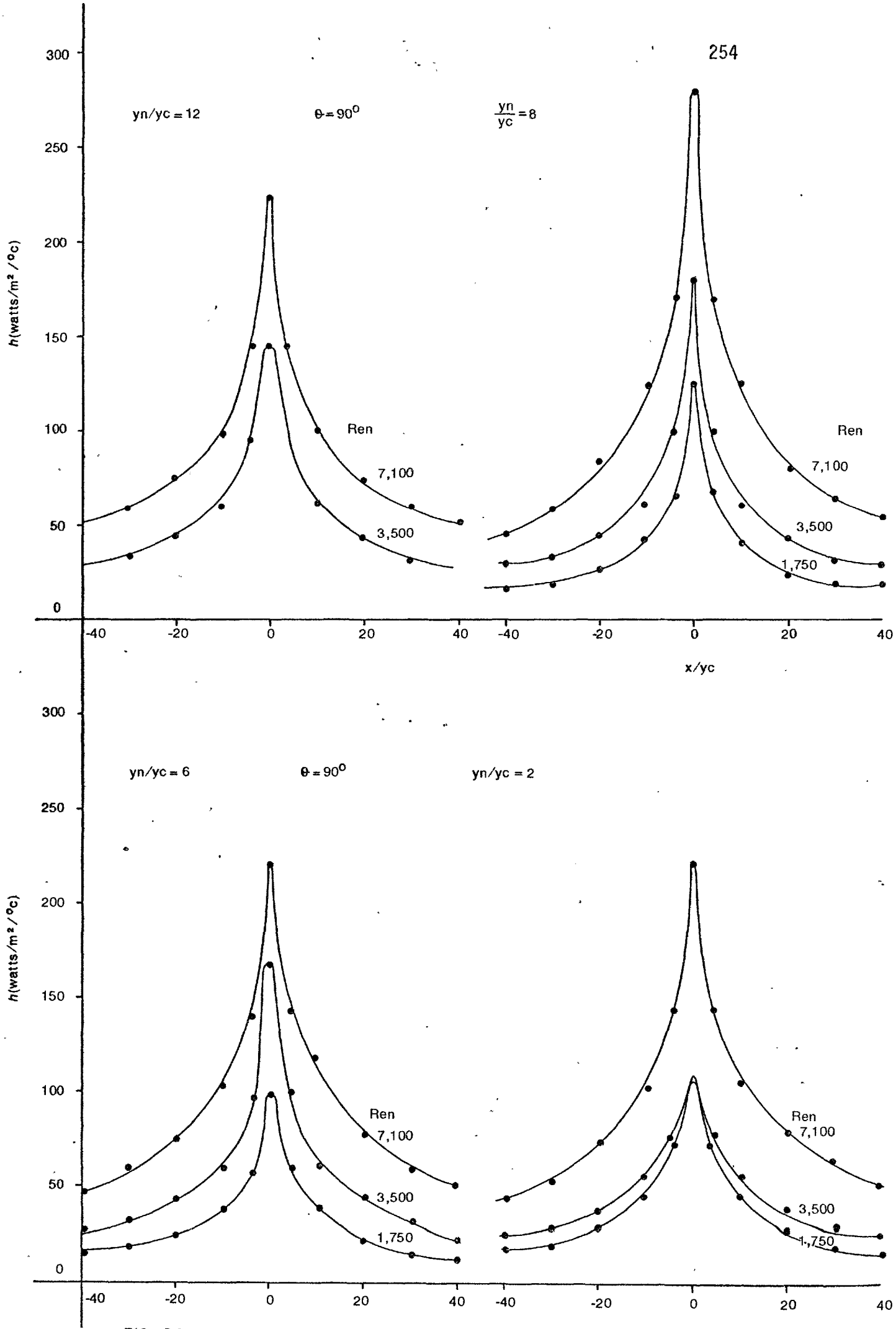

FIG. 5.2.5. Influence of slot Reynolds number

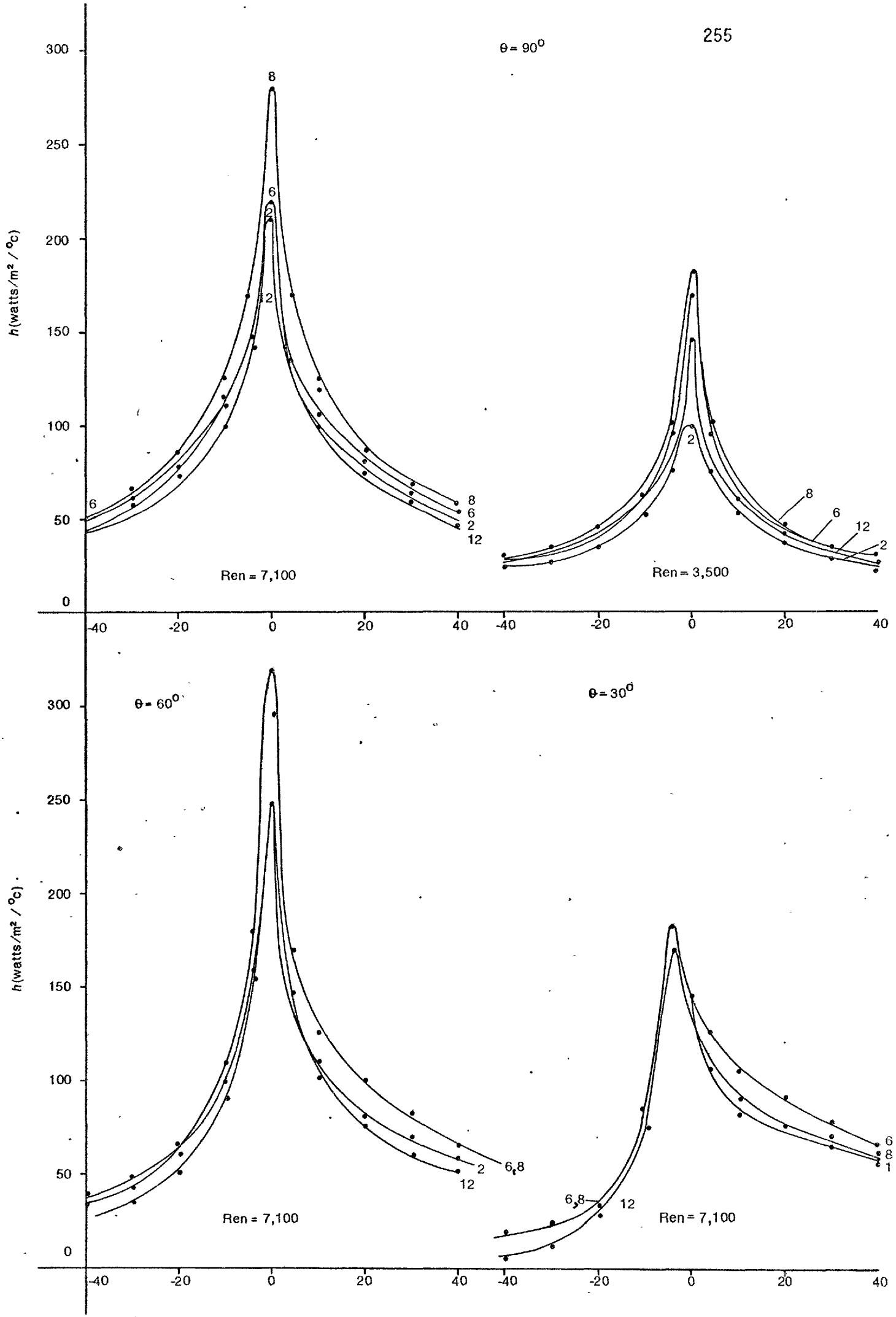

FIG. 5.2.6 Influence of nozzle – plate distance

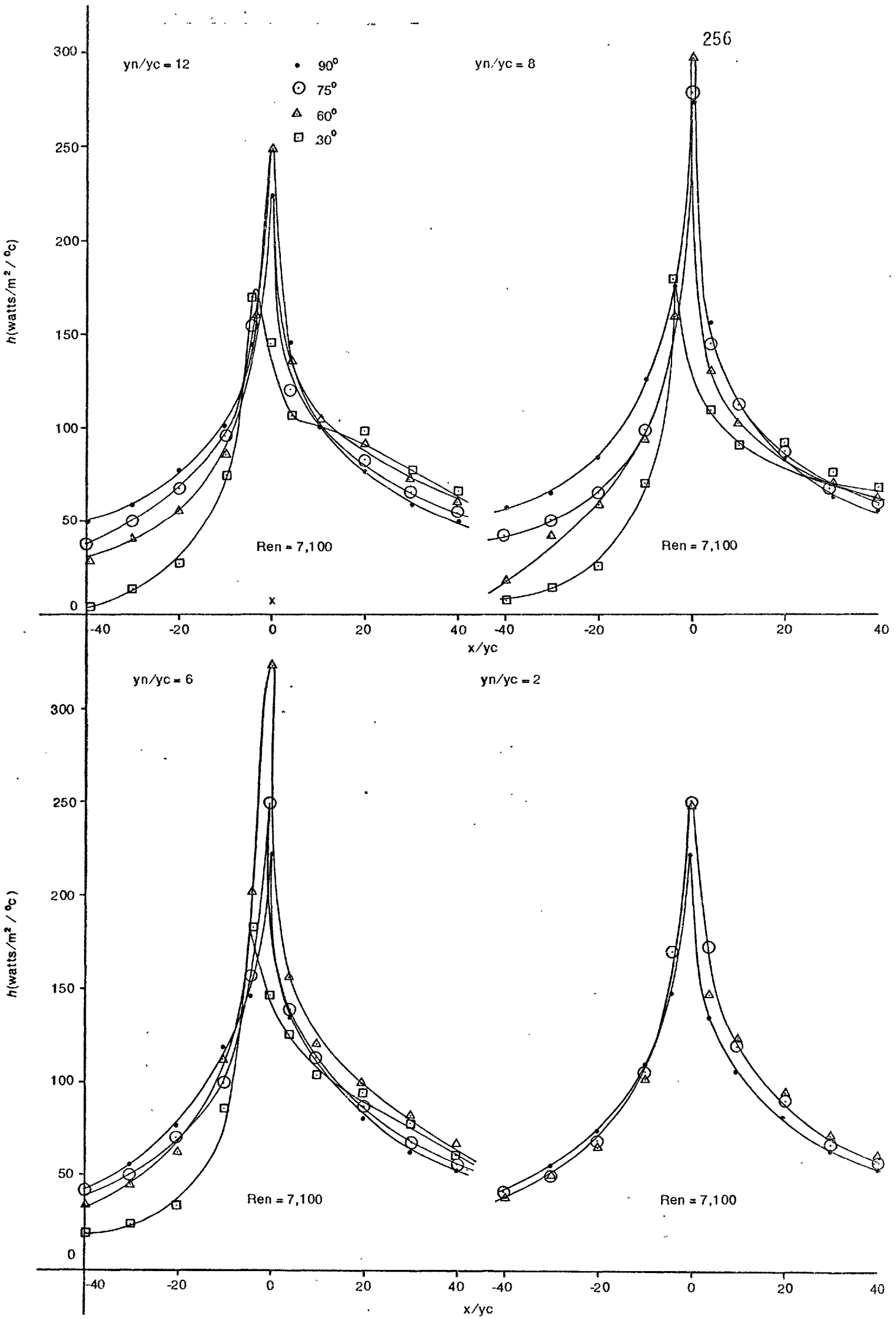

FIG. 5.2.7 Influence of impingement angle on heat transfer coeficient.

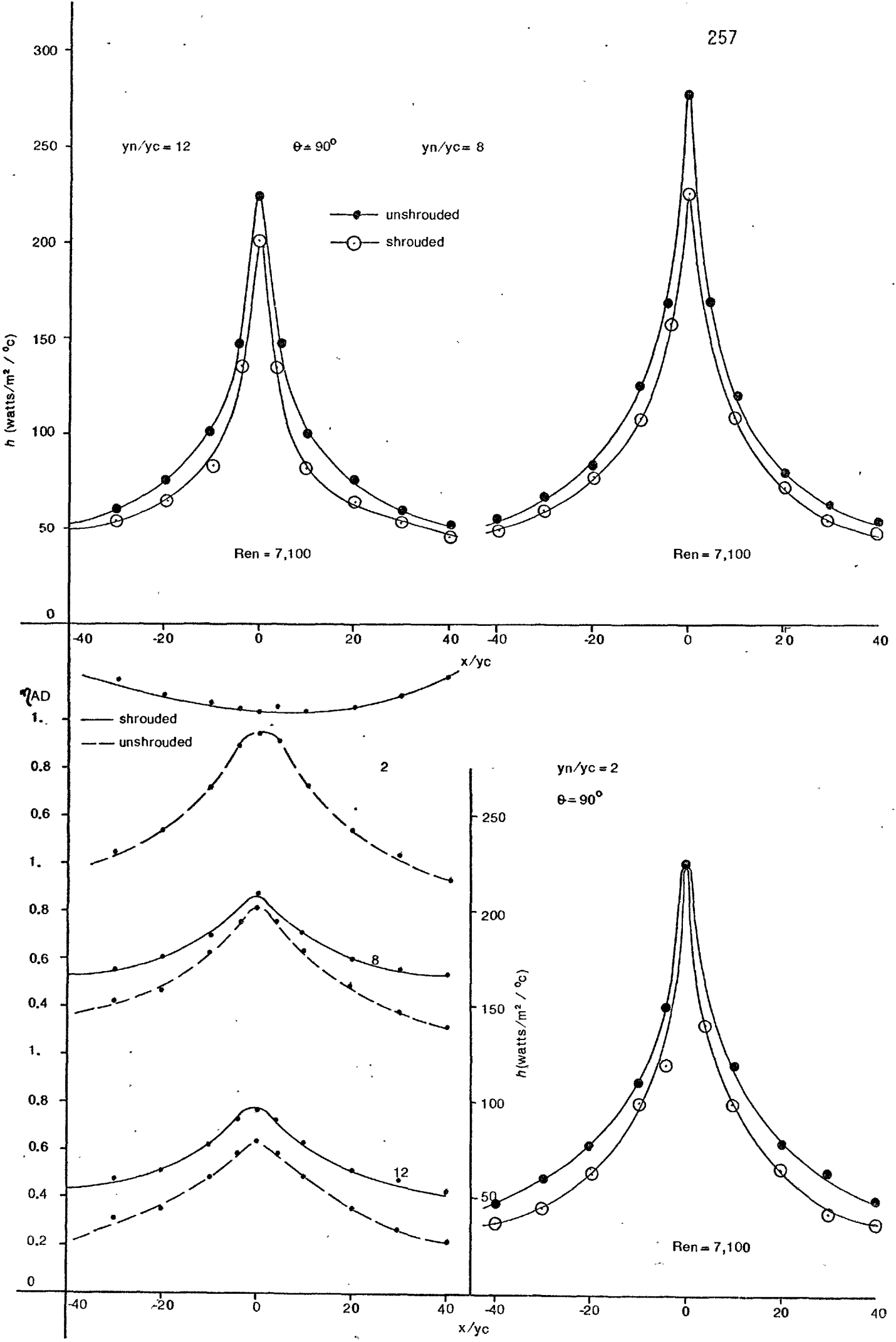

FIG. 5.2.8 Influence of shrouding plate

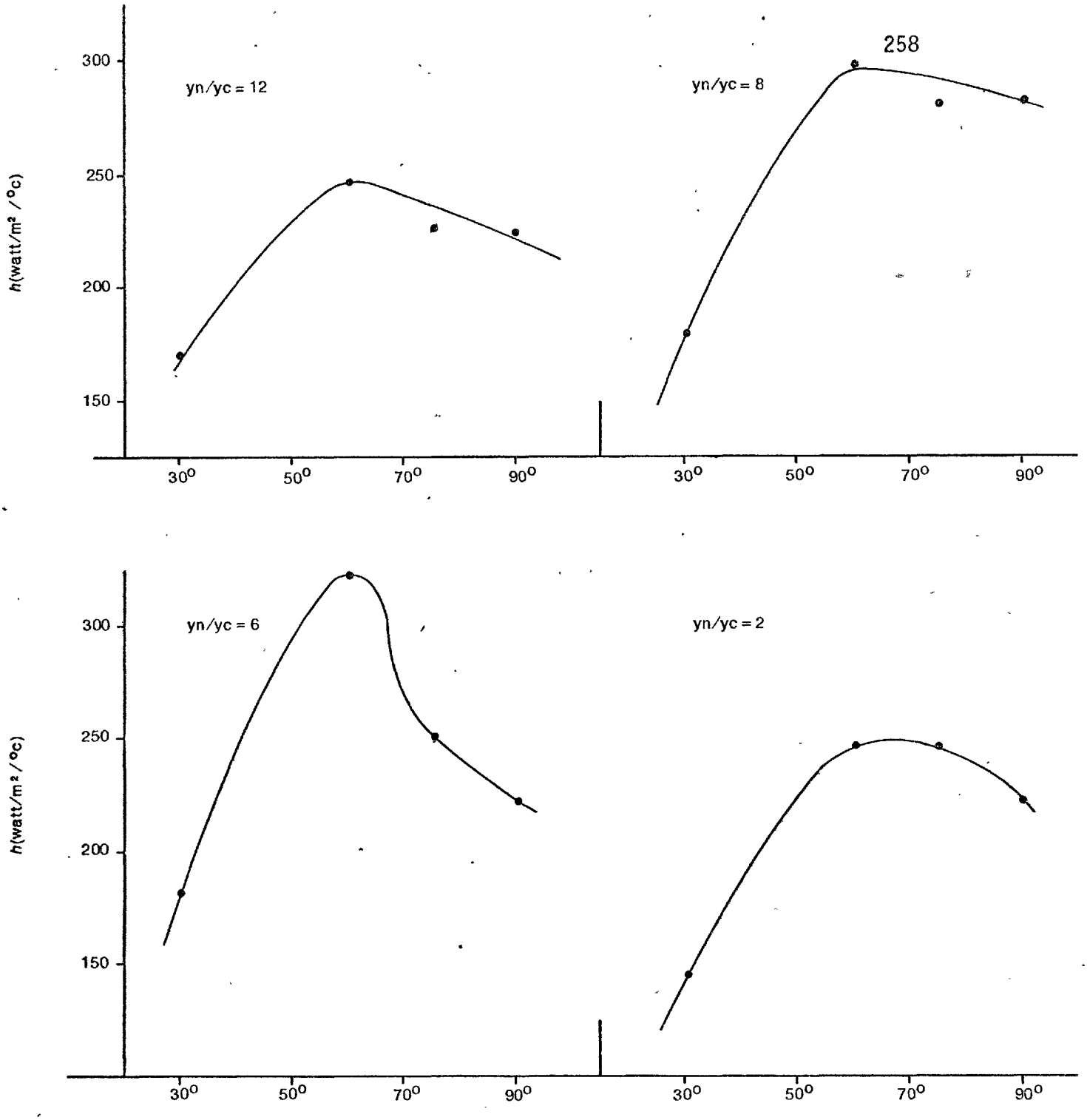

FIG. 5.2.9 Influence of impingement angle on Symmetry point heat transfer

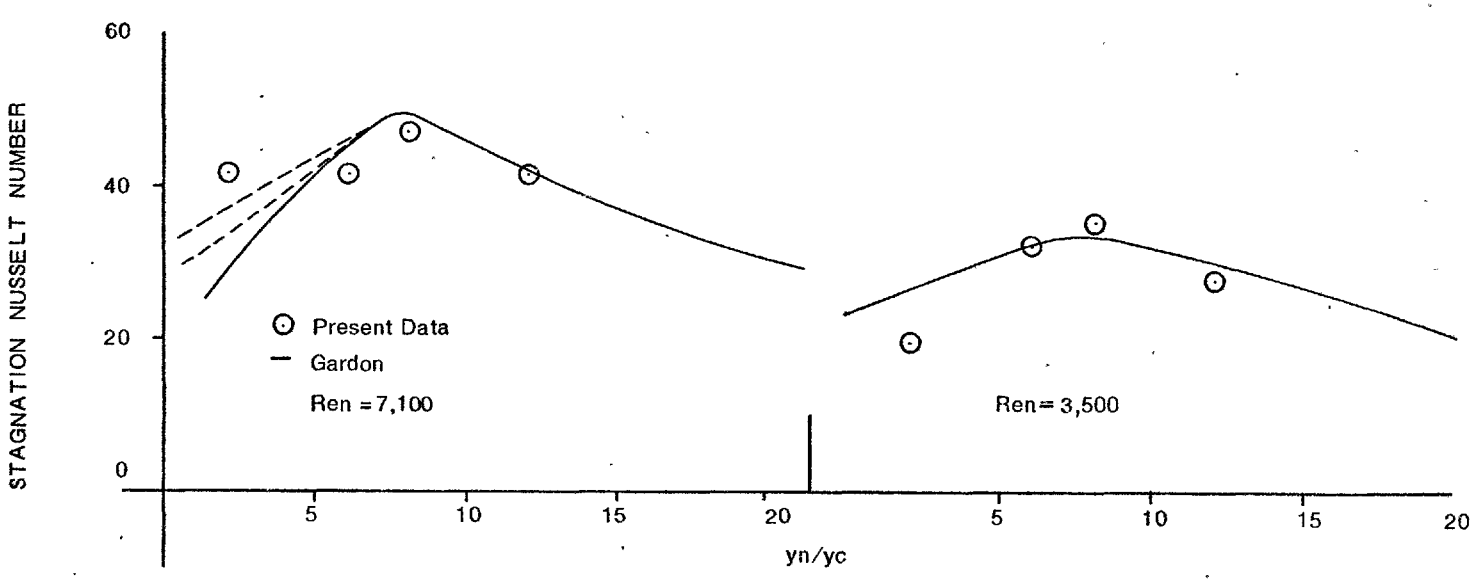

FIG. 5.2.10 Comparison of stagnation point Nusselt number with measurements of Gardon and Akfirat (51).

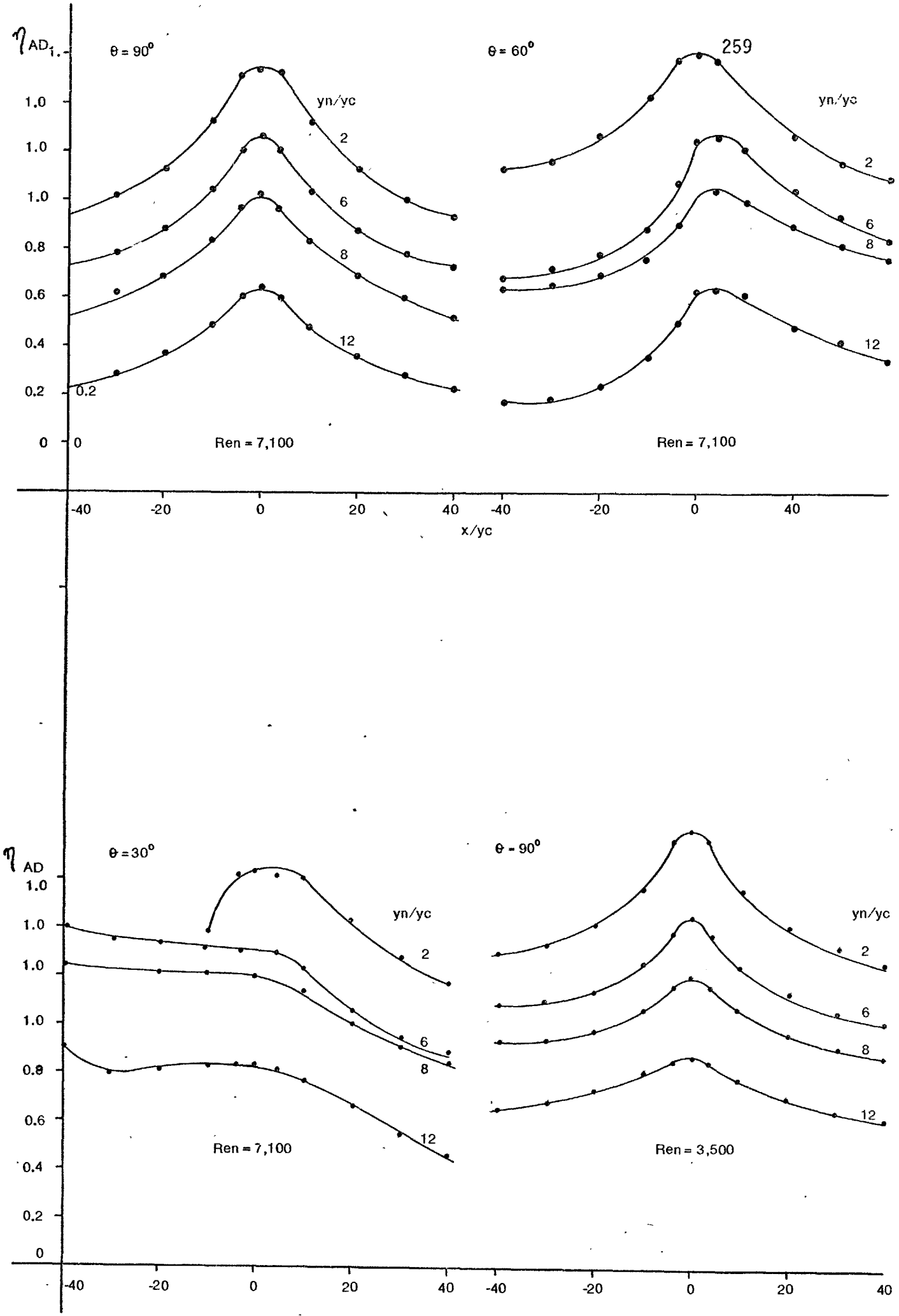

FIG. 5.2.11 Measured Adiabatic wall effectiveness.

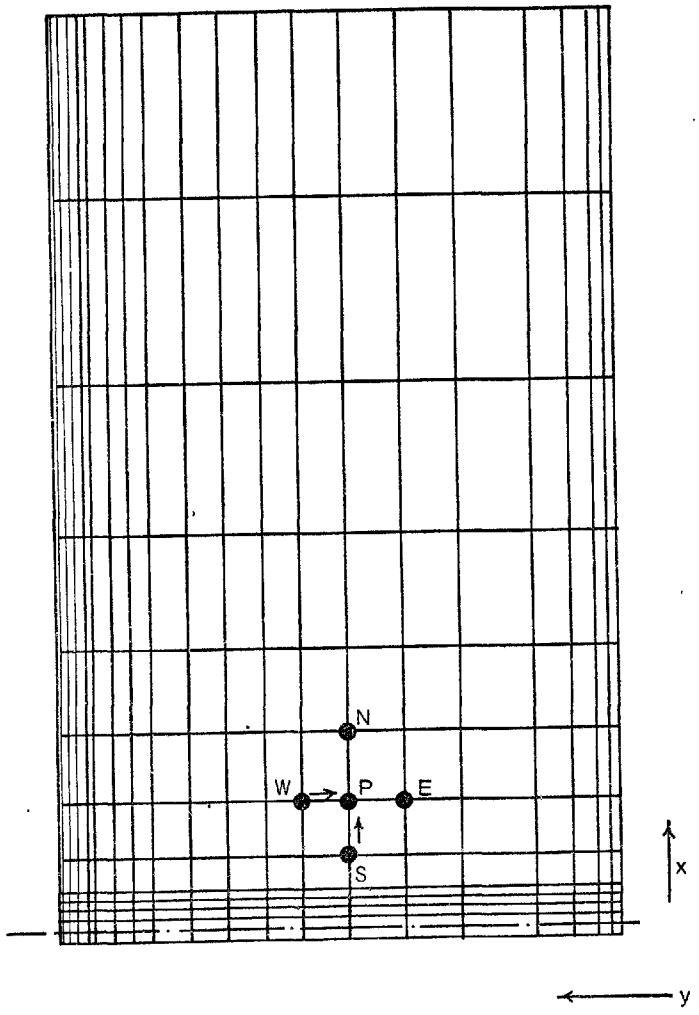

FIG. 5.3.1 Grid distribution

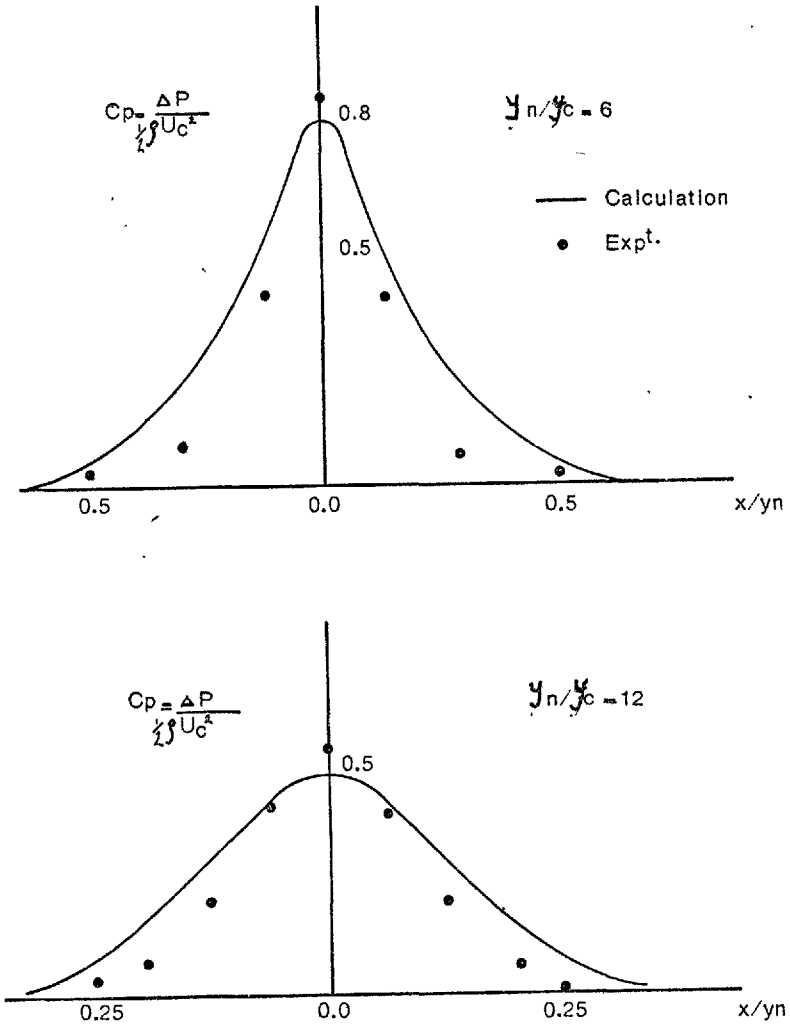

FIG. 4.3.2 Comparison of measured and calculated wall static pressures

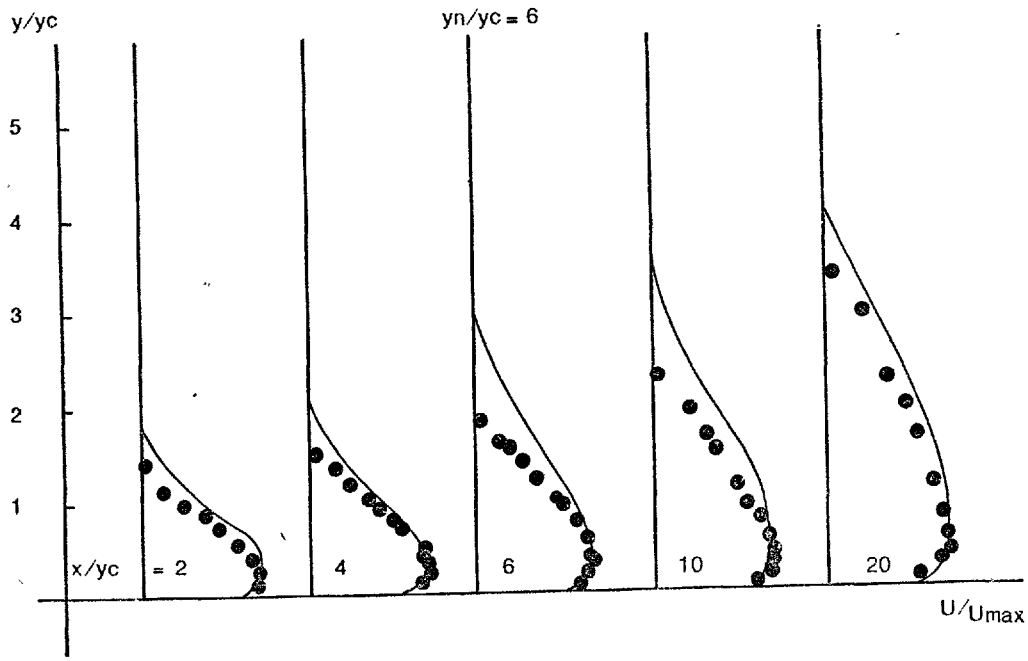

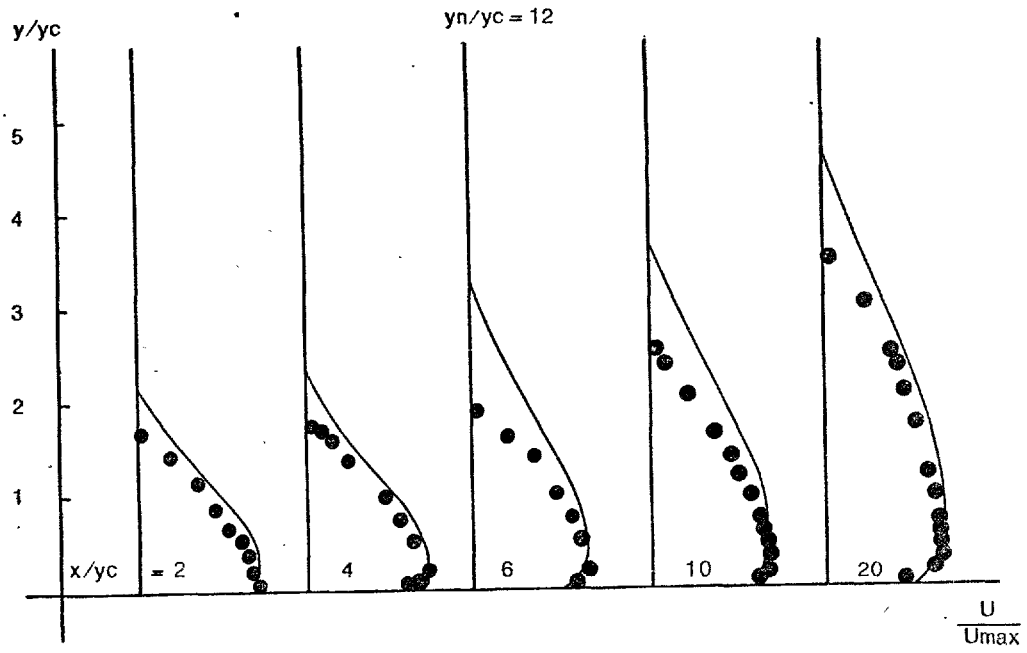

FIG. 5.3.3 Comparison of measured and calculated mean velocities parallel to the wall

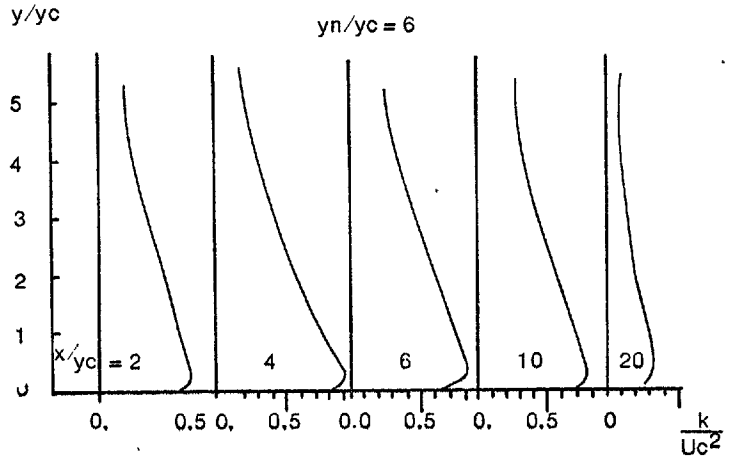

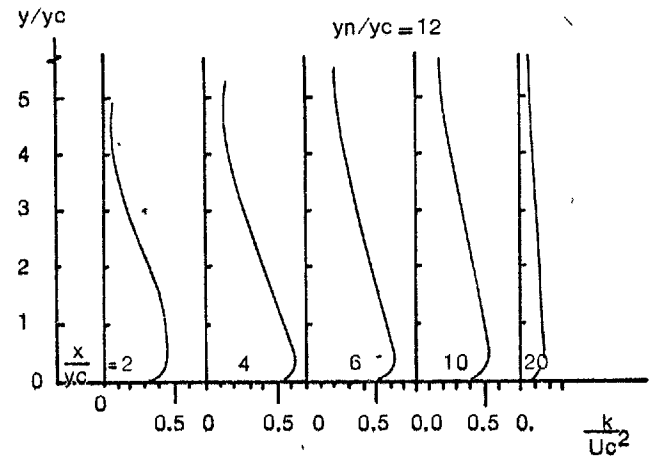

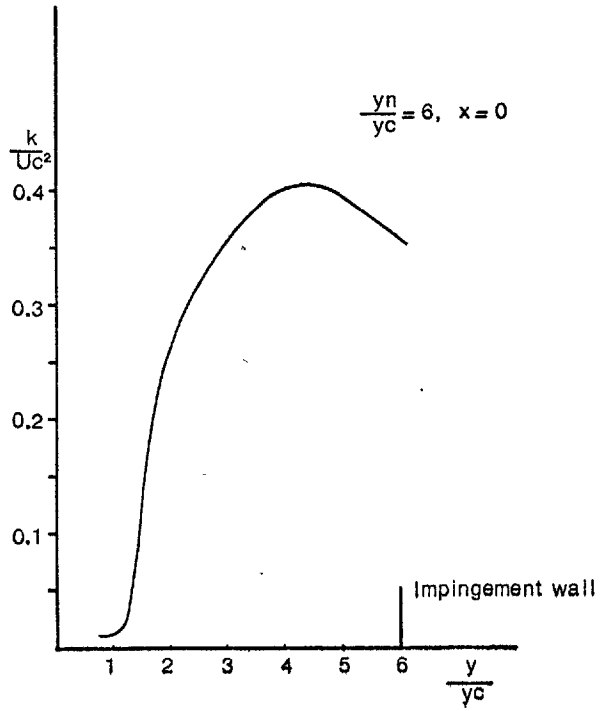

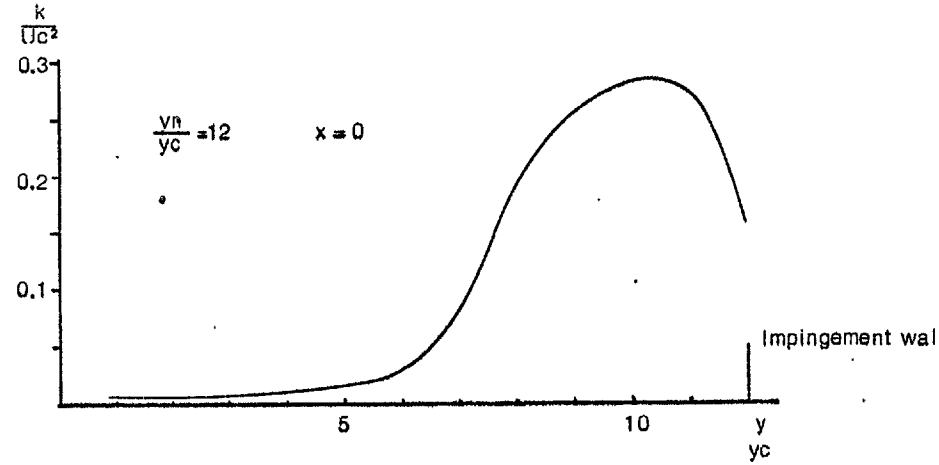

FIG. 5.3.4 Calculated turbulence kinetic energy

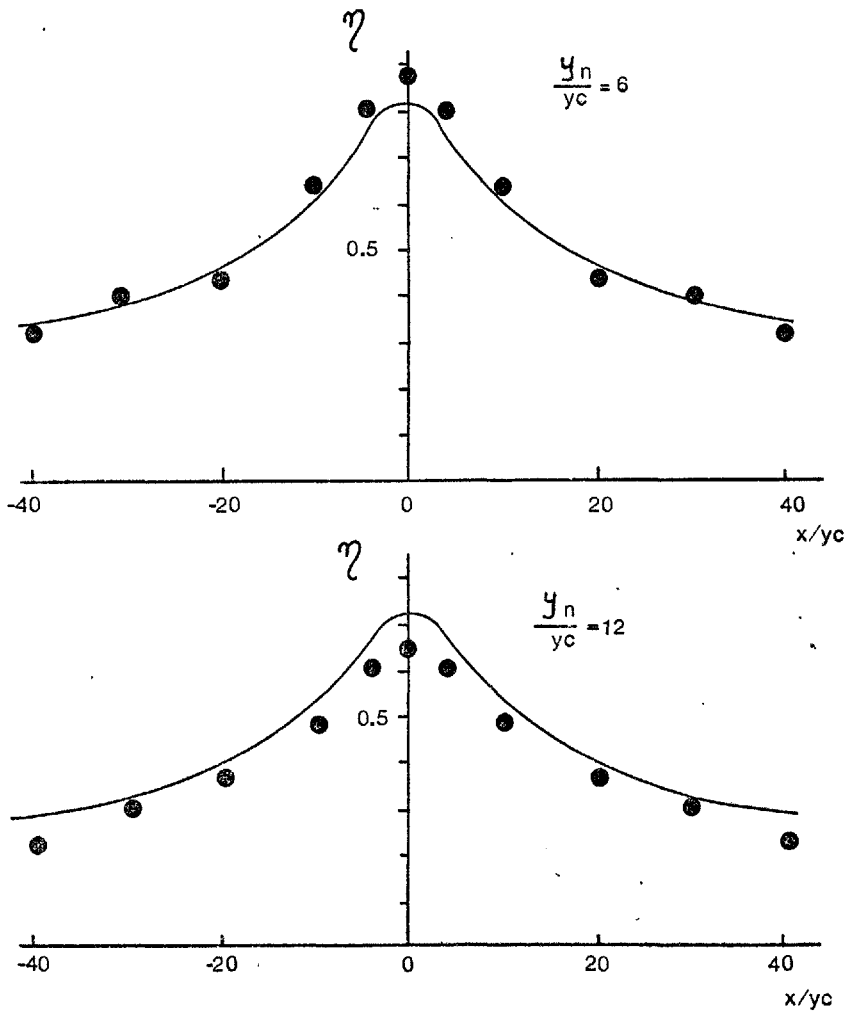

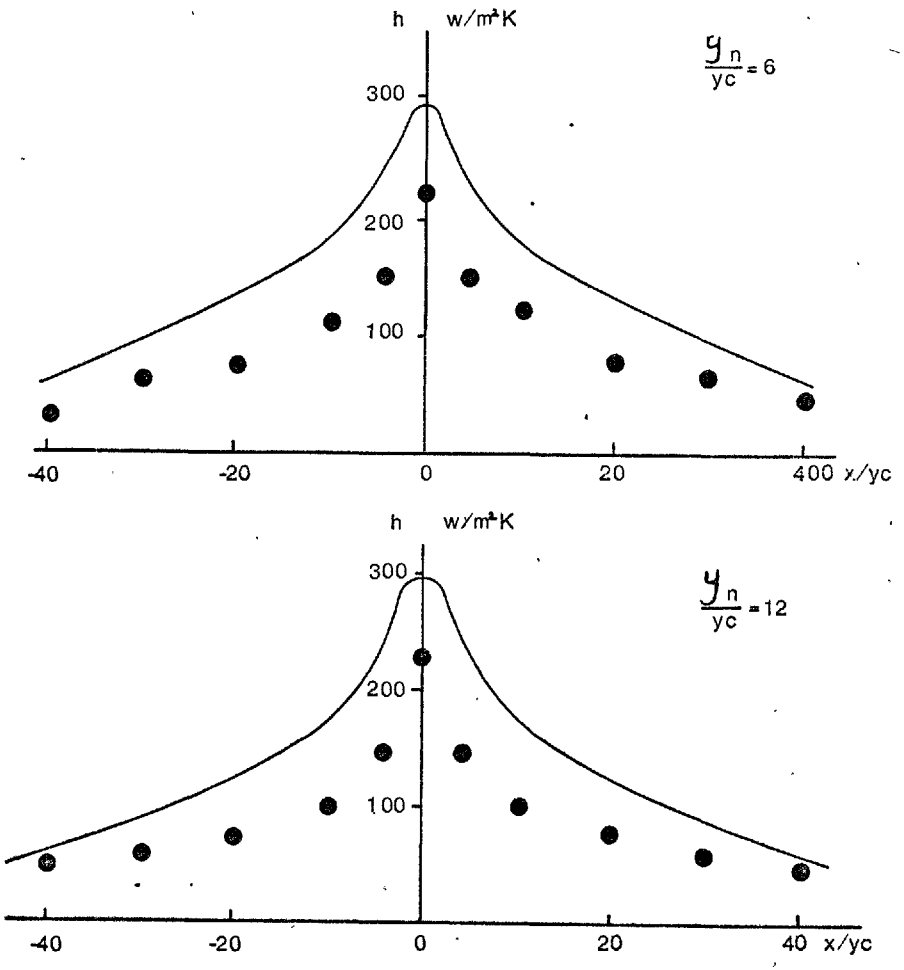

FIG. 5.3.5 Comparison of measured and calculated effectiveness and heat transfer

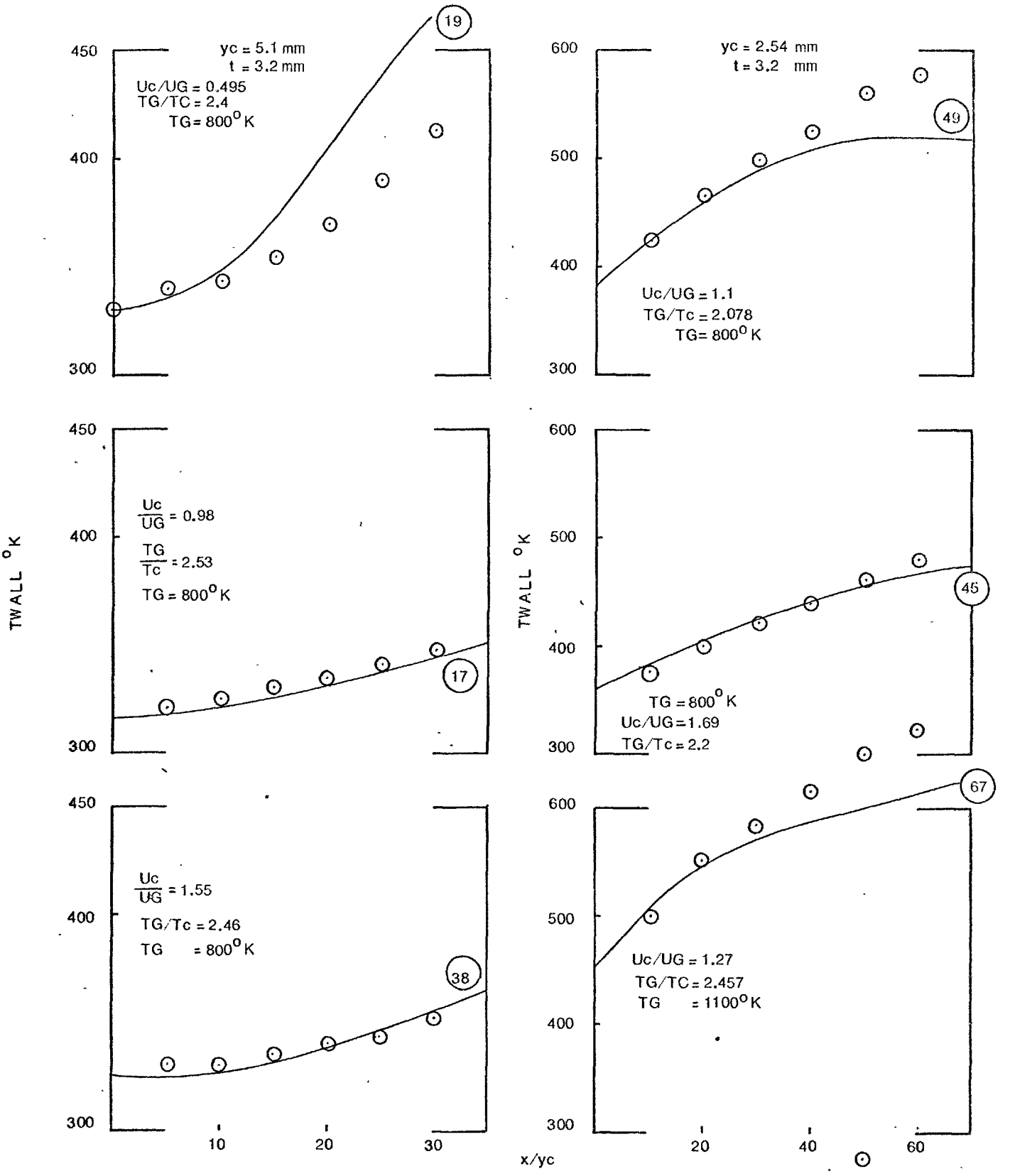

FIG. 6.3.1 Adiabatic combustor with 2 dimensional slots – Odgers and Winter (76)

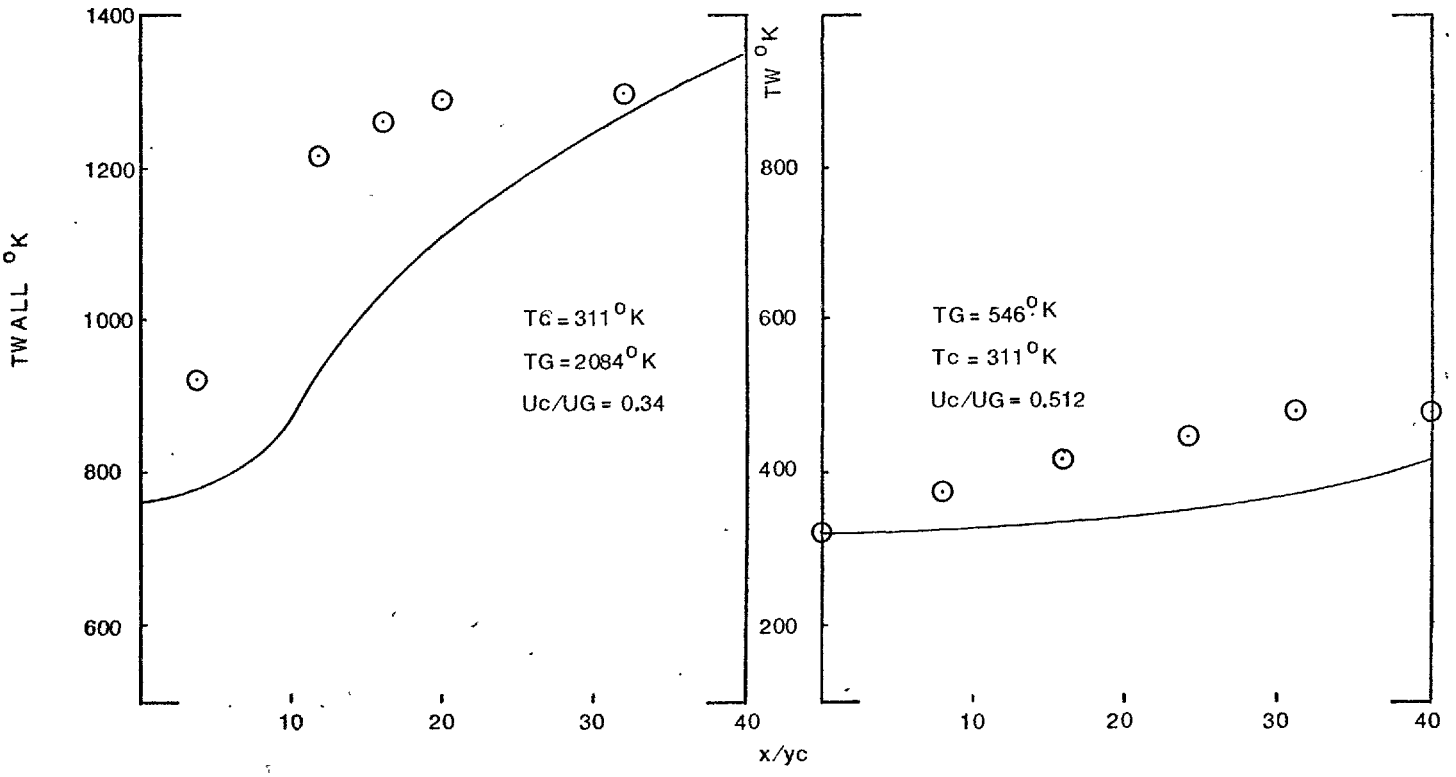

FIG. 6.3.2a Comparison between calculations and measurements Marek and Tacina (108)

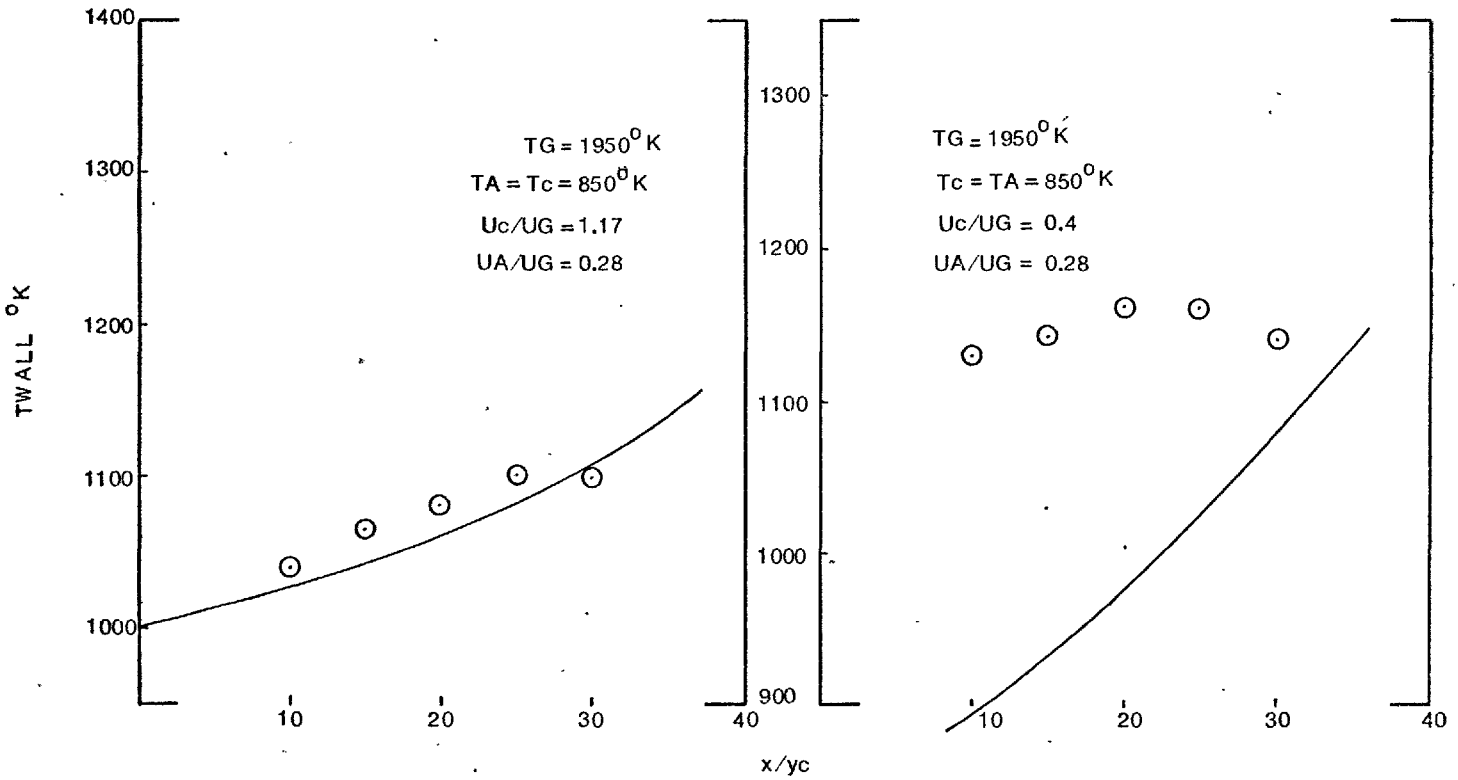

FIG. 6.3.2b Comparison between calculations and measurements Milford and Spiers (69)

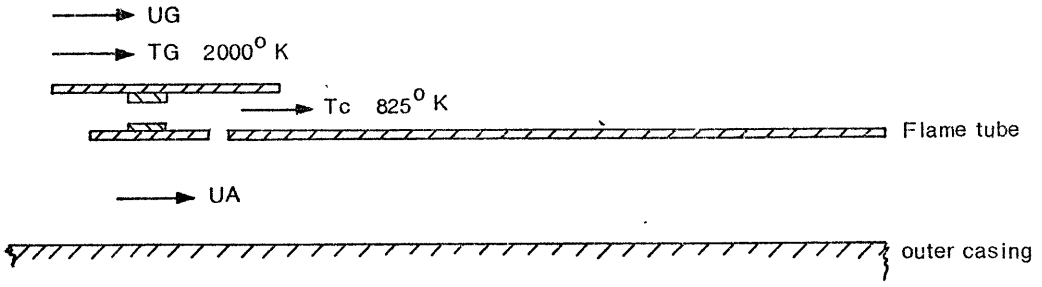

Uc/UG = 1.25
t/y = 0.3
Dt = Dn = 3.03 mm, yc = 3.5 mm

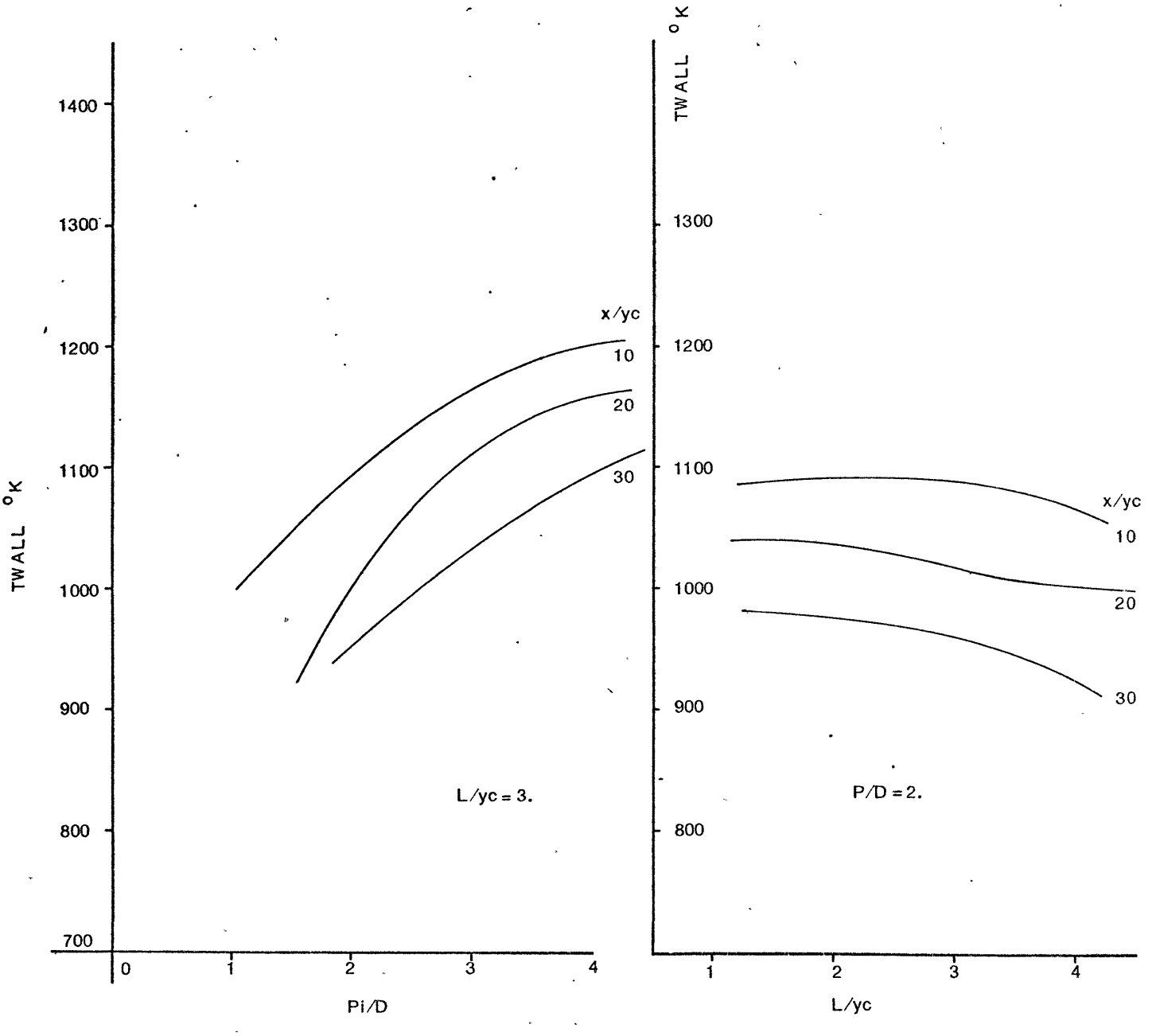

FIG. 6.3.3. Calculated influence of pitch-diameter ratio and lip-length

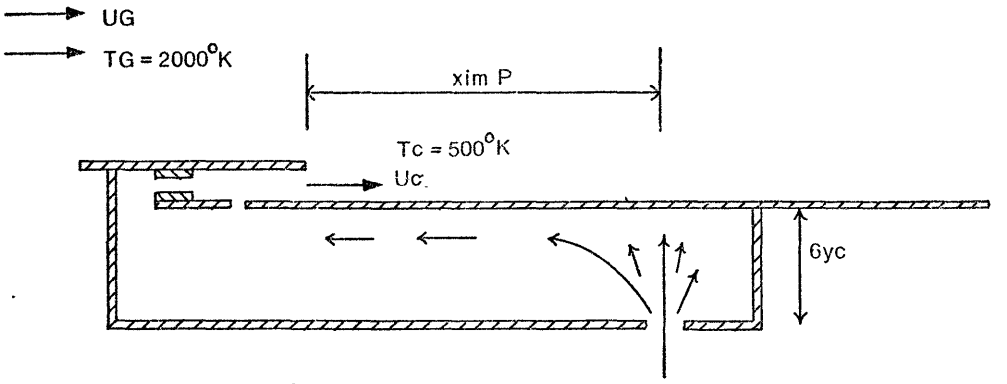

Rolls Royce ring R12/5

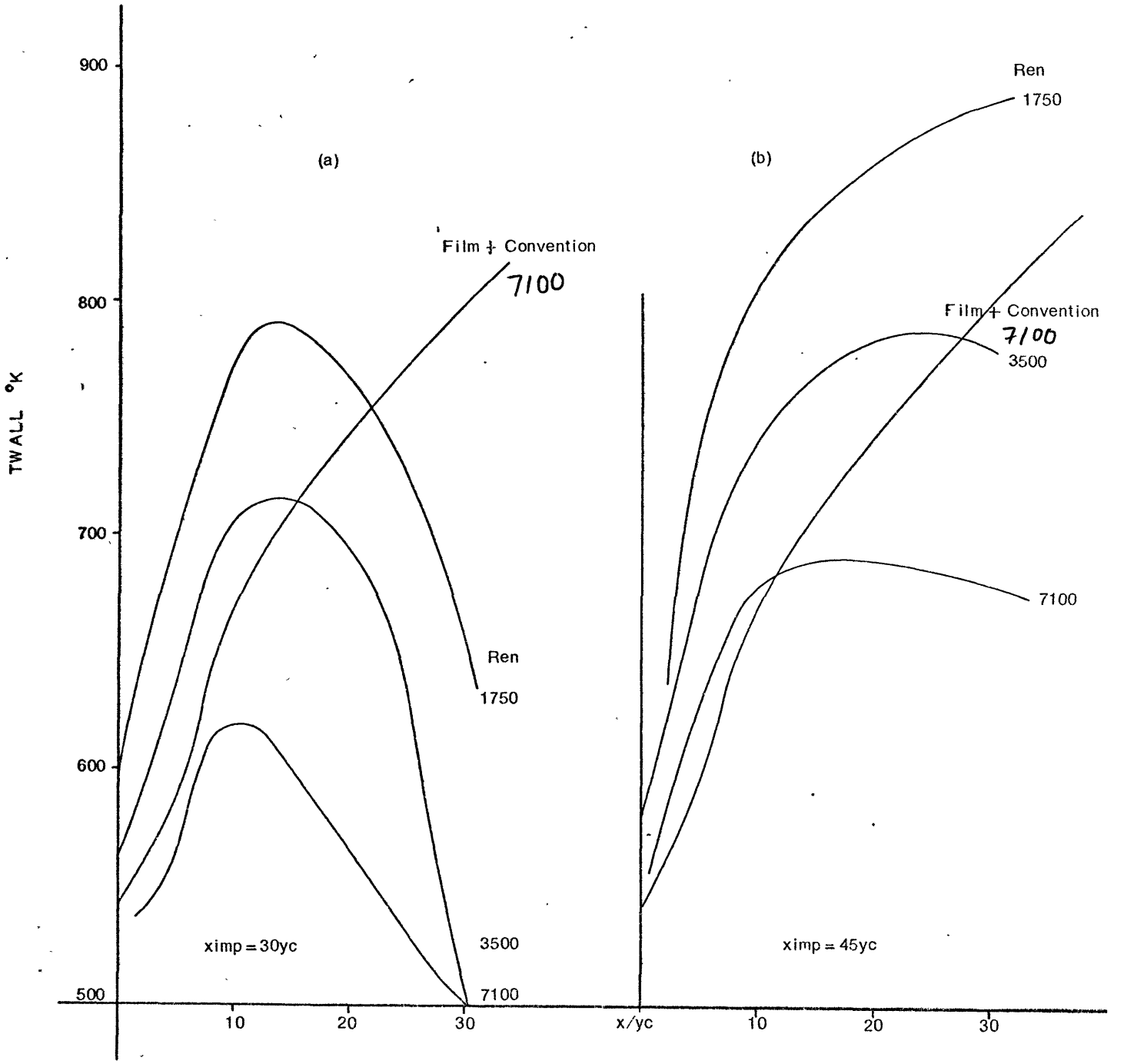

FIG. 6.3.4. Wall temperatures for impingement-film-cooled combustor

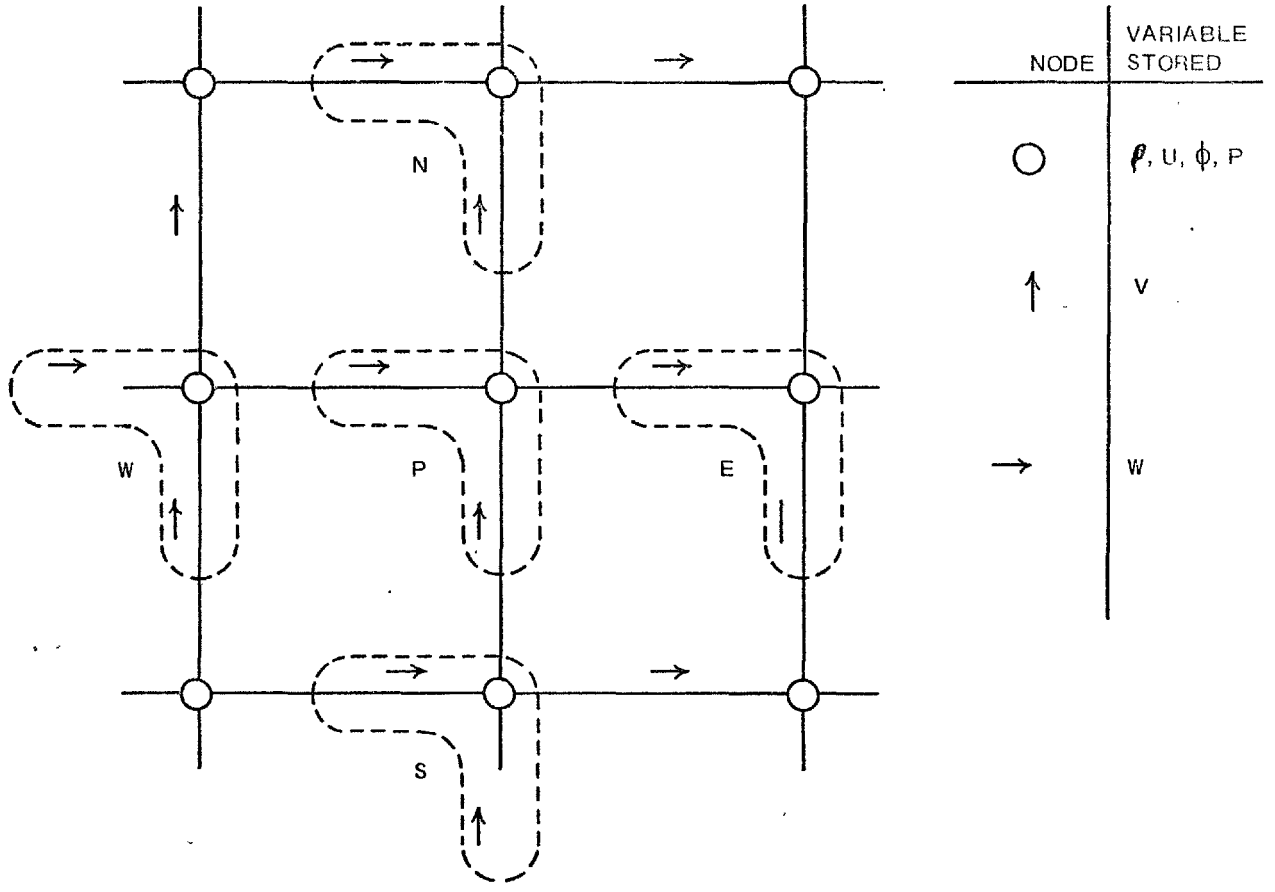

FIG. A.1. THE STAGGERED GRID ARRANGEMENT

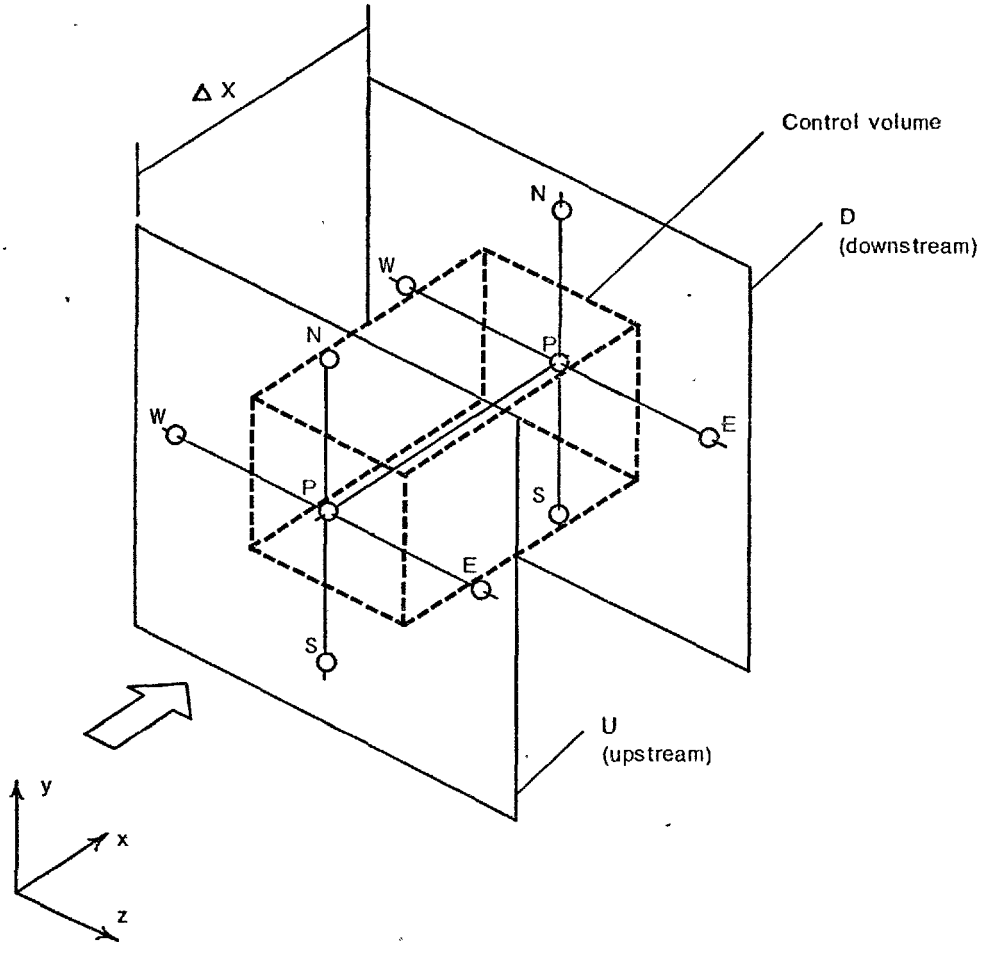

FIG. A.2. THE CONTROL VOLUME USED TO OBTAIN THE FINITE DIFFERENCE EQUATION

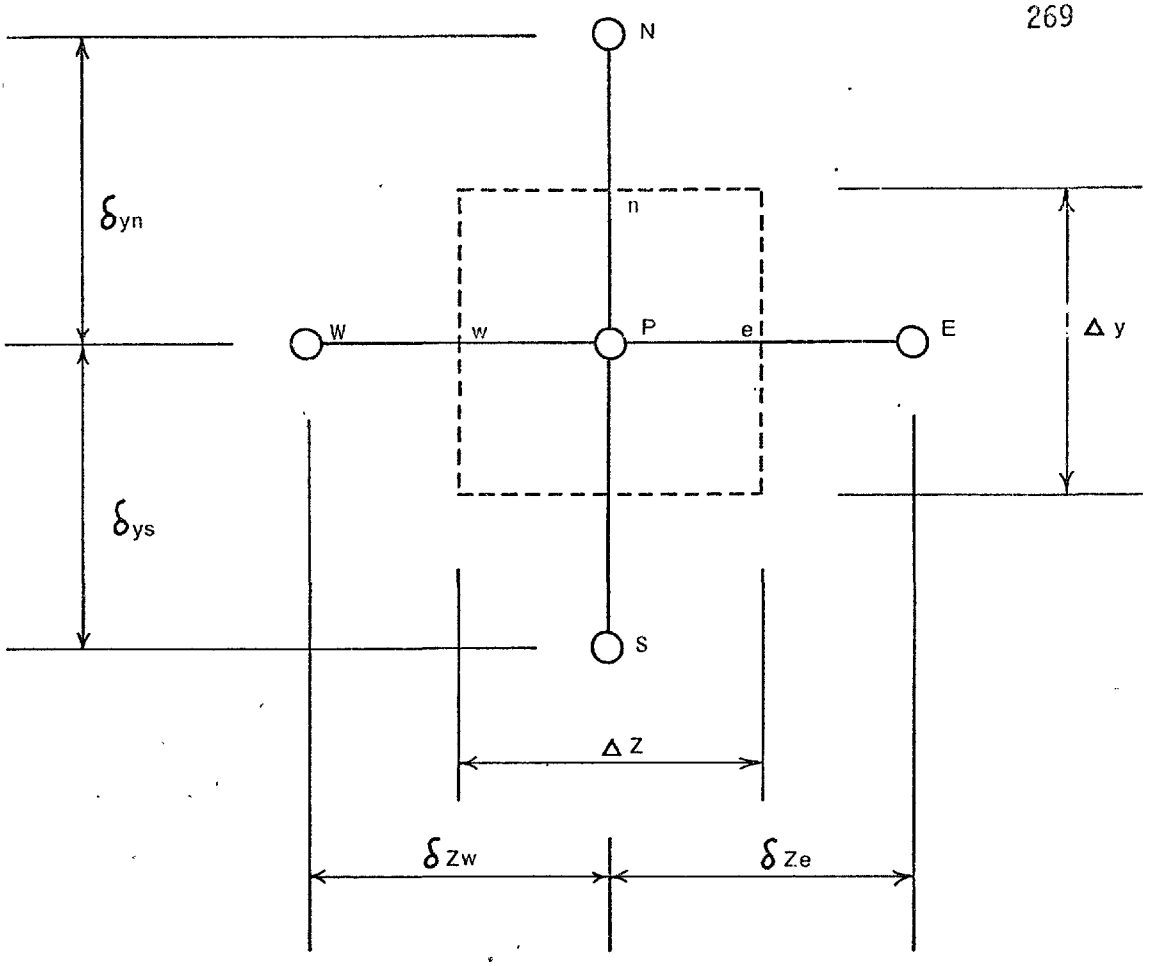

FIG. A.3. THE YZ FACE OF CONTROL VOLUME

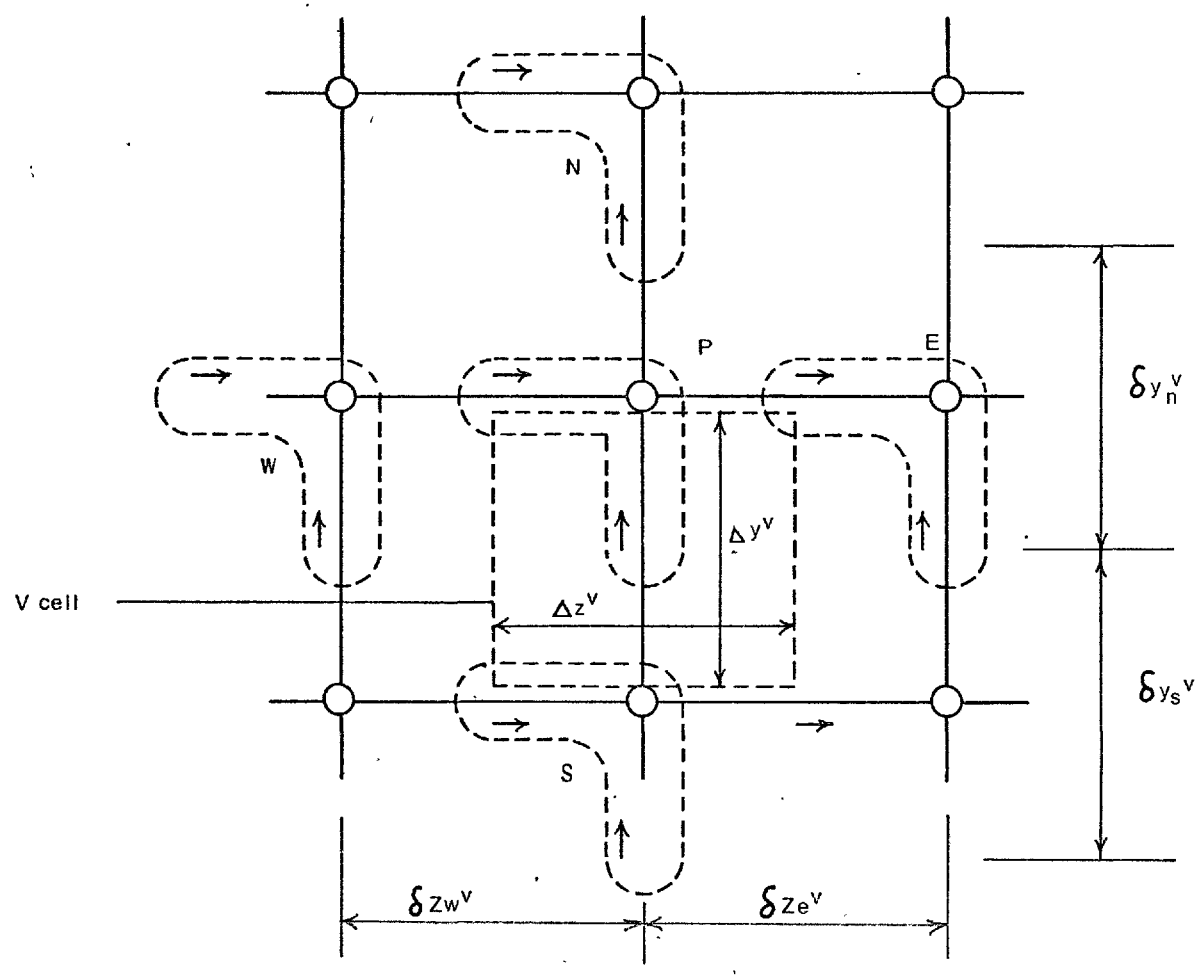

FIG. A.4. THE COMPUTATIONAL CELL FOR V

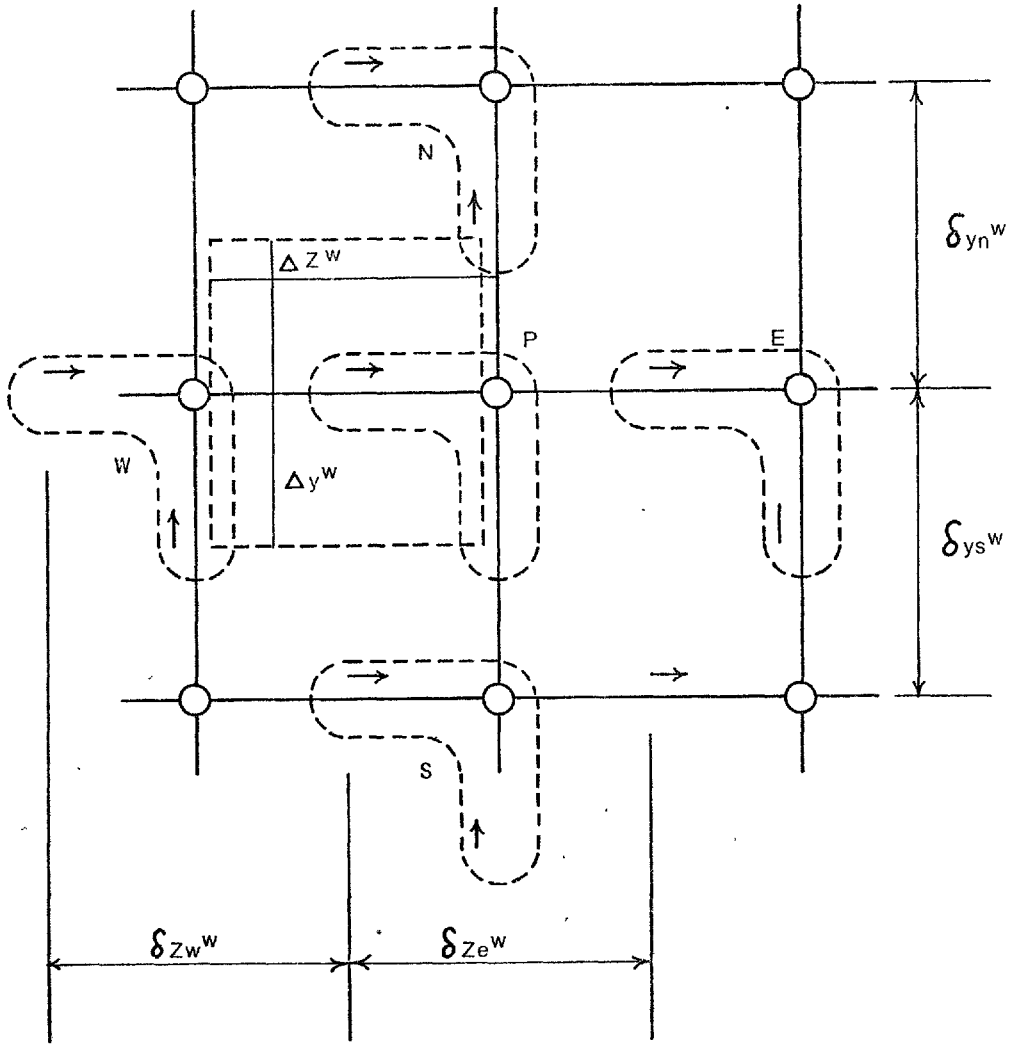

FIG. A.5. : THE COMPUTATIONAL CELL FOR W